



UNIVERSITÀ
DEGLI STUDI
DI PADOVA

Sede Amministrativa: Università degli Studi di Padova

Dipartimento di Ingegneria Industriale

CORSO DI DOTTORATO DI RICERCA IN: Ingegneria Industriale

CURRICOLO: Materiali

CICLO: XXX

Strategic metals recovery from wastes

Coordinatore: Ch.mo Prof. Paolo Colombo

Supervisore: Ch.mo Prof. Manuele Dabalà

Co-Supervisore: Ch.ma Prof. Katya Brunelli

Dottorando: Pietrogiovanni Cerchier

Abstract

The recovery of different types of metals from wastes has had a spreading interest in the last years. One reason is that wastes, and in particular e-waste, contain metals which are considered strategic. In fact, the availability of these metals is limited and decreases, as natural resources are limited, and their prices fluctuate according to the markets and the management policy of the resource country. Actually, strategic metals are generally defined as those metals that are required for the national defense of a country, but are threatened by supply disruptions due to limited domestic production. However, the definition of strategic metals can be also including those metals that are important not only for national defense, but also for industries that play an important role in the economic development of a country such as energy, aerospace, telecommunication, computer or mobile technology. Thus, it has become quite interesting and urgent to find a strategic way to recover these metals from the wastes.

In this work, the recovery of resources from different wastes was studied. In particular, after the introduction and the description of the experimental systems used in this research, the recovery of gold, together with other metals (silver, copper and tin), from the printed circuit boards (PCBs) of end of life (EOL) mobile phones is discussed in Chapter 3. Actually, both the most dangerous and the most precious metals could be founded in PCBs. In particular, it was studied a process which consists in an acid leaching process followed by the gold complexation with thiourea or thiosulphate, two substances that represent an alternative to the more toxic cyanides typically used for the selective gold dissolution. Furthermore, the effect of the ultrasound during the leaching was examined, in order to improve the recovery yield. In fact, in the latest years, ultrasound has been investigated to assist hydrometallurgical metals extraction from ores and minerals but their industrial application is until now limited, although the advantages derived from their application are: a greater metal release in shorter time, lower consumption of reagents and lower process temperature. Therefore, the use of ultrasound could represent an advantage because it increases the recovery of precious metals from the waste.

Subsequently, a study was conducted to evaluate a method to recovery silver from the end-of-life solar cells and, more generally, to design a simple and cheap process for the full recovery of the materials constituent the photovoltaic panels. In fact, different methods both hydrometallurgical and pyrometallurgical were tested and the best results were obtained using a combination of a heating treatment and three hydrometallurgical ones.

The process parameters were optimized, both for heating and chemical treatments. The results of this study are presented in Chapter 4.

Moreover, because the idea seems economically valuable, the process in lab scale was also improve at TRL 5 and the obtained results were used to apply successfully for European funding. In fact, “ReSiELP” project was approved, with the aim to improve the TRL of the technology from 5 to 7.

Successively, in Chapter 5 is described the study of recovering Tantalum from EOL capacitors and Neodymium from permanent magnets. In order to separate tantalum from silica, a new treatment with hydrofluoric acid was investigated and tested, whereas the process known in literature for neodymium recovery, was modified introducing a treatment with ammonia which increase the purity of recovered neodymium and sodium double salt.

After these studies about metals extraction from e-wastes, a method to increase the added value of recovered material was investigated. In fact, besides the intrinsic value of these metals, a further value could be achieved by recovering these metals in form of nanoparticles, which exhibit very interesting and promising properties in comparison with the corresponding bulk materials. Size-dependent properties include, but are not limited to, the following: optical, magnetic, catalytic, thermodynamic, electrochemical properties and electrical transport. Moreover, nanomaterials may provide solutions to technological and environmental challenges in the areas of solar energy conversion, catalysis, medicine, and water treatment.

Different nanoparticles were produced using as raw material the solutions in which electronic scraps were previously leached. In particular, nanoparticles of tin dioxide, silver, copper, cuprous oxide, gold and iron were synthesized and characterized and the results of the study are presented in Chapter 6. All the nanoparticles were synthesized using hydrometallurgical processes and the reagents used were environmentally friendly (like ascorbic acid or glucose syrup) as well as the technologies (ultrasound) used to produce them and to improve the yields in metals extraction from the e-waste. The use of ultrasound in nanoparticles production allows to reduce the sizes of the products thanks to the cavitation effect which produces locally extreme conditions during the nanoparticles nucleation and growth processes.

Different processes were developed to produce the six different type of nanoparticles. The materials obtained were analysed by inductive coupled plasma, scanning and transmission electron microscopy, x-ray diffraction, laser diffraction particle size analyser and UV-spectroscopy.

The results showed that the developed methods allow to recover the metals with high yield and to produce high purity nanoparticles of tin dioxide, silver, copper, cuprous oxide, gold and iron with sizes between 2 and 200 nm.

Finally, some interesting and innovative application for the recovered metals, in particular silver and copper, were also studied and the results are presented in Chapter 7 of this thesis work. The silver and copper powder were introduced into Plasma Electrolytic Oxidation coating. Plasma electrolytic oxidation (PEO), also called 'Microarc Oxidation' (MAO) is relatively new surface modification technique that shows an increasing interest in the production of oxide ceramic coatings on light alloys such as aluminium, titanium or magnesium. PEO coatings can enhance the corrosion and wear resistance properties of these metals, or can confers to the light alloys various other functional properties including anti-friction, thermal protection, optical and dielectric features. Furthermore, PEO can be used as a pre-treatment to provide load support for top layers. PEO is a process derived from conventional anodizing which shows many advantages such as

higher corrosion and wear resistance performances of the coatings, more environmental friendly electrolytes and the possibility to include into the coatings particles coming from the electrolyte. PEO of metals is a complex process that combines oxide film formation, dissolution and dielectric breakdown: the sample, as anode, is immersed in an electrolyte and it works with high voltages and current densities inside a tank which constitute the cathode of the electrolytic cell. Due to the high voltage that needs to overcome the dielectric breakdown potential of the oxide layer, the formation of a persistent anodic micro-discharges on the surface during the PEO treatment is observed. These short-lived micro-discharges are the key of the process; they move randomly over the surface and produce the growth of an oxide ceramic coating and they also allow to incorporate compounds from the electrolyte into the coating.

In the studies presented in this thesis silver and copper powder were introduced into PEO coating by direct addition into the electrolyte to improve respectively the antimicrobial/antifungal and the antifouling properties of the sample surfaces.

Sommario

Negli ultimi tempi il recupero di diversi tipi di metalli dai rifiuti ha acquistato notevole interesse. Una delle ragioni è che i rifiuti, e in particolare i rifiuti elettronici, contengono metalli considerati strategici. Infatti, la disponibilità di questi metalli è limitata e diminuisce, poiché le risorse naturali sono limitate, e i loro prezzi variano in base ai mercati e alla politica di gestione dei paesi produttori. In realtà, i metalli strategici sono generalmente definiti come metalli che sono necessari per la difesa nazionale di un paese, ma sono minacciati da interruzioni di approvvigionamento a causa della modesta produzione nazionale. Tuttavia, la definizione di metalli strategici può includere anche i metalli che sono importanti non solo per la difesa nazionale, ma anche per le industrie che svolgono un ruolo importante nello sviluppo economico di un paese, ad esempio quelle legate all'energia, all'ambito aerospaziale, a quello delle telecomunicazioni, computer e tecnologia mobile. Per queste ragioni è diventato molto interessante ed urgente trovare un modo strategico per recuperare questi metalli dai rifiuti.

In questo lavoro, è stato studiato il recupero di risorse da diversi rifiuti. In particolare, dopo l'introduzione e la descrizione dei sistemi sperimentali, nel Capitolo 3 viene discusso il recupero dell'oro, unitamente ad altri metalli (argento, rame e stagno) dalle schede di circuiti stampati (PCB) a fine vita. Si consideri che i metalli più pericolosi e preziosi sono contenuti proprio nei circuiti stampati. In particolare, è stato studiato un processo che comprende un attacco acido seguito dalla complessazione oro con tiourea o tiosolfato, due sostanze che potrebbero sostituire i ben più tossici cianuri, tipicamente utilizzati per la dissoluzione dell'oro. Inoltre, è stato esaminato l'effetto degli ultrasuoni durante la lisciviazione, al fine di verificare se il loro effetto consentisse di aumentare la resa d'estrazione. Infatti, negli ultimi anni, gli ultrasuoni sono stati studiati per assistere l'estrazione idrometallurgica dei metalli da minerale ma la loro applicazione industriale è ancora limitata, nonostante diversi vantaggi siano stati riconosciuti dalla loro applicazione: una maggiore liberazione dei metalli in tempi più brevi, minore concentrazione di reagenti necessaria e basse temperature di lavoro. Pertanto, l'uso di ultrasuoni potrebbe rappresentare un vantaggio per aumentare anche il recupero dei metalli preziosi dai rifiuti. Successivamente, è stato condotto uno studio per valutare il recupero dell'argento da pannelli fotovoltaici a fine vita e, più in generale, il processo più semplice e più economico per il completo recupero di risorse dai pannelli fotovoltaici.

Sono stati quindi testati diversi metodi sia idrometallurgici che pirometallurgici e i risultati migliori si sono ottenuti combinando un trattamento pirometallurgico e tre idrometallurgici.

I parametri di processo, come temperatura e durata del trattamento sono stati studiati e ottimizzati, sia per il riscaldamento che per i trattamenti chimici e i risultati di questo studio sono presentati nel Capitolo 4.

Inoltre, visto che l'idea sembra economicamente valida, è stata anche testata a TRL 5 e i risultati emersi sono stati utilizzati per richiedere un finanziamento europeo. Infatti, è stato approvato il

progetto "ReSiELP", che in tre anni dovrebbe costruire un impianto per esportare questa tecnologia a TRL 7.

Successivamente, nel Capitolo 5, è stato studiato un modo per recuperare il tantalio dai condensatori a fine vita e neodimio da magneti permanenti. Per separare il tantalio dalla silice, è stato studiato e testato un trattamento con acido fluoridrico, mentre nel recupero del neodimio il processo noto in letteratura è stato modificato introducendo un trattamento con ammoniaca che aumenta la purezza del sale doppio di neodimio e sodio che viene recuperato.

Dopo questi studi sull'estrazione dei metalli da rifiuti elettronici, è stato testato un metodo per aumentare il valore del materiale recuperato. Infatti, oltre al valore intrinseco di questi metalli, un ulteriore vantaggio potrebbe essere ottenuto recuperando questi metalli sotto forma di nanoparticelle, le quali presentano proprietà molto interessanti e promettenti in confronto ai corrispondenti materiali massivi. Le proprietà di quest'ultime sono ottiche, magnetiche, catalitiche, termodinamiche ed elettrochimiche. Inoltre, i nanomateriali possono fornire soluzioni alle sfide tecnologiche e ambientali nei settori della conversione energetica, della catalisi, della medicina e del trattamento dell'acqua.

In quest'ottica, sono state prodotte nanoparticelle diverse utilizzando come materie prime le soluzioni in cui erano stati precedentemente trattati i rifiuti elettronici. In particolare sono state sintetizzate e caratterizzate nanoparticelle di ossido di stagno, argento, rame, ossido di rame, oro e ferro, ed i risultati dello studio sono presentati nel Capitolo 6. Tutte le nanoparticelle sono state sintetizzate utilizzando processi idrometallurgici e l'utilizzo di reagenti il più possibile ecocompatibili (quali l'acido ascorbico o lo sciroppo di glucosio) nonché la sperimentazione di una tecnologia, quali gli ultrasuoni, considerata ecologica e già testata durante la lisciviazione dei rifiuti elettronici. In questo caso, l'applicazione degli ultrasuoni ha consentito di ridurre le dimensioni delle particelle sintetizzate grazie all'effetto di cavitazione che generano nel liquido. Sono stati sviluppati diversi processi per produrre i sei tipi di nanoparticelle. I materiali ottenuti sono stati analizzati con plasma ad accoppiamento induttivo (ICP), microscopia a scansione e trasmissione elettronica (SEM e TEM), diffrazione a raggi X, diffrazione laser e spettroscopia UV. I risultati hanno dimostrato che i metodi sviluppati consentono di recuperare i metalli con elevata resa e di produrre nanoparticelle di ossido di stagno, argento, rame, ossido di rame, oro e ferro ad alta purezza e di dimensioni comprese tra 2 e 200 nm.

Infine, è stata studiata anche un'applicazione interessante e innovativa per i metalli recuperati, in particolare argento e rame, ed i risultati riportati nel Capitolo 7 di questa tesi. In particolare, l'argento e la polvere di rame sono stati introdotti nel rivestimento di ossidazione elettrolitica al plasma.

L'ossidazione al plasma elettrolitico (PEO), chiamata anche "*Microarc Oxidation*" (MAO), è una tecnica di rivestimento superficiale relativamente nuova ma che inizia ad essere impiegata nella produzione di rivestimenti ceramici d'ossido su leghe leggere quali l'alluminio, il titanio o il magnesio. Il trattamento PEO può migliorare le proprietà di resistenza alla corrosione e all'usura

di questi metalli o conferisce diverse altre proprietà funzionali, tra cui diminuzione dell'attrito e protezione termica. Inoltre, il PEO può essere utilizzato come pretrattamento per fornire un substrato per altri rivestimenti. Il PEO deriva dall'anodizzazione convenzionale, ma presenta molti vantaggi, come ad esempio elevate proprietà dei rivestimenti di resistenza a usura e corrosione, l'impiego di elettroliti più rispettosi dell'ambiente e la possibilità di inserire nel rivestimento particelle provenienti dall'elettrolita.

Il PEO dei metalli è un processo complesso che combina la formazione di film di ossido, la dissoluzione e la rottura del dielettrico: il campione, come anodo, è immerso in un elettrolita ed il processo impiega elevate tensioni e densità di corrente all'interno di un serbatoio che funge da catodo. A causa dell'elevata tensione che deve essere al di sopra del potenziale di rottura del dielettrico, durante il trattamento PEO vi sono micro-scariche anodiche persistenti sulla superficie. Queste micro-scariche di breve durata sono la chiave del processo; si muovono casualmente sulla superficie trattata provocando la crescita di un rivestimento ceramico d'ossido e permettendo di incorporare composti nel rivestimento. Negli studi presentati in questa tesi, le polveri di argento e rame sono state introdotte nel rivestimento PEO mediante aggiunta diretta nell'elettrolita per conferire rispettivamente l'effetto antimicrobico / antimicotico e antivegetativo ai campioni.

List of Contents

Abstract	i
Sommario	v
List of Contents	ix
Chapter 1 Introduction	1
1.1 THE E-WASTE PROBLEM [1].....	1
1.1.1 <i>Definition</i>	1
1.1.2 <i>Quantities of WEEE</i>	2
1.1.3 <i>E-waste routes</i>	8
1.1.4 <i>Content of WEEE</i>	11
1.2 RECOVERY TECHNIQUES [15]	14
1.2.1 <i>Pre-treatment</i>	15
1.2.2 <i>Physical separation processes</i>	16
1.2.3 <i>Pyrometallurgy [18]</i>	18
1.2.3.1 <i>Adherent Technologies Inc.</i>	20
1.2.3.2 <i>Boliden Mineral AB</i>	20
1.2.3.3 <i>Union Mineria (UM)</i>	21
1.2.4 <i>Hydrometallurgy</i>	22
1.2.4.1 <i>Acid leaching of metals</i>	i
1.2.4.2 <i>Leaching of precious metals</i>	26
1.2.4.3. <i>Solution purification and metal recovery</i>	28
1.3 GREEN CHEMISTRY	29
1.3.1 <i>Green complexing agents: thiosulphate and thiourea</i>	33
1.3.1.1 <i>Thiourea</i>	33
1.3.1.2 <i>Sodium thiosulphate</i>	35
1.4 THE ULTRASOUND	37
1.4.1 <i>The acoustic cavitation</i>	37
1.4.2 <i>Transient and Stable Cavitation</i>	38
1.4.3 <i>Nucleation of Bubbles</i>	41
1.4.4 <i>Growth of a Bubble</i>	42
1.4.5 <i>Radiation Forces on a Bubble (Primary and Secondary Bjerknes Forces)</i>	43
1.4.6 <i>Bubble Radial Dynamics</i>	44
1.4.5 <i>Inertial Collapse (Rayleigh Collapse)</i>	46
1.4.5 <i>Three sites for chemical reaction</i>	48
1.4.6 <i>Application of Ultrasound</i>	49
1.4.6.1 <i>Nucleation of Particles by Ultrasound</i>	49

1.4.6.2 Enhancement of Mass Transfer	49
1.4.8 Ultrasonic horn	51
Chapter 2 Experimental system.....	53
2.1 SCANNING ELECTRON MICROSCOPE (SEM).....	53
2.2 X-RAY FLUORESCENCE (XRF)	55
2.3 ICP-OES	55
2.4 POTENTIOSTAT FOR ELECTRODEPOSITION.....	56
2.5 POTENTIOSTAT FOR CORROSION TESTS	56
2.6 X-RAY DIFFRACTOMETER (XRD)	57
2.7 SONICATOR	57
2.8 TRANSMISSION ELECTRON MICROSCOPE	58
2.9 LASER DIFRACTION	58
2.10 SECONDARY ION MASS SPECTROMETRY (SIMS).....	59
2.11 UV-VIS ABSORPTION	59
2.12 XPS	60
2.13 TGA	60
2.14 SVET	61
Chapter 3 Gold recovery from PCBs: thiourea and thiosulphate leaching.....	63
3.1 THE PCBs TECHNOLOGY [67]	63
3.1.1 History	65
3.1.2 Design	65
3.1.3 Raw Materials.....	66
3.1.4 The Manufacturing Process	66
3.1.4.1 Making the substrate.....	67
3.1.4.2 Drilling and plating the holes.....	67
3.1.4.6 Creating the printed circuit pattern on the substrate	67
3.1.4.7 Attaching the contact fingers	69
3.1.4.8 Fusing the tin-lead coating	69
3.1.4.9 Sealing, stenciling, and cutting the panels.....	69
3.1.4.10 Mounting the components.....	69
3.1.4.11 Packaging.....	69
3.1.4.12 Quality Control	70
3.1.5 Toxic Materials and Safety Considerations.....	70
3.2 CHARACTERIZATION	71
3.3 PRE-TREATMENT WITH ACID	75
3.4 LEACHING WITH THIOUREA	76
3.5 RECOVERY OF COPPER, GOLD AND SILVER FROM THIOUREA LEACHING PROCESS	79

3.6 LEACHING WITH THIOUSULPHATE.....	80
3.7 CONCLUDING REMARKS	82
Chapter 4 Recycling of PV panels	83
4.1 PV PANELS MARKET	85
4.1.1 Italian market.....	86
4.1.2 Estimation of the amount of wastes	86
4.1.2 Regulation about end of life PV panels	88
4.2 THE PV PANEL TECHNOLOGY [77]	89
4.2.1 The photovoltaic cell [78, 79, 80, 81]	90
4.2.2 Silicon	93
4.2.3 Silicon production.....	94
4.2.4 Importance of Silicon purity	96
4.2.5 Silicon refining	97
4.2.6 Silicon cristallinity.....	99
4.2.7 Wafer manufacturing.....	100
4.2.8 PV cells manufacturing.....	102
4.2.8.1 Saw-damaged layer removal.....	102
4.2.8.2 Texturing.....	102
4.2.8.3 Emitter diffusion (junction formation).....	102
4.2.8.4 Edge isolation.....	102
4.2.8.5 Anti-reflection coating	103
4.2.8.6 Metal contact formation (metallization)	103
4.2.8.7 Contact firing	103
4.2.9 PV modules manufacturing.....	104
4.2.9.1 Glass.....	104
4.2.9.2 EVA.....	104
4.2.9.3 Backsheet.....	104
4.2.9.4 Cell Ribbon	104
4.2.9.5 Junction Box.....	105
4.2.9.6 Frame	105
4.3 PV PANELS RECYCLING PROCESSES [89, 90, 91, 92]	106
4.3.1 Review of existing IPRs on Si-PV waste recycling	108
4.4 PV PANEL CHARACTERIZATION	109
4.4.1 Silicon cells.....	109
4.4.2 Ribbons.....	111
4.4.3 Estimation of the amount of silver	112
4.4.3.1 Busbars:	112
4.4.3.2 Fingers	112

4.4.3.3 Outline:.....	113
4.4.3.4 Amount of silver	113
4.4.4 Estimation of the amount of aluminum.....	114
4.4.5 Estimation of the amount of silicon.....	114
4.4.6 Estimation of the material in 60 cells PV module:.....	114
4.5 MATERIAL SEPARATION.....	116
4.5.1 Chemical Method.....	116
4.5.2 Thermal Method	117
4.5.3 Off-gases analysis.....	119
4.5.3.1 Methods	119
4.5.3.2 Results	119
4.5.4 Test at TRL 5	122
4.6 HYDROMETALLURGICAL TREATMENTS	124
4.6.2 Sodium hydroxide treatment	124
4.6.1 Nitric acid treatment	126
4.6.3 Test at TRL 5	129
4.7 SILVER AND SILICON RECOVERY.....	130
4.7.1 Silver recovery.....	130
4.7.1.2 Electrodeposition	130
4.7.1.2 Silver oxide precipitation	132
4.7.1.2 Silver chloride precipitation.....	134
4.7.2 Silicon refining	137
4.7.3 TEST AT TRL 5	139
4.7.3.1 Silver recovery	139
4.7.3.2 Silicon refining	139
4.8 RESELP	139
4.8.1 Recovery process workflow.....	141
4.8.2 Recovery line design	142
4.8.2.1 Design of heating treatment and material separation	143
4.8.2.2 Design of hydrometallurgical treatments	145
4.8.2 Design of gas treatment.....	147
4.8.2.1 Amount of polymer	147
4.8.2.2 Required air	148
4.8.2.3 Off-gasses composition	148
4.8.3 Timeline	150
Chapter 5 Other resources recovery	151
5.1 RECOVERY OF TANTALUM PENTOXIDE FROM OUT OF USE CAPACITORS.....	152
5.1.2 Tantalum condensers.....	154

5.1.3	Characterization	155
5.1.4	Heating treatment, grinding, magnetic separation	157
5.1.5	Chemical treatments	158
5.1.3.1	Hydrochloric acid	158
5.1.3.2	Hydrofluoric acid.....	158
5.2	RECOVERY OF NEODYMIUM FROM PERMANENT MAGNETS	160
5.2.1	NdFeB magnets	162
5.2.2	Characterization	164
5.2.3	Test for “electrolytic decriptation”	166
5.2.4	Neodymium recovery	167
5.3	CONCLUDING REMARKS	170
Chapter 6 Green synthesis of nanoparticles from e-waste.....		171
6.1	TIN OXIDE NANOPARTICLES.....	176
6.1.1	Synthesis.....	178
6.1.2	Characterization	179
6.2	SILVER NANOPARTICLES	183
6.2.1	Synthesis.....	185
6.2.2	Characterization	186
6.3	COPPER NANOPARTICLES	189
6.3.2	Copper cementation	190
6.3.3	Synthesis with L-ascorbic acid	192
6.3.4	Synthesis with sodium borohydride.....	195
6.4	COPPER OXIDE NANOPARTICLES.....	197
6.4.1	Synthesis.....	199
6.4.2	Characterization	200
6.5	GOLD NANOPARTICLES	203
6.5.1	Synthesis with L-ascorbic acid	205
6.5.2	Characterization	208
6.5.2	Brust Synthesis	209
6.6	IRON NANOPARTICLES	211
6.6.1	Synthesis with sodium borohydride.....	213
6.6.2	Synthesis with eugenol.....	215
6.7	CONCLUDING REMARKS.....	217
Chapter 7 Application of recovered metals		219
7.1	ANTIBACTERIAL AND ANTIFUNGAL EFFECT OF SILVER POWDER IN PEO COATING.....	220
7.1.1	Production of PEO coatings	222
7.1.1.1	Silver particles production	222

7.1.1.2 PEO treatment and characterization methods	223
7.1.2 <i>Surface Characterization</i>	224
7.1.3 <i>Corrosion Resistance</i>	233
7.1.4 <i>Antimicrobial Activity</i>	235
7.1.5 <i>Antifungal Activity</i>	238
7.1.6 <i>Concluding remarks</i>	240
7.2 ANTIFOULING EFFECT OF COPPER POWDER IN PEO COATING	241
7.2.1 <i>Production of PEO coatings</i>	243
7.2.1.1 Silver/copper particles production	243
7.2.1.2 PEO treatment and characterization methods	244
7.2.1.3 Antifouling tests procedure	244
7.2.2 <i>Surface Characterization</i>	246
7.2.3 <i>SVET Analysis</i>	249
7.2.4 <i>Antifouling properties in estuarine water</i>	252
7.2.5 <i>Antifouling properties in seawater</i>	257
7.2.6 <i>Concluding remarks</i>	259
Conclusions	261
A. Printed circuit boards.	261
B. PV panels.	261
C. Capacitors and permanent magnets.	262
C. Powders and nanoparticles production.....	262
D. Powders and nanoparticles applications.....	264
REFERENCES	267
Acknowledgments	1

Chapter 1

Introduction

1.1 The e-waste problem [1]

1.1.1 Definition

“Electronic waste” or “e-waste” is a generic term which includes various forms of electric and electronic equipment that have ceased to be of any value to their owners. There is, yet, no standard definition. Table 1.1 lists selected definitions. In this work, the terms “WEEE” and “e-waste” will be used synonymously and in accordance to the EU WEEE Directive.

Reference	Definition
EU WEEE Directive (EU, 2002a)	“Electrical or electronic equipment which is waste... including all components, sub-assemblies and consumables, which are part of the product at the time of discarding.” Directive 75/442/EEC, Article 1(a) defines “waste” as “any substance or object which the holder disposes of or is required to dispose of pursuant to the provisions of national law in force.”
Basel Action Network (Puckett and Smith, 2002)	“E-waste encompasses a broad and growing range of electronic devices ranging from large household devices such as refrigerators, air conditioners, cell phones, personal stereos, and consumer electronics to computers which have been discarded by their users.”
OECD (2001)	“Any appliance using an electric power supply that has reached its end-of-life.”
SINHA (2004)	“An electrically powered appliance that no longer satisfies the current owner for its original purpose.”
StEP (2005)	E-waste refers to “. . .the reverse supply chain which collects products no longer desired by a given consumer and refurbishes for other consumers, recycles, or otherwise processes wastes.”

Tab. 1.1 Definition of e-waste or WEEE.

1.1.2 Quantities of WEEE

The use of electronic devices has proliferated in recent decades, and proportionately, the quantity of electronic devices, such as PCs, mobile telephones and entertainment electronics that are disposed of, is rapidly growing throughout the world.

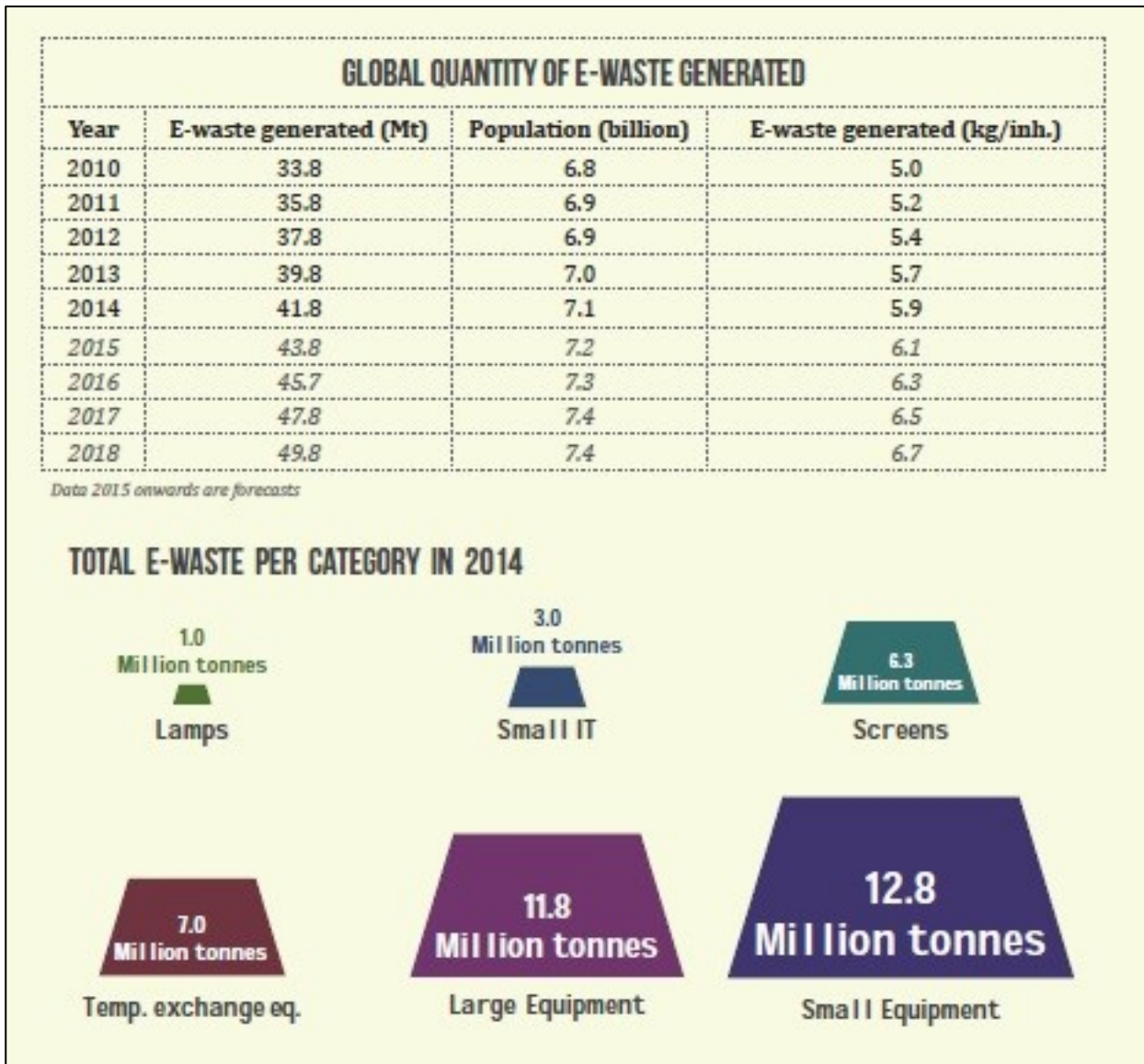


Fig. 1.1 Amount of e-waste produced.

In Fig. 1.1 [2], the data about the amount of generated e-waste with their division by category are reported whereas in Fig. 1.2 [3] there is the map of e-waste production.

In particular, every year from 20 to 50 million tons of WEEE in the world are disposed in landfill [4]. Considering for example computers, in 1994 it was estimated that approximately 20 million PCs (about 7 million tons) became obsolete. By 2004, this figure was to increase to over 100 million PCs.

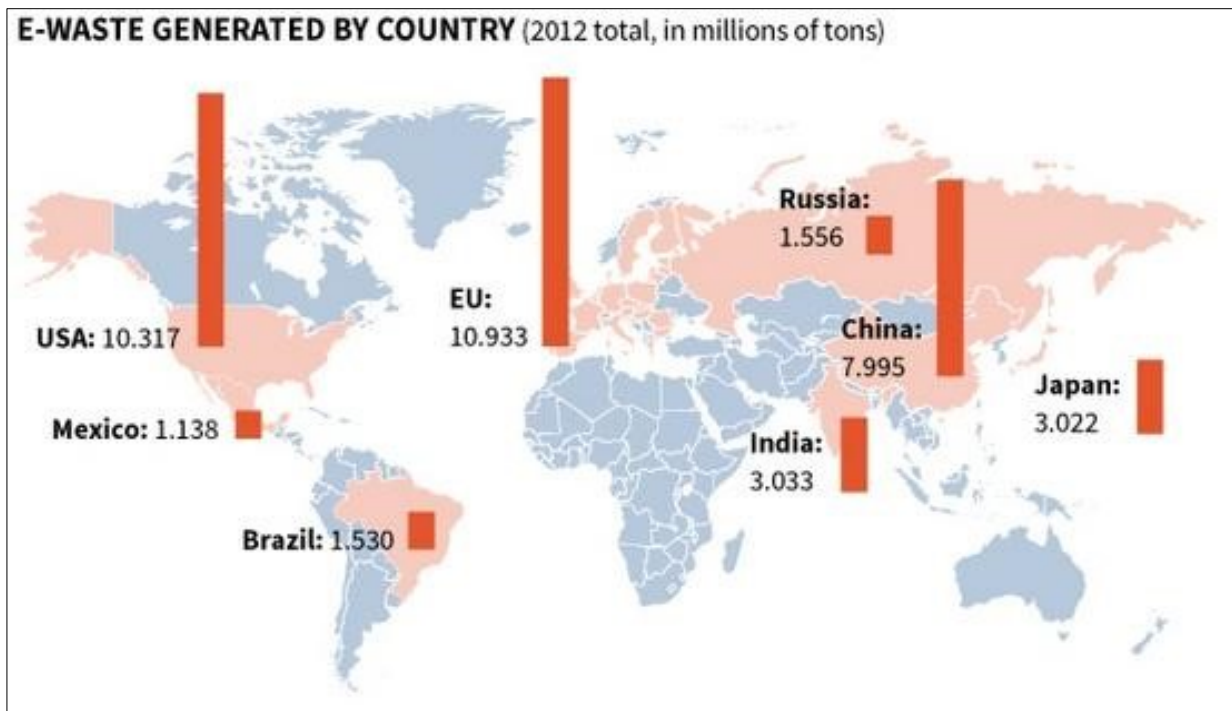


Fig. 1.2 Map of the e-waste production.

Cumulatively, about 500 million PCs reached the end of their service lives between 1994 and 2003. 500 million PCs contain approximately 2,872,000 t of plastics, 718,000 t of lead, 1363 t of cadmium and 287 t of mercury.

This fast-growing waste stream is accelerating because the global market for PCs is far from saturation and the average lifespan of a PC is decreasing rapidly — for instance for CPUs from 4–6 years in 1997 to 2 years in 2005. PCs comprise only a fraction of all e-waste.

Similar quantities of electronic waste concern all kinds of portable electronic devices such as PDAs, MP3 players, computer games and peripherals. It must also be pointed out that this continuously growing quantity do not affect only Europe, the United States or China, but also emerging countries such as India, which impose itself as a giant in computer technology [5].

Presently, e-waste is mainly generated in countries of the Organization for Economic Cooperation and Development (OECD), which have highly saturated markets for Electrical and Electronic Equipment (EEE), as Fig. 1.3 shows for the example of PCs.

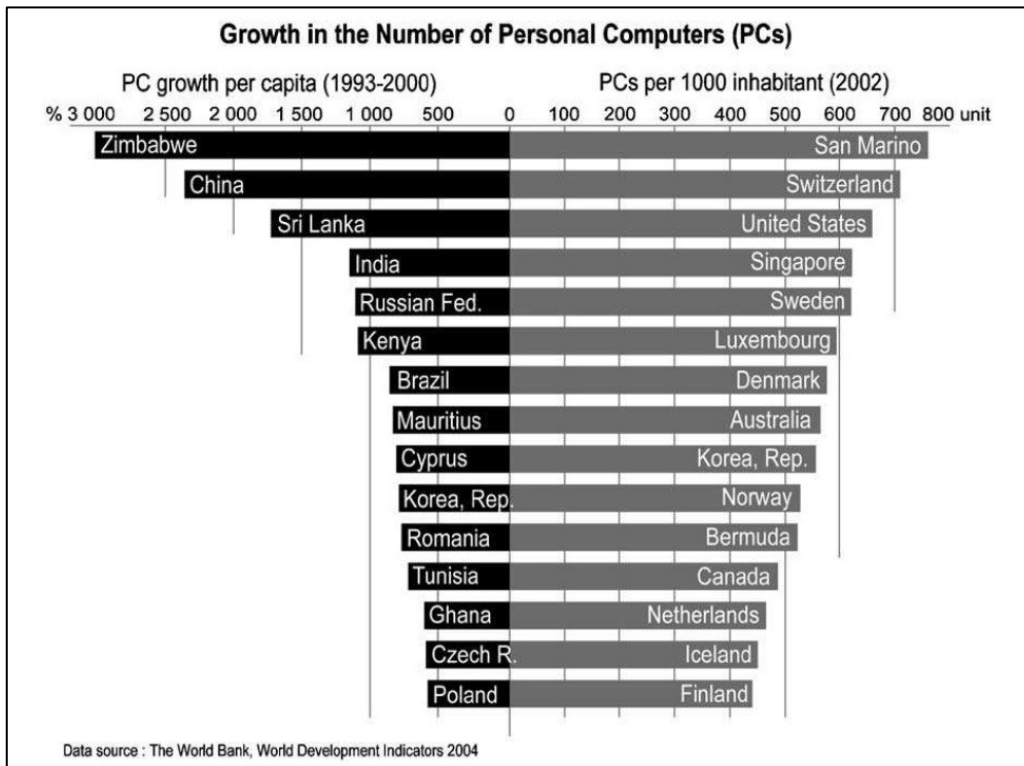


Fig. 1.3 Top scoring countries in PC growth rates (cumulated 1993 – 2000) and market saturation (2002)

Comparatively, the market penetration of EEE in industrializing countries is not very high. However, these countries show the fastest growing consumption rates for EEE, and thus large quantities of domestically generated e-waste will become part of the waste stream in them as well in the near future. Numerous methods have been suggested and used to estimate possible global quantities of WEEE. In [6] three estimation methods are described:

- the “consumption and use method”, which takes the average equipment of a typical household with electrical and electronic appliances as the basis for a prediction of the potential amount of WEEE (used in the Netherlands to estimate the potential amount of WEEE);
- the “market supply method”, which uses data about production and sales figures in a given geographical region (used by the German Electrical and Electronic Industries Association to estimate WEEE)
- the Swiss Environmental Agency’s estimates based on the assumption that private households are already saturated and for each new appliance bought, an old one reaches its end-of-life.

In the first two methods, assumptions need to be made about the average life-time of EEE products as well as their average weight (from which to derive WEEE generation in tons). Under the third method, however, the assumption of the average life-time of the appliances is irrelevant, as it

assumes a completely saturated market. Another method of estimation developed at Carnegie Mellon University by Matthews [7] is also based on sales data. Although it focuses only on computers, it includes the reuse and storage parameters for obsolete machines, which in reality delay their entry into the waste stream. However, the model is only for the US and cannot be universally applied. An adapted model for WEEE estimation based on Matthews’ model is shown in Fig. 1.4.

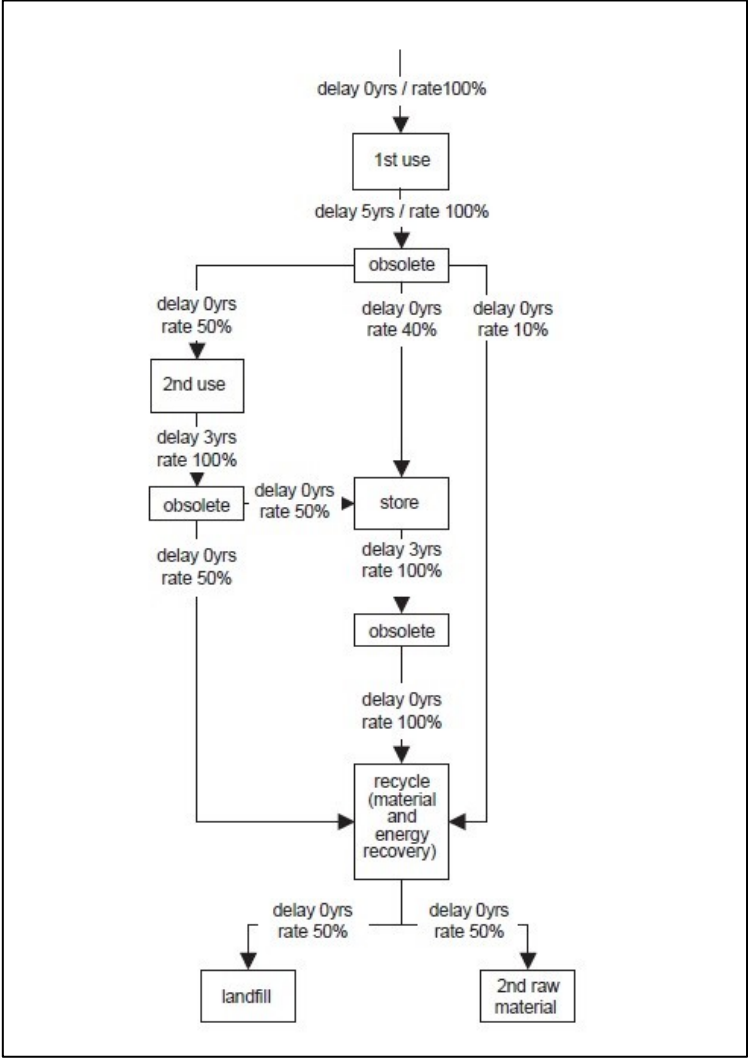


Fig. 1.4 A simple model adapted from Matthews et al. [7] to calculate expected e-waste at recyclers and/or landfills. It mainly describes usage patterns of PCs (“1st use”, “2nd use” and “store”) followed by a final destruction to recover materials and energy. Some of the material is landfilled and the rest is returned as secondary raw materials. The transfer from one stage to the next is described with a delay in years and a transfer rate in percent of the total volume at this stage in any year.

The results of WEEE estimation studies vary widely and comparisons among the studies are difficult because both the methods used and basic assumptions made differ from one study to another.

The following considerations are based on a simple model to estimate only scrap PC quantities. Fig. 1.5 displays timelines of global quantities of drop-out PCs, calculated as the difference between annual new PC sales and the annual growth of the installed PC base.

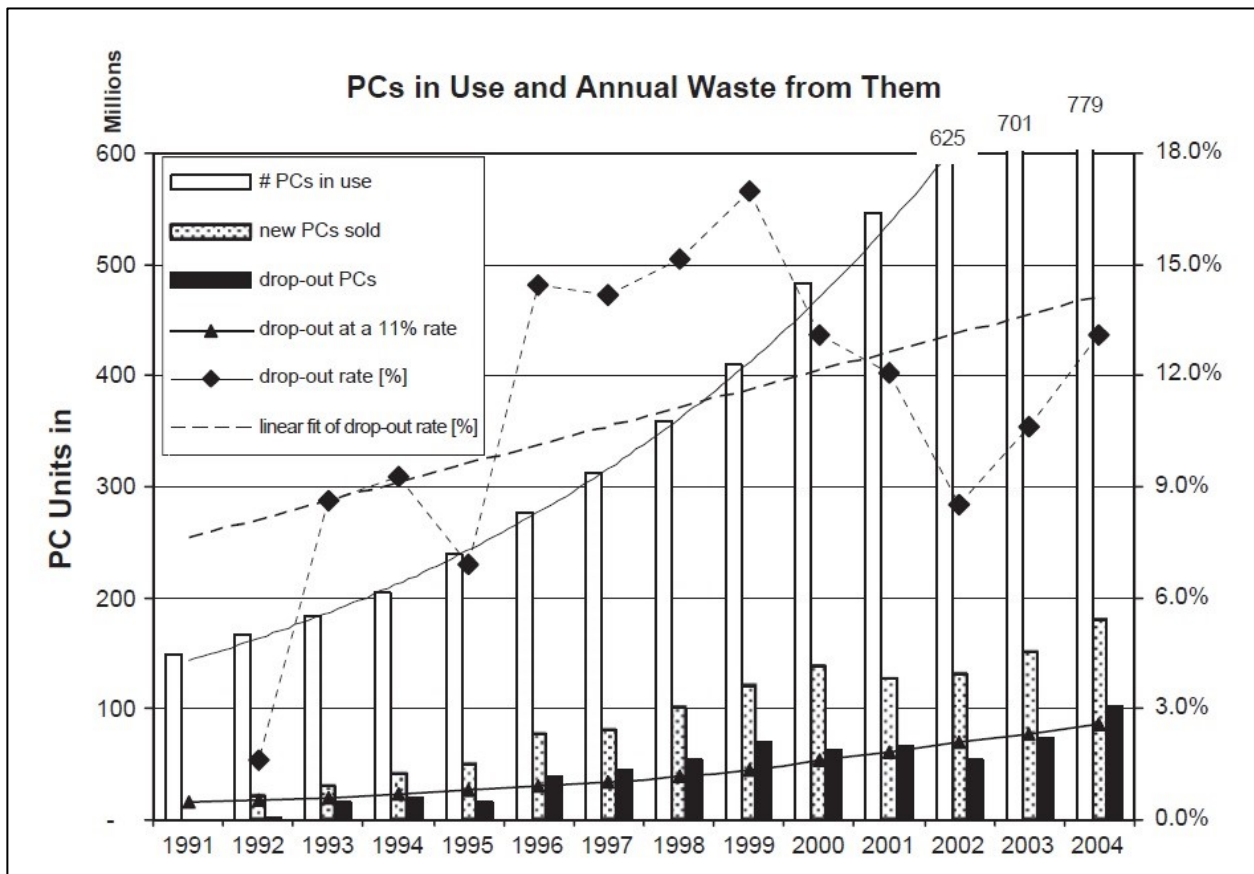


Fig. 1.5 Some facts and trends of the PC market over the last decade. The globally installed base of PCs [# PCs in use] increases exponentially. The sales of new PCs [new PCs sold] also grew substantially from 20 million (1992) to 180 million (2004). However, there is a considerable drop in new PC sales in the years 2001 and 2002, reflecting the technology bubble burst in 2000, followed by a quick recovery in the last 2 years. About half of the new PCs replace obsolete ones [drop-out PCs]. The rest adds to the installed base which results in the present growth. Comparing the number of dropped out PCs with the totally installed base, a drop-out rate between a 2% and 17% results. A trend to an increased drop out rate can be observed [linear fit of drop-out rate], clearly indicating a decreasing life span of PCs. However, this trend is overrun by the market developments in the past years: the rate was highest (17%) in 1999 at the peak of the ICT boom. The average drop-out rate over the entire period is approximately 11% which turns out to be a life span (assuming linear decay) of approximately 9 years. This in turn indicates quite a long storage time, which was confirmed by sampling tests done for SWICO in Switzerland. If we assume a constant drop-out rate of 11% (which represents the average drop-out rate over the period 1991–2004) the number of PCs which would drop out every year from the installed base [# PCs in use] gives a conservative estimate of PC scrap occurring [drop-out at a 11% rate] if extrapolated into the future.

The average drop-out rate for PCs over the period 1991–2004 is then calculated as the ratio between the drop-out PCs and the installed PC base, which turns out to be approximately 11%. This corresponds to a total life span of approximately 9 years — assuming a linear decay — which is considerably longer than the useful life of a PC and hence indicates quite a long storage time. In the former 15 European member countries (EU15) the amount of WEEE generated varies between 3.3 and 3.6 kg per capita for the period 1990–1999, and was raised to 3.9–4.3 kg per capita for the period 2000–2010 [8]. According to the study (which assessed only five appliances: refrigerators, personal computers, televisions, photocopiers and small household appliances), this amount covers only 25% of the whole WEEE stream of the EU15. Hence, these numbers correspond to other estimates of total WEEE amounts, which range from 14 to 20 kg per capita. Nevertheless, the quantity of WEEE generated constitutes one of the fastest growing waste fractions, accounting for 8% of all municipal waste. Although the per-capita waste production in populous countries such as China and India is still relatively small and estimated to be less than 1 kg e-waste per capita per year, the total absolute volume of WEEE generated in these countries is huge. Additionally, some developing and industrializing countries import considerable quantities of e-waste, even though the Basel Convention restricts transboundary trade of it, as described in 1.1.3.

1.1.3 E-waste routes



Fig. 1.6 E-waste traffic routes [300].

In 1991, Larry Summers, then Chief Economist of the World, spoke of the economic sense of exporting first world waste to developing countries. He argued that the countries with the lowest wages would lose the least productivity from “increased morbidity and mortality” since the cost to be recouped would be minimal, that the least developed countries, specifically those in Africa, were seriously underpolluted and thus could stand to benefit from pollution trading schemes as they have air and water to spare, and that environmental protection for “health and aesthetic reasons” is essentially a luxury of the rich, as mortality is such a great problem in these developing countries that the relatively minimal effects of increased pollution would pale in comparison to the problems these areas already face.

The most prominent example of an international initiative stemming against this type of thinking is the 1989 Basel Convention on the Control of Transboundary Movements of Hazardous Wastes and their Disposal (in force since 1992). The Convention puts an onus on exporting countries to ensure that hazardous wastes are managed in an environmentally sound manner in the country of import. Apart from Afghanistan, Haiti and the United States of America, all 164 signatory countries have ratified the convention (Secretariat of the Basel Convention).

The transboundary movement of electronic waste, or e-waste, is regulated by the Basel Convention, as it is considered to be dangerous to humans and the environment under the List A of Annex VIII of the Convention. There are highly toxic substances in e-waste such as cadmium, mercury and lead. However, e-waste also contains valuable substances such as gold and copper. Recovering these metals from e-waste has become a profitable business, resulting in global, transboundary trade in e-waste.

Countries such as China and India face a rapidly increasing amount of e-waste, both, from domestic generation and illegal imports. For emerging economies, these material flows from waste imports not only offer a business opportunity, but also satisfy the demand for cheap second-hand electrical and electronic equipment. In addition, the lack of national regulation and/or lax enforcement of existing laws are promoting the growth of a semi-formal or informal economy in industrializing countries. An entire new economic sector is evolving around trading, repairing and recovering materials from redundant electronic devices. While it is a source of livelihood for the urban and rural poor, it often causes severe risks to humans and the local environment. Most of the participants in this sector are not aware of the risks, do not know of better practices, or have no access to investment capital to finance profitable improvements.

Fig. 1.7 indicates the main e-waste traffic routes in Asia.

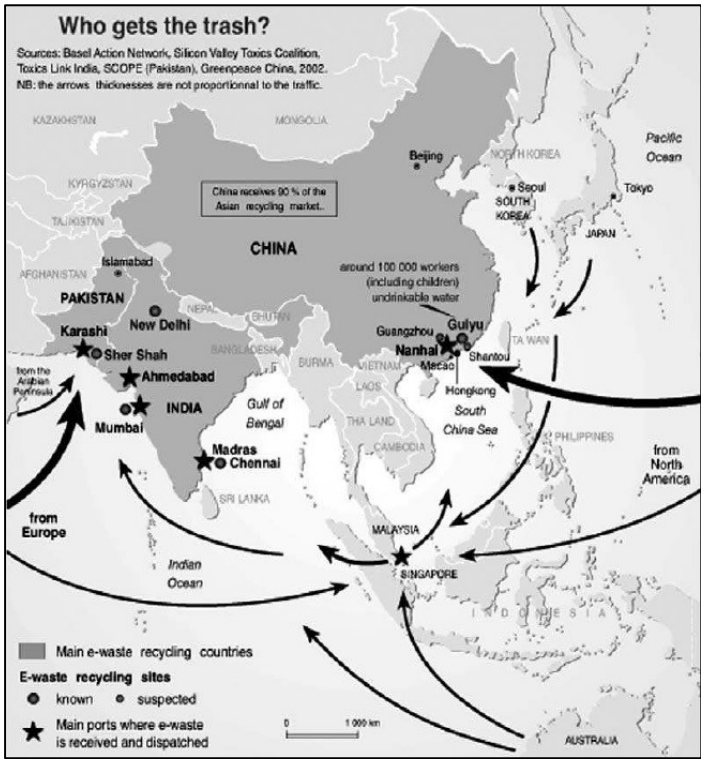


Fig. 1.7 Asian e-waste traffic

There are, however, no confirmed figures available on how substantial these transboundary e-waste streams are. From non-ratifying countries, such as the USA, estimates have been made that 50–80% of the collected domestic e-waste is not recycled domestically but rather shipped to destinations such as China.

China, India and other countries have recently adjusted their laws to fight e-waste imports. However, being large producers of EEE (China manufactures for instance 90% of the global CRT production), these countries should recognize their inherent interest in closing material cycles and obtaining access to the raw materials in the e-waste streams.

In particular, the difficulties specific to developing and transition countries are:

- Although the quantity of indigenous e-waste per capita is still relatively small, populous countries such as China and India are already huge producers of e-waste in absolute terms.
- These countries also display the fastest growing markets for electrical and electronic equipment.
- Some developing and transition countries are importing considerable quantities of e-waste. Some of them arrive as donations meant to help “the poor”, while others are simply mislabeled.

In certain developing and transition countries these difficulties are amplified by a lack of regulations and/or lax enforcement in the recycling and disposal sector. Combined with the existence of a very creative and low-income informal sector, the lack permits a profitable e-waste recycling business thriving on uncontrolled and risky low-cost techniques (examples are shown in Fig. 1.8). Most of the participants in this sector are not aware of environmental and health risks and either do not know better practices or have no access to investment capital to finance even profitable improvements or implement safety measures.



Fig. 1.8 The extraction of copper from printed wiring boards (PWB): (1) manually removing varnish, (2) recovering copper-sulphate after submerging PWBs for 12 h in sulfuric acid followed by boiling off H_2O using PWB residues as a fuel, (3) manually segregating the copper layer and glass fibers after burning multi-layer PWBs which are resistant to acid, (4) scrap iron is added to the remaining liquid to react with the dissolved copper, (5) fallen out copper slime is a third product bringing the total to 1 to 2 t of copper per month, (6) such an SME creates about 12 jobs, however at high external costs.

1.1.4 Content of WEEE

When e-wastes are disposed of or recycled without any controls, there are predictable negative impacts on the environment and human health. In fact, e-wastes contain more than 1000 different substances, many of which are toxic, such as lead, mercury, arsenic, cadmium, selenium, hexavalent chromium, and flame-retardants that create dioxins emissions when burned. About 70% of the heavy metals (mercury and cadmium) in US landfills come from electronic waste. Consumer electronics make up 40% of the lead in landfills. These toxins can cause brain damage, allergic reactions and cancer.

On the other hand, e-wastes contain considerable quantities of valuable materials such as precious metals. Early generation PCs used to contain up to 4 g of gold each; however, this has decreased to about 1 g today. The value of ordinary metals contained in e-waste is also very high: 1 ton of e-waste contains up to 0.2 tons of copper.

The double valence of e-waste as potential resource and problem is shown in Fig. 1.9 [2].

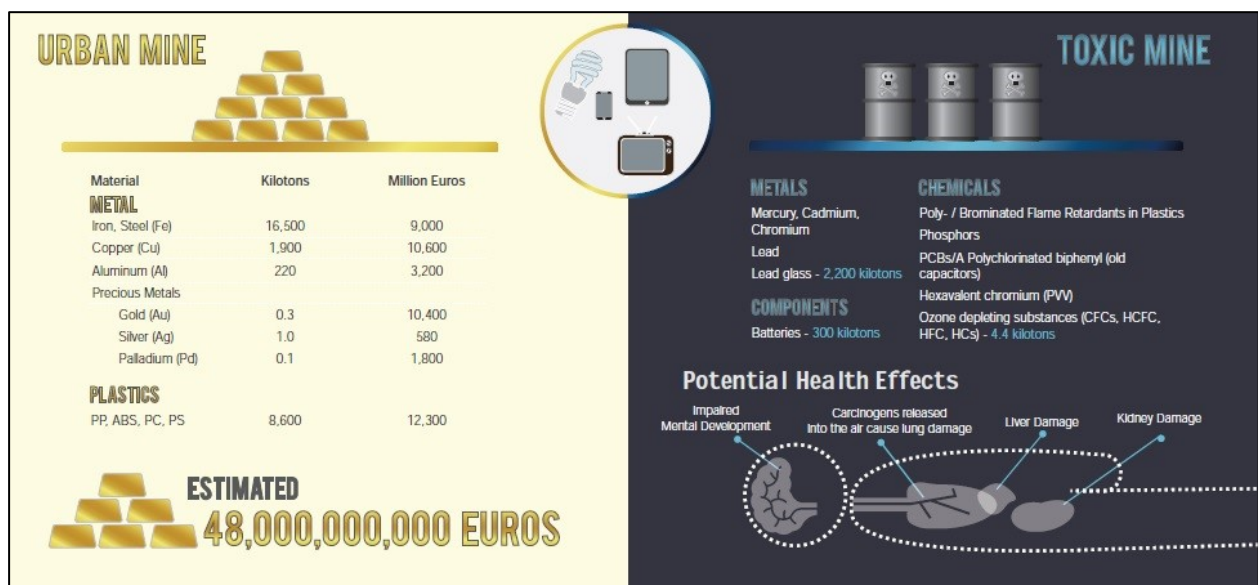


Fig. 1.9 The resources and pollutants in e-waste.

Given the different range of materials found in WEEE, it is difficult to give a generalized material composition for the entire waste stream. However, most studies examine five categories of materials: ferrous metals, non-ferrous metals, glass, plastics and “other”.

According to the European Topic Centre on Resource and Waste Management (ETC/RWM), iron and steel are the most common materials found in electrical and electronic equipment and account for almost half of the total weight of WEEE (Fig. 1.10).

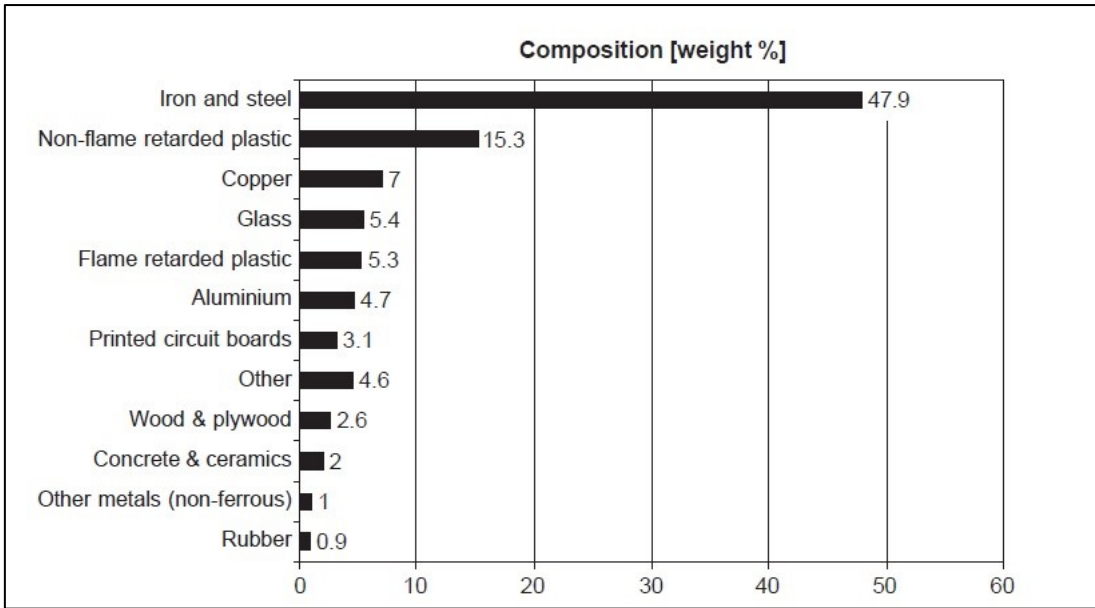


Fig. 1.10 WEEE material composition.

Plastics are the second largest component by weight representing approximately 21% of WEEE. Non-ferrous metals, including precious metals, represent approximately 13% of the total weight of WEEE (with copper accounting for 7%).

In some WEE categories, in particular, the amount of precious metals such as silver, gold, copper and platinum is not negligible and can be economically valuable, considering the high prices of these metals. For example, the price of gold (Fig. 1.11) is nowadays extremely high (above 30 € /g over the last few years) due to its high increase during the first decade of this century [9, 10]. This increase was caused mainly by the financial crisis and by the fact that gold is historically one of the main refuge assets.

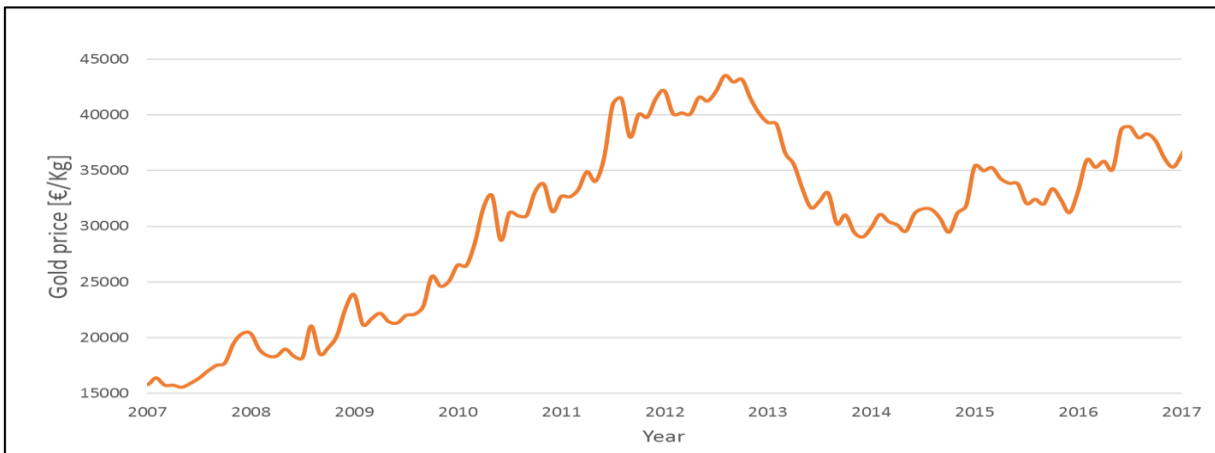


Fig. 1.11 Price of gold during the latest 10 years.

Similarly, the price of silver exhibited high increase from 2009 and 2011 and the price is now quite stable with value of about 500 €/Kg (Fig. 1.12).

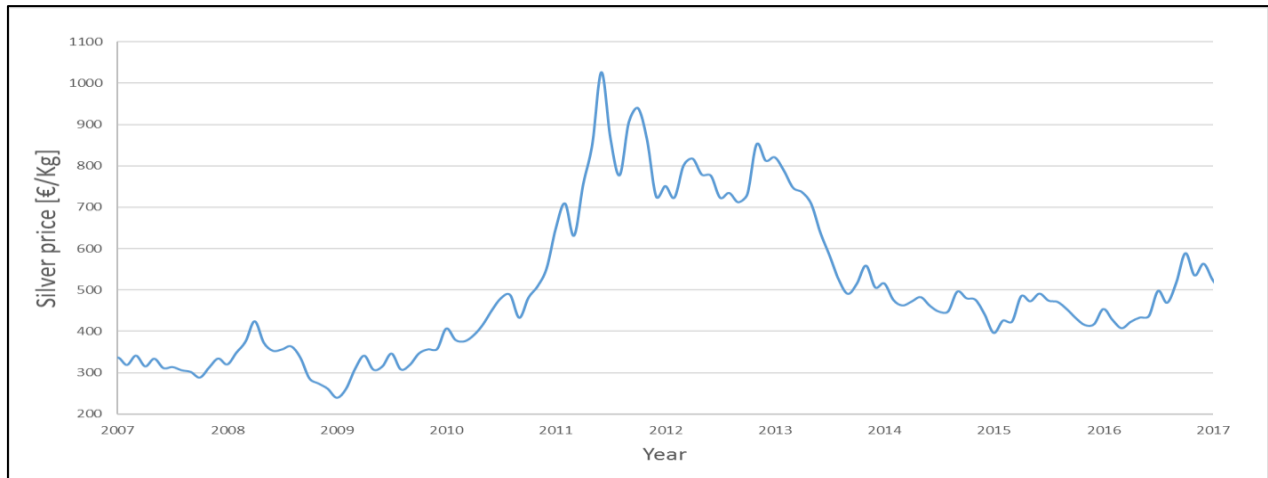


Fig. 1.12 Price of silver during the latest 10 years.

Thanks to these high specific prices and the high amount of e-waste produced, recycling of e-waste has the potential to be an attractive business and companies such as Boliden (Sweden), WEEE AS (Norway) and Citiraya (UK) are investing in the area.

Moreover, in addition to precious metals, e-waste contains many strategic metals. Strategic metals are generally defined as those metals, which are required for the national defense of a country, but are threatened by supply disruptions due to limited domestic production. The United States tends to adhere to this definition and cites access to adequate strategic materials as a key component of US national security [11].

However, the definition of strategic metals can be also including those metals that are important not only for national defense, but also for industries that play an important role in the economic development of a country such as energy, aerospace, telecommunication, computer or mobile technology.

Nowadays, the following elements are typically considered strategic: antimony, bismuth, cerium, chromium, cobalt, dysprosium, europium, gallium, germanium, indium, lanthanum, molybdenum, neodymium, niobium, palladium, platinum, praseodymium, rhodium, samarium, scandium, selenium, tantalum, tellurium, terbium, tin, titanium, tungsten, vanadium, zirconium and yttrium.

1.2 Recovery Techniques [12]

The resource recovery from end-of-life electronic and electrical equipment has become a subject of particular interest in recent years and the implementation of environmentally friendly techniques to recover metals from this type of waste is considered crucial for a sustainable development.

Heterogeneous and complex nature of WEEEs (i.e. metal diversity and metal–non-metal associations) are the main obstacles for the recovery of metals from WEEE. For recovery of metals from WEEE, various treatments based on conventional mechanical, physical, pyrometallurgical and hydrometallurgical processes are proposed. A schematic flowsheet illustrating the processes available for recovery of metals from WEEE is shown in Fig. 1.13.

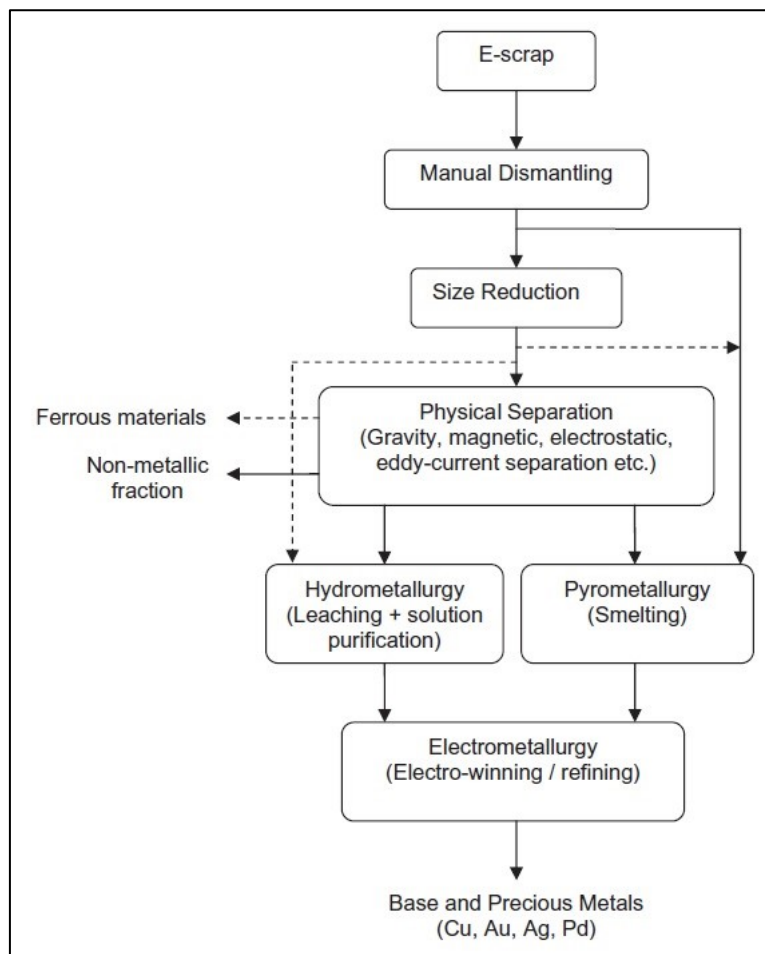


Fig. 1.13 A schematic flowsheet showing the potential process options for recovery of metals from e-scrap

Precious metal grade of wastes, metal losses, environmental impact and amount of WEEE/scale of operation are the most important factors affecting selection or development of a treatment process for WEEE. The composition of WEEE can vary considerable even within a certain type of waste and mixing different WEEE can lead to the undesired dilution of valuable metals. Carbon and material footprints are one of the important objectives of environmentally acceptable metal

recovery techniques from e-scrap. Size reduction and physical separation processes have relatively low environmental impact in that wet processing methods generate contaminated fluids and dry processes could have associated dust problems. On the other hand, hydrometallurgical processes may use large amounts of toxic, highly acidic or alkaline or flammable reagents with the generation of voluminous solid wastes and effluents. A wide range of methods are available to clean the effluent streams to meet environmental regulations, and to recover useful reagents or materials. The recycling of WEEE minimizes the volume of landfill and mitigates/prevents the pollution of soil, groundwater and air due to the release of hazardous components. Furthermore, the treatment of WEEE for the recovery of metals is important for reducing carbon and material footprint. Copper has high carbon footprint, nearly 4 kg of CO₂ produced for 1 kg of copper. Recycled gold represents a lower carbon footprint instead of primary-mined gold. Although only small amounts of gold are used in WEEE, it has the largest material footprint e.g. nearly 50 and 5000 times that of copper and aluminum. Based on the material footprint data for WEEE (PC, printer and CRC screen) Groot and Pistorius [13] suggested that recycling efforts should focus primarily on the metals such as gold and tin followed by nickel, copper and lead for sustainability.

1.2.1 Pre-treatment

For the recycling of valuable metals from e-scrap by hydrometallurgical methods, a mechanical pre-treatment step is needed. The different components and devices can be selectively dismantled and separated into various fractions such as metals (iron, copper, aluminum, magnesium, etc.), plastics, ceramics, paper, wood and devices such as capacitors, batteries, picture tubes, LCDs, and PCBs. These components can be re-used or directed to recycling process. The dismantling process also allows removal of hazardous components and pre-concentration of valuable metals increasing economic potential of wastes and their amenability to recycling. Following the removal (and sorting) of components, metal bearing components such as PCB is subjected to size reduction prior to metal recovery process. Shredders and hammer mills are extensively used to fragment, grind, rip or tear the waste. The extent of size reduction depends on the recovery process selected in that relatively coarse material can be readily smelted while fine size reduction is inherently and required for efficient recovery of metals by physical separation and hydrometallurgical processes. In this regard, Zhang and Forsberg [14] reported that almost complete liberation of copper from PC and PCB scrap could be achieved at a particle size of <2 mm and poor liberation at coarser fractions was due to the association of copper pins with plastics and the encapsulation of copper wire segments within plastics.

1.2.2 Physical separation processes

WEEE contains a variety of materials with different physical properties (i.e. specific gravity, magnetic susceptibility, electrical conductivity, etc.), which can be readily exploited to separate metals essentially from non-metal components and each other.

Table 1.2 also presents physical separation methods that utilize the differences in these properties of metals and plastics for their separation.

Methods	Separation criteria	Metals to be separated
Gravity separation	Specific gravity	Metals from plastics
Magnetic separation	Magnetic susceptibility	Iron/ferrous material, ferromagnetics from non-magnetics
Electrostatic separation (corona)	Electric conductivity	Metals/precious metals from non-metals
Eddy current separation	Electric conductivity/density	Non-ferrous metals from non-metals

Tab. 1.2 Potential physical separation methods for the recovery of metals from WEEE.

In this respect, application of various separation methods including gravity separation, magnetic separation, electrostatic separation, eddy-current and air classification by size have been demonstrated for the recovery of metals from WEEE. Fig. 1.14 illustrates a flowsheet for physical separation circuit for the removal of large components, ferrous metals and non-metals using hand sorting, two-stage magnetic separation and eddy current separation prior to smelting of base and precious metal concentrate produced.

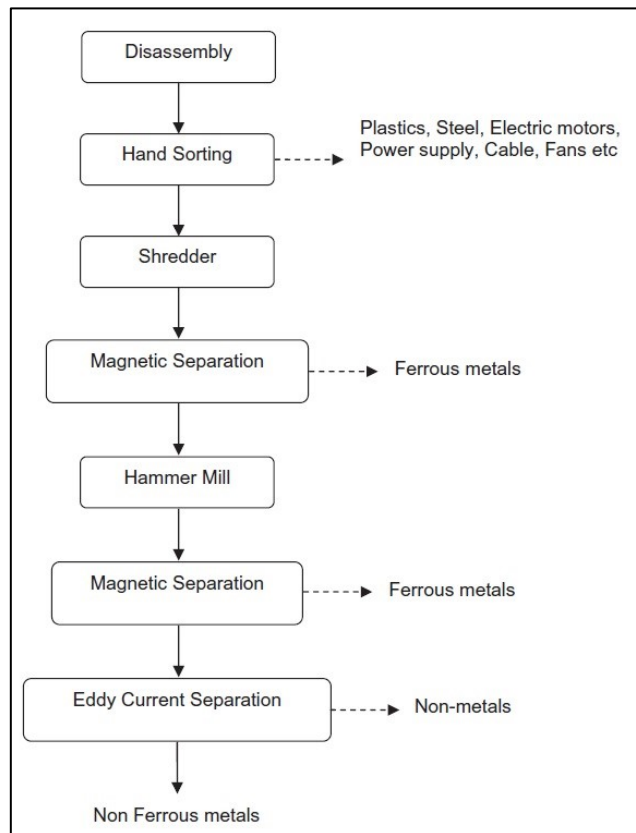


Fig. 1.14 A typical flowsheet for recovery of non-ferrous metals from WEEE prior to smelting.

Physical separation processes benefit from low capital and operating costs. One of the important detractions to physical separation processes is the valuable metal losses amounting to 10–35%. The reason for these losses includes insufficient liberation of metals due to the intimate association of valuable metals with plastics, generation of fines ($<75\ \mu\text{m}$) during size reduction and inefficiency of separation processes for metal recovery from fine fractions. After mechanical/physical treatments, the enriched fractions are further treated by pyrometallurgical and hydrometallurgical processes for the extraction of base and precious metals. Typically, the method used for e-wastes metal recovery is pyrometallurgy, while hydrometallurgy is employed to refining the recovered precious metals.

1.2.3 Pyrometallurgy [15]

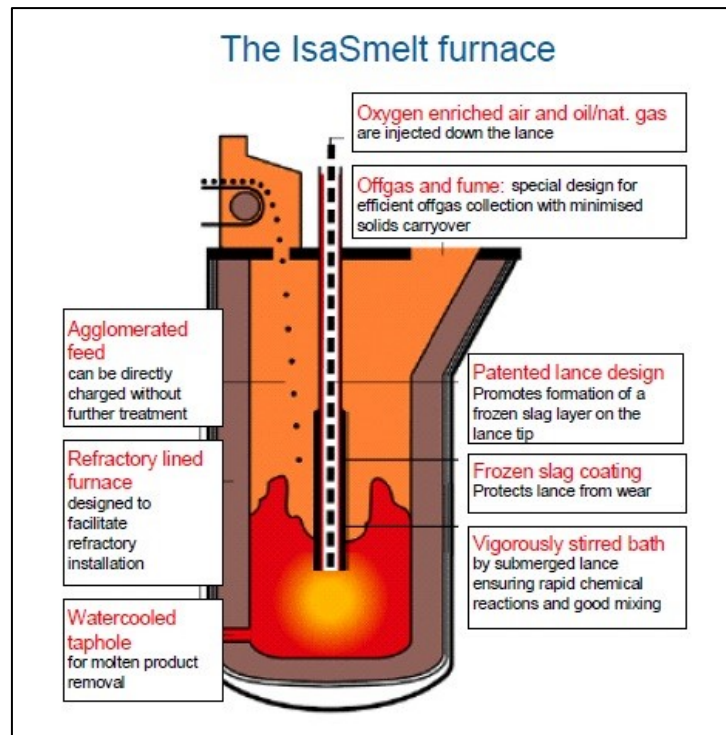


Fig. 1.15 A typical furnace used for metals recovery from e-waste [297].

Pyrometallurgy is a traditional technology for recovery of nonferrous metals as well as precious metals from WEEE (Fig. 1.15). There are several pyrometallurgical plants worldwide for the treatment of WEEE. Pyrometallurgical operations focus on the production of precious metal-bearing copper bullion. A typical pyrometallurgical process involves pre-treatment of WEEE (i.e. dismantling, shredding and physical processing) and then smelting of enriched metal product to obtain copper bullion, which is subjected to electrolytic refining to produce high purity copper. Slimes collected from copper electrorefining are further refined to recover precious metals including Ag, Au, Pt, Pd, Rh, Ru and Ir. In addition to copper and precious metals, a variety of metals can be extracted in modern smelters (Fig. 1.16).

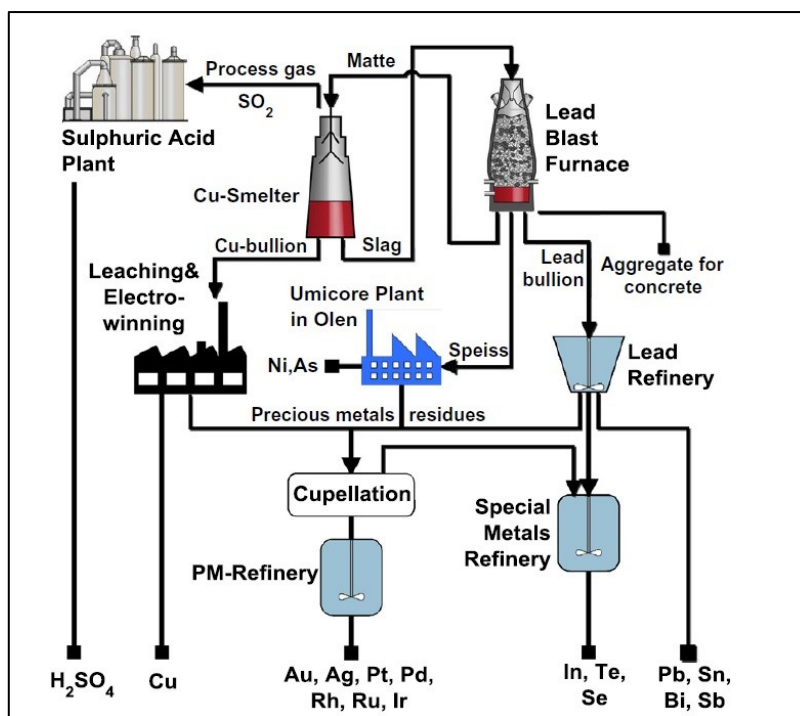


Fig. 1.16 A typical flowsheet for recovery of non-ferrous metals from WEEE prior to smelting.

Pyrometallurgical processes can be deemed potentially suitable for the treatment of WEEE in that organic constituents can partially/wholly supplant coke as fuel and reducing agent. However, they are energy intensive and high-cost processes with their particular requirement for high grade (rich in copper and precious metals) feed. Halogenated flame retardants used in PCBs, which lead to the formation of dioxins and furans, volatile metals and dust together may present environmental problems and, hence, off-gas treatment is prerequisite. By contrast, hydrometallurgy allows minor investments, and is why it is used in developing countries for metal recovery where, as mentioned, has the problem that treatments are performed without the appropriate precautions. In reviewing the components that comprise electronic waste, one can see, from a processing point of view, a material that brings metal values to the table along with an inherent reductant. The carbon and hydrogen values contained in plastics can be harnessed, facilitating the recovery of resources. Concerns over the release of heavy metals that may be entrained in e-waste material are no different from those expressed in “conventional” scrap. Efficient dust handling systems employed in every pyrometallurgical operations have already shown their ability to deal with such materials. Dioxin production/release associated with the processing of hydrocarbon-containing waste can be also be controlled/eliminated with sufficient gas handling systems. Resource recovery from e-waste has been shown to be attainable through the application of pyrometallurgical operations. Some examples of e-waste processing are given here. Depending on the background of the engineers involved in the process development, the focus is placed on different aspects of the complex waste material. Chemical engineers may focus on the recovery of the organic fraction as low molecular weight compounds, while metallurgists tend to focus on the metal recovery.

1.2.3.1 Adherent Technologies Inc.

Adherent Technologies has taken the approach of focusing on the recovery of low molecular weight organics from the polymers present in e-waste. The waste is first processed via shredder/hammer mill. Ferrous metals are removed with magnetic belt and drum operation, with aluminum being removed via eddy current separation. These processes result in a reduction of the feed by 30%. The remaining polymer-rich material is transported through a pyrolysis chamber by screw conveyor.

Thermal degradation of the material results in the evolution of low weight organic molecules that can be distilled to produce a number of saleable products. Adherent has demonstrated the ability to generate a phenol-rich liquid through vacuum distillation of this gas stream.

Reforming and other reactive distillation operations may then process this material producing commodity chemicals such as ethylbenzene, phenol or styrene.

The resulting organic-free, metal-ceramic material can then be sent to conventional metallurgical processing.

1.2.3.2 Boliden Mineral AB

Boliden's Rönnskär smelter has incorporated e-waste as part of its secondary raw materials for some time. The operation consists of a lead flash smelter and refinery, a copper smelter and refinery, a sulfuric acid and sulphur dioxide plant, a slag fuming plant and a precious metals plant. The company estimates that its plant could consume 15,000-20,000 tons per year of PC scrap, based on test-runs of 10t/charge

In a project sponsored by Boliden, Association of Plastics Manufacturers Europe (APME) and American Plastics Council (APC), the use of PC waste in the Zinc Fuming Furnace feed was studied as well as the current process of adding the e-waste to Boliden's Kaldo Furnace.

The e-waste investigated by Boliden was comprised of the entire personal computer (PC) with only selective removal of components that contained Hg. Processing of e-waste in this manner eliminates the need for complete disassembly of the components, reducing to cost of the scrap. Preparation of the PC waste was accomplished using a hammer mill with removal of iron via a magnetic separator, creating a more plastic-rich waste than was discussed above when considering circuit boards alone. The PC scrap is reduced to -30 mm and mixed with crushed revert slag in a 50:50 mixture to optimize bulk handling and silo feeding, avoiding blockages during feeding.

ZINC FUMING FURNACE: The fuming furnace is supplied with a mix of EAF dust, Revert Slag and PC waste. The plastics contained in the PC waste work with added coal fines to facilitate the fuming of zinc, lead, arsenic and related metals in addition to the contained halogens. This stream is sent to the clinker furnace. The cleaned slag is tapped from the fuming furnace to a settler furnace where copper alloy and copper sulfide are separated.

Precious metals from the e-waste follow the copper collector. In this way, almost complete recovery of the copper and precious metals from the e-waste can be obtained.

KALDO FURNACE: The total amount of secondary raw materials and lead concentrate processed by Boliden's Kaldo furnace is around 100,000 tons per year. Kaldo technology has been practiced for over 15 years to recover cable scrap and printed circuit boards.

Blended feed material is charged by skip hoist. Oxygen lance supplies the needed O₂ for combustion with an oil-oxygen burner, if needed, to reach ignition temperature. It is at this point that the value of the plastics within the PC waste is seen. With a thermal value on par with that of fuel oil, the polycarbonates supply the heat needed for the smelting operation. Off-gases are subjected to additional combustion air at around 1200°C in post-combustion. Standard gas handling system recovers thermal energy via a steam network.

The Kaldo furnace produces a mixed copper alloy that is sent to the copper smelter for recovery of metals (Cu, Au, Ag, Pd, Ni, Se, Zn) and dusts (containing Pb, Sb, In, Cd) sent to other operations for metal recovery.

PLANT OPERATION: According to [16], operational parameters (recovery, energy balance, product quality, emissions, etc.) were not affected by the addition of PC waste. Plastic additions accounted for 20% of the energy input (substituting for coal) without any appreciable change to the plant's output from either a chemical or a thermal perspective.

1.2.3.3 Union Mineria (UM)

UM's Hoboken site is comprised of copper/lead smelters and refining operations for complex non-ferrous raw materials with precious metals playing an important role.

Hoboken feed material is roughly 35:65 primary:secondary. The most important materials are:

- Complex concentrates containing lead, copper and precious metals
- Industrial by-products from other smelters and refiners e.g. drosses, mattes, copper slags, flue-dust, speiss, tank house slimes, cements, lead sulphates.
- Recycled products as sweeps, spent catalysts, electronic scrap, film ashes.

The Hoboken smelter treats 350 000 t/y of raw and recycled non-ferrous materials.

Organic phase is separated from the bulk through a two-stage pyrolytic furnace. This first oxygen-starved chamber pyrolyzes the organics, which are sent to the oxidizing (post combustion) chamber.

The furnace is equipped with its own emission system, including a Venturi scrubber and two packed towers. The incineration is run under well controlled conditions: As with Boliden's operation, waste material can be fed to the flowsheet at various points, depending on the waste's assay and physical aspects—primarily Pb- and Cu-content as well as precious metals assay. For example, copper-rich (electronic) scraps can be directly treated in the converters, collecting precious metals in the blister-copper. Converter off-gases are sent to the acid plant where any remaining hydrocarbons can be destroyed.

1.2.4 Hydrometallurgy

Hydrometallurgy is rapidly growing as preferred process for the recovery of a variety of metals, given that it is more accurate and can be controlled easily in comparison with conventional pyrometallurgical process.

In particular, compared with pyrometallurgical processes, hydrometallurgical processes offer relatively low capital cost, reduced environmental impact (e.g. no hazardous gases/dusts) and high metal recoveries with their suitability for small scale applications. These attributes make hydrometallurgical processes potential alternatives for the treatment of WEEE. A hydrometallurgical process involves the mechanical pre-treatment of waste, leaching of metals by a suitable lixiviant, purification of pregnant leach solution and recovery of metals.

Since the metallic elements are often covered with or encapsulated by various plastic or ceramic materials on printed circuit boards, a mechanical pre-treatment (i.e. size reduction) process is first needed to expose metals of interest to the action of leaching reagent and hence to facilitate their efficient extraction.

The most important peculiarity of WEEE is the presence of metals in native form and/or as alloys, which is of practical significance for selection or development of a suitable leaching process for WEEE. In general, an oxidative leaching process is required for the effective extraction of base and precious metals of interest (Eq. 1.1–1.6).



As example, Fig. 1.17 illustrates the dissolution of metallic copper from scrap TV boards in the absence and presence of H_2O_2 as the oxidant in acidic sulfate media.

A very limited copper extraction (~2%) in the absence of the oxidant is consistent with the thermodynamic data (Eq. 1.1).

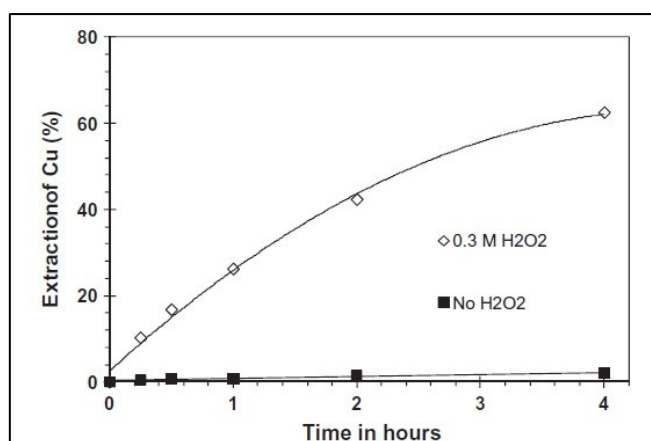


Fig. 1.17 Enhanced extraction of copper from scrap TV boards in the presence of H₂O₂ (0.3M) at 0.53M H₂SO₄ and 20°C

Acid leaching in the presence of an oxidant is extensively used for the extraction of copper from printed circuit boards (Tab. 1.3).

Scrap Type	Leaching reagent	Recycled Metals	References
Scrap integrated circuits	(i) Thiourea – ferric sulfate leaching	(i) Au (69.36%), Ag (100%), Cu (100%)	Lee et al. (2010)
	(ii) Aqua regia leaching	(ii) Au (100%), Ag (88.51%), Cu (100%)	
	(iii) NH ₃ –(NH ₄) ₂ S ₂ O ₈ leaching	(ii) Au (12.76%), Ag (100%), Cu (88.87%)	
	(iv) H ₂ SO ₄ leaching	(iv) Au (6.05%), Ag (90.37%), Cu (100%)	
Scrap TV Boards	H ₂ SO ₄ + H ₂ O ₂	Cu (>98%)	Deveci et al. (2010)
PCB	Column bioleaching (<i>Sulfobacillus thermosulfidoxidans</i> and <i>Thermoplasma acidophilum</i>)	Zn (80%), Al (64%), Cu (86%), Ni (74%)	
PCB	After thermal pre-treatment; HCl leaching	Cu (98%)	Havlik et al. (2010)
PCB	Lime Sulfur Synthetic Solution (LSSS) method	Au (92%), Ag (90%)	Li and Huang (2010)
PCB	Na ₂ S ₂ O ₃ –CuSO ₄ –NH ₄ OH leaching		
PCB	HCl + HNO ₃	Ag (98%), Pd (93%), Au (97%)	Park and Fray (2009a)
PCB	(i) H ₂ SO ₄	(i) Sn (<0.01%), Cu (<0.01%)	Castro and Martins (2009)
	(ii) H ₂ SO ₄ + HCl	(ii) Sn (96.3%), Cu (29.8%)	
	(iii) HCl	(iii) Sn (98.2%), Cu (20%)	
	(iv) HCl + HNO ₃	(iv) Sn (85.8%), Cu (34.3%)	
PCB	Bioleaching (<i>At. ferrooxidans</i>)	Cu (>99%)	Yang et al. (2009)
PCB	Tri- <i>n</i> -butyl phosphate (TBP), Cyanex 272, Cyanex 301	Zn, Ni (99%)	Park and Fray (2009b)
PCB	Bioleaching (<i>S. thermosulfidoxidans</i>)	Ni (81%), Cu (89%), Al (79%), Zn (83%)	Ilyas et al. (2007)
Computer PCB	HNO ₃ /HCl leaching	Au	Sheng and Etsell (2007)
	Cu(II)–NH ₃ –(NH ₄) ₂ SO ₄ leaching	Cu (90%)	
PCB	Electrowinning		
E-scrap	HNO ₃ /HCl leaching	Au, Cu	Madenoglu (2005)
Mobile phones PCB	(i) For Pd recycling; HCl/NaCl with HNO ₃ /H ₂ O ₂ leaching	(i) Pd (93–95%)	Quinet et al. (2005)
	(ii) For Au, Ag recycling; cyanide/thiourea leaching	(ii) Au, Ag (>95%)	
Computer PCB	Bioleaching (<i>At. ferrooxidans</i>)	37–82% Cu	Choi et al. (2004)
Non-mounted PCB	HNO ₃ leaching	Cu, Ni (>90%)	Kinoshita et al. (2003)
	Solvent extraction		
PCB	(i) H ₂ SO ₄ /H ₂ O ₂ leaching	(i) Cu, Fe, Zn, Ni, Al (>95%)	Oh et al. (2003)
	(ii) CuSO ₄ –NH ₄ OH–(NH ₄) ₂ S ₂ O ₈ leaching	(ii) Au, Ag (>95%)	
PCB	HNO ₃ leaching	Cu, Pb (>95%)	Mecucci and Scott (2002)
	Electrowinning		
	Bioleaching		
PCB dust	(i) Bacteria (<i>At. ferrooxidans</i>)	(i) Cu, Ni, Zn (>90%)	Brandl et al. (2001)
	(ii) Fungi (<i>A. niger</i>)	(ii) Cu and Sn (65%); Al, Ni, Pb, Zn (95%)	
Wasted electronic parts	KI/I ₂ and NaCl/hypochlorite leaching	Au (88%), Ag (65%)	Shibata and Matsumoto (1999)
	Solvent extraction		

Tab. 1.3 Summary of experimental work carried out on different material/reagent for metal recovery from e-scrap.

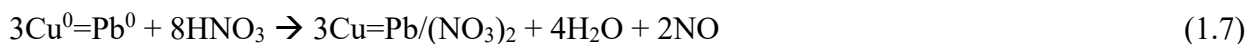
In addition, oxidative ammonia leaching can be suitably exploited for recovery of copper. Since precious metals contribute significantly to the value of WEEE, their extraction is in primary importance for the economics of a recycling operation.

Therefore, hydrometallurgical processes should focus on the extraction of precious metals. The most common leaching agents tested for recovery of precious metals include cyanide, halide, thiourea and thiosulfate. The pregnant leach solutions are then subjected to S/L separation and purification procedures such as precipitation of impurities, solvent extraction, adsorption and ion-exchange prior to the recovery of pure metals.

1.2.4.1 Acid leaching of metals

Acid leaching is often exploited as the first stage leaching for the extraction of base metals, copper in particular. Acid leaching of metals from e-waste have been extensively investigated using various mineral acids and oxidants (HCl, H₂SO₄, HNO₃/H₂O₂, HClO₄, NaClO) (Tab. 1.3). Madenoglu [17] reported that the highest extraction of copper and gold from PCBs was obtained by using HNO₃/HCl media i.e. aqua regia. He also found that pyrolysis of PCB prior to leaching adversely affected the dissolution of these metals. In a similar study, Sheng and Etsell [18] observed rapid dissolution of gold from computer PCBs in aqua regia at 90°C. Mecucci and Scott [19] achieved high copper and lead extractions (>95%) by nitric acid (HNO₃) (Eq. 1.7).

These investigators also studied electrowinning of these metals from pregnant leach solutions. Kinoshita et al. [20] also studied the purification of pregnant leach solutions (generated by nitric acid leaching) by solvent extraction using LIX984.



Hydrogen peroxide is a strong oxidant, which is commonly used in combination with acids (Eq. 1.8) to enhance metal extraction.

The oxidation reaction is highly exothermic ($\Delta H^0 = -411.2$ kJ/mol) and control of temperature may be needed. As also confirmed by recent studies, concentration of H₂O₂ and temperature are the most influential factors affecting metal extraction from e-waste. Oh et al. [21] proposed sulfuric acid (H₂SO₄) leaching of PCBs in the presence of H₂O₂ as a first stage process where Cu, Fe, Zn, Ni and Al were extracted at high recoveries of >95%.



In the second stage, they targeted at the recovery of precious metals using ammoniacal thiosulfate (CuSO₄-NH₄OH-(NH₄)₂S₂O₃) as lixiviant. Quinet et al. [22] also considered sulfuric acid leaching as the first stage process at which various oxidants including H₂O₂, O and Fe³⁺ were tested for the extraction of copper. These investigators proposed an integrated flowsheet for the treatment of PCBs of mobile phones (Fig. 1.18).

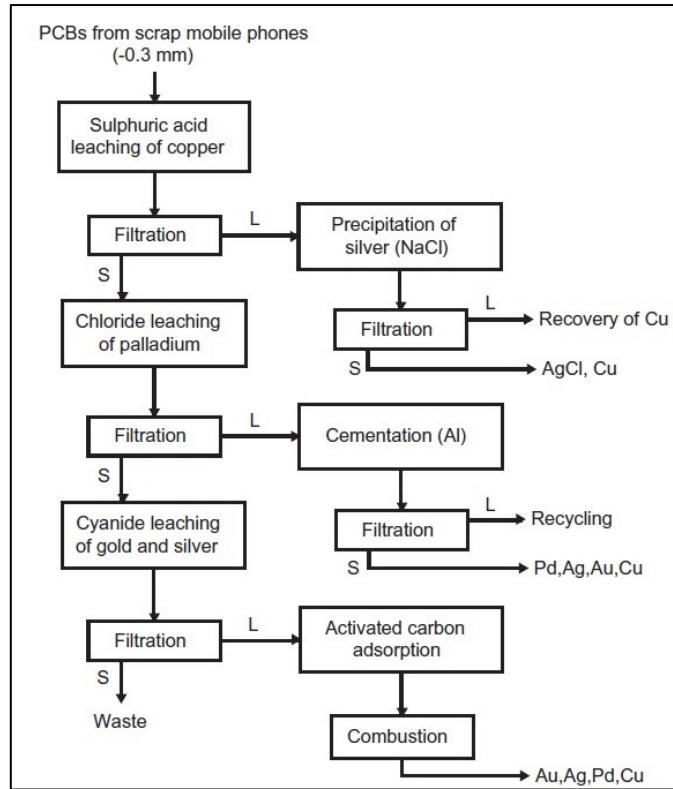


Fig. 1.18 A process flowsheet proposed for hydrometallurgical extraction of copper and precious metals (Au, Ag and Pd) from PCBs of scrap mobile phones.

In addition to chemical leaching, bioleaching of e-waste as a low cost and environmentally friendly process has also received attention in recent years. Although bioleaching processes are particularly suitable for the treatment of low-grade materials and small scale applications, they suffer from long residence time for metal extraction, low pulp density (i.e. <20%) and metal toxicity. Bioleaching of metals from e-wastes is often performed using iron oxidizing strains of acidophilic bacteria (*Acidithiobacillus ferrooxidans* and *Leptospirillum ferrooxidans*), which readily oxidize ferrous iron (Fe^{2+}) to generate ferric iron (Fe^{3+}) (Eq. 1.9).



The latter is a powerful oxidizing agent with a standard reduction potential of 0.77 V and readily oxidize metals (e.g. Cu) leading their dissolution (Eq. 1.10).



Maintenance of an acidic environment (<pH 2) is prerequisite for bioleaching to keep metals (i.e. iron, in particular) in solution.

Brandl et al. [23] investigated the bioleaching of dust generated during the size reduction of e-waste and found that metals including Cu, Al, Ni and Zn could be readily extracted (>90%) by using mesophilic bacteria (*At. ferrooxidans* and *L. ferrooxidans*).

However, they observed low extractions for Al and Cu at high pulp densities at which the precipitation of Cu occurred apparently due to the persistently high pH. They also attributed these low metal extractions to toxicity of metals as their concentration increased at high pulp densities. Ilyas et al. [24] demonstrated that metal tolerance of bacteria can be improved by adaptation. Ilyas et al. [25] also examined the bioleaching performance of moderately thermophilic bacteria (*Sulfobacillus thermosulfidooxidans*) with the final metal extractions of >89% Cu, 81% Ni and 83% Zn. In addition to acidophilic bacteria, other microorganisms including fungi (i.e. *Aspergillus niger*) and cyanide-generating bacteria (*Pseudomonas fluorescens* and *Chromobacterium violaceum*) were also studied for bioleaching of e-waste. Bioleaching may be appropriately considered as the first stage leaching process for those metals soluble in sulfate media and, hence, precious metals as well as Pb essentially remain in bioleaching residues, which can be further treated in a suitable lixiviant to recover these metals.

1.2.4.2 Leaching of precious metals

Many WEEEs contain appreciable quantities of precious metals including gold, silver and palladium. Therefore, extraction of these precious metals will be the primary objective of a leaching process. Leaching of precious metals is also of interest for refining of precious metals after a pyrometallurgical treatment of WEEE. There are many potential lixiviant systems that can be exploited for extraction of precious metals from WEEE. Those lixiviants that have also received interest for the treatment of WEEE include cyanide, thiosulfate, thiourea and halide with their ability to form highly stable complexes with gold (Tab. 1.4).

Lixiviants	Reagents	Chemistry	Species and their stability	Conditions
Cyanide	CN ⁻ , Air (O ₂)	$4\text{Au} + 8\text{CN}^- + \text{O}_2 + 2\text{H}_2\text{O} = 4\text{Au}(\text{CN})_2^- + 4\text{OH}^-$	Au(CN) ₂ ⁻ (log K = 38.3) Ag(CN) ₂ ⁻ (log K = 20.3)	E ⁰ : -0.67 V pH >10 25 °C
Thiosulfate	S ₂ O ₃ ²⁻ , NH ₃ , Cu ²⁺	$4\text{Au} + 8\text{S}_2\text{O}_3^{2-} + \text{O}_2 + 2\text{H}_2\text{O} = 4[\text{Au}(\text{S}_2\text{O}_3)_2]^{3-} + 4\text{OH}^-$	Au(S ₂ O ₃) ₂ ³⁻ (log K = 28.7) Ag(S ₂ O ₃) ₂ ³⁻ (log K = 13)	E ⁰ : 0.274–0.038 V pH >8–11 25 °C
Thiourea	CSN(NH ₂) ₂ , Fe ³⁺	$2\text{Au} + 4\text{CS}(\text{NH}_2)_2 + 2\text{Fe}^{3+} = 2\text{Au}(\text{CS}(\text{NH}_2)_2)_2^+ + 2\text{Fe}^{2+}$	Au(CS(NH ₂) ₂) ₂ ⁺ (log K = 22) Ag(CS(NH ₂) ₂) ₂ ⁺ (log K = 13)	E ⁰ : 0.38 V pH 1–2 25 °C
Halide	Cl ⁻ /Cl ₂ , Br ⁻ /Br ₂ , I ⁻ /I ₂	$2\text{Au} + 11\text{HCl} + 3\text{HNO}_3 = 2\text{HAuCl}_4 + 3\text{NOCl} + 6\text{H}_2\text{O}$	AuCl ₄ ⁻ (log K = 29.6)	E ⁰ : 1.00 V pH <4 25 °C

Tab. 1.4 Summary of features of potential leaching systems for extraction of gold from WEEE

Leaching of precious metals from WEEE in these lixiviants is well-established, industrially practiced or demonstrated at large scale. Tab. 1.4 summarizes main features of these lixiviant systems.

Table 1.5 also present their advantages and disadvantages for process development, and their comparison with cyanide for economics, applicability and toxicity based on the experience in precious metal ore leaching and refining.

	Pros	Cons
Cyanide leaching	Very effective for leaching gold, economically extract gold with grades as low as 1–3 Au g/t, well established process	Environmental problems due to high toxicity
Thiosulfate leaching	Low cost, environmentally friendly, fast leaching rate	Low chemical stability, downstream metal recovery
Thiourea leaching	Fast leaching rate	Potential carcinogen, low chemical stability
Halide leaching	Relatively healthy and safe, high chemical stability	More difficult to apply, low developmental stage

Tab. 1.5 Pros and cons of potential leaching reagents for precious metals.

Quinet et al. [22] examined oxidative leaching of palladium using HNO_3 or H_2O_2 in chloride media (HCl and NaCl) (Eq. 1.11, 1.12) whereby high extractions (93–95% Pd) were achieved at 75 °C.



The residues from palladium leaching stage were submitted by these investigators to cyanide leaching for the extraction of gold and silver. Sheng and Etsell [18] reported the extraction of gold from computer chips via sequential leaching in nitric acid to separate base metals and then in aqua regia after the crushing of the nitric acid residues. Park and Fray [26] observed that, in contrast to gold, silver and palladium remained mainly in the residue during the leaching of printed circuit boards in aqua regia. They examined the residue and confirmed the formation of a red palladium precipitate ($\text{Pd}(\text{NH}_4)_2\text{Cl}_6$).

Oh et al. [21] reported high gold (95%) and silver (100%) recoveries from printed circuit boards by thiosulfate leaching. In a similar study, Ha et al. [27] found rapid extraction of gold (i.e. 98% in 2 h) from scrap in a lixiviant solution containing 20 mM copper, 0.12 M thiosulfate and 0.2 M ammonia. However, they observed discernibly slow leaching of gold (i.e. 90% in 10 h) from printed circuit boards under the same leaching conditions. Lee et al. [28] achieved complete extraction of gold, silver and copper by thiourea leaching after the pre-treatment of scrap integrated circuit involving roasting, size reduction and magnetic separation.

1.2.4.3. Solution purification and metal recovery

For purification of pregnant leach solutions and recovery of base/precious metals from these solutions, several methods including solvent extraction, adsorption on activated carbon, ion exchange, precipitation, cementation and electrowinning can be readily exploited. Selection and development of downstream purification and metal recovery processes are based essentially on the factors such as leaching reagent system (i.e. Cl^- , SO_4^{2-} , etc.), concentration of metal(s) and impurities. Quinet et al. [22] proposed a flowsheet for the treatment scrap mobile phones for the recovery of copper and precious metals (Fig. 1.18). They recovered Ag from the first stage sulfuric acid leaching solutions by precipitation with NaCl. They also used cementation by aluminum for the recovery of precious metals (Ag, Pd and Au) from chloride solutions and activated carbon adsorption from cyanide leach solutions. Alam et al. [29] developed a recovery process based on the cementation of silver by copper powder and then the removal of other metals (Co, Zn, Ni, Al, Mn, etc.) by solvent extraction (using LIX 26) from ammoniacal leach solutions prior to the electrowinning of copper. Le et al. [30] studied the purification of nitric acid leach solutions by solvent extraction (using LIX984) and proposed the use of electrowinning or hydrogen reduction for subsequent copper recovery. Kamberovic et al. [31] removed Ag from sulfuric acid solutions by cementation on copper prior to the electrowinning of copper. They also used zinc cementation for the control of impurities such as Fe and Ni in spent electrolyte and for the recovery of Au and Ag from thiourea leach solutions. Yang et al. [32] also reported the recovery of copper from sulfate media by crystallization (as $\text{CuSO}_4 \cdot 5\text{H}_2\text{O}$). Sheng and Etsell [18] used ferrous sulfate to precipitate gold from chloride solutions. Park and Fray [33] recovered gold from aqua regia solutions by liquid–liquid extraction with toluene. They converted the extracted gold to nano-particles by treatment with dodecanethiol and sodium borohydride.

1.3 Green chemistry

Green chemistry is a term coined by Paul Anastas in 1991 to describe a chemical philosophy that seeks to reduce the negative impact of chemistry on the environment by preventing pollution and using fewer natural resources. The idea can be summarized in 12 principles that prescribe a process with high yield in terms of energy and materials, a use of environmentally friendly substances and an effort to create less waste as possible. In others words: reducing the environmental impact of the chemical process [34].

These 12 principles are [35]:

1. It is better to prevent waste than to treat or clean up waste after it is formed.
2. Synthetic methods should be designed to maximize the incorporation of all materials used in the process into the final product.
3. Wherever practicable, synthetic methodologies should be designed to use and generate substances that possess little or no toxicity to human health and the environment.
4. Chemical products should be designed to preserve efficacy of function while reducing toxicity.
5. The use of auxiliary substances (e.g., solvents, separation agents, and so forth) should be made unnecessary wherever possible and innocuous when used.
6. Energy requirements should be recognized for their environmental and economic impacts and should be minimized. Synthetic methods should be conducted at ambient temperature and pressure.
7. A raw material or feedstock should be renewable rather than depleting wherever technically and economically practicable.
8. Unnecessary derivatization (blocking group, protection/deprotection, temporary modification of physical/chemical processes) should be avoided whenever possible.
9. Catalytic reagents (as selective as possible) are superior to stoichiometric reagents.
10. Chemical products should be designed so that at the end of their function they do not persist in the environment and break down into innocuous degradation products.
11. Analytical methodologies need to be developed further to allow for real-time in-process monitoring and control before the formation of hazardous substances.
12. Substances and the form of a substance used in a chemical process should be chosen so as to minimize the potential for chemical accidents, including releases, explosions, and fires.

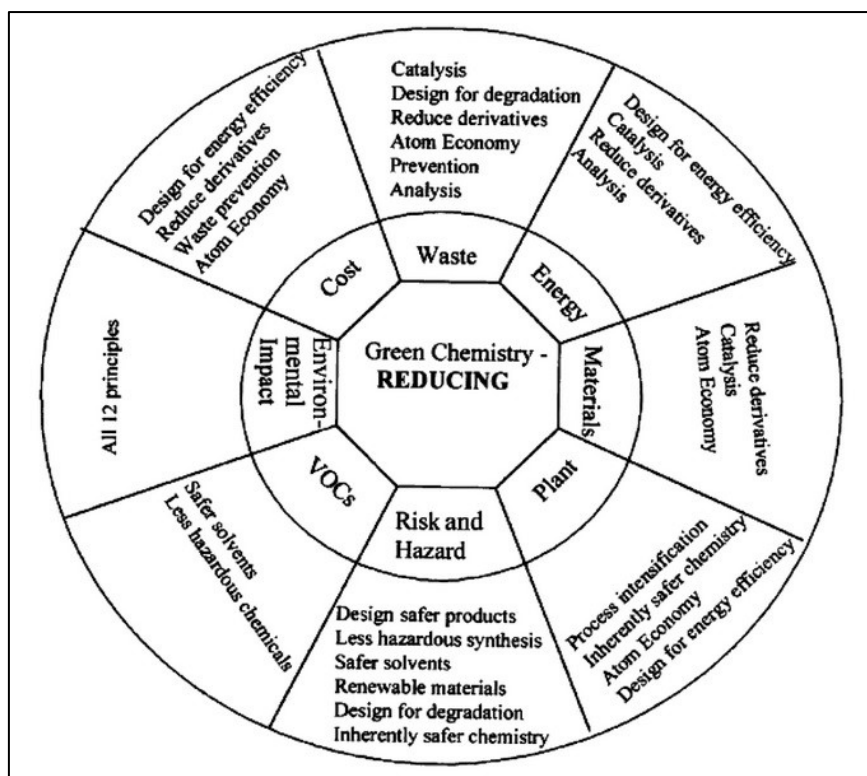


Fig. 1.19 Green chemistry as a reduction process [34].

The challenge for chemists and others is to develop new products, processes and services that achieve the societal, economic and environmental benefits that are now required. This requires a new approach which sets out to reduce the materials and energy intensity of chemical processes and products, minimize or eliminate the dispersion of harmful chemicals in the environment, maximize the use of renewable resources and extend the durability and recyclability of products—in a way which increases industrial competitiveness.

Some of the challenges for chemists include the discovery and development of new synthetic pathways using alternative feedstocks or more selective chemistry, identifying alternative reaction conditions and solvents for improved selectivity and energy minimization and designing less toxic and inherently safer chemicals. In chemical synthesis, the ideal will be a combination of a number of environmental, health and safety, and economic targets (Fig. 1.20).

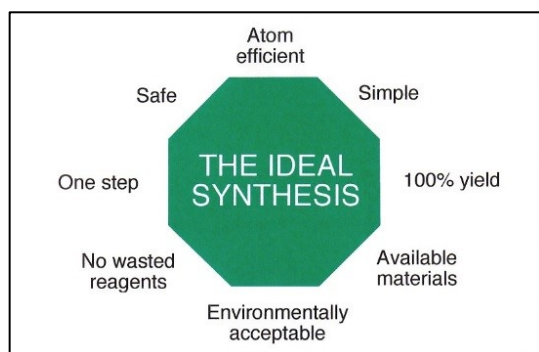


Fig. 1.20 The ideal synthesis.

Although many chemists, and some large and smaller companies, are actively pursuing ‘green chemistry’ there are still many barriers to progress. These include a general lack of awareness and training in schools, universities and industry and a management perception that green chemistry is a cost without benefits. The drive towards clean technology in the chemical industry with an increasing emphasis on the reduction of waste at source will require a level of innovation and new

technology that the chemical industry has not seen in many years. Mature chemical processes, that are often based on technology developed in the first half of the 20th century, may no longer be acceptable in these environmentally conscious days. ‘Enviro-economics’ will become the driving force for new products and processes. This can be seen by considering the ever-escalating and various ‘costs of waste’ (Fig. 1.21).

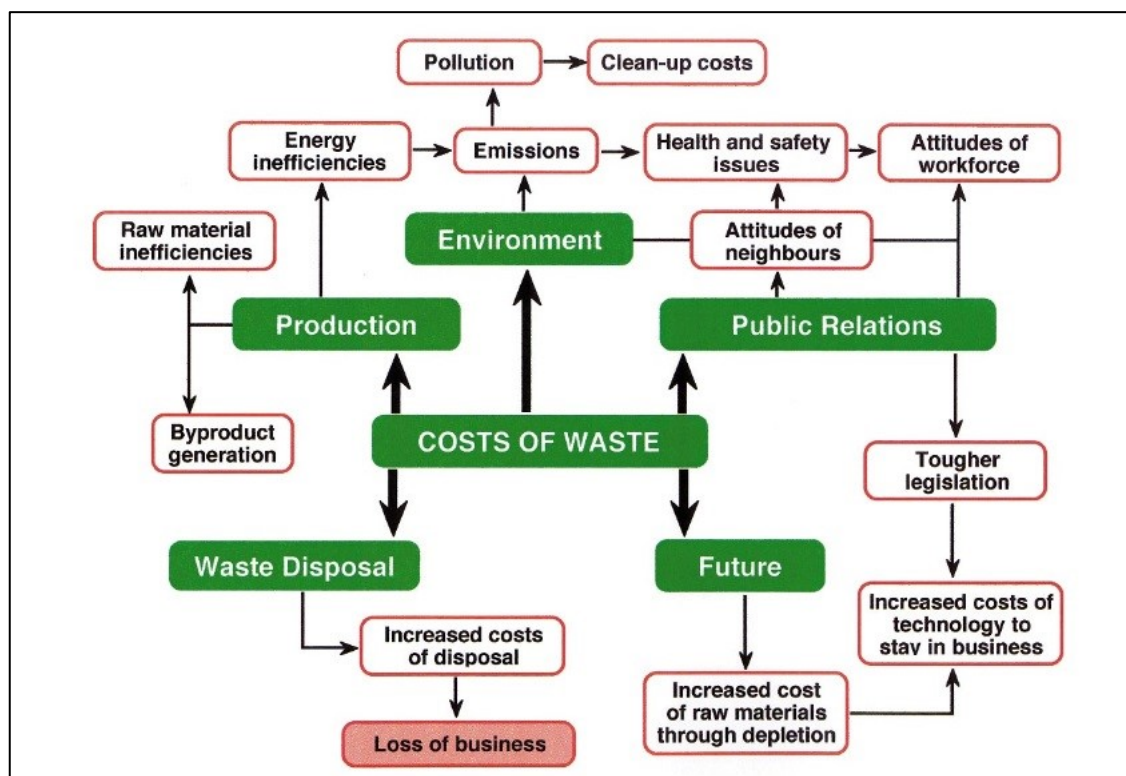


Fig. 1.21 *The costs of waste*

The costs of waste can truly be enormous. It has been estimated that compliance with existing environmental laws will cost new EU member states \$130 billion. In the US, \$115 billion was spent in 1992 on waste treatment and disposal. New European legislation and tighter national laws will make matters worse.

Industry and academe are now reacting to these challenges and many are seeing the opportunities—be they in winning research funding, unprecedented opportunities for translating new, greener chemistries from the research bench to the production plant or in gaining commercial advantage from the application of new low-waste processes or the marketing of new environmentally friendly products or technologies. The rapidly growing interest in green chemistry is partly witnessed by the growth in relevant conferences with regular events now being held in the USA, Europe and Asia. The Gordon Green Chemistry conferences (held alternately in the USA and Europe since 1995) along with other recent international meetings are good examples of effective meetings of industrial, academic and governmental chemists and engineers with a

variety of backgrounds, interests and areas of expertise but with the common goal of seeing the application of green chemistry throughout the chemical and allied industries.

Additionally, the emergence of Green Chemistry organizations in the USA, Italy and the UK are indications of the growing interest in the concept and the recognition of the value of networking such diverse activities. It is particularly significant to note that many of these organizations place education as high on their agenda as research—the long-term future of the subject and indeed of the industry will depend on future generations. In the US, a particularly important and strategic development was the emergence of the Presidential Green Chemistry Challenge awards. These have had numerous benefits, not least the open disclosure of many new and exciting products and processes that will be of real benefit to the environment and to the image of chemistry.

1.3.1 Green complexing agents: thiosulphate and thiourea

Recent investigations about the recovery of precious metals from different types of ores have showed that thiourea and thiosulfate can be used as complexing agent to replace cyanide in gold and silver leaching, with the advantages of faster leaching, lower toxicity and higher efficiency [36, 37, 38, 39, 40, 41, 42].

1.3.1.1 Thiourea

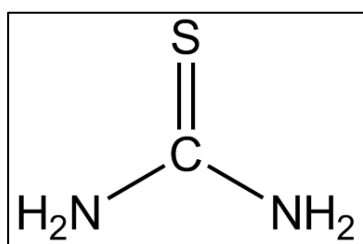
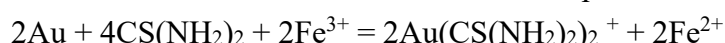


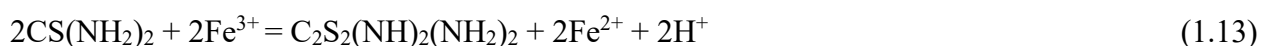
Fig. 1.22 Thiourea

Thiourea, $\text{SC}(\text{NH}_2)_2$, is an organosulfur compound which dissolves easily in acid solution in a stable molecular form. Gold dissolves in acidic thiourea solution to form a stable complex,

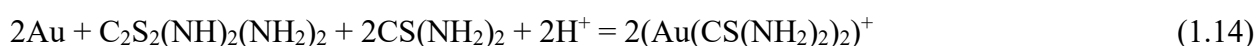


In the thiourea reaction, ferric iron is used as an oxidizing agent, whereas the cyanide process uses oxygen from the air, dissolved in the leach solution. Part of the ferric iron needed is most the time

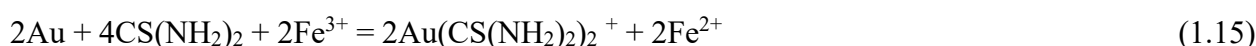
present in the ore. In the case of highly oxidized ores, enough ferric ions will be set free, and then the addition of an oxidant can be reduced. But these ores could content higher amounts of carbonates, which will increase the acid consumption. One could use hydrogen peroxide, sodium peroxide, ozone, potassium permanganate or formamidine disulfide as oxidant; however ferric ion is the most effective. Formamidine is interesting because it can be formed in acid solution by the thiourea oxidation by the presence of an oxidant agent such as ferric iron. Successfully leaching of thiourea depends on an understanding of the role of formamidine which is a compound very active during gold leaching. In the first step thiourea is oxidized to formamidine disulfide:



Oxidation thiourea is reversible. Thus, with a specific reducing agent, formamidine can be converted back into thiourea. In the next step, gold is oxidized by formamidine and forms a cationic gold thiourea complex:



Formamidine acts as an oxidizer as well as a complexing agent, supplying about 50% of the ligands to the complexation. This explains the higher leaching rates observed with thiourea compared to cyanidation. The general reaction is as follow,



Thiourea must be present in a stoichiometric excess. The ratio of complexing and oxidizing agents must be carefully adjusted. An uncontrolled oxidation of the thiourea solution will lead to

unwanted reagent consumption. In a final and irreversible step, formamidine breaks down to cyanamide and elemental sulphur. This forms two effects. First, the elemental sulphur will come in a fine, sticky form, which might passivate the feed ore. Second, loss of silver could occur because of a reaction which leads to precipitation of silver salts. The breakdown can be unpredictable, but it seems that the event is accelerated by high concentrations of formamidine. The corrective measure is to keep the concentration of thiourea itself low and prevent uncontrolled oxidation. High amounts of free thiourea result in rapid leaching, but they are vulnerable for a fast breakdown. The use of acidic solutions at potentials well below those required for the formation of oxide film on the gold surface obviates any possible passivation of the gold by oxide films and extractions in thiourea solutions are high. Of the several oxidants, only ferric ions offer any promise of practical application. The initial rate of dissolution of gold in freshly prepared thiourea solutions containing ferric ions is high, and is controlled only by the rate of diffusion of the oxidant to the gold surface. However, due to the slow oxidation of thiourea and the partial passivation of the gold surface by the products of oxidation, the rate of dissolution decreases with the age of the lixiviant, and this can lead to excessively high consumption of the reagent. The excess can be more than 5 kg/t.

One of the main advantages of thiourea is the high rate of gold dissolution. The leaching rate can be four to five times faster than cyanidation. This could be an important aspect for plants which process ore containing coarse gold particles. The much higher leaching time reduce the investment costs for a new processing plant. The thiourea leaching process can be modified for a given designed plant and for given ore conditions, whereas the leaching conditions of the cyanide process can only be modified within a narrow range. The costs of gold leaching process with thiourea are principally determined by thiourea consumption, which is related to thiourea and oxidant concentrations, pH and the solution potential. Thiourea concentrations between 5 to 50 g/l have been used in lab and pilot test. Sufficient amount of oxidant (i.e. ferric ion) is required to oxidize thiourea to formamidine disulfide to obtain optimal leaching conditions. The presence of excess oxidant increases thiourea consumption significantly. For this reason, close control of solution potential would be required through all stages of leaching in any commercial process. Thiourea consumptions of 1-4 kg/t have been estimated for optimized thiourea leaching systems based on currently available technologies. Such high consumptions, coupled with the requirements of sulfuric acid for pH control, and also agents for potential control, are the most important costs in the process, which are estimated between 1.5 to 2.1 times the cost of a cyanidation process.

1.3.1.2 Sodium thiosulphate

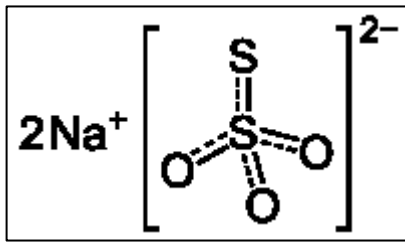


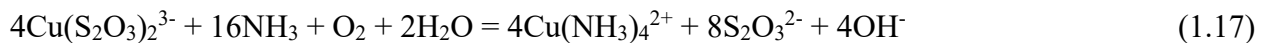
Fig. 1.23 Sodium thiosulphate.

Sodium thiosulfate is an inorganic compound with the formula $\text{Na}_2\text{S}_2\text{O}_3 \cdot \text{H}_2\text{O}$. It is a component of an alternative lixiviant to cyanide for extraction of gold. The advantage of this approach is that thiosulfate is essentially not toxic and that ore types that are refractory to gold cyanidation (e.g. carbonaceous or Carlin-type ores) can be leached by thiosulfate. The oxidation of gold in the presence of thiosulphate ions can be expected to produce

the gold complex $\text{Au}(\text{S}_2\text{O}_3)_2^{3-}$, but because thiosulphate does not work in acid solutions, alkaline solutions must be used. Few oxidants are suitable for use in alkaline solutions. Although oxygen is an effective reagent for cyanidation, it is not electrochemically active at the required potential for thiosulphate leaching. The reaction is:



The rate of dissolution is dependent on thiosulphate and dissolved oxygen concentrations and temperature. Leaching rate is improved by copper in ammonium solution.



Silver chloride and silver sulfide are easily leached. The thiosulphate compounds are consumed by several oxidations and association reactions.



Thiosulphate can be stabilized by the addition of small amounts of sulfite ions which react with sulfide sulphur and regenerate thiosulphate. This prevents the precipitation of silver as the insoluble sulfide. In the anodic area, gold is oxidized and complexed with ammonia. This complex can be replaced by a more stable gold thiosulphate complex. In the cathodic area, the cupric amine complex is reduced and the oxygen present in the ammonia solution oxidizes the cuprous complex to a cupric compound. Ammonia and copper are recycled in the system. It has been reported that the thiosulphate consumption is very high such as 29 kg/t, but it can be reduced by adding reducing agents as chelates which can give a consumption of 13 kg/t. Obviously, there are many factors that influence thiosulphate consumption. Some of these factors are: sulfide minerals present in the ore which react with thiosulphate; oxidant compounds increase the consumption of thiosulphate, and the solid percentage in the system. Thiosulphate does not present a good stability when it is exposed to ultraviolet light, or in presence of heavy metals, or if exist a high number of cations dissolved in the water. Gold recoveries by leaching can be higher than 90%, but, as was mentioned, with a high consumption of thiosulphate. The pH can be in the range 10.0 to 10.5 and the pulp

density can be in the range 40 to 45% solids. Pregnant solutions obtained with thiosulphate don't give a good recovery with activated carbon or resins. The best results were obtained by cementation with zinc, copper or iron [43].

1.4 The ultrasound

During the hydrometallurgical process, the use of ultrasound could represent a further advantage, since they could increase the yield, reduce the reagent and the energy consumption, and reduce thermal supplying [44, 45, 46, 47].

In next paragraphs, the theoretical fundamentals of ultrasound application to hydrometallurgical reaction are reported [48, 49].

In fact, the use of ultrasound in liquids produces a particular effect called cavitation that allows to de-agglomerated and individually scrub into the micron domain particles and increase molecular diffusion and mass transfer rates. The cavitation also induces an increase of instantaneous velocity of particles, improving both wetting and liquid-solid interface reactions [46, 47, 44, 45].

In this work, ultrasound will be applied both to increase the yield during metals recovery from wastes and to reduce the sizes of nanoparticles during their synthesis.

1.4.1 The acoustic cavitation

An acoustic wave (sound) is a propagation of pressure oscillation in medium such as air or liquid water with the sound velocity. Ultrasounds are inaudible sounds which frequency higher than 20 kHz (20,000 oscillations per second). For convenience, an acoustic wave above 10 kHz in frequency is sometimes called an ultrasonic wave.

When the pressure amplitude of an acoustic wave in liquid or solid exceeds the ambient pressure (atmospheric pressure), the instantaneous pressure becomes negative during the rarefaction phase of an acoustic wave. Negative pressure is defined as the force acting on the surface of a liquid (or solid) element per surface area to expand the element. For example, consider a closed cylinder filled with liquid with a movable piston. When a piston is pulled strongly, the liquid volume slightly increases. At this moment, the pressure in the liquid is negative. Negative pressure is possible only in liquid or solid.

When the instantaneous local pressure becomes negative in liquid irradiated by ultrasound, bubbles are generated because the gas dissolved in the liquid can no longer be dissolved in the liquid under negative pressure. This is called acoustic cavitation. For a static condition, vapor bubbles are generated when the static pressure is lower than the saturated vapor pressure, which is called boiling. In acoustic cavitation, the instantaneous local pressure is negative thanks to the short low-pressure time. The difference between acoustic cavitation and boiling is the collapsing of bubbles in acoustic cavitation. Under ultrasound, a generated bubble expands during the rarefaction phase and collapses during the compression phase. The speed of the bubble collapsing increases to the sound velocity in liquid. Accordingly, the bubble collapsing is a quasi-adiabatic process where “quasi” means that considerable thermal conduction takes place between the interior of a bubble and the surrounding liquid.

The temperature and pressure inside a bubble increase to thousands of Kelvin and thousands of bars, respectively at the end of the bubble collapsing. Furthermore, a bubble emits a shock wave

through the surrounding liquid just after the end of the bubble collapsing. This effect is absent in boiling. As the temperature and pressure dramatically increase inside a bubble at the end of the collapse, water vapor and oxygen, if present, are dissociated inside a bubble and oxidants such as OH, O, and H₂O₂ are created. They dissolve into the liquid and solutes are oxidized by them. This is called sonochemical reaction. For example, potassium iodide (KI) in aqueous solution is oxidized by the irradiation of ultrasound (Eq. 1.20), and the solution is gradually colored by the product (I₃⁻) as the irradiation time increases.



1.4.2 Transient and Stable Cavitation

There are two types of acoustic cavitation. One is transient cavitation and the other is stable cavitation. There are two definitions in transient cavitation. One is that the lifetime of a bubble is relatively short such as one or a few acoustic cycles, as a bubble is fragmented into daughter bubbles due to its shape instability. The other is that bubbles are active in light emission (sonoluminescence (SL)) or chemical reactions (sonochemical reactions). Accordingly, there are two definitions in stable cavitation. One is that bubbles are shape stable and have a long lifetime. The other is that bubbles are inactive in SL and chemical reactions. However, there exist some bubbles which are both shape stable and active in SL or chemical reactions.

They are classified into stable cavitation bubbles by the former definition and called “high-energy stable cavitation” bubbles. On the other hand, they are classified into transient cavitation bubbles by the latter definition and called “repetitive transient cavitation” bubbles. Whenever the terms transient and stable cavitation are used, it is necessary to indicate which definition is used, shape stability or activity.

In Fig. 1.24, the parameter region for transient and stable cavitation bubbles is shown in R₀ (ambient bubble radius) – p_a (acoustic amplitude) plane. The ambient bubble radius is defined as the bubble radius when an acoustic wave (ultrasound) is absent. The acoustic amplitude is defined as the pressure amplitude of an acoustic wave (ultrasound). Here, transient and stable cavitation bubbles are defined by their shape stability. This is the result of numerical simulations of bubble pulsations. Above the thickest line, bubbles are those of transient cavitation. Below the thickest line, bubbles are those of stable cavitation. Near the left upper side, there is a region for bubbles of “high-energy stable cavitation” designated by “Stable (strong nf₀)”. In the brackets, the type of acoustic cavitation noise is indicated. The acoustic cavitation noise is defined as acoustic emissions from acoustic cavitation. Every pulsating bubble under ultrasound radiates a secondary acoustic wave, which is the origin of the acoustic cavitation noise. “Strong nf₀” means that strong harmonics components are to be observed in the frequency spectrum of acoustic cavitation noise (Fig. 1.25a). In Fig. 1.25a, the harmonics components are sharp peaks. From the other space in Fig. 1.24 for stable cavitation bubbles designated by “stable (weak nf₀)”, the harmonics components are very

weak as the bubble pulsation is much milder. From transient cavitation bubbles, broad-band noise is to be observed as well as the harmonics components (Fig.1.25b). The broad-band noise is the

Type	Pulsation	Noise spectrum
Stable (Low energy)	Periodic (period T)	Weak nf_0
	Periodic (period T)	Strong nf_0
(High energy)	Periodic (period T)	nf_0 + broad-band
	Periodic (period 2T)	$nf_0/2$ + broad-band
Transient	Periodic (period 4T)	$nf_0/4$ + broad-band
	Chaotic (steady-state)	Broad-band
	Chaotic (initial transient)	Broad-band

Tab. 1.2 *The relationship between the type of cavitation bubbles and that of the cavitation noise spectrum in the parameter space shown in Fig. 1.24. “Chaotic (initial transient)” means nonperiodic pulsation only at the initial transient stage although the pulsation becomes periodic at the steady-state.*

continuum component in the frequency spectrum of the acoustic cavitation noise. Temporal fluctuation in the number of bubbles results in the broad-band noise. In transient cavitation, bubbles occasionally fragment into daughter bubbles, coalesce each other, and are nucleated, which results in a temporal fluctuation of the bubbles number. Some bubbles pulsate with a period of 2T or 4T where T is the acoustic period, which results in the subharmonic and ultraharmonic components in the acoustic cavitation noise. The relationship between the type of cavitation and the acoustic cavitation noise is listed in Table 1.2.

Some bubbles pulsate non-periodically as designated by “chaotic”, which also results in the broad-band noise without any peaks.

However, its contribution to the total broad-band noise is minor at least under the condition studied in Fig. 1.24. From Fig. 1.24, it is seen that stable cavitation bubbles are tiny bubbles of a few mm ambient radius or relatively large bubbles which radius is about 10 mm or more at 515kHz. The range of ambient radius for transient cavitation bubbles becomes wider as the acoustic amplitude increases and ultrasonic frequency decreases.

Roughly speaking, stable cavitation bubbles are more frequently seen when acoustic amplitude is lower and ultrasonic frequency is higher. In other words, transient cavitation bubbles are more frequently seen when acoustic amplitude is higher and ultrasonic frequency is lower. It is possible to control the population of stable cavitation bubbles relative to that of transient ones by the addition of a surfactant to the liquid because coalescence of bubbles is strongly retarded by a surfactant and the ambient radius of bubbles becomes sufficiently small for stable cavitation bubbles.

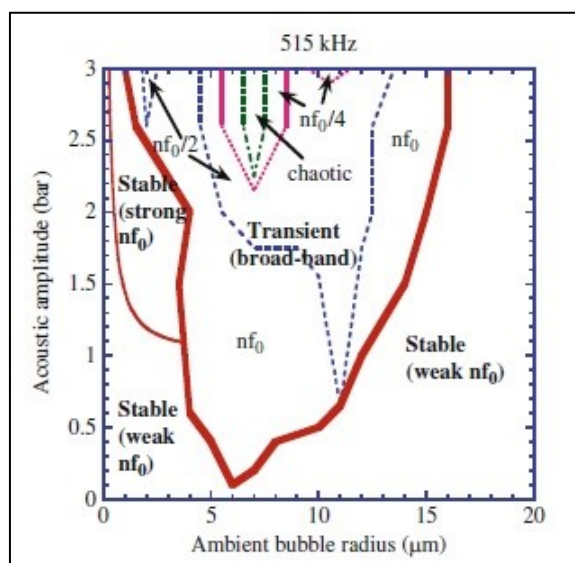


Fig. 1.24 The regions for “transient” cavitation bubbles and “stable” cavitation bubbles when they are defined by the shape stability of bubbles in the parameter space of ambient bubble radius (R_0) and the acoustic amplitude (p_a). The ultrasonic frequency is 515 kHz. The thickest line is the border between the region for “stable” cavitation bubbles and that for “transient” ones. The type of bubble pulsation has been indicated by the frequency spectrum of acoustic cavitation noise such as nf_0 (periodic pulsation with the acoustic period), $nf_0/2$ (doubled acoustic period), $nf_0/4$ (quadrupled acoustic period), and chaotic (non-periodic pulsation). Any “transient” cavitation bubbles result in the broad-band noise due to the temporal fluctuation in the number of bubbles.

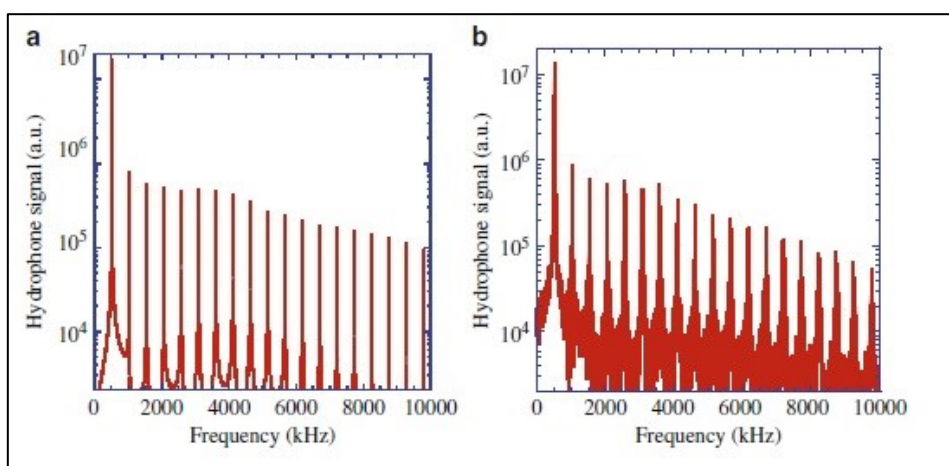


Fig. 1.25 Numerically simulated frequency spectra of the hydrophone signal due to acoustic cavitation noise. The driving ultrasound is 515 kHz in frequency and 2.6 bar in pressure amplitude. (a) For stable cavitation bubbles of 1.5 mm in ambient radius. (b) For transient cavitation bubbles of 3 mm in ambient radius.

1.4.3 Nucleation of Bubbles

How is a bubble created in acoustic cavitation? There are three mechanisms in nucleation of a bubble in acoustic cavitation. One is the nucleation at the surface of solids such as a liquid container, motes or particles in liquid, if present.

Nucleation takes place especially at crevices of motes, particles or a liquid container (Fig. 1.26).

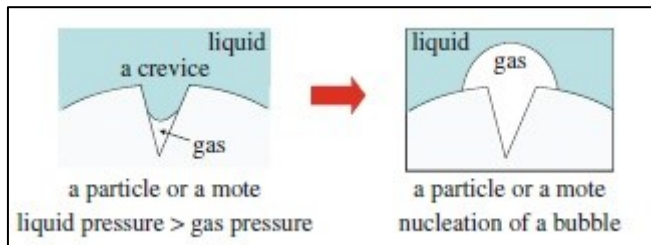


Fig. 1.26 Nucleation of a bubble from a crevice

In a crevice, the surface of a gas pocket is concave and the surface tension of a gas pocket reduces the pressure inside the pocket. It means that a gas pocket is stabilized against dissolution into the liquid because the partial pressure of dissolved gas in the liquid is higher than that in a gas pocket. When the liquid is irradiated by

ultrasound, a gas pocket in a crevice expands during the rarefaction phase of ultrasound and gas diffuses into the pocket from the surrounding liquid as the pressure inside a pocket further decreases. During the compression phase of ultrasound, a gas pocket shrinks and the gas pressure increases in the pocket. It results in the diffusion of gas out of the pocket into the liquid. Nevertheless, a gas pocket grows as the amount of gas diffusing into the pocket during the expansion is larger than that diffusing out of the pocket during the compression. This is because the surface area of a pocket is larger during expansion than that during compression (the area effect). Furthermore, the boundary layer for gas diffusion in the liquid is thinner during expansion than that during compression because the volume of the boundary layer is nearly constant and the surface area is larger during expansion (the shell effect). It results in the higher rate of diffusion during expansion because the gradient in concentration of the gas in the liquid is larger. Finally, a gas bubble is created from a crevice when the gas pocket sufficiently grows. The presence of particles in liquid reduces the threshold acoustic pressure for cavitation due to the above mechanism.

The second mechanism for nucleation is the initially present bubble nuclei which are stabilized against dissolution by the coverage of its surface with surfactants slightly present in the liquid as impurities. Without surfactants, bubbles with radius smaller than 1 mm should dissolve within a few seconds in the absence of ultrasound unless the liquid is supersaturated with gas. It is because the gas pressure inside a bubble is larger than the partial pressure of the dissolved gas in the liquid due to the surface tension of a bubble (The excess gas pressure inside a bubble is $\Delta p = 2\sigma/R$, where σ is the surface tension and R is the bubble radius).

Thus, the gas inside a bubble gradually dissolves into the surrounding liquid. On the other hand, bubbles larger than 1 mm in radius should float to the liquid surface by a buoyant force. Nevertheless, bubble nuclei (tiny bubbles of a few mm in radius) have been experimentally observed in liquids even in the absence of an acoustic wave (ultrasound). It suggests that such

bubble nuclei are stabilized by surfactants which strongly retard the mass (gas) diffusion across the bubble surface. Under ultrasound, these stabilized nuclei grow by coalescence and gas diffusion, which initiates acoustic cavitation.

The third mechanism for nucleation is the fragmentation of active cavitation bubbles. A shape unstable bubble is fragmented into several daughter bubbles which are new nuclei for cavitation bubbles. Shape instability of a bubble is mostly induced by an asymmetric acoustic environment such as the presence of a neighboring bubble, solid object, liquid surface, or a traveling ultrasound, or an asymmetric liquid container etc. Under some condition, a bubble jets many tiny bubbles which are new nuclei. This mechanism is important after acoustic cavitation is fully started.

1.4.4 Growth of a Bubble

There are two mechanisms for the bubble growth in acoustic cavitation. One is the coalescence of bubbles. The other is the gas diffusion into a bubble due to the area and shell effects described before. This is called rectified diffusion.

The coalescence of bubbles is driven by the two mechanisms. One is the attractive radiation force between bubbles called secondary Bjerknes force. The other is the radiation force called the primary Bjerknes force which drives active bubbles to the pressure antinode of a standing wave field. It should be noted, however, that too strong acoustic wave repels bubbles from the pressure antinode. The bubble growth rate due to rectified diffusion strongly depends on acoustic amplitude and frequency. For a very weak driving such as 0.2 bar at 20 kHz, the bubble growth rate is in the order of a few mm per 100s for the initial radius of 35mm. For a much stronger driving such as 2 bar at 30 kHz, it ranges from 10 to a few hundred mm per second depending on the initial radius. It decreases as ultrasonic frequency increases for the same acoustic pressure amplitude.

Relative importance of coalescence and rectified diffusion in the bubble growth is still under debate. After acoustic cavitation is fully started, coalescence of bubbles may be the main mechanism of the bubble growth. On the other hand, at the initial development of acoustic cavitation, rectified diffusion may be the main mechanism as the rate of coalescence is proportional to the square of the number density of bubbles which should be small at the initial stage of acoustic cavitation. Further studies are required on this subject.

1.4.5 Radiation Forces on a Bubble (Primary and Secondary Bjerknes Forces)

Both the primary and secondary Bjerknes forces are originated from the pressure gradient across a bubble.

$$\vec{F}_B = -\langle V(t) \nabla p(\vec{x}, t) \rangle \quad (1.21)$$

Where \vec{F}_B is the primary or secondary Bjerknes force, $V(t)$ is the instantaneous bubble volume, $\nabla = (\frac{\partial}{\partial x}, \frac{\partial}{\partial y}, \frac{\partial}{\partial z})$ in xyz-coordinate, $p(\vec{x}, t)$ is the instantaneous local pressure at position \vec{x} , and $\langle \quad \rangle$ denotes the time average. For the primary Bjerknes force, $p(\vec{x}, t)$ is the driving ultrasound. On the other hand, for the secondary Bjerknes force, $p(\vec{x}, t)$ is the acoustic wave radiated by a neighboring bubble.

When the driving ultrasound is a standing wave, $p(\vec{x}, t)$ is expressed as follows for the primary Bjerknes force.

$$p(\vec{x}, t) = p_a \cos(\vec{k} \times \vec{x}) \sin(\omega t) \quad (1.22)$$

where p_a is the acoustic pressure amplitude, \vec{k} is the wave vector, and ω is the angular frequency. Then, the primary Bjerknes force (\vec{F}_B) is given by the following equation.

$$\vec{F}_B = p_a \vec{k} \sin(\vec{k} \times \vec{x}) - \langle V(t) \sin(\omega t) \rangle \quad (1.23)$$

When the bubble pulsation is in phase with the driving ultrasound, a bubble is attracted to the pressure antinode of a standing wave field. For a very low driving such as less than 0.1 bar in acoustic amplitude, bubble pulsation is nearly linear and this condition coincides with smaller ambient radius than the linear resonance radius. For active bubbles, pulsation is strongly nonlinear, and the situation is more complex. For example, at 20 kHz, an active bubble of smaller ambient radius than the linear resonance radius is repelled from the pressure antinode when the acoustic pressure amplitude is larger than about 1.8 bar. This is because a bubble continues expanding even during the compression phase of ultrasound due to the inertia of the surrounding liquid. To active bubbles (“transient cavitation bubbles” by the definition based on activity of bubbles), the linear theory cannot be applied.

In a traveling wave of ultrasound, most active bubbles are pushed toward the direction of the wave propagation by the primary Bjerknes force. Furthermore, there is a fluid flow in the direction of the wave propagation called acoustic streaming. Acoustic streaming is caused by the attenuation of a traveling wave resulting in the net radiation force in the direction of the wave propagation.

The attenuation is caused by both viscosity of the liquid and the cavitation bubbles. Furthermore, moving bubbles driven by the primary Bjerknes force drag the surrounding fluid. The resulting fluid flow is called quasi acoustic streaming.

While the secondary Bjerknes force is always attractive if the ambient radius is the same between bubbles, it can be repulsive if the ambient radius is different.

The magnitude as well as the sign of the secondary Bjerknes force is a strong function of the ambient bubble radii of two bubbles, the acoustic pressure amplitude, and the acoustic frequency. It is calculated by:

$$\vec{F}_{1 \rightarrow 2} = \frac{\rho}{4\pi d^2} \langle \ddot{V}_1 V_2 \rangle \vec{e}_r \quad (1.24)$$

Where $\vec{F}_{1 \rightarrow 2}$ is the secondary Bjerknes force acting on bubble 2 from bubble 1, ρ is the liquid density, d is the distance between the bubbles 1 and 2, \ddot{V}_1 is the second-time derivative of the volume of bubble 1, V_2 is the volume of bubble 2, $\langle \ \rangle$ denotes the time average, and \vec{e}_r is the radial unit vector directed from bubble 1 to bubble 2. For a very low driving (such as less than 0.1 bar in acoustic amplitude) or for very large bubbles, the bubble pulsation is nearly linear and bubbles with the ambient radii both less (more) than the linear resonance radius pulsate in phase resulting in the attractive secondary Bjerknes force. On the other hand, when the ambient radius of a bubble is less than the linear resonance radius and that of the other bubble is more than it, it is repulsive. For active bubbles, however, the bubble pulsation is strongly nonlinear and the situation is much more complex. The theory for linear pulsation of bubbles should not be applied to active bubbles as already noted.

1.4.6 Bubble Radial Dynamics

Bubble radial dynamics is well described by the Rayleigh-Plesset equation or its modified version such as Keller and Herring equations. The Rayleigh-Plesset equation is derived as follows. Consider a liquid volume surrounding a pulsating bubble such that the liquid volume is much larger than the bubble volume and that the radius of the liquid volume is much smaller than the acoustic wavelength.

The kinetic energy (E_K) of the liquid volume is given by:

$$E_k = \frac{1}{2} \int_R^{R_L} \dot{r}^2 4\pi r^2 dr = 2\pi\rho R^3 \dot{R}^2 \quad (1.25)$$

where ρ is the liquid density, R_L is the radius of the liquid volume, R is the instantaneous bubble radius, r is the radial distance from the bubble center, the dot denotes the time derivative, and the liquid incompressibility condition ($\dot{r}/\dot{R} = R^2/r^2$) as well as the condition $R \ll R_L$ has been used. The work done by a pulsating bubble (W_{bubble}) to the surrounding liquid is given by Eq. 1.26).

$$W_{bubble} = \int_{R_0}^R 4\pi r^2 p_B dr \quad (1.26)$$

where R_0 is the ambient bubble radius, and p_B is the liquid pressure at the bubble wall. If the liquid is incompressible, the liquid volume does some work to the surrounding liquid (W_{liquid}) as it moves outward associated with the bubble expansion.

$$W_{liquid} = \int_{R_0}^R 4\pi r^2 p_{\infty} dr \quad (1.27)$$

where p_{∞} is the pressure at the surface of the liquid volume including the acoustic pressure. The conservation of energy requires the following relationship.

$$W_{bubble} = E_K + W_{liquid} \quad (1.28)$$

Differentiation of Eq. 1.28 with respect to R results in the following equation

$$\frac{p_B - p_{\infty}}{\rho} = \frac{3\dot{R}^2}{2} + R\ddot{R} \quad (1.29)$$

where the following relationship has been used.

$$\frac{\partial(\dot{R}^2)}{\partial R} = \frac{1}{\dot{R}} \frac{\partial(\dot{R}^2)}{\partial t} = 2\ddot{R} \quad (1.30)$$

The liquid pressure at the bubble wall (p_B) is related to the gas pressure inside a bubble (p_g) as follows

$$p_B = p_g - 2\frac{\sigma}{R} - \frac{4\mu\dot{R}}{R} \quad (1.31)$$

where σ is the surface tension, and μ is the liquid viscosity. The pressure at the surface of the liquid volume is the sum of the acoustic pressure ($p_s(t)$) and the ambient static pressure (p_0). Then the Rayleigh-Plesset equation is derived from Eq. 1.29.

$$R\ddot{R} + 3\frac{\dot{R}^2}{2} = \frac{1}{\rho} \left(p_g - 2\frac{\sigma}{R} - \frac{4\mu\dot{R}}{R} - p_0 - p_s(t) \right) \quad (1.32)$$

In this equation, liquid has been assumed as incompressible. In the following Keller and Herring equations, the liquid compressibility has been taken into account to the first order of $\frac{\dot{R}}{c_{\infty}}$, where c_{∞} is the sound velocity in the liquid far from a bubble.

$$\left(1 - (\lambda + 1) \frac{\dot{R}}{c_{\infty}} \right) R\ddot{R} + \frac{3\dot{R}^2}{2} \left(1 - \frac{1}{3}(3\lambda + 1) \frac{\dot{R}}{c_{\infty}} \right) = \frac{1}{\rho} \left(1 + (1 - \lambda) \frac{\dot{R}}{c_{\infty}} \right) \left[p_B - p_s \left(t + \frac{R}{c_{\infty}} \right) - p_0 \right] + \frac{R}{c_{\infty}\rho} \frac{dp_B}{dt} \quad (1.33)$$

where $\lambda=0$ or 1 for Keller or Herring equation, respectively, and $p_s \left(t + \frac{R}{c_{\infty}} \right)$ is the instantaneous acoustic pressure at time $t + \frac{R}{c_{\infty}}$. As a similar equation, Gilmore equation has also been widely used.

1.4.5 Inertial Collapse (Rayleigh Collapse)

Now the bubble collapse is discussed using the Rayleigh-Plesset equation. After the bubble expansion, a bubble collapses. During the bubble collapse, important terms in the Rayleigh-Plesset equation are the two terms in the left-hand side of Eq. 1.32.

Then, the bubble wall acceleration is expressed as follows.

$$\ddot{R} = -\frac{3\dot{R}^2}{2R} \quad (1.34)$$

Thus, it is always negative. It means that the speed of the bubble collapse increases with time (The negative bubble-wall velocity further decreases). As the speed of the bubble collapse increases, the magnitude of the bubble wall acceleration increases according to Eq. 1.34. It means that the speed of the bubble collapse automatically increases more and more with time. This is caused by the inertia of the surrounding liquid ingoing into a collapsing bubble as well as the spherically shrinking geometry. Such a bubble collapse is called inertial collapse or Rayleigh collapse. It has been shown theoretically that the speed of the bubble collapse is limited by the sound speed in the liquid at the bubble wall. The sound speed is a function of pressure and density of the liquid as follows.

$$c_{L,B} = \sqrt{7,15(p_B + B)/\rho_{L,i}} \quad (1.35)$$

where $c_{L,B}$ is the sound speed in the liquid at the bubble wall, $B=3,049*10^8$ Pa, and $\rho_{L,i}$ is the liquid density at the bubble wall. The sound speed ($c_{L,B}$) increases as the bubble collapses up to about 3000 m/s (about two times of the ambient sound speed (1500 m/s) in water), which is the upper limit for the speed of the bubble collapse.

Finally, the bubble collapse stops when the pressure inside a bubble (p_g) in the right-hand side of Eq. 1.32 dramatically increases as the density inside a bubble nearly reaches that of a condensed phase (A bubble is almost completely occupied by the van der Waals hard-cores of gas and vapor molecules at that moment). At the same time, the temperature and pressure inside a bubble dramatically increase.

In Fig. 1.27a, an example of the radius-time curve for a stably pulsating bubble calculated by the modified Keller equation is shown for one acoustic cycle.

After the bubble expansion during the rarefaction phase of ultrasound, a bubble strongly collapses, which is the inertial or Rayleigh collapse. After the collapse, there is a bouncing radial motion of a bubble. In Fig.1.27b, the calculated flux of OH radicals from a bubble is shown as a function of time for one acoustic cycle.

OH radicals are created at each strong collapse, which diffuses out of a bubble into the surrounding liquid especially at the end of the strong collapse.

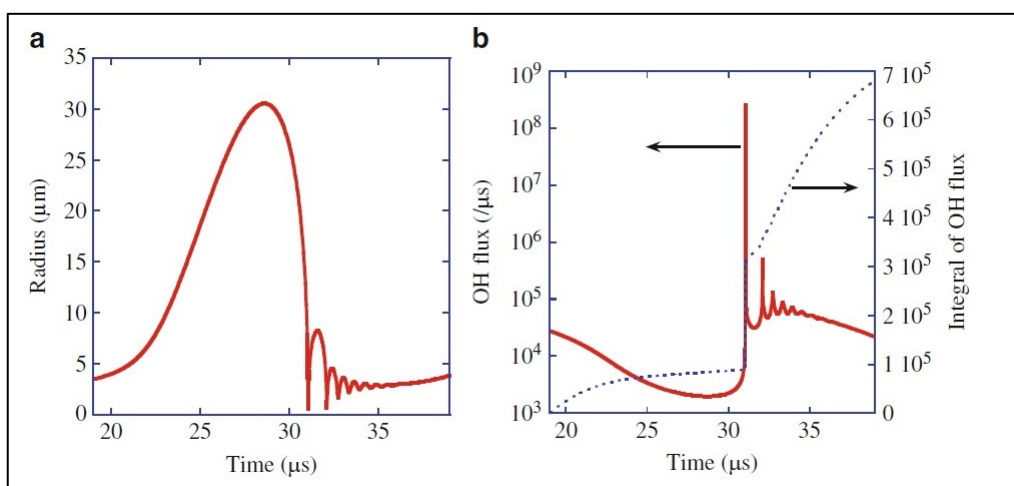


Fig. 1.27 The calculated results for one acoustic cycle when a bubble in water at 3 °C is irradiated by an ultrasonic wave of 52 kHz and 1.52 bar in frequency and pressure amplitude, respectively. The ambient bubble radius is 3.6 mm. (a) The bubble radius. (b) The dissolution rate of OH radicals into the liquid from the interior of the bubble (solid line) and its time integral (dotted line).

In Fig. 1.28, the details of the inertial or Rayleigh collapse are shown. In Fig. 1.28a, the bubble radius and the temperature inside an air bubble are shown as a function of time only for 0.1 ms at around the end of the collapse. The temperature dramatically increases at the end of the collapse to 6500 K. As a result, water vapor, oxygen and nitrogen are dissociated inside a bubble and many chemical species are created as shown in Fig. 1.28b. The production of oxidants inside a bubble such as OH, O, and H₂O₂ is one of the major origins of sonochemical reactions. In other words, the inertial or Rayleigh collapse is essential for sonochemistry.

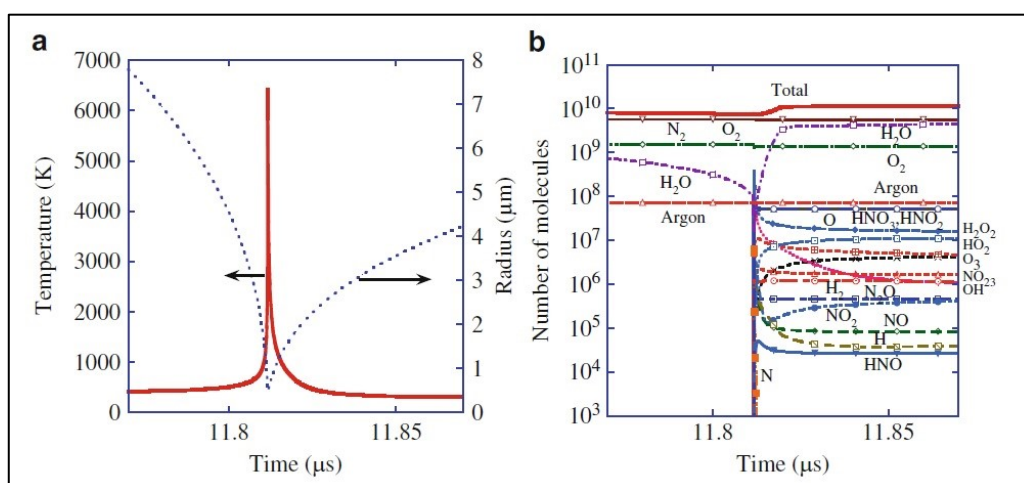


Fig. 1.28 The calculated results for an air bubble at around the end of the inertial collapse only for 0.1 ms. (a) The bubble radius and the temperature inside a bubble. (b) The number of molecules inside a bubble.

1.4.5 Three sites for chemical reaction

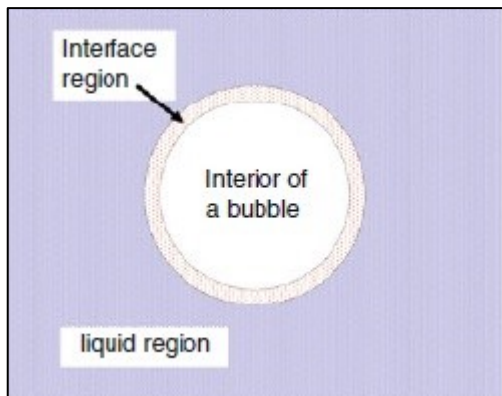


Fig. 1.29 *Three sites for chemical reactions for a cavitation bubble.*

There are three sites for chemical reactions for a cavitation bubble as shown in Fig. 1.29. One is the interior of a bubble. Another is the interface region at around the bubble surface. The other is the liquid region outside the interface region. The liquid region is at the ambient temperature where chemical species with a relatively long lifetime such as H_2O_2 diffusing out of the interface region chemically react with solutes. In the interface region, the temperature dramatically increases due to the thermal conduction from the heated interior of a bubble where radicals with a relatively short lifetime such as OH and O react with

solutes or radicals themselves. However, the actual temperature in the interface region is not known while several authors have estimated it. Some researchers have suggested that in the interface region there is supercritical water. Surfactants absorbed at the bubble surface can dissociate at the interface region due to both heat and radical attack. In the interior of a bubble, volatile solutes which evaporate into the region are dissociated by high temperature.

1.4.6 Application of Ultrasound

1.4.6.1 Nucleation of Particles by Ultrasound

Cavitation bubbles work as nucleation sites of particles. For example, in a supercooled sucrose solution, nucleation of ice crystals induced by cavitation bubbles has been experimentally observed. This phenomenon has been called sonocrystallization. Although there are some papers on the mechanism of sonocrystallization, it has not yet been fully understood. It has been reported that the distribution of crystal size in sonocrystallization is narrower than that without ultrasound. It may be related to the narrower size distribution of sonochemically synthesized particles compared to that without ultrasound. Further studies are required for the mechanism of particle nucleation by ultrasound.

1.4.6.2 Enhancement of Mass Transfer



Fig. 1.30 *Asymmetrical collapse of bubble at 25kHz [299].*

Acoustic cavitation increases a rate of mass transfer toward or from a solid surface.

When a solute gradually diffuses onto a solid surface as in the case of electrolysis, a diffusion layer is formed near the solid surface in which the concentration of a solute changes from the saturated one at the solid surface to nearly the ambient one at the edge of the layer. A similar diffusion layer is formed when the solid material gradually dissolves into the liquid. Acoustic cavitation makes a diffusion layer

thinner and the mass transfer rate is increased as it is proportional to the gradient in concentration (Fig. 1.31).

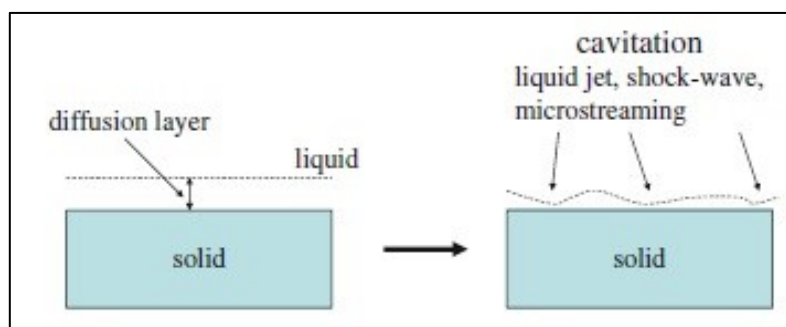


Fig. 1.31 *Thinning of a diffusion layer by acoustic cavitation*

The effect of acoustic cavitation is originated from the following three phenomena. One is liquid jets impacting on the solid surface from collapsing bubbles. Another is shock waves emitted from collapsing bubbles. The other is the microstreaming induced by pulsating bubbles near the solid surface. When a bubble collapses near a solid surface, the speed of the collapse is higher for the liquid side than that for the solid side. As a result, a liquid jet penetrates into a bubble

toward the solid surface and finally hits it. When a bubble symmetrically collapses in liquid, on the other hand, a spherical shock wave is emitted from a bubble into the surrounding liquid. Furthermore, a pulsating bubble induces a liquid flow around the bubble called microstreaming. These effects enhance a mass transfer toward or from the solid surface. An example of enhancement in mass transfer by acoustic cavitation is the increase in the limiting current density in electrolysis. The electrochemistry with ultrasound is called sonoelectrochemistry. Another example is ultrasonic cleaning. Soluble contaminants on a solid surface dissolve into the liquid faster with acoustic cavitation. Insoluble contaminants are also removed from a solid surface with ultrasound. This is also induced by acoustic cavitation in many cases, but in some other cases it is by acoustic streaming.

1.4.8 Ultrasonic horn

Ultrasounds are generally produced by exploiting the piezoelectric effect discovered by Jacques and Pierre Curie in 1880. The two brothers demonstrated that some crystals, and especially quartz, have the property to polarize if subjected to mechanical effort.

The sonicator, a device that generates ultrasounds, is therefore essentially a transducer composed of a piezoelectric material in which the inverse effect is exploited: a high-frequency wave applied to the crystal generates ultrasonic vibrations.

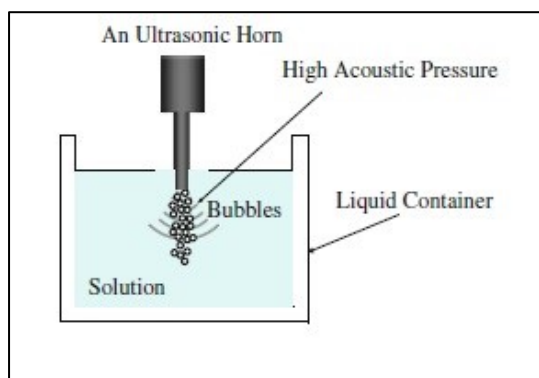


Fig. 1.32 An ultrasonic horn immersed in the liquid.

In order to generate a high intensity ultrasound, an ultrasonic horn will be used in next Chapters (Fig. 1.32).

An ultrasonic horn has a small tip from which high intensity ultrasound is radiated. The acoustic intensity is defined as the energy passing through a unit area normal to the direction of sound propagation per unit time. Its units are watts per square meter (W/m^2). It is related to the acoustic pressure amplitude (P) as follows for a plane-traveling wave.

$$I = \frac{P^2}{\rho c} \quad (1.17)$$

where I is the acoustic intensity, ρ is the liquid density, and c is the sound velocity in the liquid. Thus, as the acoustic intensity increases, the acoustic pressure amplitude increases. The acoustic intensity increases as the surface area decreases if the total acoustic energy is the same. Thus, a horn tip produces an intense ultrasound.

The ultrasound radiated from a horn tip, however, is not a plane wave. The acoustic pressure amplitude is more accurately calculated by Eq. 1.18 along the symmetry axis.

$$P(x) = \rho c v_0 \left| 2 \sin \left(\frac{\pi}{\lambda} (\sqrt{x^2 + a^2} - x) \right) \right| \quad (1.18)$$

where $P(x)$ is the acoustic pressure amplitude at distance x from the horn tip along the symmetry axis, v_0 is the velocity amplitude of the circular piston (horn tip), λ is the wavelength of ultrasound, and a is the radius of the circular piston (horn tip). In Fig. 1.15, numerical values of Eq. 1.18 are shown. With cavitation bubbles, however, the acoustic pressure amplitude is much lower than that estimated by Eq. 1.18 as shown in Fig. 1.15 due to the lower value of ρc in a bubbly liquid. Further studies are required on this topic. For a plane traveling wave, a simpler relationship holds.

$$p = \rho c u \quad (1.19)$$

where u is the velocity amplitude of a plane traveling wave

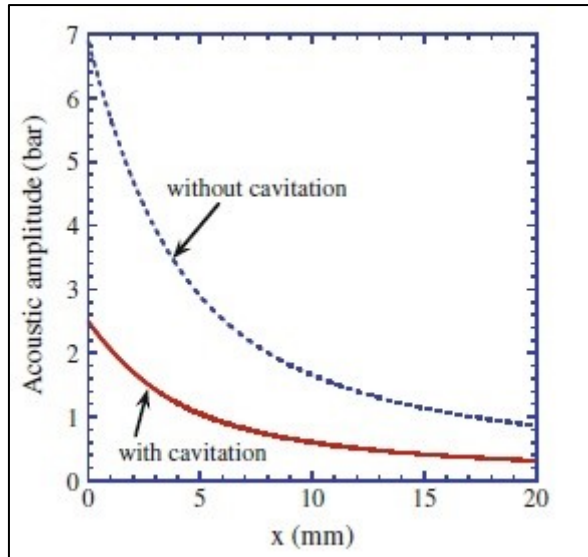


Fig. 1.33 Calculated acoustic amplitude under an ultrasonic horn as a function of the distance from the horn tip on the symmetry axis. The dotted curve is the calculated result by (1.21) when $v_0 = 0.77$ m/s, $l = 51.7$ mm (29 kHz), and $a = 5$ mm. The solid curve is the estimated one in a bubbly liquid.

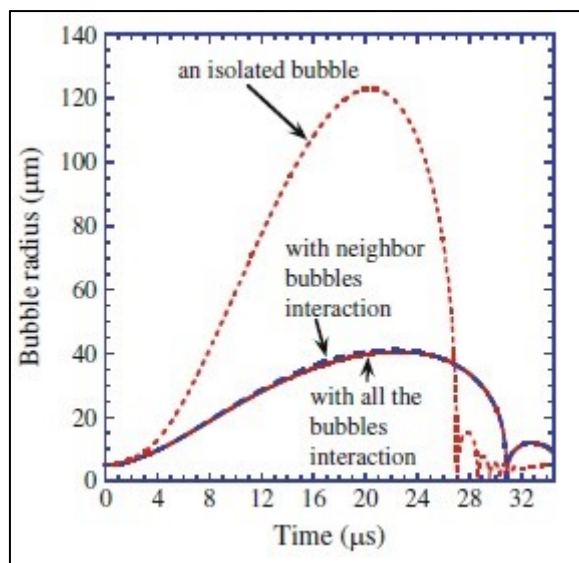


Fig. 1.34 Calculated radius of a bubble in a bubble cloud as a function of time for one acoustic cycle at 29 kHz and 2.36 bar in frequency and pressure amplitude of ultrasound, respectively. The ambient radius is 5 mm. The dotted curve is the calculated result for an isolated bubble. The dashed one is the calculated result with the interaction only with neighboring bubbles. The solid one is the calculated result taking into account all the interactions with surrounding bubbles.

Chapter 2

Experimental system

In next Chapters, different instruments will be used for the characterization both of the e-wastes and the achieved products. These instruments are here reported.

2.1 Scanning Electron Microscope (SEM)

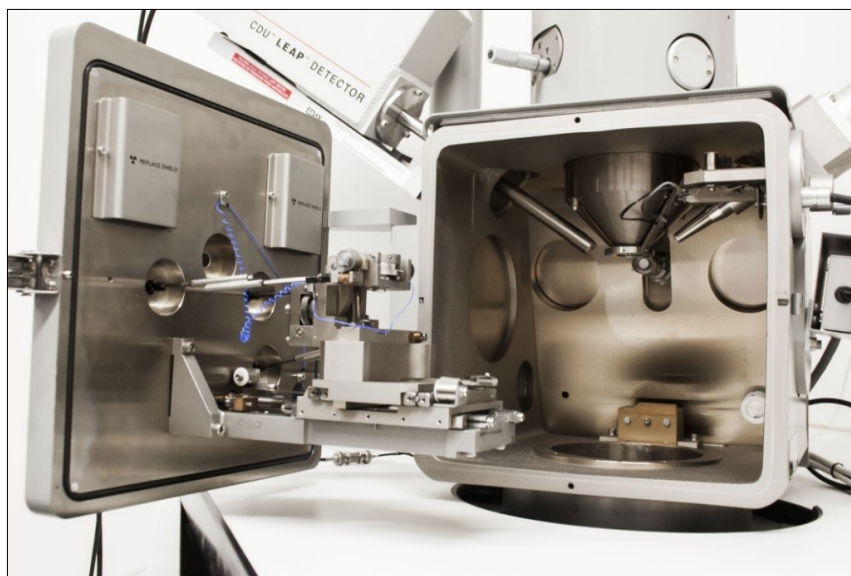


Fig. 2.1 *Cambridge Stereoscan 440 used for characterization of the samples.*

Scanning Electron Microscope allows obtaining images with high quality and great depth of field. The use paired with a microanalysis system widens the possibility of working: it is possible to obtain qualitative and quantitative information about the elements present on a given area of the sample.

Secondary electron images are usually used to study the morphology of the samples. The contrast in the images, thus obtained, depends on the relative variation in the number of detected secondary electrons, to which two effects contribute: change in number of electrons emitted from the sample and variation in the population of electrons collected by the detector. Regarding the first effect, the number of emitted secondary electrons is always proportional to the number of primary electrons incident, while, the fraction of electrons collected by the detector depends only on the angle of incidence. The combination of the two discussed effects implies that, the number of detected secondary electrons depends essentially on the angle of incidence of the local probe, therefore on the sample topography.

The contrast in the images obtained through backscattered electrons is due, equally, to the material's nature of sample and to the topography of the surface; in fact, the backscattering coefficient is a function of the atomic number of the sample. The final image quality depends on the resolving power of the instrument.

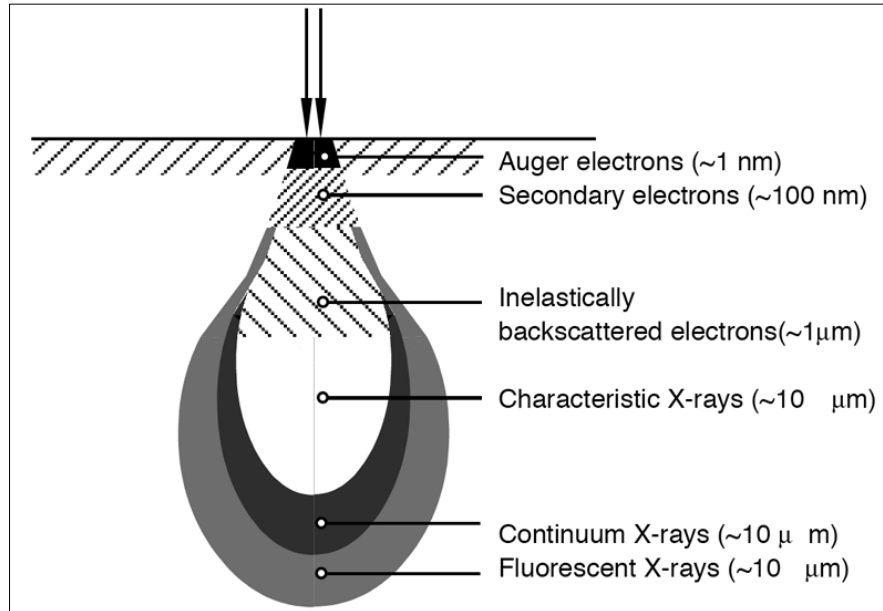


Fig. 2.2 Emission volumes of the various signals generated from a sample excited with an electronic probe

Using SEM, the achievable resolution depends on the section of the electronic probe, on the penetration and diffusion effects within the sample, on the signal/noise ratio, on the accidental presence of external interference fields, on the presence of vibration. Generally, the resolution is comparable to 10-30 nm in the secondary electron images, while it is worst (50-200 nm) in those to backscattered electrons. In this work, the characterization of the samples was performed with a Cambridge Stereoscan 440 scanning electron microscope (SEM), equipped with a Philips PV9800 EDS (Fig. 2.1) [50].

2.2 X-ray fluorescence (XRF)



Fig. 2.3 *Spectro X-Lab 2000 used for XRF analyses.*

X-ray fluorescence is a non-destructive spectroscopic analysis technique that allows to know the elemental composition of a sample.

In fact, X-ray radiation are emitted by the atoms of the sample because it is irradiated with high-energy X-ray. By studying the emission spectrum, due to Moseley's law, it is possible to correlate the different frequencies to the chemical elements.

For the study, SPECTRO X-LAB 2000 (Fig. 2.3 [51]) was used and the lithium-doped Silicon-based detector was cooled with liquid nitrogen.

2.3 ICP-OES

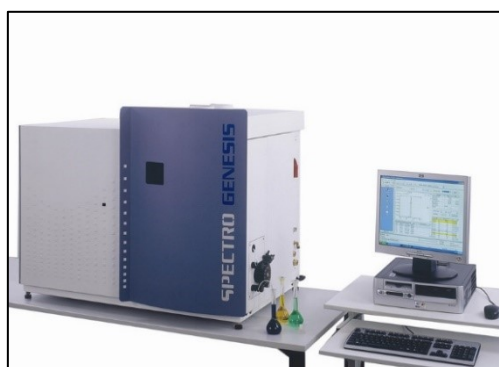


Fig. 2.4 *Spectro Genesis used for ICP analyses.*

ICP-OES (Inductively Coupled Plasma - Optical Emission Spectroscopy) is a highly sensitive spectroscopic technique for detecting concentrations of elements in liquid samples.

In particular, a Spectro GENESIS inductively coupled plasma (ICP) spectrometer (Fig. 2.4) [52] was used and data were elaborated with Smart Analyzer VISION Software.

Before the measurements, methods of analysis are created, in which the calibration functions are stored for each chemical element to be detected. By means of the methods created, the concentrations of the individual elements are then calculated from the measured intensities.

2.4 Potentiostat for electrodeposition



Fig. 2.5 Potentiostat used for electrodeposition tests.

Potentiostat is a fundamental tool for electrochemical analysis that allows to control of three electrodes. In particular, it allows maintaining the desired electric potential difference between working and reference electrode. It controls the current flowing between the working electrode and a third electrode, said counter electrode, which is precisely intended to close the circuit. By means of a retroactive process, a voltage deviation from the desired value is used to change the current in transit, thus varying the potential (V).

The potentiostat therefore provides values, among others, like current and potential: these data allow constructing the curves (V-i) for the study of redox reactions.

Among the various analytical techniques for which the device is used, one of the most interesting is the cyclic voltammetry used in Chapter 3. The potentiostat used was an AMEL 7060 (Fig. 2.5).

2.5 Potentiostat for corrosion tests

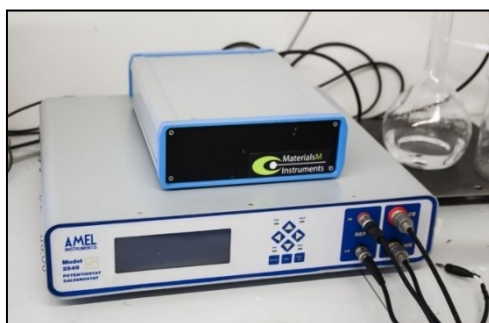


Fig. 2.6 Experimental setup used for corrosion tests on PEO coatings

The corrosion resistance of the PEO coatings in Chapter 7 was evaluated with potentiodynamic polarization tests. Anodic polarization tests were performed with an AMEL 2549 Potentiostat (Fig. 2.6), using a saturated calomel electrode as the reference electrode (SCE) and a platinum electrode as the counter electrode, with a scan rate of $8 \times 10^{-4} \text{ Vs}^{-1}$.

2.6 X-Ray Diffractometer (XRD)

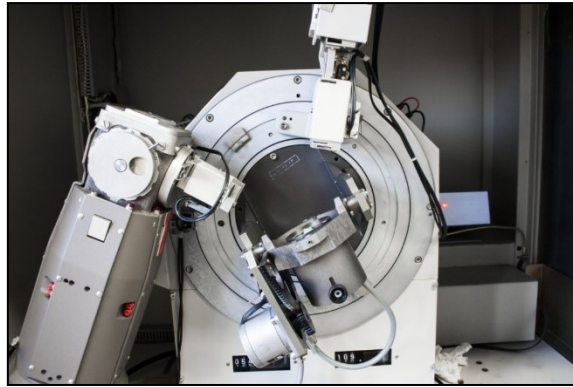


Fig. 2.7 Siemens D500 X-ray diffractometer used for XRD analyses.

XRD analyses were performed using a Siemens D500 X-ray diffractometer (Fig. 2.7 [50]) using CuK α -radiation.

2.7 Sonicator



Fig. 2.8 Sonopuls HD 3200 used for ultrasound generation.

Ultrasound assistance was used to assist both leaching process in Chapter 3 and nanoparticles synthesis in Chapter 6.

The low frequency (20 kHz) ultrasound was generated by a probe, made of titanium alloy (Ti-6Al-4V), immersed into the solution and linked to the generator of ultrasound Bandelin mod. Sonopuls HD 3200 sonicator, capable of supplying an ultrasonic power in the range of 0÷75 W/cm² (during the tests a value of 60 W/cm² was used).

2.8 Transmission Electron Microscope



Fig. 2.9 *JEOL 200CX used for TEM analyses.*

TEM was used in Chapter 7 for nanoparticles and powders characterization. In particular, TEM analyses allowed to determine size and structure of the powders.

The instrument was a JEOL 200CX (Fig. 2.9). Before TEM observation, the powder was dispersed in isopropyl alcohol and sonicated for 1 min.

2.9 Laser Diffraction



Fig. 2.10 *Zetasizer Nano ZS used for laser diffraction.*

The Malvern Zetasizer Nano ZS (MZN) (Fig. 2.10) [53] is a high-performance dimensional analyzer for particles, which can reveal the presence of aggregates and measure the size of very small particles in very diluted samples. It is typically used to measure size of particles or molecules in solution. This model can in particular measure the particle size between 10 μm and 0.3 nm.

2.10 Secondary Ion Mass Spectrometry (SIMS)

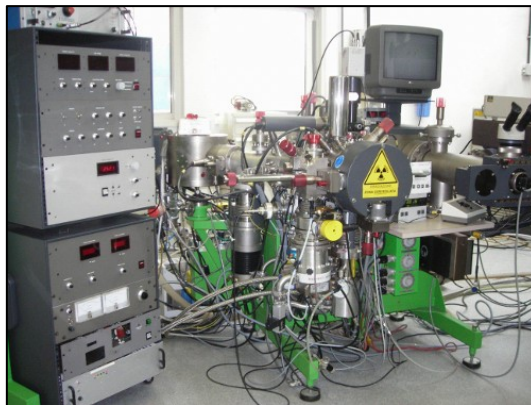


Fig. 2.11 CAMECA IMS-4f used for Secondary Ion Mass Spectrometry.

Secondary Ion Mass Spectrometry (SIMS) analyses were performed with CAMECA IMS-4f (Fig. 2.11) [54] spectrometer to study, in Chapter 4, the surface composition of the Si wafer, before and after the leaching treatments.

2.11 UV-vis absorption



Fig. 2.12 CAMECA IMS-4f used for Secondary Ion Mass Spectrometry.

UV spectroscopy, used to characterize nanoparticles synthesized in Chapter 6, was performed with a (Jasco, Easton, USA) Model V-530 Spectrophotometer (Fig. 2.12) [55].

2.12 XPS

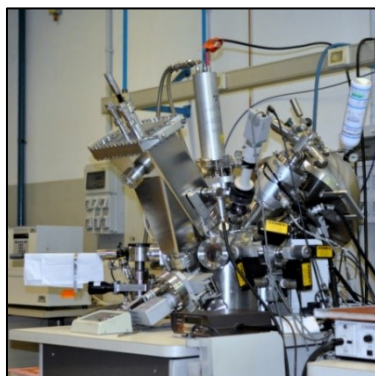


Fig. 2.13 Perkin-Elmer $\Phi 5600ci$ spectrometer used for XPS analyses.

XPS analysis were performed to characterized PEO coatings in Chapter 7 with a Perkin-Elmer $\Phi 5600$ ci spectrometer (Fig. 2.13) [56] using standard Al K_{α} radiation (1486.6 eV) working at 250 W. The working pressure was $<5 \cdot 10^{-8}$ Pa. The spectrometer was calibrated by assuming the binding energy (BE) of the Au4f_{7/2} line at 83.9 eV with respect to the Fermi level. The standard deviation for the BE values was 0.15 eV. The reported BE was corrected for the charging effects, assigning, in the outer layers where contamination carbon is still present, to the C1s line of carbon the BE value of 284.6 eV [57]. Survey scans (187.85 pass energy, 1 eV/step, 25 ms per step) were obtained in the 0-1300 eV range. The atomic composition, after a Shirley type background subtraction [58], was evaluated using sensitivity factors supplied by Perkin [59]. The assignments of the peaks were carried out by using the values reported in the reference handbook [59], in the NIST XPS Database [60, 61].

2.13 TGA



Fig. 2.14 Pyris 1 Thermobalance used for TGA analyses

The polymeric decomposition of EVA and Tedlar[®] which compose PV panel, that occurs during the heat treatments processes, was studied with Pyris 1 Thermobalance [62] coupled with Spectrum 100 FTIR spectrometer.

2.14 SVET

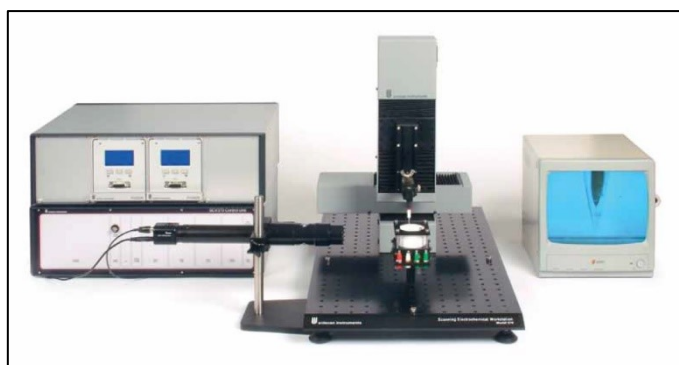


Fig. 2.15 *Uniscan SCV370 used for SVET analyses*

SVET was applied to verify if the Cu microparticles present in the PEO coating could induce the corrosion of the adjacent aluminium alloy matrix due to the formation of local galvanic couplings. For this purpose, both PEO-coated AA7075 samples (in the presence and absence of Cu microparticles) were mounted in epoxy resin and their cross-sections were exposed by means of mechanical grinding (SiC paper up to the 2000 grade). Prior to the SVET measurements, the surfaces were rinsed with ethanol, distilled water and then dried with compressed air. The commercial equipment employed was the Uniscan SCV370 equipped with a Pt probe ($\text{\O} = 50 \text{ }\mu\text{m}$). The following operational parameters were employed: probe-sample distance equal to $180 \text{ }\mu\text{m}$; vibration amplitude equal to $25 \text{ }\mu\text{m}$ (peak-to-peak); scan speed equal to $500 \text{ }\mu\text{m/s}$; step size equal to $50 \text{ }\mu\text{m}$; and a sensitivity equal to $800 \text{ }\mu\text{V}$. The scanned area varied between $3 \times 4 \text{ mm}^2$ and $3 \times 16 \text{ mm}^2$. The tests were performed in near-neutral aerated 12.00 mM NaCl solution [63] ($\text{pH} \approx 6$, conductivity, $k \approx 1300 \text{ }\mu\text{S cm}^{-1}$, volume $\approx 800 \text{ mL}$). Each measurement had a total duration of 3 h (comprising 6 consecutive scans) and was repeated twice.

Chapter 3

Gold recovery from PCBs: thiourea and thiosulphate leaching

In this chapter, gold leaching using thiosulphate and thiourea as complexing agents was studied among with the effect of different parameters such as temperature, reagents concentrations and the effect of the ultrasound during the leaching process.

As raw material PCBs (Printed Circuit Boards) of end of life mobile phones were used.

Before the leaching with thiourea or thiosulphate, the powders were pre-treated with different acids (nitric and hydrochloric with oxygen peroxide) at 60 °C with the aim to remove the major amount of copper, without attacking gold.

Then the powder were leached with thiosulphate or thiourea solution.

The experiments with thiourea were carried out in a solution at pH 1.5, by adding sulfuric acid, and with different ratio thiourea/gold: 5, 10, 15 and 20. As oxidant reagent, were used oxygen peroxide, ferric sulphate and ferric chloride. Different temperatures and processing time were tested.

The leaching tests carried with thiosulphate were performed at pH 10, by adding ammonia using different concentration (0.12 M, 0.24 M, 0.5M, 1M and 2M). Different temperatures and times of reaction, were studied. Heating was provided by a water bath thermostat and the temperature of the liquid was periodically controlled. The experiments were conducted in a 200 ml Pyrex-glass, containing 60 ml of leaching and 3 g of powder (liquid/solid ratio of 20).

The low frequency (20 kHz) ultrasound was generated by a probe described in Chapter 2.7.

In the conventional leaching, *e.g.* performed without ultrasonic irradiation, a constant stirring speed of 400 rpm was used to ensure the suspension of the particles.

At the end of each leaching test, the solid residue was separated from leach liquor by centrifugation. The solid residue was analyzed by XRF, whereas the leach liquor was analyzed by inductively coupled plasma spectroscopy (ICP). Moreover, the solid residues were treated with aqua regia and the solutions were analyzed by ICP. The yields were calculated with the data obtained by ICP.

3.1 The PCBs technology [64]

A printed circuit board, or PCB, is a self-contained module of interconnected electronic components found in devices ranging from common beepers, or pagers, and radios to sophisticated radar and computer systems. The circuits are formed by a thin layer of conducting material deposited, or "printed," on the surface of an insulating board known as the substrate. Individual electronic components are placed on the surface of the substrate and soldered to the interconnecting circuits. Contact fingers along one or more edges of the substrate act as connectors to other PCBs or to external electrical devices such as on-off switches. A printed circuit board may have circuits that perform a single function, such as a signal amplifier, or multiple functions.

There are three major types of printed circuit board construction: single-sided, double-sided, and multi-layered. Single-sided boards have the components on one side of the substrate. When the number of components becomes too much for a single-sided board, a double-sided board may be used. Electrical connections between the circuits on each side are made by drilling holes through the substrate in appropriate locations and plating the inside of the holes with a conducting material. The third type, a multi-layered board, has a substrate made up of layers of printed circuits separated by layers of insulation. The components on the surface connect through plated holes drilled down to the appropriate circuit layer. This greatly simplifies the circuit pattern.

Components on a printed circuit board are electrically connected to the circuits by two different methods: the older "through hole technology" and the newer "surface mount technology." With through hole technology, each component has thin wires, or leads, which are pushed through small holes in the substrate and soldered to connection pads in the circuits on the opposite side. Gravity and friction between the leads and the sides of the holes keeps the components in place until they are soldered. With surface mount technology, stubby J-shaped or L-shaped legs on each component contact the printed circuits directly. A solder paste consisting of glue, flux, and solder are applied at the point of contact to hold the components in place until the solder is melted, or "reflowed," in an oven to make the final connection. Although surface mount technology requires greater care in the placement of the components, it eliminates the time-consuming drilling process and the space-consuming connection pads inherent with through hole technology. Both technologies are used today.

Two other types of circuit assemblies are related to the printed circuit board. An integrated circuit, sometimes called an IC or microchip, performs similar functions to a printed circuit board except the IC contains many more circuits and components that are electrochemically "grown" in place on the surface of a very small chip of silicon. A hybrid circuit, as the name implies, looks like a printed circuit board, but contains some components that are grown onto the surface of the substrate rather than being placed on the surface and soldered.

3.1.1 History

Printed circuit boards evolved from electrical connection systems that were developed in the 1850s. Metal strips or rods were originally used to connect large electric components mounted on wooden bases. In time the metal strips were replaced by wires connected to screw terminals, and wooden bases were replaced by metal chassis. But smaller and more compact designs were needed due to the increased operating needs of the products that used circuit boards. In 1925, Charles Ducas of the United States submitted a patent application for a method of creating an electrical path directly on an insulated surface by printing through a stencil with electrically conductive inks. This method gave birth to the name "printed wiring" or "printed circuit."

In the 1943, Paul Eisler of the United Kingdom patented a method of etching the conductive pattern, or circuits, on a layer of copper foil bonded to a glass-reinforced, non-conductive base. Widespread use of Eisler's technique did not come until the 1950s when the transistor was introduced for commercial use. Up to that point, the size of vacuum tubes and other components were so large that the traditional mounting and wiring methods were all that was needed. With the advent of transistors, however, the components became very small, and manufacturers turned to printed circuit boards to reduce the overall size of the electronic package.

Through hole technology and its use in multi-layer PCBs was patented by the U.S. firm Hazeltyn in 1961. The resulting increase in component density and closely spaced electrical paths started a new era in PCB design. Integrated circuit chips were introduced in the 1970s, and these components were quickly incorporated into printed circuit board design and manufacturing techniques.

3.1.2 Design

There is no such thing as a standard printed circuit board. Each board has a unique function for a particular product and must be designed to perform that function in the space allotted. Board designers use computer-aided design systems with special software to layout the circuit pattern on the board. The spaces between electrical conducting paths are often 0.04 inches (1.0 mm) or smaller. The location of the holes for component leads or contact points are also laid out, and this information is translated into instructions for a computer numerical controlled drilling machine or for the automatic solder paster used in the manufacturing process.

Once the circuit pattern is laid out, a negative image, or mask, is printed out at exact size on a clear plastic sheet. With a negative image, the areas that are not part of the circuit pattern are shown in black and the circuit pattern is shown as clear.

3.1.3 Raw Materials

The substrate most commonly used in printed circuit boards is a glass fiber reinforced (fiberglass) epoxy resin with a copper foil bonded on to one or both sides. PCBs made from paper reinforced phenolic resin with a bonded copper foil are less expensive and are often used in household electrical devices.

The printed circuits are made of copper, which is either plated or etched away on the surface of the substrate to leave the pattern desired. The copper circuits are coated with a layer of tin-lead to prevent oxidation. Contact fingers are plated with tin-lead, then nickel, and finally gold for excellent conductivity.

Purchased components include resistors, capacitors, transistors, diodes, integrated circuit chips, and others.

3.1.4 The Manufacturing Process

Printed circuit board processing and assembly are done in an extremely clean environment where the air and components can be kept free of contamination. Most electronic manufacturers have their own proprietary processes, but the following steps might typically be used to make a two-sided printed circuit board.

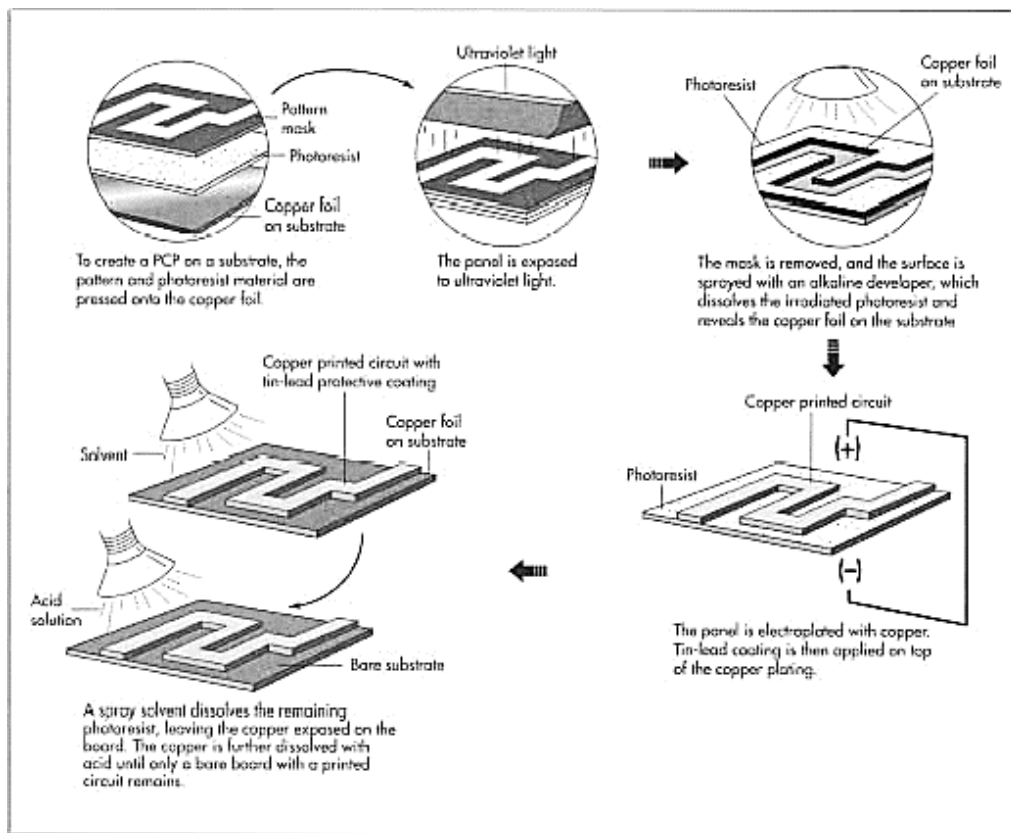


Fig. 3.1. Making the substrate of a PCB.

3.1.4.1 Making the substrate

- Woven glass fiber is unwound from a roll and fed through a process station where it is impregnated with epoxy resin either by dipping or spraying. The impregnated glass fiber then passes through rollers which roll the material to the desired thickness for the finished substrate and also remove any excess resin.
- The substrate material passes through an oven where it is semicured. After the oven, the material is cut into large panels.
- The panels are stacked in layers, alternating with layers of adhesive-backed copper foil. The stacks are placed in a press where they are subjected to temperatures of about 170°C and pressures of 100 bars for an hour or more. This fully cures the resin and tightly bonds the copper foil to the surface of the substrate material.

3.1.4.2 Drilling and plating the holes

- Several panels of substrate, each large enough to make several printed circuit boards, are stacked on top of each other and pinned together to keep them from moving. The stacked panels are placed in a CNC machine, and the holes are drilled according to the pattern determined when the boards were laid out. The holes are deburred to remove any excess material clinging to the edges of the holes.
- The inside surfaces of the holes designed to provide a conductive circuit from one side of the board to the other are plated with copper. Non-conducting holes are plugged to keep them from being plated or are drilled after the individual boards are cut from the larger panel.

3.1.4.6 Creating the printed circuit pattern on the substrate

The printed circuit pattern may be created by an "additive" process or a "subtractive" process. In the additive process, copper is plated, or added, onto the surface of the substrate in the desired pattern, leaving the rest of the surface unplated. In the subtractive process, the entire surface of the substrate is first plated, and then the areas that are not part of the desired pattern are etched away, or subtracted. The additive process is here described.

- The foil surface of the substrate is degreased. The panels pass through a vacuum chamber where a layer of positive photoresist material is pressed firmly onto the entire surface of the foil. A positive photoresist material is a polymer that has the property of becoming more soluble when exposed to ultraviolet light. The vacuum ensures that no air bubbles are trapped between the foil and the photoresist. The printed circuit pattern mask is laid on top of the photoresist and the panels are exposed to an intense ultraviolet light. Because the

mask is clear in the areas of the printed circuit pattern, the photoresist in those areas is irradiated and becomes very soluble.

- The mask is removed, and the surface of the panels is sprayed with an alkaline developer that dissolves the irradiated photoresist in the areas of the printed circuit pattern, leaving the copper foil exposed on the surface of the substrate.
- The panels are then electroplated with copper. The foil on the surface of the substrate acts as the cathode in this process, and the copper is plated in the exposed foil areas to a thickness of about 0.025-0.050 mm. The areas still covered with photoresist cannot act as a cathode and are not plated. Tin-lead or another protective coating is plated on top of the copper plating to prevent the copper from oxidizing and as a resist for the next manufacturing step.
- The photoresist is stripped from the boards with a solvent to expose the substrate's copper foil between the plated printed circuit pattern. The boards are sprayed with an acid solution which eats away the copper foil. The copper plating on the printed circuit pattern is protected by the tin-lead coating and is unaffected by the acid.

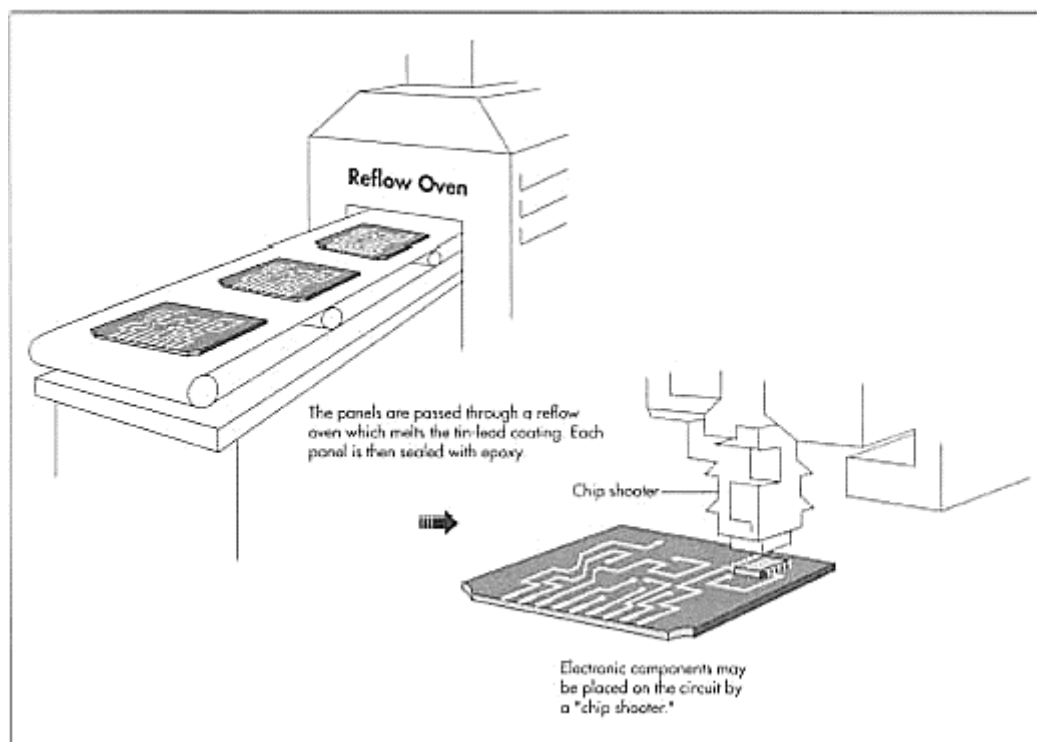


Fig. 3.2. Addition of electrical components to the PCB, during PCB production.

3.1.4.7 Attaching the contact fingers

- The contact fingers are attached to the edge of the substrate to connect with the printed circuit. The contact fingers are masked off from the rest of the board and then plated. Plating is done with three metals: first tin-lead, next nickel, then gold.

3.1.4.8 Fusing the tin-lead coating

- The tin-lead coating on the surface of the copper printed circuit pattern is very porous and is easily oxidized. To protect it, the panels are passed through a "reflow" oven or hot oil bath which causes the tin-lead to melt, or reflow, into a shiny surface.

3.1.4.9 Sealing, stenciling, and cutting the panels

- Each panel is sealed with epoxy to protect the circuits from being damaged while components are being attached. Instructions and other markings are stenciled onto the boards.
- The panels are then cut into individual boards and the edges are smoothed.

3.1.4.10 Mounting the components

- Individual boards pass through several machines which place the electronic components in their proper location in the circuit. If surface mount technology is going to be used to mount the components, the boards first pass through an automatic solder paster, which places a dab of solder paste at each component contact point. Very small components may be placed by a "chip shooter" which rapidly places, or shoots, the components onto the board. Larger components may be robotically placed. Some components may be too large or odd-sized for robotic placement and must be manually placed and soldered later.
- The components are then soldered to the circuits. With surface mount technology, the soldering is done by passing the boards through another reflow process, which causes the solder paste to melt and make the connection.
- The flux residue from the solder is cleaned with water or solvents depending on the type of solder used.

3.1.4.11 Packaging

- Unless the printed circuit boards are going to be used immediately, they are individually packaged in protective plastic bags for storage or shipping.

3.1.4.12 Quality Control

Visual and electrical inspections are made throughout the manufacturing process to detect flaws. Some of these flaws are generated by the automated machines. For example, components are sometimes misplaced on the board or shifted before final soldering. Other flaws are caused by the application of too much solder paste, which can cause excess solder to flow, or bridge, across two adjacent printed circuit paths. Heating the solder too quickly in the final reflow process can cause a "tombstone" effect where one end of a component lifts up off the board and doesn't make contact. Completed boards are also tested for functional performance to ensure their output is within the desired limits. Some boards are subjected to environmental tests to determine their performance under extremes of heat, humidity, vibration, and impact.

3.1.5 Toxic Materials and Safety Considerations

The solder materials used for electrical connections on a PCB contains lead, which is considered a toxic material. The fumes from the solder are considered a health hazard, and the soldering operations must be carried out in a closed environment. Before discharging to the atmosphere, fumes must to be treated with an appropriate extraction and cleaning processes. Many electronic products containing PCBs became obsolete within 12-18 months. The potential for these obsolete products entering the wastestream and ending up in landfills has many environmentalists concerned. Recycling efforts for electronic products include refurbishing older products and reselling them to customers that don't need, or have access to, newer, state-of-the-art electronics. Other electronics are disassembled and the computer parts are salvaged for resale and reuse in other products.

In many countries in Europe, the legislation requires to the producers to buy back their used products and render them environmentally safe before disposal. For electronics manufacturers, this means they must remove and reclaim the toxic solder from their PCBs. This is an expensive process and has spurred research into the development of non-toxic means of making electrical connections. One promising approach involves the use of water-soluble, electrically conductive molded plastics to replace the wires and solder.

3.2 Characterization

First of all several mobile phones were dismantled and the PCBs were recovered (Fig. 3.3). The boards were analyzed by SEM to verify the presence and distributions of the different metals.

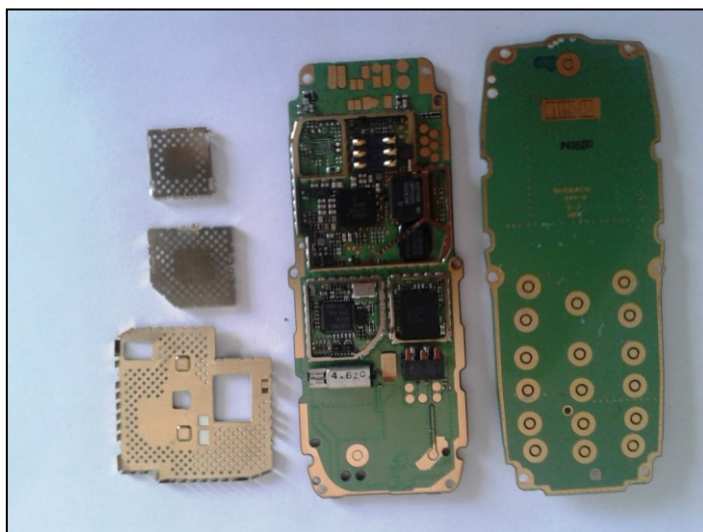


Fig. 3.3. *The PCB used for the tests recovered from end-of-life cell phones.*

First, to verify the presence of gold, SEM analysis was performed on the powder coming from the golden part of the PCB (Fig. 3.4).

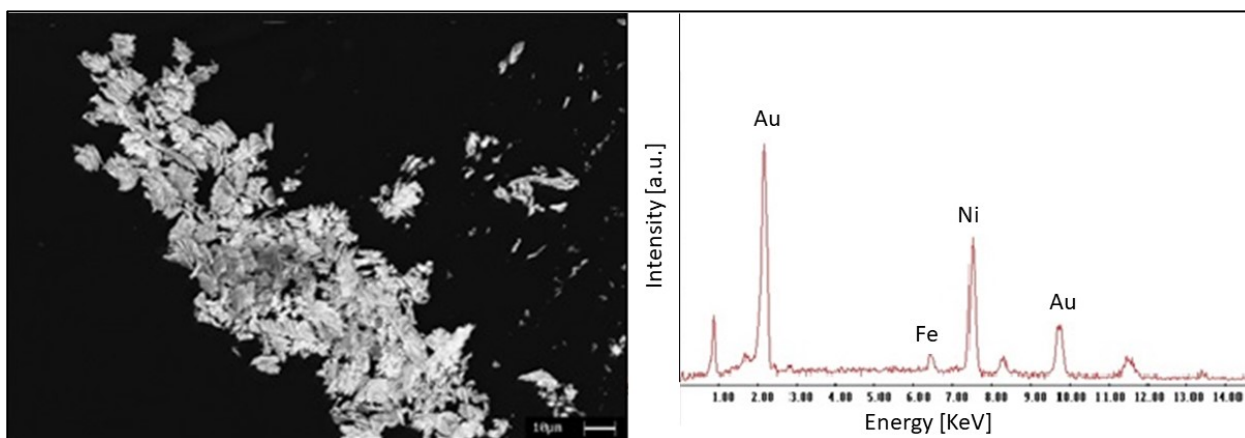


Fig. 3.4. *SEM-BSE (Backscattered Electron) image of the powder scraped from the golden parts of PCBs and EDS spectra of the powder.*

This powder in fact results made of gold and nickel. A contact between the electronic card and the SIM card was also observed at SEM (Fig. 3.5).

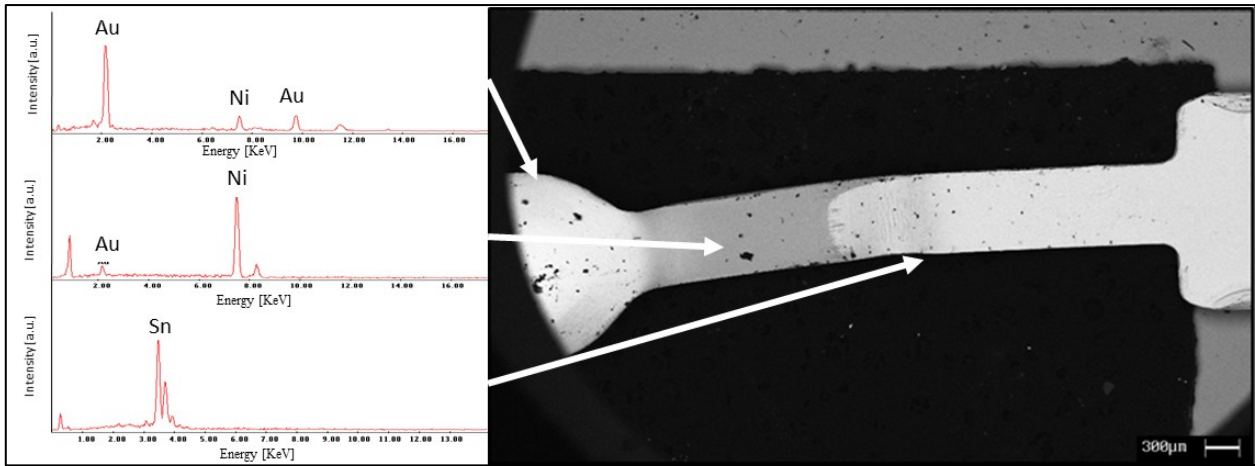


Fig. 3.5. SEM-BSE (Backscattered Electron) image of the SIM contact EDS spectra.

SEM analysis in this case revealed that there are several metals constituting in the contact. In particular, the hemispherical head in contact with the SIM card was coated with gold, whereas nickel prevailed in the central part, and there was tin in the part in contact with the phone card. Moreover, it was possible to evaluate by SEM the morphology of the different surfaces, in particular: gold, nickel and tin in contact, and Cu-Ni-Zn alloy in the grid (Fig. 3.6).

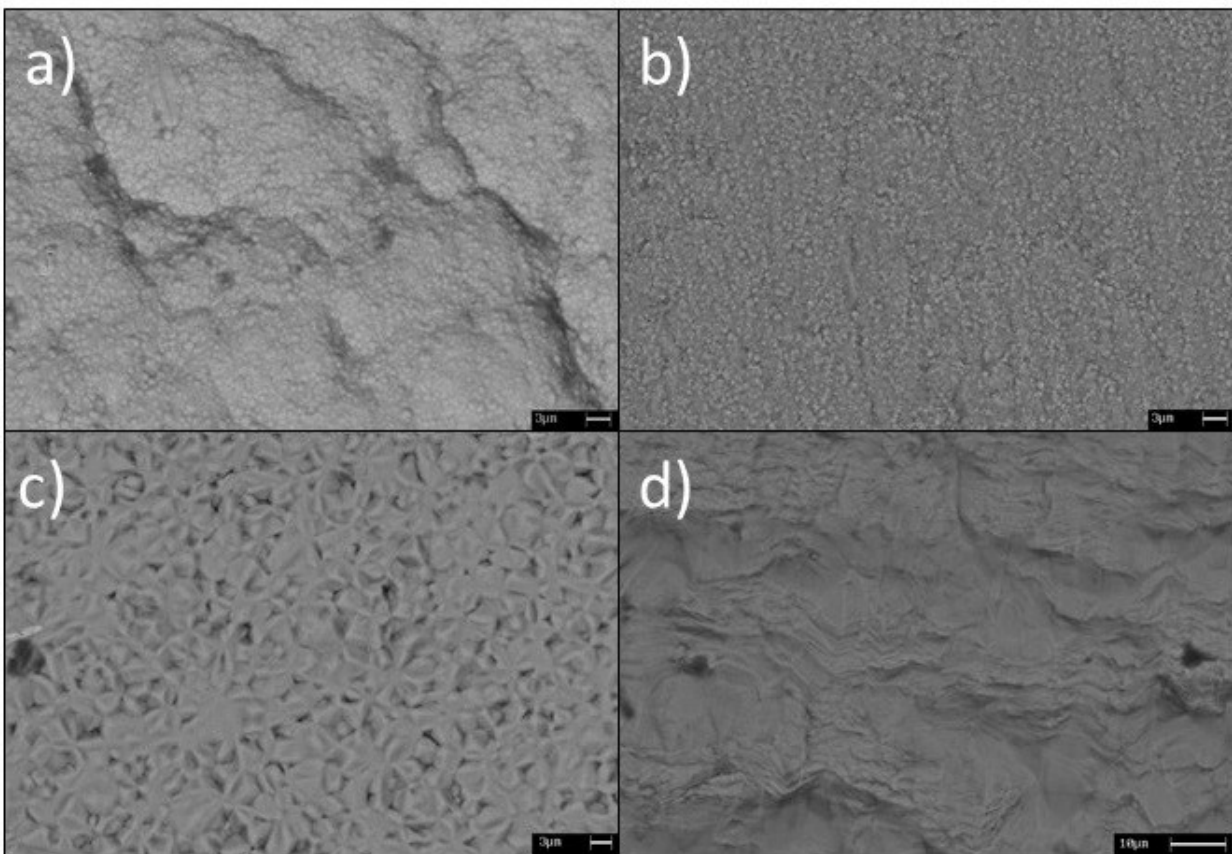


Fig. 3.6. SEM-BSE (Backscattered Electron) images of different surfaces of the PCBs: a) gold coating b) nickel coating c) tin coating d) Cu-Ni-Zn grid.

It was observed that gold and nickel had similar structures (Figure 3.6a and 3.6b), with good surface finishing and 'dotted' appearance. This morphology was supposed to result from electroless deposition. The hypothesis is confirmed by the presence of phosphorus in the nickel, which is an element typically used for this process. Therefore, it is supposed that gold coating has performed by Electroless Nickel Immersion Gold (ENIG) technique.

Instead, tin surface (Figure 3.6c) appears constituted of small crystals. However, in this case, a solidification structure is assumed, because tin is used to solder electronic components on the board.

Successively, the cross section of PCB was observed at the SEM and several copper sheets were observed inside it (Fig. 3.7a). Moreover, in the golden parts (Fig 3.7b) there was a nickel layer on copper and finally the gold coating, which was about 0.4 micron thick. The electrical contacts were found to be in copper coated with gold, whereas the grid was completely constituted of the Nickel-Copper-Nickel alloy previously analyzed.

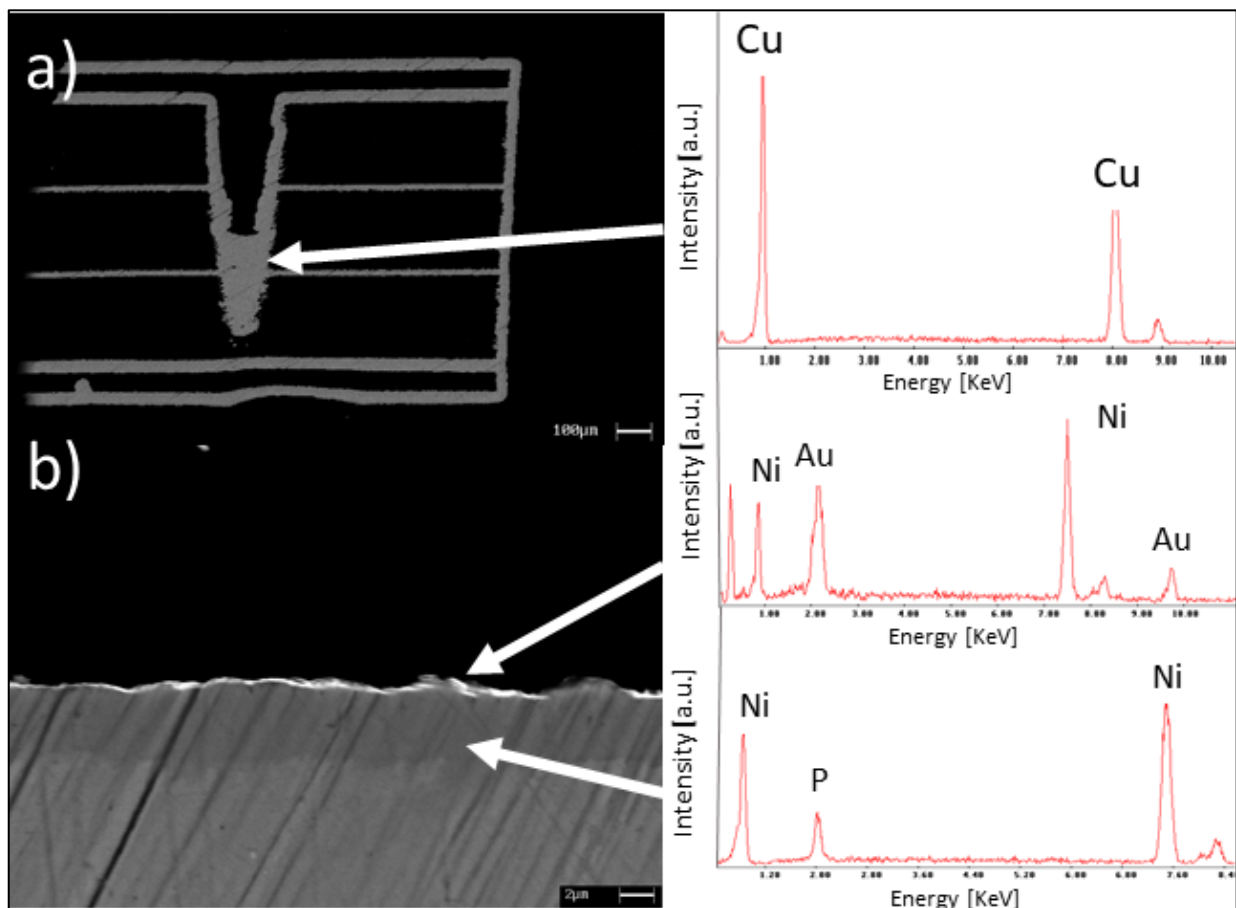


Fig. 3.7. a) SEM-BSE image of an electronic board section with EDS spectrum of the copper sheets inside the board; b) SEM-BSE image and EDS spectra of the cross section of the gold coating of the PCB.

After SEM characterization of PCBs, the crushing of the boards was carried out by F.A.R. company in Reana del Roiale (UD), through a 4x6 inch jaw crusher.

The mobile phones scraps were crushed and powders with two different size distributions were obtained: a fine one with the particles size lower than 2 mm and a coarse one between 2 mm and 4 mm. To achieve such thin dimensions, the machine was set in close-eye-setting mode (where the jaws from the machine are in contact with each other). During grinding, it was observed that the central part of the electronic board, due to the high copper content, had ductile behavior, unlike the tinned components (resistances, capacitors,) that broke fragile, producing in fine dust.

Since the amount of gold in these components was little or absent, this could be the reason why the fine dust contained less gold than coarse powders, made mostly of the board parts.

The powders coming from the crushing process were analyzed by XRF and the results are summarized in Tab. 3.1. The amount of gold was ranging between 0.03 to 0.3 Wt%, whereas the amount of silver was about 0.3 Wt%.

Element	Cu	Si	Al	Ni	Sn	Fe	Mg	Ti	Mn	Pb
Wt%	51.25	18.07	13.59	3.8	2.5	1.6	1.39	0.87	0.39	0.34

Tab. 3.1. XRF compositions of grounded PCBs.

3.3 Pre-treatment with acid



Different pre-treatments were carried out in order to optimize the parameters for copper removal, leaving gold in the powders.

The pre-treatment with hydrochloric acid and hydrogen peroxide result efficient in removal higher amount of copper, but also it dissolves gold. The treatment with nitric acid instead was very efficient in copper removal, without leaching gold.

The powder size influenced the efficiency of copper removal. In fact, copper is present also in the inner part of the scraps and in coarse powder was not possible to remove it completely.

Fig. 3.8. Nitric acid solution used for etching of PCBs coarse powder.

The results of some experiments are reported in Tab. 3.2. Almost all the silver was removed during the acid pre-treatment.

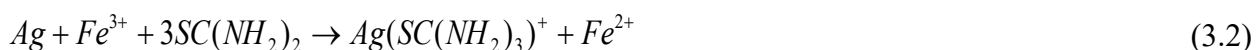
Copper, silver and tin were subsequently recovered from the nitric acid solution by different processes, described in Chapter 6.

Powder 3 g	%Cu ; %Au	Solution				ICP Analysis (ppb Au)	% Cu ; %Au
		H ₂ O (ml)	HNO ₃ (ml)	HCl (ml)	H ₂ O ₂ (ml)		
fine	40.2 ; 0.2	60	6	-	-	0	5.9 ; 0.9
coarse	35.6 ; 0.2	60	6	-	-	0	28.2 ; 0.8
fine	38.8 - 0.3	60	-	6	3	63	7.2 ; 0.5
coarse	43.4 - 0.3	60	-	6	3	210	13.7 ; 0.4

Tab. 3.2. Results of the pre-treatment with acids.

3.4 Leaching with thiourea

The leaching test using thiourea as complexing agent, were carried out with and without ultrasound. The reaction for dissolution of gold and silver needs an oxidant agent as reported in Eq. 3.1 and 3.2.



For these preliminary experiments, the amount of thiourea was 10 times the stoichiometric, because thiourea reacts also with copper.

$$M_{SC(NH_2)_2} = \frac{M_{Au}}{196.9} \times 2 \times 76.12 \quad (3.3)$$

$$M_{SC(NH_2)_2} = \frac{M_{Ag}}{107.87} \times 3 \times 76.12 \quad (3.4)$$

Tests made on different oxidant reagents, all performed without the use of ultrasound, evidenced that use of H₂O₂ resulted ineffective, and that, between Fe chloride and Fe sulphate, Fe sulphate was the most efficient oxidant reagent, as reported in Fig. 3.9. In fact, ferric sulphate allowed to obtain highest yield in gold recovery and the lowest one in copper.

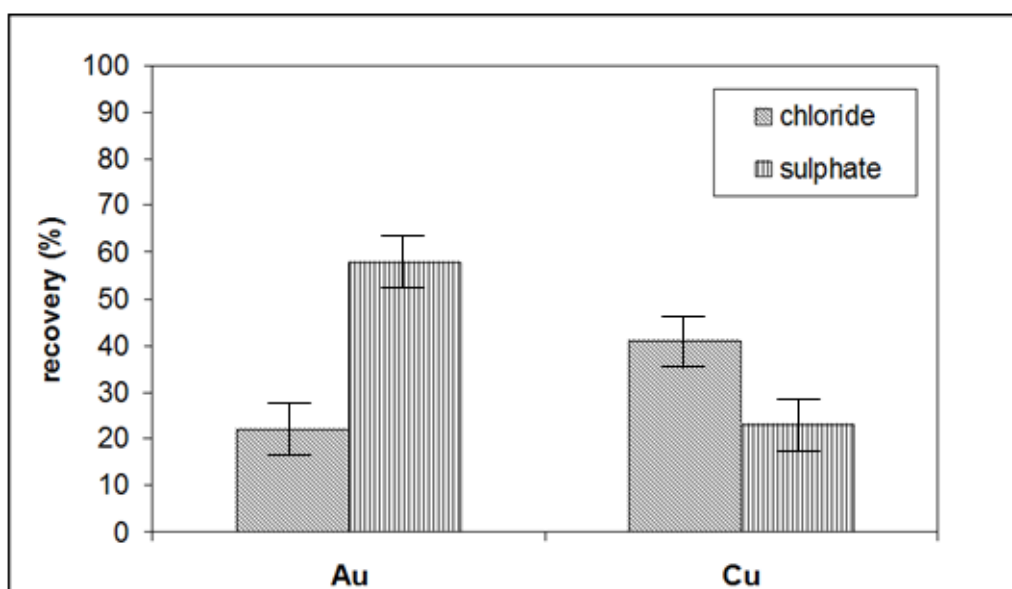


Fig. 3.9. Comparison between ferric sulphate and ferric chloride.

The ratio thiourea/precious metals have been varied from 5 to 20, for a process time of 30 min and 60 min, with conventional leaching. The amount of ferric sulphate, was calculated in proportion to the amount of thiourea. The results are summarized in Fig. 3.10, where it observed that a ratio of 10 allowed the highest gold recovery, and that an increase of this value reduced it.

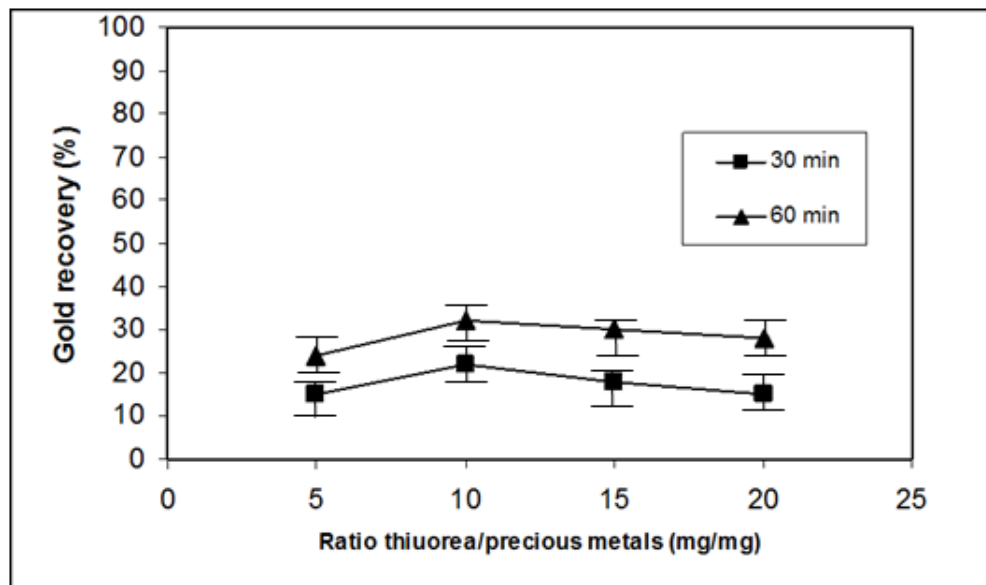


Fig. 3.10. Gold recovery in function of different amount of thiourea using fine powder.

Further investigation was carried out to optimize the reaction time and to evaluate the effects of ultrasound on the gold recovery. These tests were performed using the fine powder fraction.

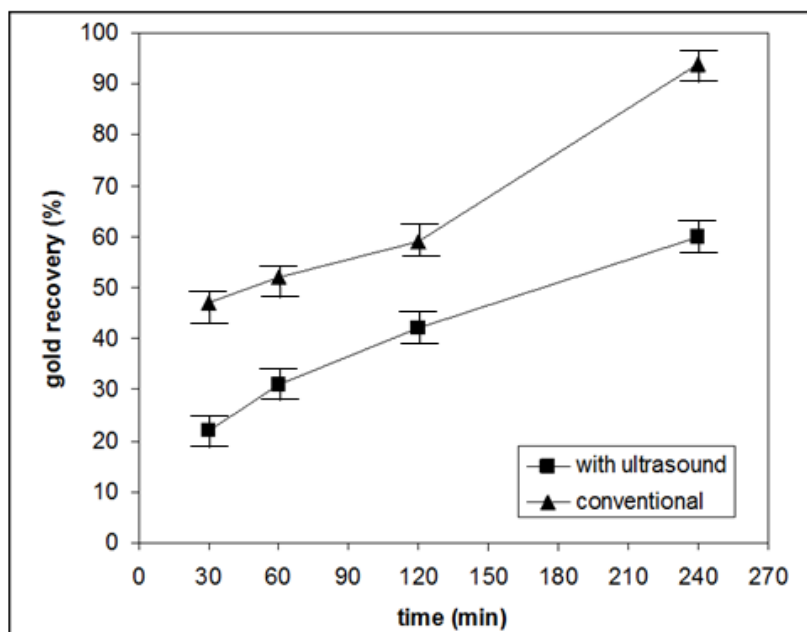


Fig. 3.11. Gold recovery for different reaction times with conventional and assisted ultrasound leaching of the finer powder.

As shown in Fig. 3.11, for the conventional leaching, an increase in the reaction time allowed a higher recovery of gold from the powders and after a process time of 240 min it was possible to obtain a recovery of about 70 %. The use of ultrasound allowed to achieve higher yield than conventional leaching, for all the reaction time investigated. An increase in the yield between 30 and 100% was observed and after 240 min of leaching a gold recovery of 94 % was recorded.

Although it is demonstrated that ultrasound increased the extraction yields of several metals from their ore, the exact mechanism is not well clear. Swamy and Narayana developed a model to illustrate the mechanism that can be adopted in this study to clarify the different results obtained by conventional and ultrasound-assisted leaching [68].

During ultrasound-assisted leaching, the explosion of the cavitation bubble generated high effective temperature and pressure. The increase in temperature improved solubility of the analytes in the leachant, and the high pressure promoted the penetration of leachant. The collapse of cavitation bubble in proximity of the surface of the particles, produced high speed micro-jets, causing surface erosion. Moreover, the particles-liquid interface was partially destroyed by acoustic streaming, promoting the dissolution of the metals.

The powder size distribution affected the gold and copper recovery, as shown in Fig. 3.12.

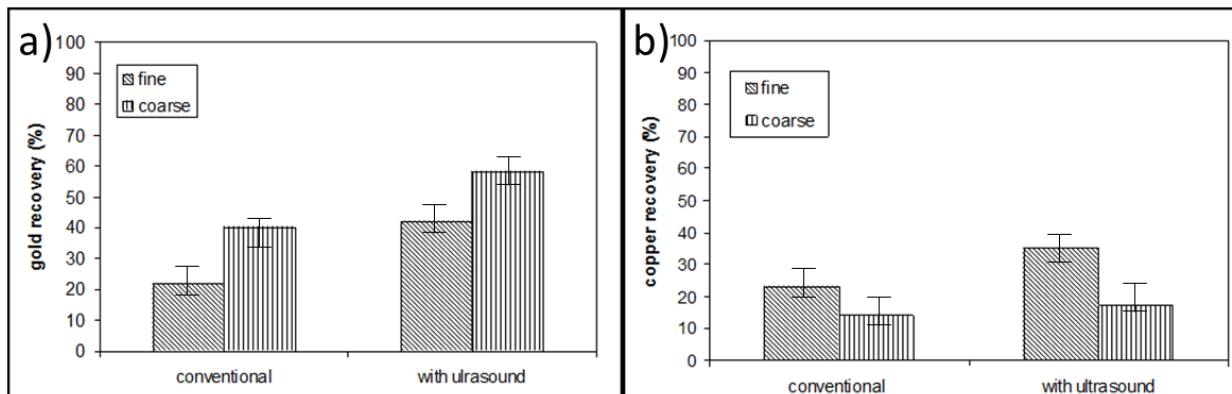


Fig. 3.12. Gold (a) and copper (b) recovery for the fine and coarse powder, with conventional and ultrasound assisted leaching.

The leaching test carried out with the coarse powder allowed to higher gold recovery and this is probably due to lower amount of copper available: the copper was also in the inner side of particles, and therefore it was not possible to remove it. Therefore, a lower amount of copper participated to the reaction with thiourea.

3.5 Recovery of copper, gold and silver from thiourea leaching process

The ICP and XRF analysis showed that about 90% and 80% of copper and silver, respectively, were recovered during acid pre-treatment. Copper was recovered by cementation process with iron whereas silver was precipitated as AgCl, adding acid chloride to the solution (Chapter 6). Also copper recovery by electrodeposition was investigated. In this case, for the determination of the potential of Cu reduction, a series of voltammetry cycles were performed using the solution coming from the acid nitric pre-treatment (Fig. 3.13).

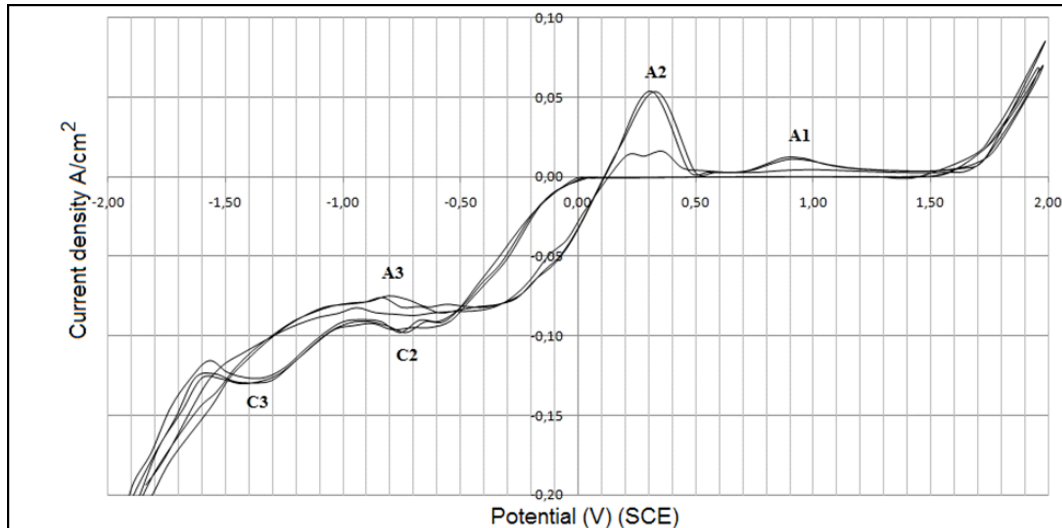


Fig. 3.13. Voltammetry cycles of the solution coming from the nitric acid pretreatment.

For the recovery of gold from the solution coming from thiourea leaching, two different methods were adopted: electrodeposition and cementation with zinc powder. For the determination of the Au reduction potential a series of voltammetry cycles were carried out (Fig. 3.14).

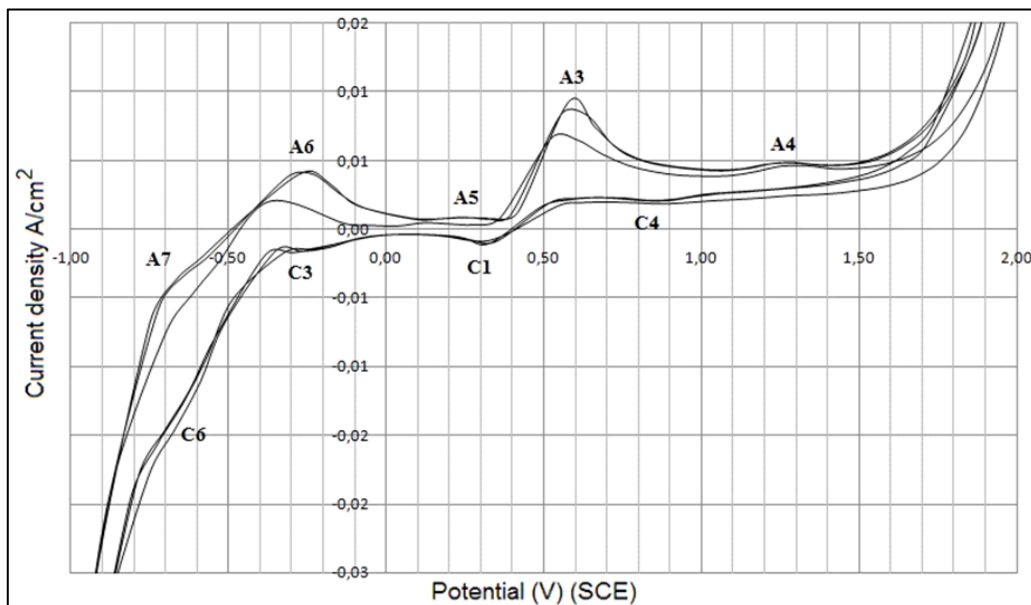


Fig. 3.14. Voltammetry cycles of the solution coming from the thiourea leaching.

3.6 Leaching with thiosulphate

The dissolution of gold in an ammoniacal thiosulfate solution is an electrochemical reaction catalysed by cupric ions [65], as shown in the following reaction:



Initially, the effect of ultrasound on the recovery of gold using low concentration (0.12-0.24 M) of thiosulfate, 0.01 M of NH_3 and 0.03 M of $CuSO_4$ was investigated.

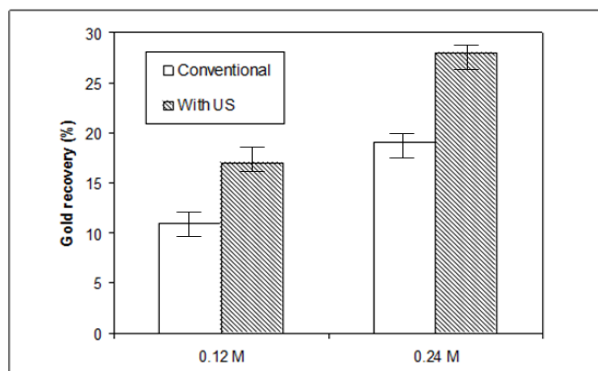


Fig. 3.15. Gold recovery of the coarse powder with conventional and ultrasound leaching at 60°C for 1 h.

The use of ultrasound allowed to obtain higher recovery of gold than conventional leaching. The yield increasing was about 40% at 0.12 M and about 50% at 0.24 M. Negligible differences in gold recovery yields was observed between fine and coarse powder fractions. At low concentration of NH_3 (0.01 M), the temperature influenced the recovery of gold. As a matter of fact, for the tests carried out at 60°C, it was necessary to continuously monitor the pH of the solution and correct it by adding NH_3 .

In Fig. 3.16 it is shown the effect of the temperature for the tests of conventional leaching carried out with 0.12-0.24 M of thiosulfate, 0.01 M of NH_3 and 0.03 M of $CuSO_4$. Increasing the temperature allowed to obtain higher extraction of gold.

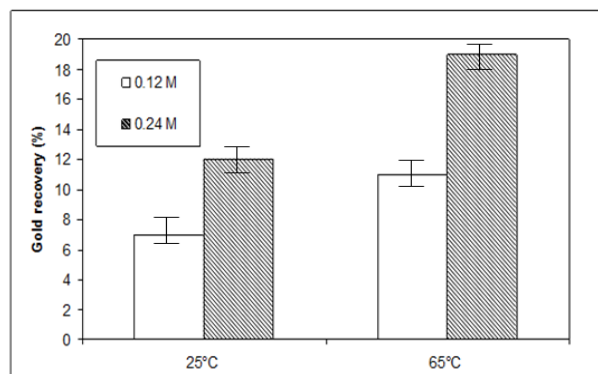


Fig. 3.16. Gold recovery of the coarse powder with conventional leaching.

In Fig. 3.17 it is shown the effect of the thiosulfate concentration on gold extraction from the powders, with conventional and ultrasound assisted leaching, using 2 M of NH_3 and 0.1 of CuSO_4 at 25°C for a reagent time of 1 h. As expected, the recovery of gold increase with the concentration of thiosulfate [36].

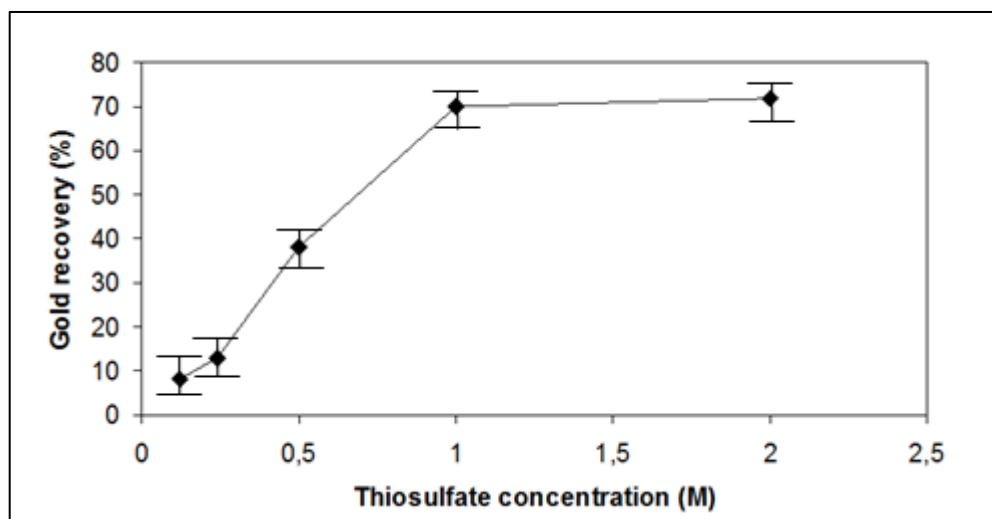


Fig. 3.17. Gold recovery of the coarse powder with conventional leaching at 25°C .

In Fig. 3.18 it is shown the effect of the ultrasound for the experiments carried out at 65°C using different concentration of thiosulfate. The use of ultrasound allowed to get higher recovery of gold at all the investigated conditions, even if its effect is less marked at higher concentrations of thiosulfate.

The gold was recovered by the different solutions of thiosulfate by cementation with zinc powder [43].

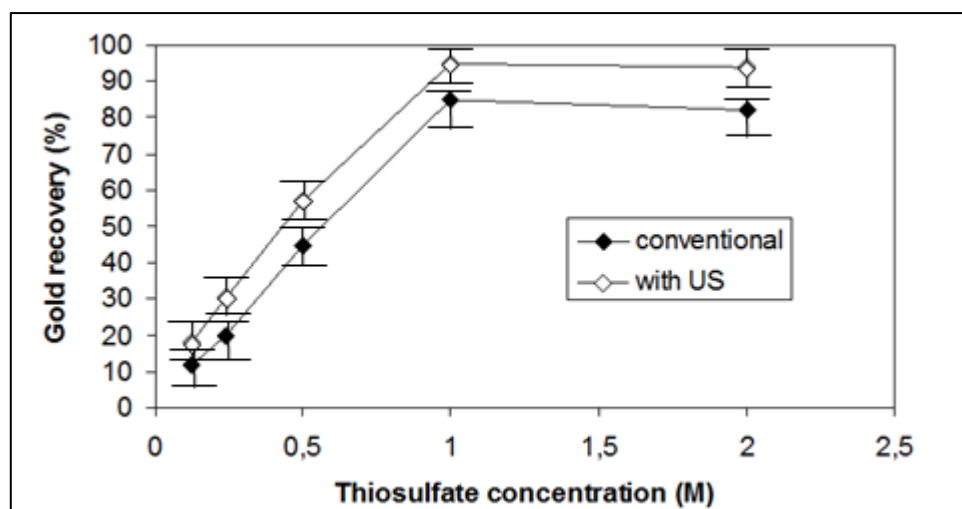


Fig. 3.18. Gold recovery of the coarse powder with conventional leaching and ultrasound assisted leaching at 65°C .

3.7 Concluding remarks

In this Chapter the effect of ultrasound on the mobile phones electronic scraps leaching for the recovery of precious metals, was studied.

As complexing agent, thiosulphate and thiourea were used. The electronic scraps were crushed and the obtained powders contained, besides 50 wt.% of copper, an amount of gold between 0.03 and 0.3 wt.% and 0.3 % of silver. The powders were submitted to a pre-treatment with nitric acid, which resulted the most efficient in copper removal. Concentration of reagents as well as temperature (60°C) and treatment time increase recovery yield. The leaching experiments carried out with thiourea showed that the use of ultrasound allowed a gold recovery 30% higher than conventional leaching. Similar results were obtained using thiosulphate as complexing agent.

Gold was recovered from the leaching solution by electrodeposition and cementation.

Copper, silver and tin leached during the pre-treatment with nitric acid, were recovered using three different processes, that will be described in detail in Chapter 6.

Chapter 4

Recycling of PV panels

In this chapter the results coming from the recycling of end of life PV panels are reported.

Initially, it is presented a theoretical review of all the various components of the photovoltaic system, their functionality and their operation. The production processes of silicon photovoltaic panels are also reported. Subsequently, the components of a photovoltaic module were characterized.

The research in PV-panels recycling begun studying the silver recover, but soon evolved in developing a process to treat the complete panels in order to recover also the others materials like silicon and glass.

The experimental part starts describing the tests performed on different methods of delamination of PV module, i.e. mechanical, chemical and thermal methods, evaluating its effect on the various components.

Once the cell was released from the encapsulating material, it was then possible to test various methods for separating silver and aluminum from the silicon wafer. Pyrometallurgical and hydrometallurgical techniques were tested.

In the hydrometallurgy part, different leaching solutions were studied to remove the aluminum backsheet and silver contacts and the effect of different parameters were studied.

Then, different methods to recover silver from these solutions were investigated: silver electrodeposition process and silver recovery by precipitation as silver oxide or silver chlorides. In the case of recovery of silver as a compound, different reduction methods have been evaluated. Also the refining of silicon was studied, in particular, during the production of the photovoltaic cell, the silicon wafer is treated with doping techniques to create a p-n junction by introducing into the metal boron and phosphorus. After research into literature, the effectiveness of an acid solution that could remove this heavily doped layer was verified. Various tests were carried out to evaluate the effect of etching time. A final characterization with the SIMS finally gave us an idea of how the dopants concentration varied after attacks and confirmed the deletion of the p-n junction.

In conclusion, this study allows to identify the most convenient solution to treat the panels and led to an Italian patent application. Nevertheless, because the idea seemed interesting from economical point of view, it was presented to a business plan competition of the University of Padova, where it was selected among the ten best ideas. After that, it was the basis for a submission of a European upscaling project, which involved other European partners and it was financed with the name of ReSiELP. ReSiELP, that has the objective of bringing to TRL7 the recycling process, started

officially in 1st of April 2017 and, in this chapter, the first results obtained in the improvement of the technology to industrial level are also reported.

The process selected for the recycling begins with the panel delamination, which is necessary to release cells from the encapsulating and protective effect provided by EVA and all the layers that make up the photovoltaic sandwich. This can be achieved by heat-treating the panel at a temperature of 500 ° C in order to remove all polymeric parts.

Once released, the cells are treated with a sodium hydroxide solution to remove the aluminum backsheet and a nitric acid solution to dissolve the silver metallic surface contacts into the solution. A further step is than to recover silver from the acid solution. This can be done by adding sodium chloride to obtain silver chloride precipitation.

The silver chloride is then heat treated with the addition of sodium carbonate, causing the reduction to metallic silver. The refining of silicon wafer was also studied. A mixture of acids found in the literature was tested to eliminate the doped surface layer with phosphorus and hence the p-n junction. The specimens were then characterized by a SIMS analysis that confirmed the junction elimination and therefore the actual refining of the silicon.

This treatment with hydrofluoric acid, however, was not consider necessary at the beginning of the ReSiELP project proposal but, as the project goes on, it seemed that it could be necessary.

In addition to this, the upgrade of the method at TRL 7 required other analysis: economic considerations, the parameters corrections according to the difference between the material constituting the PV panels coming from different producers which will be treated in the plant, the automation of some operations previously performed manually, the study of the proper disposal both of the fumes generated during the thermal treatment and of the solution coming from the hydrometallurgical ones.

4.1 PV panels market

Photovoltaic technology is considered a clean energy source, as there is no polluting or climatic emission during the energy production.

It is also a relatively recent technology and, over the past ten years, photovoltaic installations have grown at an unprecedented rate, exceeding all predictions. To date, this growth has predominantly taken place in Europe. In particular, Belgium, France, Germany, Italy, Spain, Slovakia and the United Kingdom account for more than 90% of total photovoltaic installations in Europe according to EPIA.

At the end of 2012, the global installed photovoltaic capacity was slightly greater than 102 GW, with 31.1 GW accounting for new installations, approximately a third of the cumulative capacity. In 2012, like in 2011, Europe was the leader with the highest new installed capacities on its territory, respectively 55% and 74% of cumulative installed capacity. In Europe, Germany accounted for the market with the highest absolute growth in 2012 with 7.6 GW of new installations, followed by Italy with 3.4 GW.

Moreover, as can be seen from the Fig. 4.1 [66], much of the world market is based on crystalline silicon (monocrystalline or polycrystalline) modules.

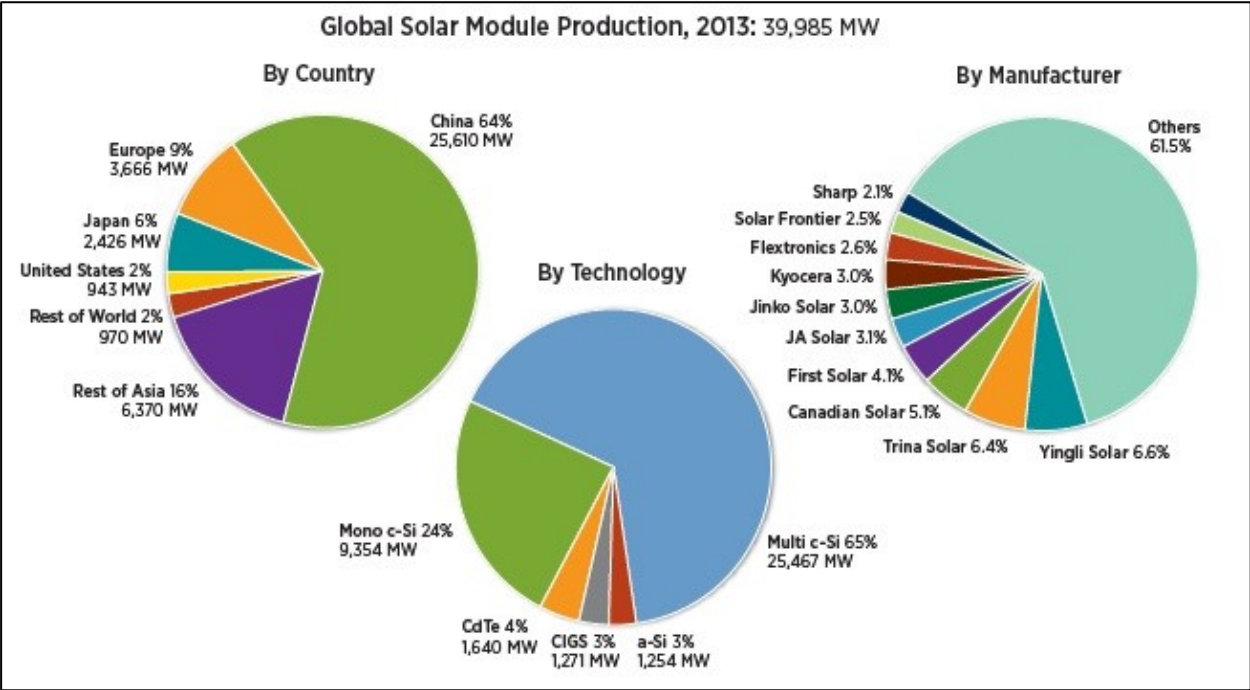


Fig. 4.1 Global photovoltaic module production in 2013 divided by country, technology and manufacturer.

4.1.1 Italian market

Italy was one of the first country to install this technology. In 1979, at the Passo della Mandriola, in the community of Appennino Cesenate, the first Italian 1 kW photovoltaic plant was installed, resulting from a collaboration between the LAMEL institute of CNR, ENEL, Riva Calzoni and the Helios Technology. From those beginnings the photovoltaic sector began its spread. Only twenty years after that first installation, in the 1990s, Italy was the first country in Europe for the power installed in photovoltaic plants (about 25 MW), and in 1993 the National Photovoltaic Plan was set up specifically, including ENEA, ENI, Eurosolar and Helios Technology. Since then, the number of installed plants has been unimaginable, although the main factor that in Italy lead to the spread of this technology were the state incentives that began in 2000 and in different form, still exist today.

Since 2005, Italians have been able to take advantage of the so-called "Conti Energia" projects, which have greatly influenced the installation of the plants with substantial incentives (up to the 75% payment of the plant). During the First "Conto Energia", in force from 19 September 2005 to 31 December 2005, 9121 installation requests were approved and 79 MW installations were installed. The Second "Conto Energia" also further increased the installations and in 2008 approximately 22,000 installed plants totaled 260 MW, with an exponential growth rate. During the next "Conto Energia", in the 2010-2011 biennium, the installed power increased from 3470 MW to 12773 MW [67].

4.1.2 Estimation of the amount of wastes

With such an abundant market, the estimation of photovoltaic waste volumes is becoming a crucial issue [68]. In fact, the estimated life of a photovoltaic plant is around 20-25 years, beyond which poor performance makes it necessary the disposal. Nevertheless, the end of life is not the only case where the PV panels can become waste and some data are reported in Fig. 4.2. In detail, most

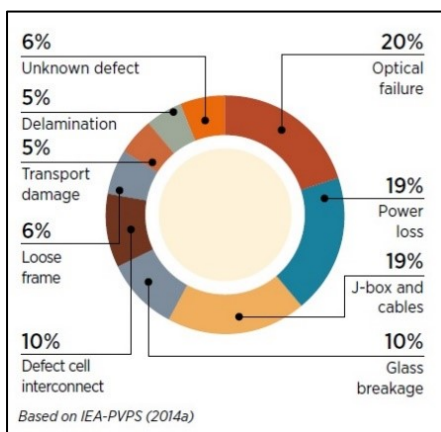


Fig. 4.2 Failure rates according to customer complaints.

waste is typically generated during four primary life cycle phases of any given PV panel.

These are 1) panel production 2) panel transportation 3) panel installation and use, and 4) end-of-life disposal of the panel. From installation data it is in fact possible to estimate the volume of PV panels waste for the next years.

IRENA in particular studied accurately the global PV panels market and made accurate PV panel waste projections, reported in Fig. 4.3 [69].

This forecast model covers all life cycle stages except production. This is because it is assumed that production waste is easily managed, collected and treated by waste

treatment contractors or manufacturers themselves and thus not a societal waste management issue.

As can see in Fig. 4.3, is it expected that the amount of PV waste will increase exponentially in next years.

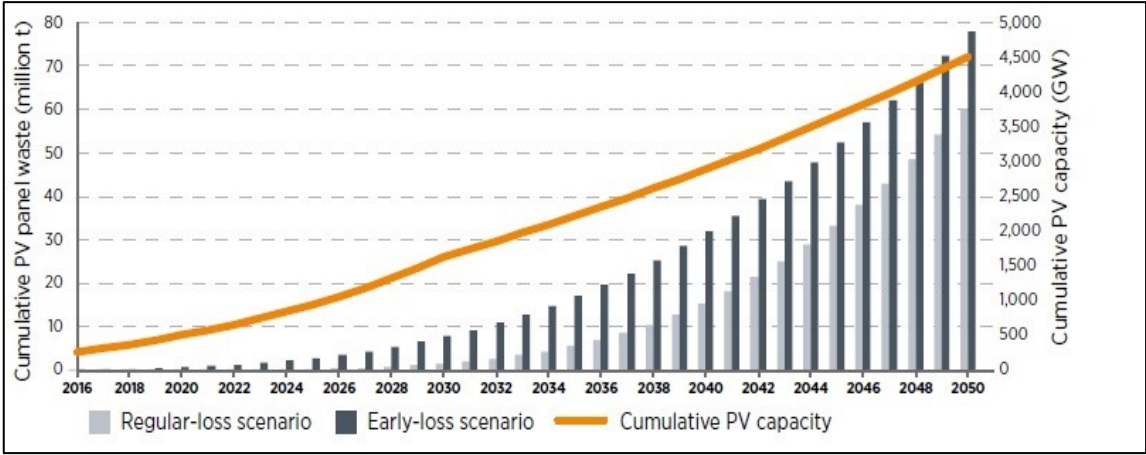


Fig. 4.3 Estimated cumulative global waste volumes (million t) of end-of-life PV panels

As far as the Italian market is concerned, the number of installations currently in operation in Italy is 550,533, with a corresponding power of 17,698,255 MW (GSE data updated on 11/7/2015) and it can be estimated that in 2035 their uninstillation will produce a cumulative of more than 1.5 million tons of photovoltaic waste.

In particular, it can be made an approximate estimation of the amount of waste using the installation data of GSE and, considering an average life of the modules of 20 years. The result is that represented in Fig.4.4.

From the data, it is possible to see (in logarithmic scale) the high increase of the amount of PV

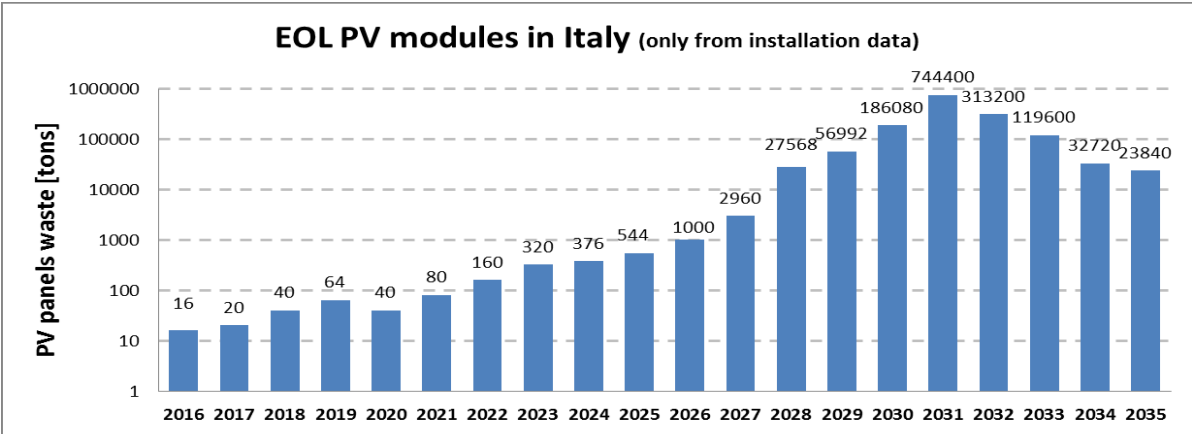


Fig. 4.4 Estimated waste volumes of end-of-life PV panels for Italy.

waste that is expected from 2022. It must be also noticed that the estimation for these years is not realistic, as it do not consider the panels broken during installation or before the estimated life (i.e. for hailstorm or overheating).

4.1.2 Regulation about end of life PV panels

Nowadays the most important law concerning the photovoltaic panels disposal is the Directive 2012/19/EU of the European Parliament and of the Council of 4 July 2012 on waste electrical and electronic equipment (WEEE).

This directive, not only declare that PV panels are effectively to be considered WEEE, but also place at his core the extended-producer-responsibility principle. Consequently it has a global impact, since producers which want to place products on the EU market are legally responsible for end-of-life management, no matter where their manufacturing sites are located.

This combination of producer legal liability for product end-of-life, EEE dedicated collection, recovery and recycling targets, and minimum treatment requirements ensuring environment and human health protection may be a reference point for PV waste management regulation development globally. The 2012/19/ EU for the first time include specifics on end-of-life management of PV panels. Each one of the 28 EU member states is now responsible for establishing the regime for PV panel collection and treatment in accordance with the directive. As the WEEE Directive is based on the extended-producer-responsibility principle, producers are liable for the costs of collection, treatment and monitoring and they must fulfil a certain number of requirements and responsibilities.

The directive in Italy was applied through the D.L. 49/2014, integrating PV waste into Group 4 of WEEE. It led to the creation of consortia that can collect most of end-of-life PV panels.

Moreover, the WEEE Directive is important as also fixed the annual collection and recovery targets (mass %), reported in Tab. 4.1 [70].

WEEE Directive (2012/19/EU)	Annual collection targets	Annual recycling/Recovery targets
from 15/8/2016 to 14/8/2018	45% (by mass) of all equipment put on the market	80% recovered and 70% prepared for reuse and recycled
from 15/8/2018 and beyond	65% (by mass) of all equipment put on the market or 85% of waste generated ¹³	85% recovered and 80% prepared for reuse and recycled

Tab. 4.1 *Estimated waste volumes of end-of-life PV panels for Italy.*

4.2 The PV panel technology [71]

It is estimated that about 90% of photovoltaic modules installed in the world are based on crystalline silicon, while the remaining slice of the market is composed of thin film technologies where semiconductor materials such as amorphous silicon (a-Si), Copper-Indium-Gallium Selenide (CIGS), Cadmium Telluride (CdTe), and Organic Photovoltaic Cells (OPC).

Silicon based photovoltaic technology can be further divided into several categories depending on its crystalline phase. These are:

1. **Monocrystalline silicon (sc-Si):** wafers are produced from high purity monocrystalline ingots

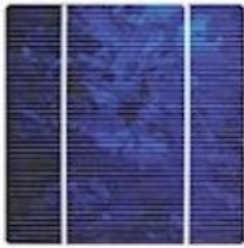


Fig. 4.5 *sc-Si cell.*

generally obtained with the Czochralski process. Lab efficiencies of 26.6 percent for (heterojunction back-contact type) mono-Si cells are the highest in the commercial PV market, ahead of polysilicon with 21.3 percent and all established thin-film technologies namely, CIGS cells (22.6%), CdTe cells (22.1%), and a-Si cells (14.0%). The efficiency is because of the high purity and the absence of grain borders.

2. **Polycrystalline silicon (poly-Si or mc-Si):**

represents the technological base of 35% of the total installed photovoltaic systems. Polysilicon consists of small crystals, also known as crystallites, giving the material its typical metal flake effect. While polysilicon and multisilicon are often used as synonyms, multicrystalline usually refers to crystals larger than 1 mm. This technology is less expensive to produce than monocrystalline silicon, but it is also less efficient.



Fig. 4.6 *mc-Si cell.*

3. **Ribbon silicon:** the name describes the manufacturing process, where

a sheet of silicon the ribbon is pulled vertically from a bath of molten silicon to form a multi-crystalline silicon crystals. The ribbon is then cut into lengths, which are treated with traditional processes to form solar cells. These cells have lower efficiencies than poly-Si, but they avoid the waste encountered when sawing wafers from ingots. This manufacturing process uses about half the amount of input silicon required by traditional processes. Currently, they cover 5% of silicon based systems.

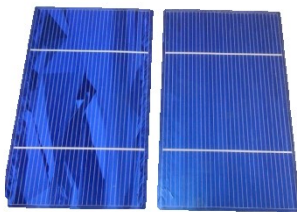


Fig. 4.7 *ribbon Si cell.*

4. **Amorphous silicon (a-Si) or thin-film silicon solar cells,** it is deposited in thin films onto a variety of flexible substrates, such as glass, metal and plastic: in this type of cell, silicon is not organized in crystalline structures and is obtained by Chemical Vapor Deposition. The result is a semiconductor amorphous layer with thickness of few microns.

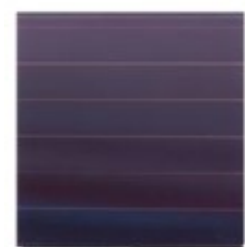


Fig. 4.8 *a-Si cell.*

4.2.1 The photovoltaic cell [72, 73, 74, 75]

The research in photovoltaic systems developed various types of cells that differ in the material used, the structure, production method and applications. There is, however, a theoretical electrical model underlying the operation of any photovoltaic cell that consists in the junction between a semiconductor material of the type "n" and a semiconductor material of type "p" enclosed between two conductors and connected to form a closed loop. Essentially, a cell can be considered as a diode consisting of semiconductor material that allows absorbing solar energy and transforming it into electric potential difference between the two sides of the cell. Its structure is schematized in Fig. 4.9.

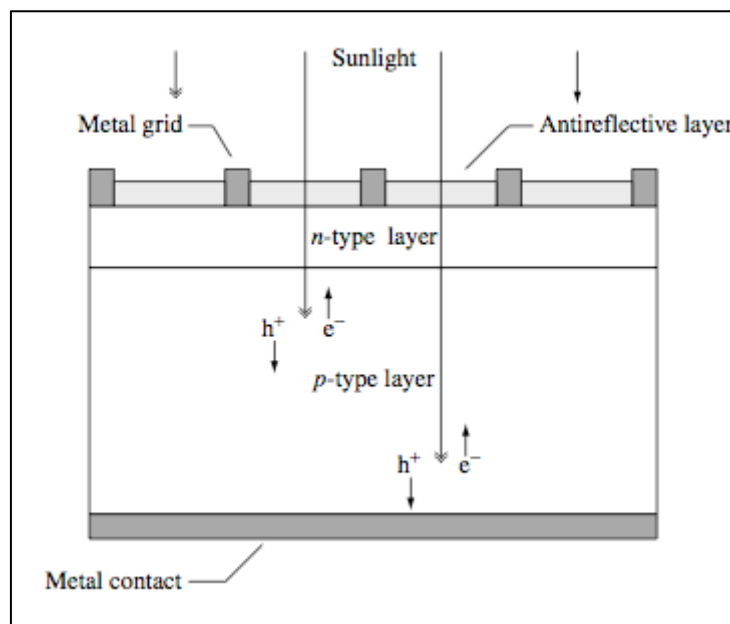


Fig. 4.9 Typical structure of a photovoltaic cell.

The junction between the two doped semiconductors n and p generates an internal electric field that separates the electric charges generated by the photovoltaic effect. When a sufficient energy photon hits the cell, it creates an electron-gap pair. The electric field created by the p-n junction then pushes the two charges towards the material to where the energy level is lower: the electrons will migrate to the semiconductor type n, while the gaps will migrate to the p semiconductor. When the junction is connected to conductors and the circuit is closed, the charge flow that is generated in the junction generates electrical current in the circuit.

In particular, the physical phenomenon that regulates the creation of an electron-gap pair takes the name of "photovoltaic effect". This phenomenon occurs when a valence band electron of the material, by absorbing a photon, acquires a sufficient amount of energy to pass through the conduction band. This is possible only if the electromagnetic radiation that reaches the material gives to the electron belonging to an outer shell of the atom an amount of energy above a threshold value that allows it to overcome a band gap band present in the semiconductor material. In this case, in

fact, the electron will have the possibility to move away from the atom passing from the so-called "valence" to the "conduction" band where it is free to "move". The absence of the electron from the band of valence takes the name of "hole" and, although it is actually the absence of a negative charge, it can be considered as a positive charged particle.

The described effect occurs only in semiconductor materials. In fact, in the case of insulating materials, the theory provides a very high energy band gap of atoms so that the energy of a photon is not enough to overcome it. In the case of conductive materials, instead, the band gap energy is small or nonexistent, so the creation and annihilation of electron-gap pairs is continuously and independently performed at room temperature due to thermal radiation.

When a suitable light energy source invests the crystalline lattice of a semiconductor material, it provokes the transition of some electrons to the conducting band, resulting in the formation of an equal number of gaps in the valence band, thus making it possible to obtain charge-carriers that can generate an electric current. This current can be obtained applying an electric field inside the cell and, in this case, thanks to the characteristics of the junction p-n, in which there is an excess of cations in the semiconductor p zone and anion excess in n zone.

This junction is usually obtained by doping the material, so incorporating into the semiconductor small percentages of atoms different from the base material (10^{13} – 10^{20} atoms/cm³). In particular, in the "p" layer there are some atoms that have less electrons compared to the base material and, consequently, an excess of holes, and in a "n" layer, there are atoms with more electron in comparison with the base material and an excess of electrons.

In the case of silicon, the "p" layer is realized by doping the base with elements belonging to the III group, which therefore have three valence electrons: typically, boron atoms are used. The "n" layer is instead made by doping the base with elements belonging to the IV group that have five electrons in the valence shell: in this case, the most used dopant is phosphorus.

The doped layer with donor atoms (n) thus exhibits a weakly negative charge due to the excess electron in the base material and, likewise, the doped-doped layer (p) has an excess of positive charge. The separation zone between the two doped regions therefore takes the name of "p-n junction".

It is important to emphasize that the obtained material is not electrically charged since the atoms used in doping are not.

In fact, after joining p-type and n-type semiconductors, electrons from the "n" region near the p–n interface tend to diffuse into the "p" region leaving behind positively charged ions in the "n" region and being recombined with holes, forming negatively charged ions in the "p" region.

The regions near the p–n interface lose their neutrality and most of their mobile carriers, forming the "space charge region" or "depletion layer", shown in Fig. 4.10.

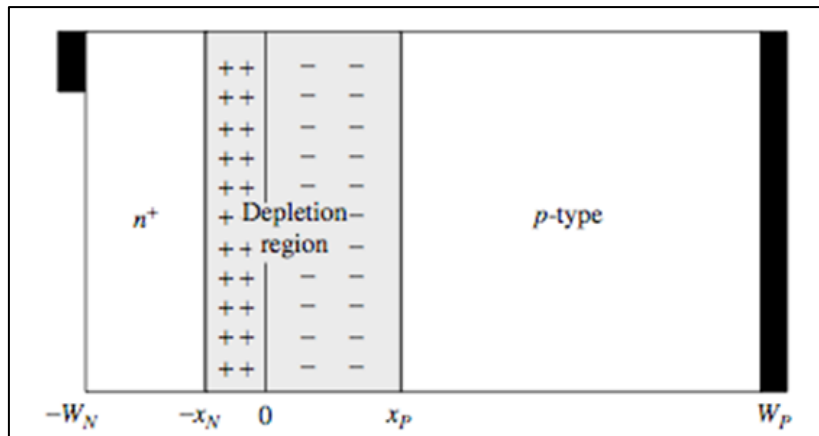


Fig. 4.10 The p-n junction.

Moreover, in a p–n junction, without an external applied voltage, an equilibrium condition is reached in which a potential difference is formed across the junction. This potential difference is called built-in potential.

This potential therefore allows to push the electrons and the gaps, generated when a photon strikes the material, in the opposite directions. When the junction is connected to an external conductor, electrons move from the layer “n” to the “p” layer, so generating the electrical current.

The internal structure of photovoltaic cells is therefore characterized by two regions, the “n” and the “p”, which have very different thicknesses. The thicker region is called "base", while the slimmer area is called "emitter".

Moreover, it is possible to distinguish two type of solar cells: p-type and n-type.

Most commercial photovoltaic cells are p-type. The term p-type refers to the fact that the cell is built on a positively charged (hence p-type) silicon base. Indeed, the wafer is doped with boron, which has one electron less than silicon. The top of the wafer is then negatively doped (n-type) with phosphorous, which has one electron more than silicon.

Instead, n-type solar cells are built the other way around, with the n-type doped side serving as the basis of the solar cell.

The first solar cell produced by the Bell Laboratories in 1954 was a n-type, back contact, solar cell. The very first years saw a rapid and important increase of efficiency. Progressively, the p-type structure took the lead, historically because in the early days of its development, the solar technology was mainly used for space applications and it turned out that p-type structure had better resistance to radiations for space applications. Then the industry developed and structured and could enjoy the benefits of economies of scale [76].

4.2.2 Silicon

Currently the most used material in photovoltaic systems is the silicon, especially the crystalline one. The primary processing steps for the production of silicon solar cells from quartz are as follows: bulk production of metallurgical-grade silicon via carbothermic reduction in a submerged furnace, refining of metallurgical-grade silicon via the chemical means to polycrystalline silicon, or through the metallurgical route to solar-grade silicon, wafer manufacturing, and, lastly, silicon solar cell manufacturing [77].

The earth's crust is made up of 27.7% by weight of silicon, which is the second most abundant element in the earth's crust, second only to oxygen. It is naturally found as pure silicon dioxide and as silicates. The silicon dioxide is found as huge deposits of quartzite or quartz sand. Moreover, many rocks contain quartz crystals. Therefore, it can be concluded that the resources of silicon are virtually unlimited (although purity varies considerably).

In nature, however, it is never in the metallic state because of its high reactivity, and so it is always combined with oxygen in the form of various oxides and silicates (aluminum, magnesium and other elements). Its reduction and purification are therefore extremely expensive.

Silicon is a semiconductor element. Even if it absorbs very well the luminous radiation with wavelength between $0.4\mu\text{m}$ and $1.5\mu\text{m}$, and the spectrum of solar light power is maximum in that range, the silicon's band gap (1.1 eV) is below the range with maximum of solar cell energy conversion efficiency limits, which is between 1.4eV and 1.6eV [78].

As a consequence, silicon is not the best material for solar energy conversion and it is no surprise that there is extensive research going into the search for new materials for solar cells. Thin-film semiconductors are gaining popularity in industry, particularly cadmium telluride (CdTe).

However, there are other important factors to be considered for an ideal solar cell material, like material availability, non-toxic materials, easy production methods suitable for mass production, photovoltaic conversion efficiency and long-term stability of the solar cell material.

The dominance of silicon in the photovoltaic industry is so attributable to historic reasons, availability of high-quality material in large quantities for the semiconductor market.

Silicon is classified according to its degree of purity. The purity of silicon used directly in metal industry is 98% and commonly called metallurgical-grade silicon (MG-Si). A small portion of silicon is used in the electronic/semiconductor industry as electronic chips such as transistors, liquid crystal displays, diodes, etc. The purity of the silicon used in this industry is 99.999999% (eight nines or 8N) or higher, and referred to as electronic-grade silicon (EG-Si). Finally, there is silicon used for solar photovoltaic (PV) panel wafers. For this application, silicon must be purified to at least 99.9999% (six nines or 6N) purity, and is usually called solar-grade silicon (SOG-Si) [79].

4.2.3 Silicon production

The silicon production industry uses as the starting material high purity siliceous sands and quartz.

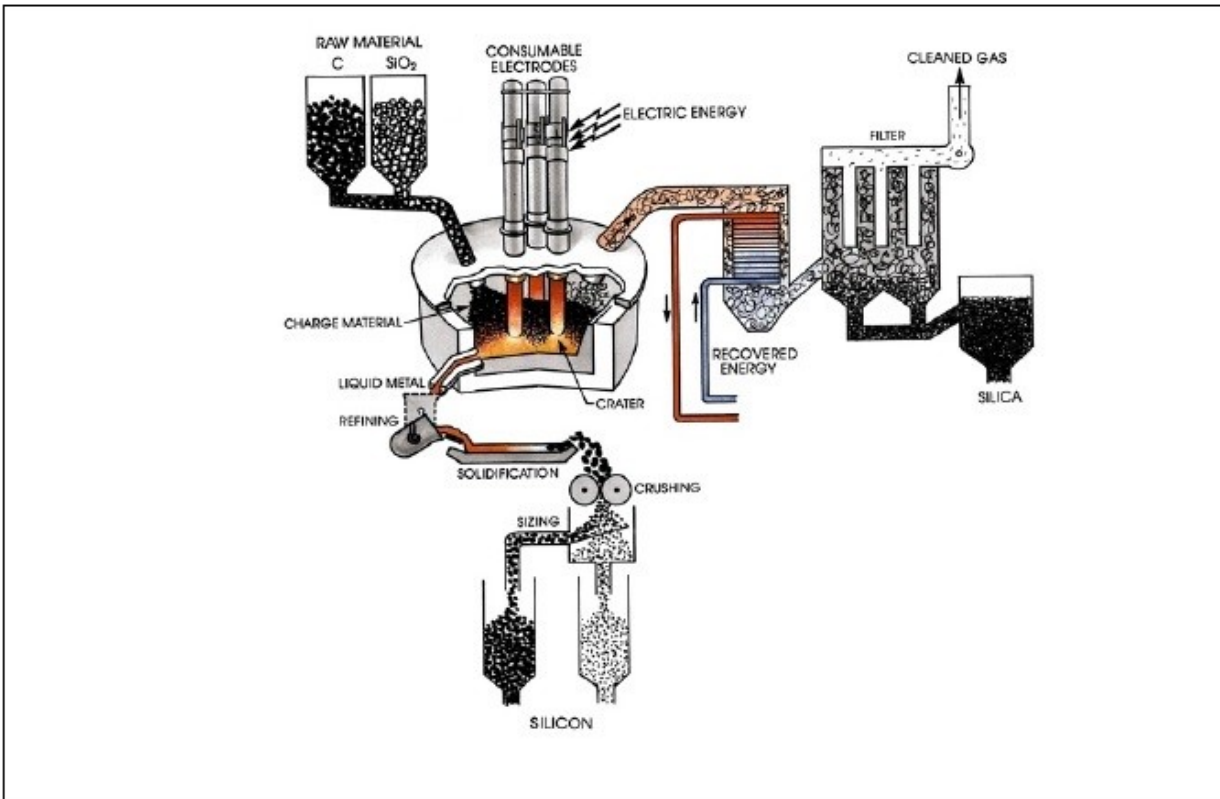


Fig. 4.11 Schematic representation of a furnace for production of metallurgical grade silicon.

Quartzite and sand are placed inside a graphite crucible, which is then introduced into a submerged arc furnace with graphite electrodes. During treatment, temperature of about 2000 °C is reached and, with the addition of reducing substances, the reaction of carboreduction occurs:



Liquid crude silicon then contains 1 to 3% impurities depending on the raw materials and the type of electrodes. The main impurities are reported in Tab 4.2.

Fe [%]	Al [%]	Ca [%]	Ti [%]	C [%]
0.2–1	0.4–0.7	0.2–0.6	0.1–0.02	0.1–0.15

Tab 4.2 Schematic representation of a furnace for production of metallurgical grade silicon.

As most of the applications of silicon require further refining, the crude silicon is tapped as liquid in large ladles (containing up to 10 MT of silicon) and treated when still liquid with oxidative gas and slag-forming additives, mainly silica sand (SiO₂) and lime/limestone (CaO/CaCO₃). Other chemicals such as dolomite (CaO–MgO), calcium fluoride (CaF₂) and others are used depending on plant practice and customer requirements. Elements less noble than silicon such as Al, Ca and

Mg are so oxidized and the degree of refining is determined by distribution equilibriums (Eq. 4.2-4.5), where the (parentheses) refer to components dissolved in a slag phase and the underscored symbols refer to dissolved elements in liquid silicon:



Theoretically it is possible to remove Al and Ca to very low levels, but in practice this is prevented by the large heat losses occurring during this operation. Temperature drops from 1700 to 1500°C, and to avoid freezing of the melt, some of the silica needed for slag formation is provided by direct oxidation of Si(l) in order to heat silicon to keep it liquid. A disadvantage of this operation is the loss of silicon.

After completion of oxidative refining in the ladle, the slag, which contains part of the impurities, is removed mechanically or by gravity and liquid silicon is poured into a casting mold. The slag-forming additives influence the slag density and viscosity, hence the practical separation of slag and the ultimate purity of the poured silicon.

Carbon is present in crude liquid silicon mainly as dissolved C and suspended SiC particles. The fraction of SiC increases as the temperature is lowered; SiC particles are then captured by the slag phase and thus are removed from liquid silicon during the ladle treatment and the subsequent pouring. SiC is also removed simply by mechanical separation, precipitated particles sticking to the walls of the ladle and the other devices containing the liquid silicon. Dissolved carbon in the range of 80 to 100 ppm(m) in best cases will finally remain in the purified alloy of metallurgical silicon. This first step allows obtaining metallurgical silicon which, however, still has a too high impurity concentration to be used in the photovoltaics or electronics.

4.2.4 Importance of Silicon purity

In fact, impurities can lead to the formation of defects, and enhance the formation of dislocations, which act as recombination centers of photo-carriers and can compromise both mechanical and electrical properties as well as decrease the solar cell efficiency. Moreover, impurities in solar cells generally introduce allowed levels into the forbidden gap and thereby act as recombination centers, and an increased density of such centers decreases the cell efficiency. The effect of metallic impurities on silicon solar cells is shown in Fig. 4.12.

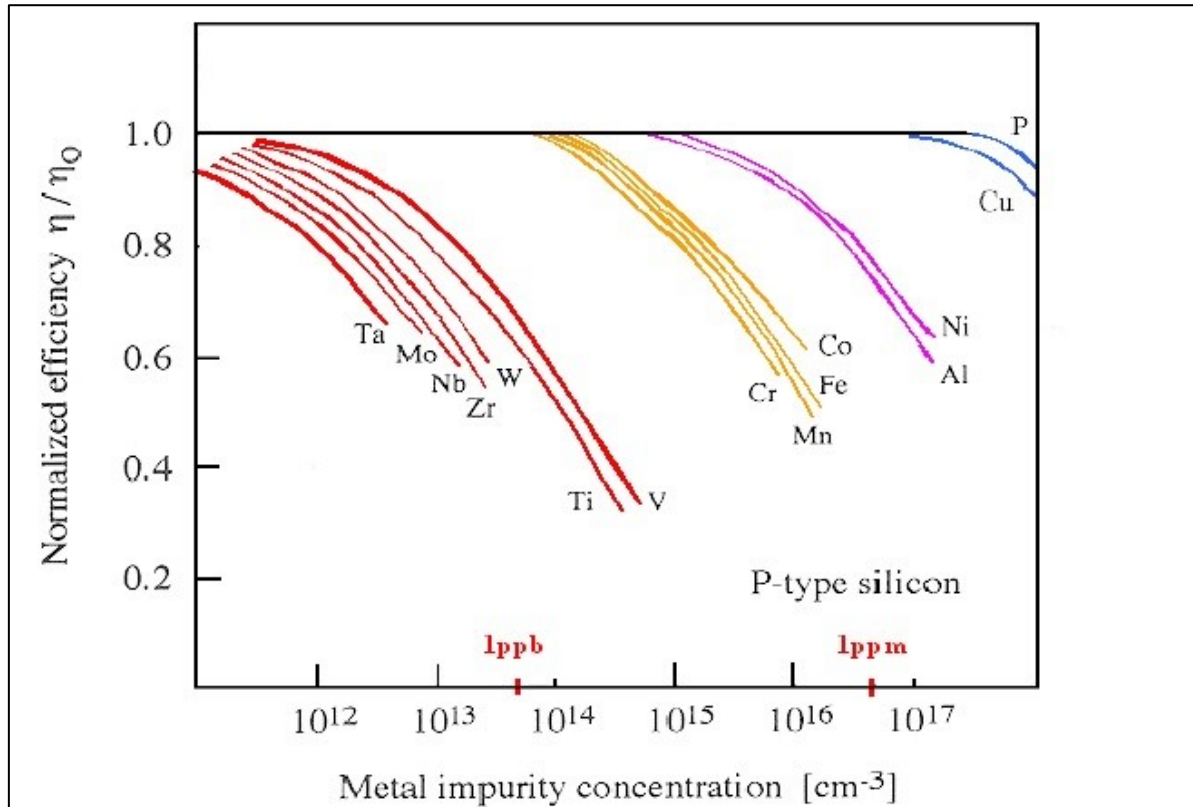


Fig. 4.12 Silicon solar cell performance as a function of atoms of impurity per cm^3 in p-type silicon.

Consequently, in case of photovoltaic application, a further process of purification is necessary [80].

4.2.5 Silicon refining

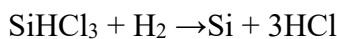
Many processes to produce polysilicon have been tested, patented and a few operated for many years. Only three large commercial processes are currently active:

- The most used process is referred as Siemens process (the name of the company that first carried out it) and was originally developed for the production of electronic-grade silicon in the 1950s. During this process, powdered MG-Si reacts with hydrochloric acid, in the presence of catalyst, to produce trichlorosilane. The reaction, that occurs at 300 °C in a fluidized bed reactor, is:



During this reaction impurity such as Fe, Al, and B react to form their halides (e.g. FeCl_3 , AlCl_3 , and BCl_3). The SiHCl_3 has a low boiling point of 31.8 °C and distillation is used to purify the SiHCl_3 from the impurity halides. The resulting SiHCl_3 has then electrically active impurities (such as Al, P, B, Fe, Cu or Au) of less than 1 ppb.

Finally, the pure SiHCl_3 is reacted with hydrogen at $T > 1100^\circ\text{C}$ for ~200–300 hours to produce a very pure form of silicon, according to the reaction:



The reaction takes place inside large vacuum chambers and the silicon is deposited onto thin polysilicon rods to produce high-purity polysilicon rods of diameter 150-200mm.

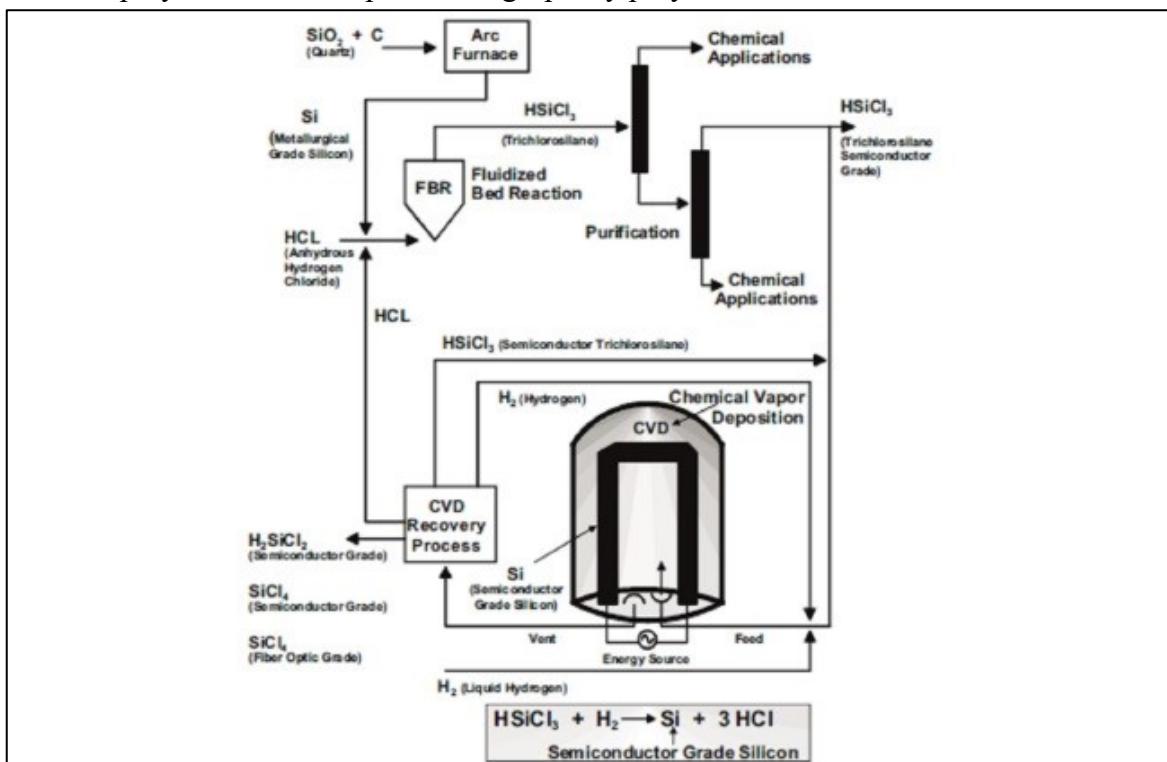


Fig. 4.13 Scheme of Siemens process for silicon refining.

In 2001 this process still accounted for at least 60% of the worldwide production of polysilicon.

- In a more recent process developed by Union Carbide Chemicals in the United States of America, the trichlorosilane has been replaced by monosilane SiH₄, but the principle of decomposition on a heated silicon rod inside a closed deposition chamber is maintained.



This process, presently run by the company Advanced Silicon Materials, LLC. has gained during the past 15 years a significant market acceptance.

- Finally, in the third process, also making use of monosilane SiH₄, the heated silicon rod in the closed reaction chamber has been replaced by a heated fluidized bed containing silicon particles. The particles act as seeds on which SiH₄ is continuously decomposed to larger granules of hyper-pure silicon. Unlike previous ones, this process is a continuous one. This process is known as the Ethyl Corporation process, after the name of the US chemical company that developed it.

Another common process to refine silicon is the metallurgical route. The metallurgical route entails obtaining solar-grade silicon directly from metallurgical-grade silicon via a series of metallurgical refining steps. Solar grade silicon produced via the metallurgical route is often referred to as upgraded metallurgical-grade silicon. The energy consumption of the metallurgical route is expected to be significantly lower than that of the Siemens process.

Most metallic elements have a low segregation coefficient in silicon, which means that the solid rejects impurities into the liquid during crystallization. The refining techniques based on this principle include both directional solidification and acid leaching. Directional solidification can also be used as a casting step for preparation of single-crystal and multi-crystal ingots from which wafers are prepared.

Other impurities have high segregation coefficients in silicon; these include boron, carbon, oxygen, and phosphorus. Therefore, such impurities cannot be removed from silicon via the above-mentioned refining techniques. However, phosphorus can be volatilized from silicon, and removed via vacuum refining whereas boron can be removed from silicon by slag refining, or via plasma refining where carbon and oxygen are also removed. It is common in the metallurgical route to employ high-purity raw materials, i.e. purified quartz, carbon black, and high-purity electrodes; this renders low impurity levels in the upgraded metallurgical-grade silicon product.

Since the refining techniques used in the metallurgical route tend to be effective in removing specific impurities, combinations of the refining steps are employed in industry for effective refining of metallurgical-grade silicon to solar-grade silicon.

4.2.6 Silicon crystallinity

As previously described, different there are different kind PV cells that differ for the crystallinity of the silicon. Monocrystalline silicon, necessary for sc-cells but also for microelectronics industry is mainly obtained with Czochralski process, even if it can be obtained also by Floating Zone (FZ): a vertical zone refining without crucible, which produces a purer single crystal but is more expensive than CZ.

The Czochralski process (Fig. 4.14) [81] is a batch process, where polysilicon is melted under vacuum to promote the evaporation of surface contaminants in a quartz crucible, which itself is located in a graphite crucible, and subsequently solidified on a mono-crystalline silicon seed crystal which is then slowly pulled out under rotation, producing a cylindrical mono-crystalline silicon ingot. It takes about two days to complete a production cycle of an ingot.

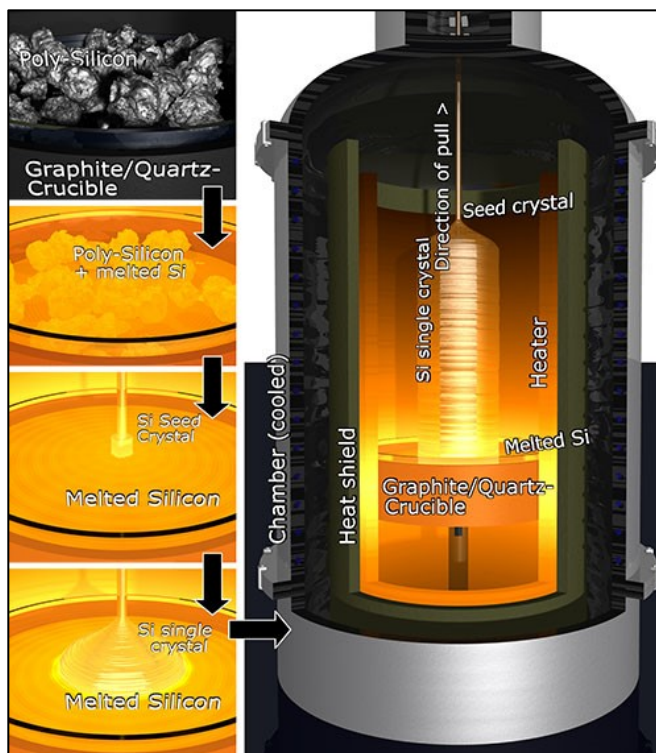


Fig. 4.14 Scheme of Czochralski process.

Most of the multi-crystalline silicon for the photovoltaic industry is produced by the crystallization of liquid silicon in the form of a block; an example of such a process is the Bridgman process. The multi-crystalline ingot casting process entails melting solar-grade or polycrystalline silicon material in a crucible, and controlling the cooling rate. The crystal-liquid interface moves upwards from the bottom of the crucible. The temperature gradient and growth rate are controlled to favor the growth of a high-quality crystal structure, i.e. low thermal stresses. Generally, the goal is to obtain vertically aligned grains which indicate good directional growth. This unidirectional grain growth will avoid high thermal stress, and reduce the dislocation density in the multi-crystalline ingot. It will also ensure a consistent quality of the wafers, as the wafers are cut horizontally. Refining will also be achieved, as metal impurities will be pushed to the top of the ingot. The crucibles used are made of silica, and lined with a Si_3N_4 coating to prevent liquid silicon from sticking on the walls. Because of the multi-grained structure, the material is referred to as multi-crystalline, and the grains vary in size between several millimeters to centimeters.

4.2.7 Wafer manufacturing

Prior to wafer manufacturing, the ingots undergo sectioning where the peripheral sections are cut. The mono-crystalline cylindrical ingots undergo sectioning such that cubic ingots are produced, while multi-crystalline ingots are sectioned for the removal of highly contaminated peripheral regions. The ingots are then cut to blocks with a cross-sectional area equal to the wafer size.

About 25% and 15% of the material is lost from cutting of the mono-crystalline and multi-crystalline ingots respectively. The silicon industry has been moving towards wafers of larger area. In the past, the standard size of silicon wafers was 10 x 10 cm, which was increased to 12.5 x 12.5 cm. At present, the majority of cells are 15.6 x 15.6 cm. The driving force for an increase in cell size is the decreasing cost per watt peak for increasing cell size.

The next step in the wafer production process is to cut mono or poly-crystalline silicon ingots into slices with a thickness varying between 150 and 300 μm .

Wafer thickness has always been tightly bound with cutting technology, as the thickness reductions are strongly limited by the increased fragility of the wafer. At present, cutting process is done using multi-wire saw machines, and their continuous technological evolution has allowed for cutting thicknesses of 120-140 μm , thus decreasing the amount of material needed for each cell and thus the cost of the finished product. During the process, a single wire of stainless steel of 120-140 microns in diameter and several kilometers in length is moved across the crystal in an abrasive slurry suspension. Each wire is wound around a series of guides to give rise to a horizontal warp of parallel turns, and is maintained at a variable speed of between 5 and 25 m/s. Speed control and penetration force must be finely calibrated to avoid wire breaks and imperfections in cutting.

As a basis for the suspension, water, glycols or structured mineral oils are used, which allow for obtaining cutting conditions with high heat dispersion, excellent surface finishes with low roughness while ensuring high cutting forces. The whole process must follow very strict specifications regarding chemical purity control, crystallographic order, micrometric mechanical tolerances, total absence of dust as well as temperature and humidity.

Even if technological advancement allows the development of saws with smaller diameter wires and arrangements of the splines ever closer to be able to achieve slender slices with less workflow, approximately 30% of the silicon is wasted as sawdust kerf loss. After the cutting phase, the wafers are then lapped to uniform the surface, cleaned with solvents to remove any surface pollutants and then sent to the actual cell production process.

The plant layout for industrial production of crystalline silicon wafers is shown in Fig. 4.15.

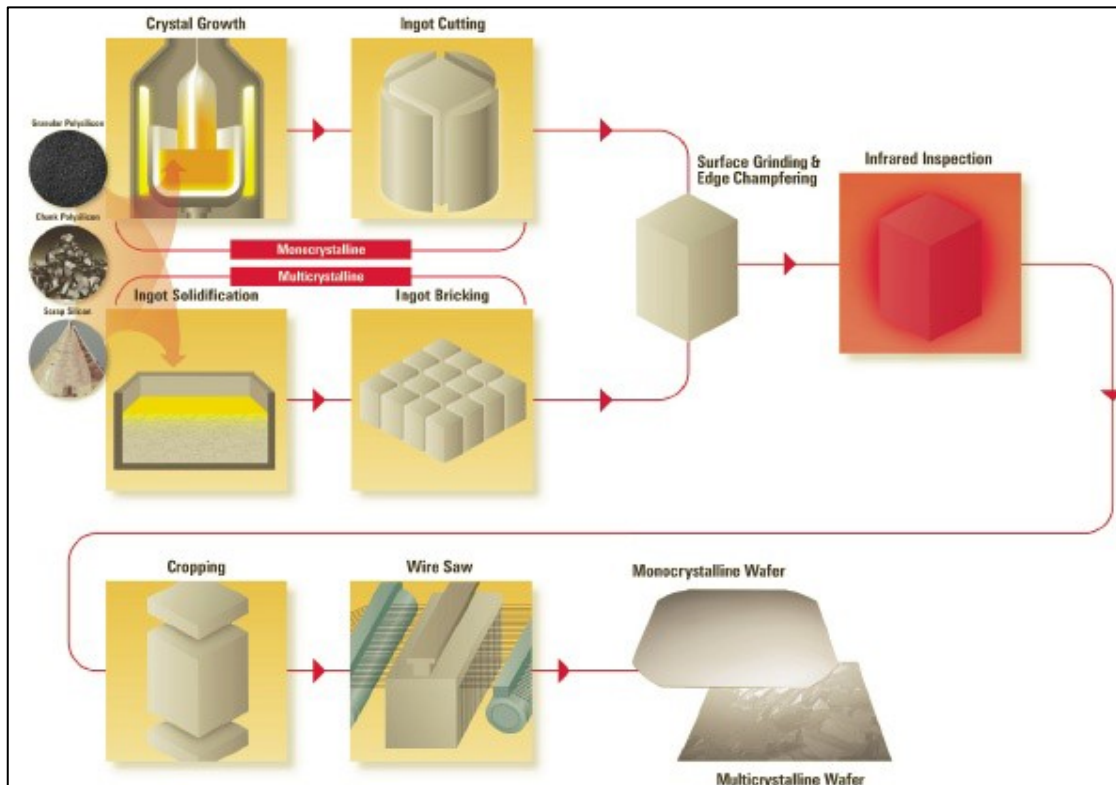


Fig. 4.15 Typical plant layout: industrial production of crystalline silicon wafers silicon.

Wafer manufacturing makes up about 30% of the wafer cost. Moreover, the crystalline silicon wafer up to this stage of processing accounts for nearly half of the final module costs. These costs show that there is potential to decrease the cost of producing crystalline silicon wafers.

4.2.8 PV cells manufacturing

The silicon solar cell manufacturing step is important, both technically and economically, as endeavors can be undertaken during this step to minimize solar cell losses, i.e. maximize efficiency. Moreover, the silicon solar cell manufacturing costs account for approximately 25% of the final module cost.

The production scheme for silicon solar cells is detailed below.

4.2.8.1 Saw-damaged layer removal

Silicon wafers usually contain a saw-damaged and contaminated surface layer, which has to be removed at the beginning of the solar cell manufacturing process. Typically, 10 to 20 microns is etched from both sides of wafers cut by a wire saw. Alkaline etches are commonly used, with subsequent rinsing in deionized water.

4.2.8.2 Texturing

Subsequent to etching, the silicon wafer surface is shiny and reflects more than 35% of incident light. The wafer surface therefore undergoes texturing in order to minimize reflectance. The reflection losses in commercial solar cells are reduced mainly by random chemical texturing. Mono-crystalline silicon wafers can be textured in a weak solution of sodium hydroxide and potassium hydroxide with additions of isopropanol at 80°C producing randomly distributed pyramids. Due to the nature of anisotropy in multi-crystalline silicon wafers, the random texturing process is not effective on these silicon wafers. Mechanical texturing renders sound results for microcrystalline silicon wafer texturing. The optical reflection can be decreased to less than 10% in this processing step.

4.2.8.3 Emitter diffusion (junction formation)

Emitter diffusion is one of the critical steps in the manufacture of silicon solar cells. The starting silicon wafers are usually boron-doped, i.e. p-type. It follows that phosphorus, an n-type impurity, is introduced to form the p-n junction. The process is carried out in a furnace at a temperature of approximately 900°C for phosphorus diffusion. Typical processing time is limited to about 30 minutes, and a penetration depth of about 0.5 microns is achieved. A common dopant source is POCl_3 . Other dopant deposition methods include screen printing, or chemical vapor deposition.

4.2.8.4 Edge isolation

During an n-type diffusion from the gas phase on p-type substrates, the emitter is usually formed on the entire surface of the wafer. Consequently, shunts are formed between the n-type and the p-type region of the silicon solar cell. Edge isolation techniques are applied to isolate the front and the rear side emitter. The techniques for edge isolation include mechanical, laser cutting, or plasma etching. Plasma etching is particularly synonymous with edge isolation of screen-printed silicon

solar cells. In plasma etching, the silicon wafers are stacked, and loaded into a vacuum chamber for etching in a fluoride or oxide plasma environment, and approximately 2 to 5 microns of silicon wafers are removed from the edges, thereby electrically isolating the front and the rear emitter. Careful handling of the silicon wafers is necessary to avoid damages.

4.2.8.5 Anti-reflection coating

The reduction in the front surface reflectance of a crystalline silicon solar cell presents a possibility for improved cell efficiency. An anti-reflection coating is applied to minimize surface reflectance. Several materials with refractive indices ranging between 1.4 and 2.7 can be used as anti-reflective coating on silicon solar cells. Titanium dioxide was the industrial choice for antireflection coatings. Currently, silicon nitride deposited by plasma-enhanced chemical vapor deposition is the dominant anti-reflection coating for silicon solar cells, due to its optimal refractive index and an additional benefit of bulk passivation properties.

4.2.8.6 Metal contact formation (metallization)

The process of contact formation is a vital solar cell processing step because it strongly affects various properties of the silicon solar cell, such as short circuit current, open circuit voltage, series resistance, shunt resistance, and the fill factor. The front side metallization technique employed determines the shadowing and series resistance losses; the emitter diffusion profile and surface of doping concentration; as well as the choice of certain passivation techniques.

For high-efficiency solar cells, it is desired that front electrodes have low series resistance and low area coverage. The most widely used metal contacting technique for silicon solar cells is screen-printing. This technology is simple, time saving, cost effective, and it reduces chemical wastes with little or no environmental impact. Moreover, this is a well-established technology that has been in practice since the beginning of the 1970s. The front side contacting is achieved by a screen-printed silver paste, while the rear side electrode formation and surface passivation are achieved by alloying a screen-printed aluminum paste with silicon. The pastes are subsequently dried in an oven at a temperature of approximately 300°C.

4.2.8.7 Contact firing

The screen-printed contacts initially lie on top of the insulating anti-reflection coating. The silicon solar cells undergo a short heat treatment at temperatures up to 900°C, using a belt-driven furnace. During the firing process, the antireflection coating layer experiences selective dissolution such that the contacts penetrate through the anti-reflection coating onto the emitter while avoiding deep penetration into bulk silicon. Moreover, the back surface field formation with aluminum is achieved.

4.2.9 PV modules manufacturing

After the cells production they are inserted inside the PV module. A typical PV module is composed of several parts (Fig. 4.16) that are:

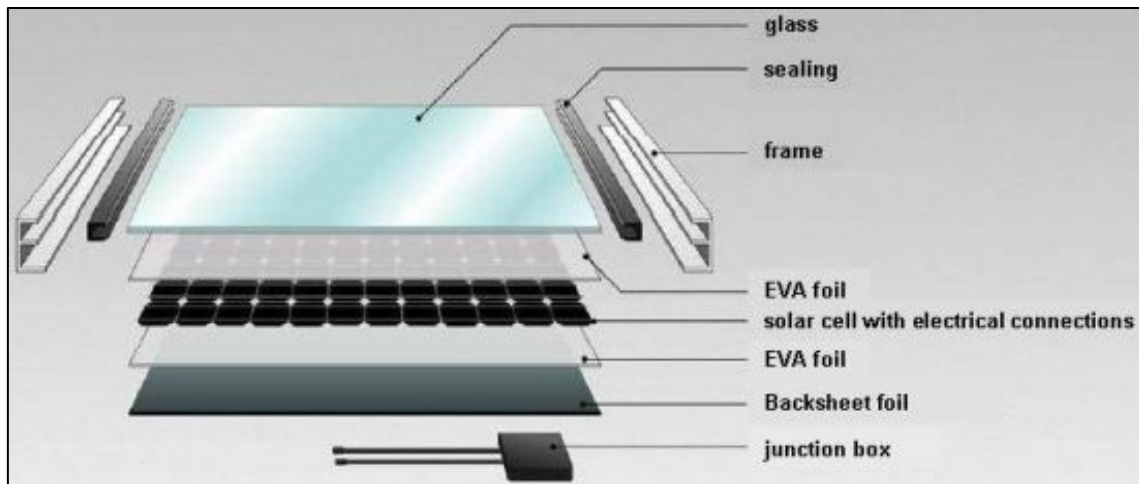


Fig. 4.16 Detail of the SEM image of the aluminum backsheet (left) and of the silver contact (right).

4.2.9.1 Glass

The front glass is the heaviest part of the photovoltaic module and it has the function of protecting and ensuring robustness to the entire photovoltaic module, maintaining a high transparency.

4.2.9.2 EVA

One of the most important materials is the encapsulant, which acts as a binder between the various layers of the PV panel. The most common material used as an encapsulant is EVA - Ethylene vinyl acetate. It is a translucent polymer sold in a roll. It must be cut in sheets and deposited before and after the photovoltaic cells. When subjected to a thermal process of vacuum cooking, this particular polymer becomes similar to a transparent gel and incorporates the photovoltaic cells.

4.2.9.3 Backsheet

The term backsheet literally means the sheet on the back. It is made from a plastic material that has the function to electrically isolate, protect and shield the PV cells from weather and moisture. This particular sheet is usually white in color and is sold in rolls or sheets. There are particular versions that can be different in thickness, in color and in the presence of particular materials for a greater shielding or for a higher mechanical strength.

4.2.9.4 Cell Ribbon

Interconnect ribbon is a hot dip tinned copper conductor installed in photovoltaic/solar panels. The interconnect ribbon is soldered directly onto silicon crystal to interconnect solar cells in a solar panel. The interconnect ribbon carries the current generated in solar cells to the PV bus bar.

4.2.9.5 Junction Box

The junction box has the function of bringing the electrical connections of the PV module outside. It contains the protection diodes for shadows and the cables for the connection of the panels in the field. In choosing the Junction box we pay attention to the quality of plastic, the goodness of sealing, the type of connection of the ribbon and the quality of by-pass diodes.

4.2.9.6 Frame

One of the last parts to be assembled is the frame. It is normally made of aluminum and has the function to ensure robustness and a practical and safe coupling to the photovoltaic module. Together with the frame, also a layer of sealant is deposited around the walls of the panel as a moisture barrier. For this purpose the most widely used material is silicon, although sometimes a special sealing tape is used.

The production process is shown in Fig. 4.17 [82].

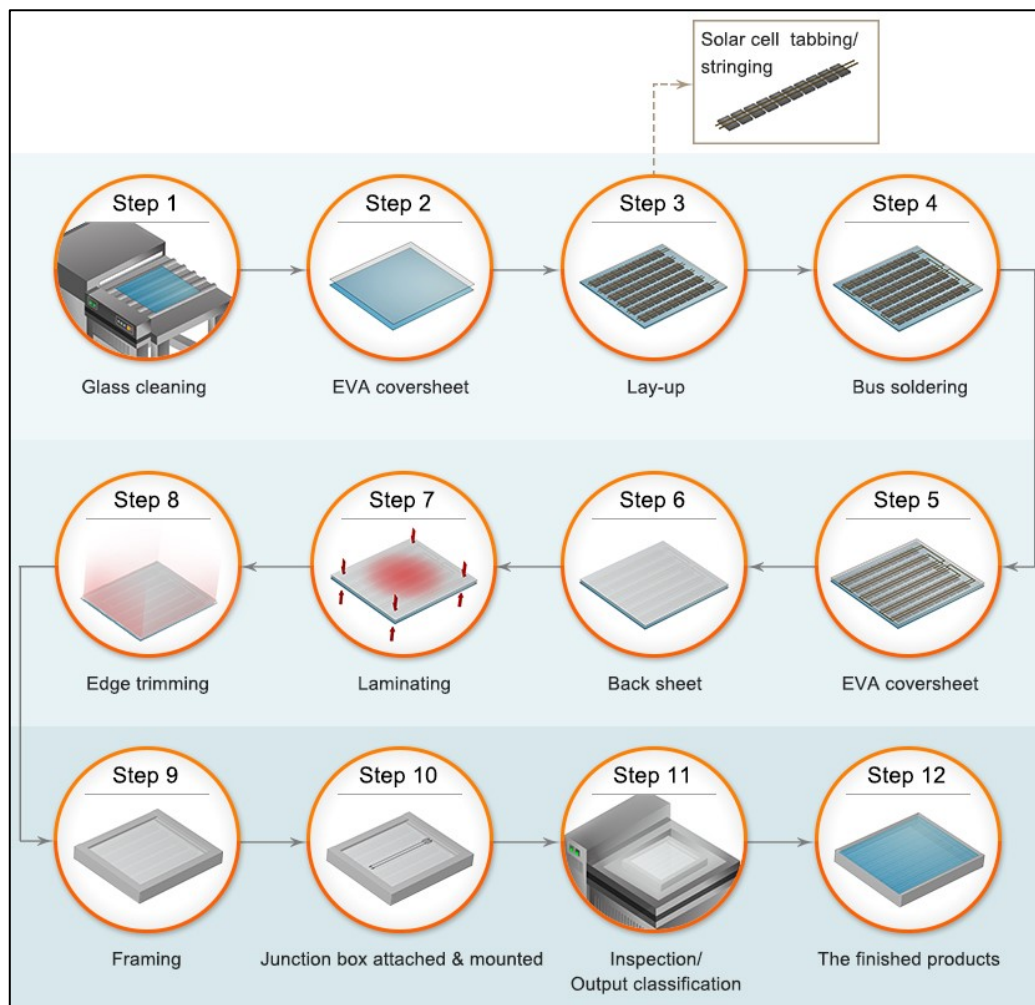


Fig. 4.17 Scheme of PV panels production process.

4.3 PV panels recycling processes [83, 84, 85, 86]

Since currently only moderate PV waste quantities exist on the global waste market, there are not sufficient quantities or economic incentives to create dedicated PV panel recycling plants. End-of-life PV panels are thus typically processed in existing general recycling plants. Here, the mechanical separation of the major components and materials of PV panels is the focus. In fact, the major components of c-Si panels, including glass, aluminum, and copper, can be recovered at cumulative yields greater than 85% by panel mass through a purely mechanical separation. However, without a combination of thermal, chemical [87, 88] or metallurgical steps, impurity levels of the recovered materials could be high enough to reduce resale prices. Separation of the major components such as laminated glass, metal frames, wiring and polymers is the first step in current and first-generation recycling processes. This still achieves high material recovery by panel mass even although some higher value materials (that are small in mass) may not fully be recovered [69].

On the other hand, recycling technology for PV panels have been carried out from 90s from different PV companies. This led to study different treatments for this waste, reported in Tab. 4.3 [70] that are here briefly described. However, among these treatments, only Deutsche Solar process was up to now implemented to commercial level. All the other methods are still not fully-developed and the time for their industrialization is difficult to estimate [89].

Operator	Process	State
Deutsche Solar (Solar World)	Thermal separation, chemical processing	Pilot production
First Solar (Solar Cells Inc.), BNL	Thermal decomposition in inert gas	Laboratory
Isofoton	Cell recycling, Swelling, Shredding, Repairable module	Laboratory
AIST, Sharp, Asahi	Water recycling with mineral acids, solvent swelling (CellSEPA-process), Repairable module	Laboratory
Photovoltaeltech	Repairable module	Laboratory
BP Solar,	Water recycling with mineral acids	Laboratory
Seghers, Soltech	water recycling in fluidized bed	Laboratory
Pilkington Solar International	Thermal separation	Laboratory
Siemens Solar, Shell Solar, Showa Ahell	Ferrosilicon production, High pressure water jet	Laboratory
Others	Module shredder, Mechanical separation, Acid treatment, Smelter, MWI, Concrete aggregate Road construction	Laboratory
Disposer	Removal of frames and cable, disposal, incineration	Production

Tab. 4.3 Processes to recycle photovoltaic panels.

The recycling process of Deutsche Solar in Freiberg enables, at a pilot plant scale, the recovery of wafers from crystalline solar modules. The process, after aluminum frame removal, comprises a heating treatment at 600°C to remove plastic parts. Copper bars and metals fractions are manually removed and subsequently the metallization, anti-reflection coating and pn-junction of the cell are removed in an etching line [90].

Deutsche Solar claims that 73% of the silicon is recycled: 59% with 6N (99,9999%) purity, and 41% with 4N purity. The 94% of glass is recycled too with 5N purity.

The First Solar instead developed a process which slowly heat the Eva in order to allow the manually removing of Tedlar backsheet. Then EVA is pyrolyzed in inert gas atmosphere at 500°C. The cost of this technology is \$ 0.13/Wp (\$ 1,5/Wp are needed for a new panel). This technology cannot be realized in Germany because licensing for pyrolysis plants requires very stringent requirements and nowadays the process is not in use. Another developed process is the CELLSEPA®, which consists of swelling EVA layers and separating them using limonene, obtained from citrus fruits. This process, however, is not suitable for the recovery of unbroken cells, as they break due to the tensions caused by the swelling of EVA, and it requires a long period of swap-out for the swelling. The process developed by Pilkington Solar International GmbH involves a heat treatment separation and was initially developed with the idea of using existing recycling facilities for laminated glass. Experiments conducted in FH Amberg showed that it is not possible to reach a sufficient degree of purity of the recovered materials and a good separation between glass, semiconductor and plastic materials. Subsequent developments by the Dutch ECN research center, based on low temperature incineration, did not solve the problems of purging exhausted gases. The process is not used today. The Seghers/Soltech process was developed in a research project funded by the European Community. It is similar to the First Solar process with pyrolysis in saturated nitrogen atmosphere and allows obtaining high yield, up to 80%. The method seems simple and with low cost (\$ 0.22/panel). The major difficulty was the separation of extremely fine powders in the fluid bed system. However, up to now, the process is not used [89]. BP Solar instead was presented in 1994 at the Photovoltaic conference in Amsterdam. The process involves the decomposition of the EVA by the action of mineral acids that leave the wafer intact. However, it is only applicable to certain types of plastic material and formulations and it is still not used.

4.3.1 Review of existing IPRs on Si-PV waste recycling

As mentioned, several processes have been developed for the treatment of silicon based PV panels. In particular, a first patent (EP0893250) was registered by Deutsche Solar AG on 20/07/1998 and claims a heating treatment to separate the components of laminated glazing.

Similarly, First Solar deposited a patent (US2008/0105597) for the pyrolysis treatment, heating the panel in inert atmosphere.

The number of patent regarding end of life photovoltaic panels recycling increased than significantly from 2012, when Yingli Green Energy Holding (CN102544239, CN202316491, CN102500602) claims different processes based on grinding the material, vibrating and screening or melting and centrifugally the material.

Compton (WO2013057035) claims a method that remove glass with counter rotating toothed rolls and Eco Recycling S.R.L. (WO2014184816) a process comprising grinding and chemically treating the panels. Other patents are CN103978021 regarding the chemical treatment and CN10397810 on the pyrolysis.

JP20140005143, presented in 2014, described instead a method the controlled heating rate for the photovoltaic panels in order to avoid glass damages. However, this method cannot be applied in most cases as the panels are typically collected with the glass that is already broken.

JP2015192942 claims particular crushing conditions and JP2015110201 exfoliation process through EVA softening. WO201592734 is about a particular system of crushing and sieving the material. Finally, FR3017551 is about backsheets exfoliation and WO2016110825 about a treatment with acetone and ethylene.

4.4 PV panel characterization

4.4.1 Silicon cells

First of all, the photovoltaic cells were characterized. The first material to be characterized and to be used in the experiments were 30 silicon cells provided thank to prof. Fabrizio Dughiero, of the University of Padova.

These cells were recovered from the production process and so were like those that are inside the PV panels even if they were not yet inserted in the panels.

The cells were analyzed by X-ray fluorescence and the results were summarized in Tab. 4.4 and 4.5.

Front-side composition [%]		Back-side composition [%]	
Si	97,73	Al	70,24
Al	1,586	Si	28,11
Mg	0,544	Mg	1,275
Ag	0,06152	Pb	0,1567
Pb	0,03452	S	0,07633
S	0,01066	Ag	0,04395
P	0,0084	Fe	0,04099
Fe	0,00788	P	0,0232
Ti	0,00585	Zn	0,01263
V	0,0019	V	0,01016

Tab. 4.4, 4.5 XRF analysis of the front-side and back-side of the analyzed photovoltaic cell.

The analysis showed that the front side is made of silicon and silver whereas the backside was made of aluminum with traces of lead. Unfortunately, the Si-Al-Mg alloy sample holder partially offset the values found for these three elements.

After that the cell was observed with SEM, and it was noted that the aluminum deposit is composed of spherical particles. This fact confirmed that it is obtained by screen printing of aluminum paste, as particles of micrometric dimensions were visible.

In fact, aluminum is typically deposited on the cell in paste form. A typical aluminum paste contains metal powders, glasses and additives mixed in an organic medium. The Al Paste variables such as metal powder, glass chemistry and additives have an influence on electrical performance, wafer bowing and solar cell adhesion [91].

Moreover, EDS analysis confirmed the presence of lead in the backside. It was possible to observe the section of the cell and then measure its thickness.

The white fingers and busbars present on the front side of the cell were also observed in section and, thanks to the microanalysis, it was verified that they are composed of pure silver. In addition, from the image it was possible to get data about the thickness of the deposited silver, in order to estimate the amount of this metal in one cell.

In Fig. 4.18 it is possible also to appreciate the structure of aluminum layer and silver contacts.

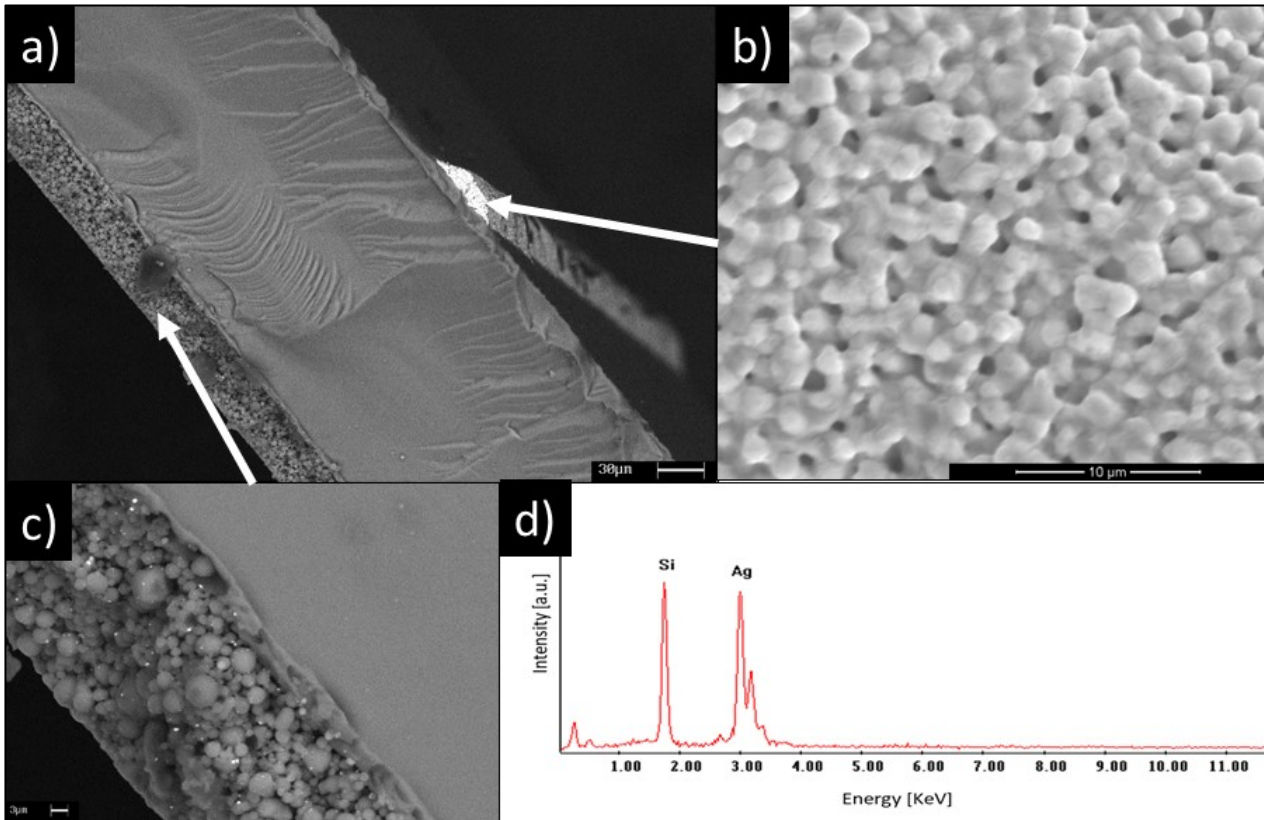


Fig 4.18 a) SEM image of the section of a photovoltaic cell. It is possible to see the structure of the aluminum layer (c) and the porous structure of the silver contacts (b). d) EDS analysis of silver contact.

4.4.2 Ribbons

Each element of the photovoltaic module is connected in series by a metallic strips called ribbons, which are positioned both in front and behind the cells. These items were analyzed with SEM and results are reported in Fig. 4.19.

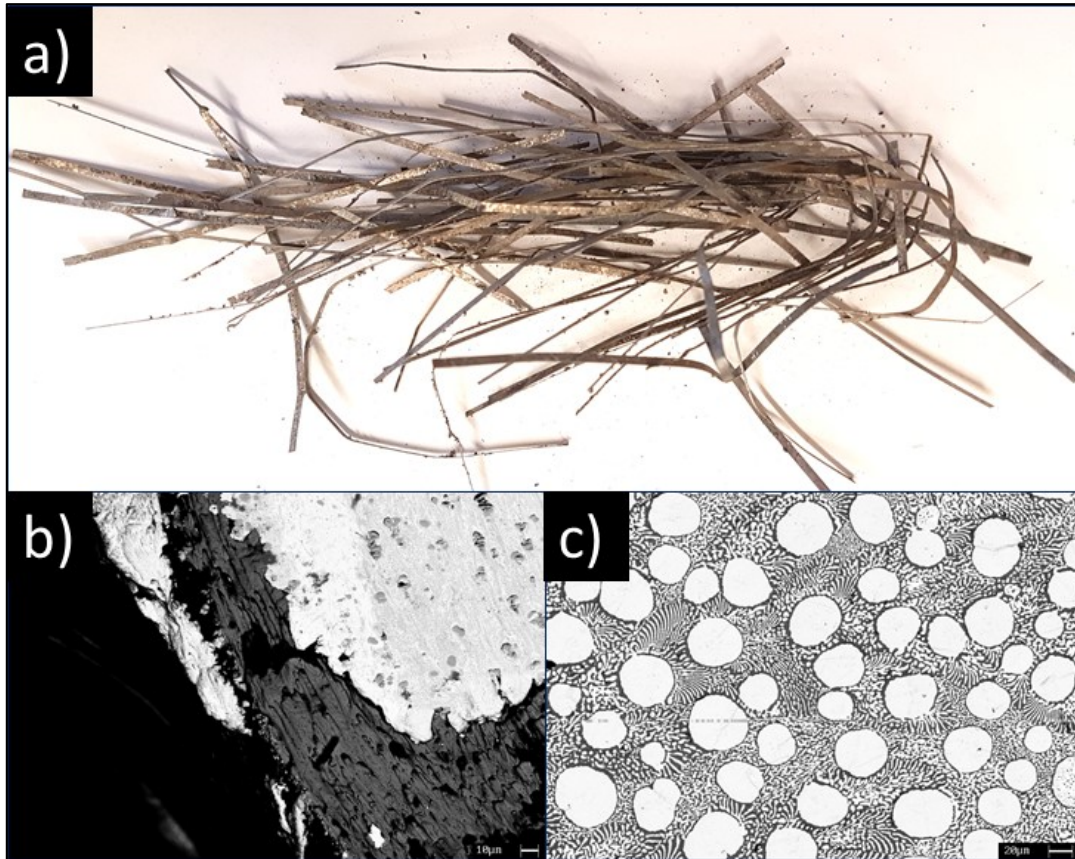


Fig. 4.19 a) the copper ribbons; b) SEM image of copper ribbons covered with Sn-Pb alloy (the white zone) and c) the microstructure of the Sn-Pb alloy.

In particular, from micrographic and chemical analysis, it was possible to establish that the contact is composed of a copper core and a lead-tin alloy coating. Copper is used for its excellent conductor qualities, due to its good workability and relatively low cost, while the lead-alloy alloy is used as copper protection. In addition, this alloy, thanks to its low melting temperature, enable welding between the various bandages making it the electrical interconnection.

4.4.3 Estimation of the amount of silver

The amount of silver present in the kind of cell characterized was estimated with simple geometric considerations. Three types of bands have been identified: big (Busbar), fine (Finger) and an outline. For each type of bandwidth, the area, height and volume were calculated separately. The three volumes were finally added together to get the total volume.

4.4.3.1 Busbars:

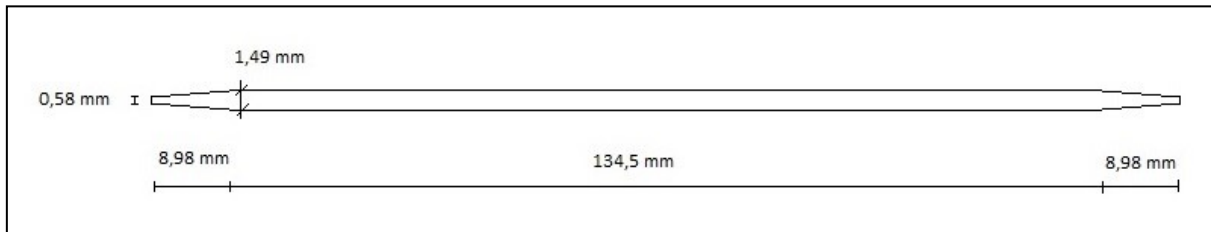


Fig. 4.20 Shape of the silver busbars.

In every cell there are three busbars, like the one in Fig. 4.20, the estimated area and volume is:

$$h = 0,01594mm$$

$$Area1 = 3 \times (134,5 \times 1,49 + 2 \times (1,49 + 0,58) \times \frac{8,98}{2}) = 3 \times 218,99mm = 656,98mm^2$$

$$Volume1 = 656,98 \times 0,01594 = 10,47mm^3$$

4.4.3.2 Fingers

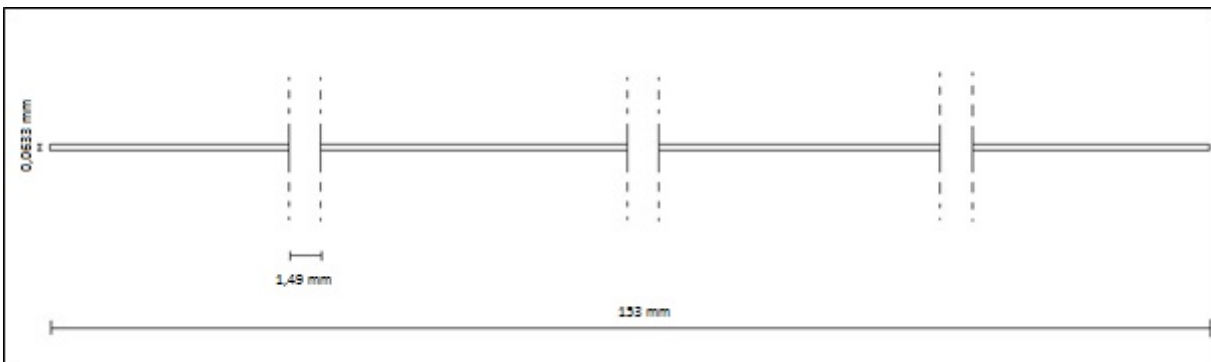


Fig. 4.21 Shape of the silver finger.

In every cell there are 83 fingers, the estimated area and volume are:

$$h = 0,01137mm$$

$$Area2 = 83 \times (0,0633 \times (153 - 3 \times 1,49)) = 780,20mm^2$$

$$Volume2 = 780,20 \times 0,01137 = 8,87mm^3$$

4.4.3.3 Outline:

Finally, there is an outline on the four sides:

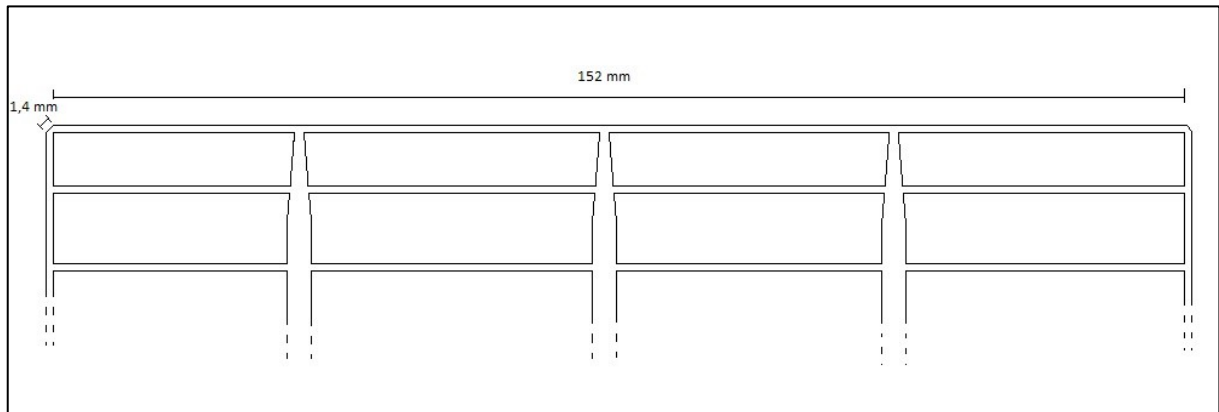


Fig. 4.22 Shape of the silver outline.

$$h = 0,01137\text{mm}$$

$$\text{Area}_3 \approx 4 \times (0,0633 \times (152 + 1,4)) = 38,84\text{mm}^2$$

$$\text{Volume}_3 = 38,84 \times 0,01137 = 0,44\text{mm}^3$$

4.4.3.4 Amount of silver

$$\text{Volume} = \text{Volume}_1 + \text{Volume}_2 + \text{Volume}_3 = 10,47 + 8,87 + 0,44 = 19,78\text{mm}^3$$

Throughout the image analysis, it was estimated that the silver paste have $\approx 16\%$ porosity.

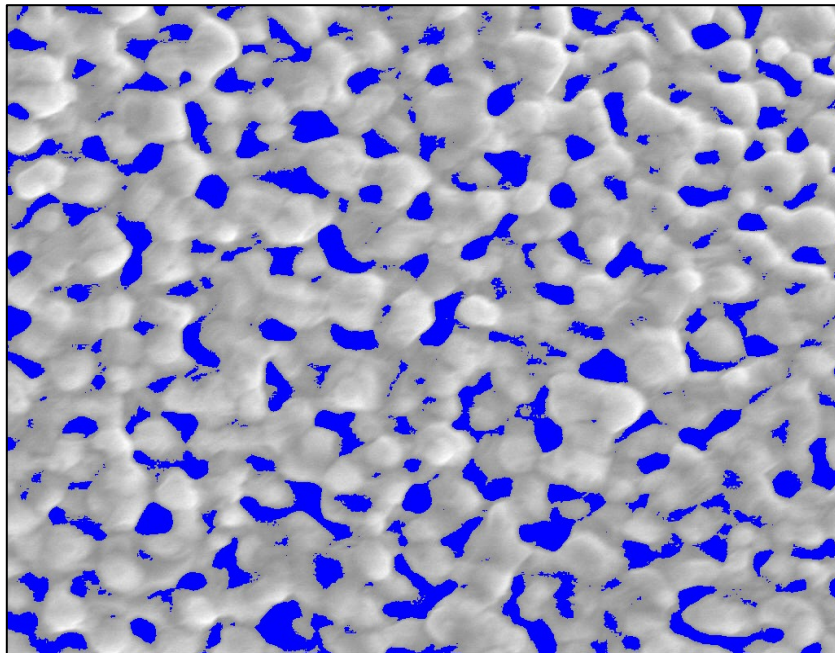


Fig. 4.23 Image analysis used to estimate the porosity of silver contacts.

The estimation of the real silver volume in a cell is therefore:

$$Volume = 19,78 \times 0,84 = 16,62mm^3$$

Considering a silver density of 10.49 mg/mm³, for each cell the estimated mass of silver is:

$$Mass = 16,62 \times 10,49 = 174,34mg$$

The weight of a cell is 11.98g, so silver would be 1.49% of total weight.

This percentage, which may seem low, is indeed high if compared to the typical silver content of the mineral from which it is extracted: 0.01%.

4.4.4 Estimation of the amount of aluminum

As has been done with silver, by geometric consideration the amount of aluminum was calculated. Aluminum in each cell is a layer with an area of 23714 mm² and a thickness of 0.033 mm. Considering a 22% porosity and a density of 2.7kg/dm³, a mass of 1.875g of aluminum was estimated for each cell.

4.4.5 Estimation of the amount of silicon

The silicon wafer has a square-like shape with length of each side of ~154mm (Fig. 4.22). Its thickness is 0.180 mm and density of silicon is 2.33kg/dm³. It is so estimated a 9.99g of silicon for each cell.

4.4.6 Estimation of the material in 60 cells PV module:

Previous calculation are useful in order of calculate the recovery yield of the hydrometallurgical tests. Moreover, two 60 cell modules were dismantled in order of estimating the amount of the different materials constituting the PV panels. This estimation was useful to calculate the recovery yield of the studied process.

In particular, there were analyzed two standard 60 cells PV modules as this kind of panel is the most common format for domestic application.

The supplier of the module was *IEIS srl*, a company that work in the electric installations sector. Moreover, one module (named A), produced by *Scenerg industry*, had unbroken glass whereas the other module (named B), produced by *Azimut srl*, had broken glass.

In addition, the modules A and B had also two different glass thickness respectively of 3,123mm and 3,823mm. The composition is reported in Tab. 4.6 and it is in accordance with data available in literature, reported in Tab. 4.7 [92]. After characterization, the panels were heat treated, as described in 4.5.4.

Weights [kg]	Module A	Module B	Average A e B	%Wt
Glass*	12,86	15,74	14,3	70
Aluminum frame	2,80	2,20	2,5	12
Plastic****	2	3,04	2.52	12
Cells**	0,72	0,72	0,72	4
Power optimizer	0,20	0,21	0,2	1
Contacts***	0,20	0,20	0,20	1
Total	18,70	22,00	20,35	100

Tab. 4.6 Measured and estimated weight of the composition of the firsts 60 cells modules used for the tests.

* The amounts of glass were estimated from the Area (1660x992mm²), the thicknesses (3,123mm and 3,823mm) and glass density ($\approx 2,5\text{g/cm}^3$).

** The mass of the cells was obtained multiplying for 60 the weight of one cell.

*** The mass of the contacts was estimated multiplying for 180 the weight of one contact after the treatment (0,92g) and considering a part of tin lost (0,03g) during the treatment.

**** The amount of plastic was estimated by difference.

Component	%Wt
Glass, containing antimony (0.01–1%/kg of glass)	70
Aluminum frame	18
Polymer-based adhesive (EVA) encapsulation layer	5.1
Back-sheet layer (based on Polyvinyl Fluoride)	1.5
Solar cell, containing silicon metal	3.65
Cables (containing copper and polymers)	1
Internal conductor, aluminum	0.53
Internal conductor, copper	0.11
Silver	0.053
Other metals (tin, lead)	0.053
Total	100

Tab. 4.7 Mass composition of 1000 kg of PV panel waste.

4.5 Material separation

The first step to resource recovery from photovoltaic panels is the separation process [93]. The delamination is one of the most difficult part as the material in the panels are intimately jointed together, as described in 4.2.9.

Among the different methods, the idea of only mechanical separation, such as grinding and sieving, was not studied because of the low efficiency in the material separation and the excessive decrease in the size of the silicon cells pieces, which would have led to losses of material during the successive parts of the recovery process.

4.5.1 Chemical Method

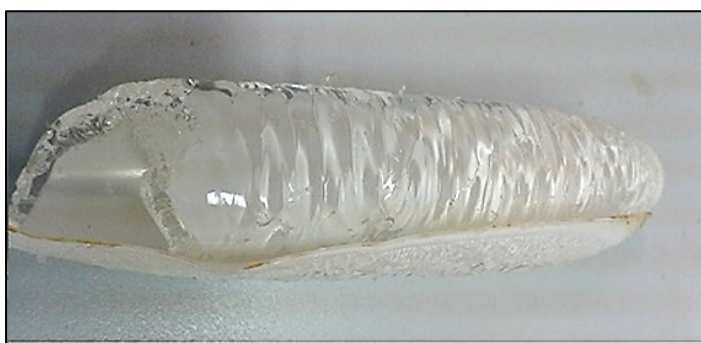


Fig. 4.24 Image of Eva and Tedlar after tetrachloroethylene treatment

At first, the use of solvents that could degrade or dissolve the EVA was studied. A first issue of this method, however, it is the long time required to the solvent to reach the EVA material, as the encapsulant is between glass and Tedlar, almost impermeable to the solvent. To overcome this disadvantage, it is possible to break the

tempered glass, so that the solvent can pass through the glass cracks.

Initially, the efficacy of the nitro diluent was verified: a cell portion was then immersed into the liquid. However, the treatment did not affect the adhesion between the components even if it was partially absorbed by EVA.

Better results were obtained using tetrachloroethylene. A PE container was used for the test, in which a portion of laminate with the broken front glass was immersed. In this case, an accentuated swelling of the EVA layer and the detachment of glass portions occurred after about 24 hours. However, it was not possible to completely remove the adhesive from the silicon surface, as it was not possible to obtain complete EVA dissolution.

The ethylene vinyl acetate residues on the surface of the cells prevent the application of hydrometallurgical techniques, since the glue would act as a barrier against the solutions.

Finally, considering that the use of solvents involves environmental problems because of the toxicity of the solutions used and the difficulties concerning the disposal, the chemical method for material separations seemed not very convenient.

4.5.2 Thermal Method

EVA is a thermoplastic elastomer material whose mechanical properties strongly depend on the temperature. In particular, the behavior changes from rubbery to viscous when heated above 60°C [94]. The EVA softening seems a possibility to separate the material [95].

To verify this option 1 cm² of PV panel was heated for 1 h at different temperature (100°C, 150°C, and 200°C). It was possible to separate Tedlar from glass only at 200°C but the glass pieces removal was not simple and the cells remained inside the resin.

As a consequence, the complete thermal degradation of the polymeric part was tested.

For the study of optimum treatment temperatures, from literature [96] it is known that when EVA is heated and undergoes thermal degradation, the first product evolved is acetic acid (HAc). This deacetylation reaction starts at about 290°C, the maximum reaction rate being observed 30°C higher. This result is probably because every short sequence of vinyl acetate (VA) in the copolymer re-quires its own initiation step [97]. The mechanism of formation of HAc is based on ester pyrolysis, which takes place through a cross-linking mechanism [98] as showed in Fig. 4.25.

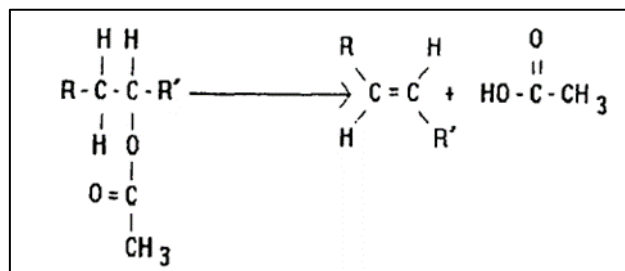


Fig. 4.25 Scheme of the deacetylation of EVA

Moreover, EVA undergoes a two-stage decomposition, the first stage is HAc evolution, i.e. the loss in mass is proportional to the amount of acetate groups initially present in the system. The second decomposition stage is due to chain scission.

As can be seen in Fig. 4.26, the thermal degradation is complete at about 500°C.

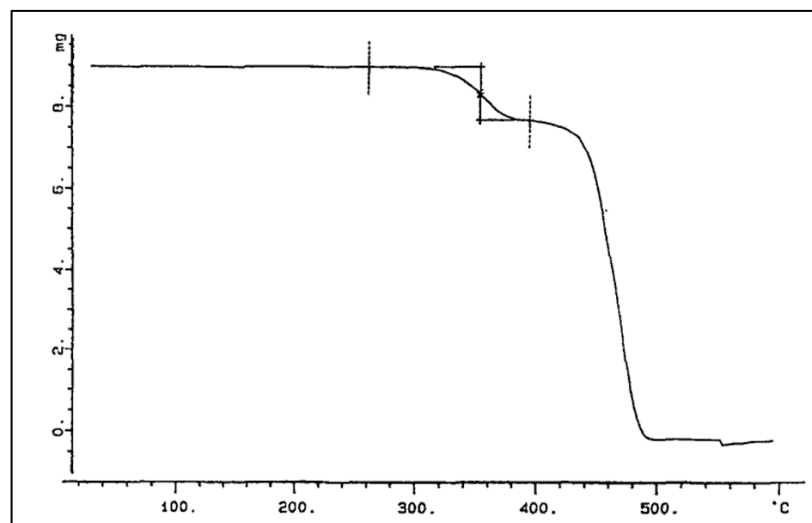


Fig. 4.26 TG curve for an EVA sample heated in N₂ atmosphere.

Different tests were performed treating $5 \times 3 \text{ cm}^2$ samples for 1 h at 300°C , 400°C and 500°C . The results are shown in Fig. 4.27, where it can be observed the complete separation of the glass from the other components of the panels.

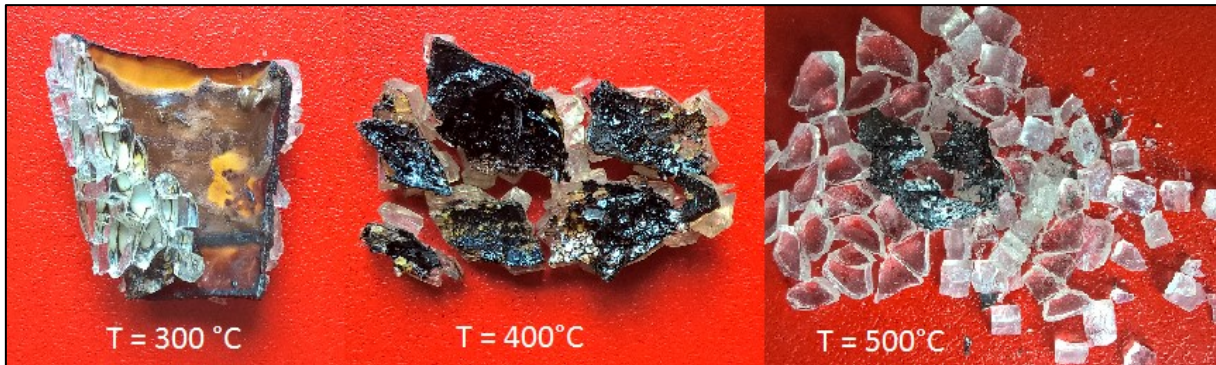


Fig. 4.27 The samples of PV module treated at different temperatures.

Some black residues are still on the samples as the combustion occurred in a closed container, therefore in the defect of oxygen.

Moreover, some additives were tested in this condition at 500°C . In particular $\text{Ca}(\text{OH})_2$ resulted useful in order to help the complete combustion and, probably, to react with the hydrofluoric acid produced by Tedlar degradation [99, 100]. The results are reported in Fig. 4.28.

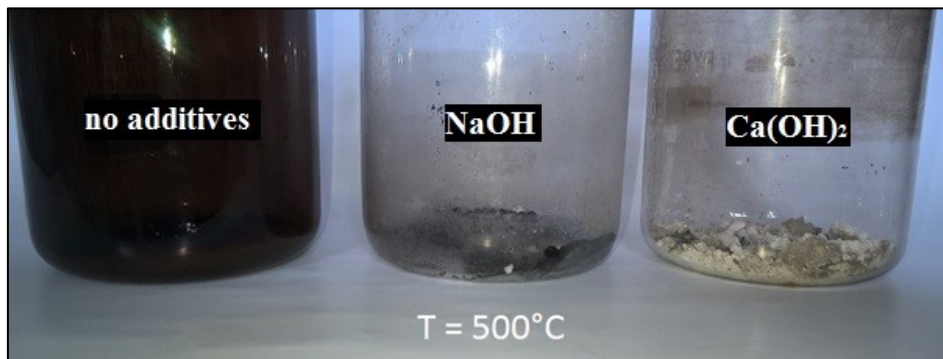


Fig. 4.28 The samples of PV module treated with different additives.

4.5.3 Off-gases analysis

Besides the tests on combustion of polymeric parts in PV panels, an analysis on the composition of the off gases was performed [101, 102]. In particular, it was interesting to verify the presence in these gases of the hydrofluoric acid that is released by Tedlar during the treatment.

4.5.3.1 Methods

About 20 mg of sample (EVA+Tedlar) was placed in platinum crucible and loaded into Pyris 1 (Perkin Elmer) thermobalance. The sample was heated from 30°C to 700°C at a rate of 20 °C/min in an oxidizing atmosphere (O₂/N₂ about 1:3). The recorded thermogram represents the percentage change in temperature. The derivative of the thermogram (D-TG) is also reported. Peaks on the D-TG curve are in correspondence with the temperature at which a weight change reaches its maximum speed. With this representation, it is therefore easier to identify individual processes than the analysis of the thermogram only.

The qualitative analysis of the gases developed by the sample during heating was conducted by FTIR spectrophotometry. The gases developed during heating were sent via a 280 °C thermostated transfer line (T-Logy, RedShift) to the spectrophotometer FTIR Spectrum 100 (Perkin Elmer). The spectra were recorded between 4000 and 600 cm⁻¹. Spectrum analysis software (Perkin Elmer) was used for spectral analysis. For each identified substance, the variation in the height of a characteristic peak expressed as a function of temperature allowed to obtain the profiles of the individual gaseous substances (FTIR thermograms) produced during the TGA stroke.

4.5.3.2 Results

The weight of the sample remains stable up to approx. 280 °C. Between 280°C and 600°C, different thermal processes were observed and are responsible for a total weight loss of about 97%.

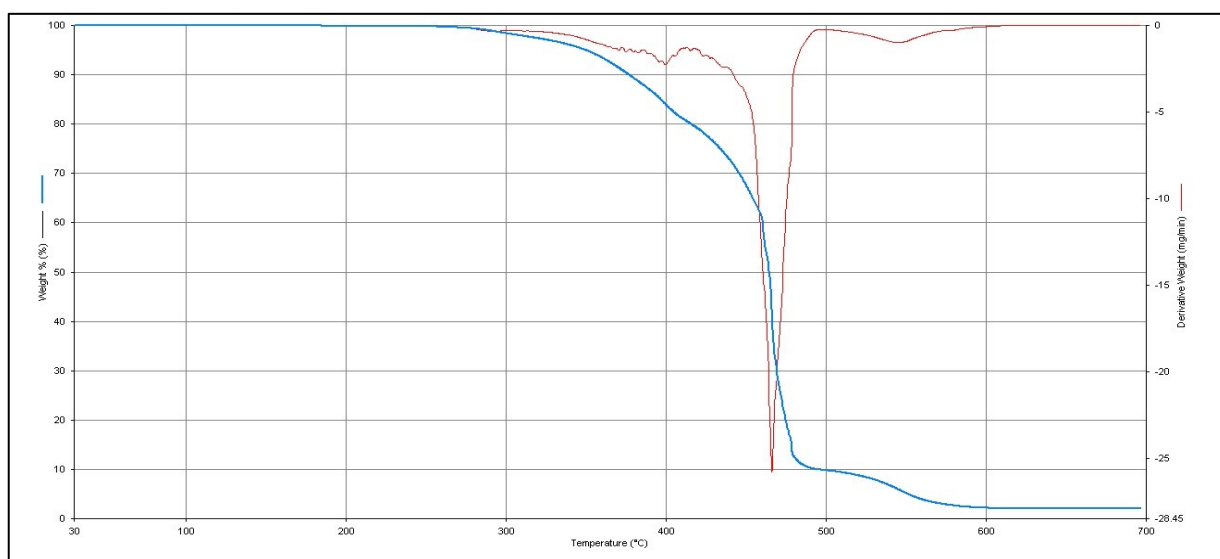


Fig. 4.29 TGA (blue curve) and D-TG (red curve) recorded in the temperature range of 30-700 °C at 20°Cmin⁻¹ in oxidizing atmosphere.

- 280-415 °C: In this range of temperatures, the sample undergoes a weight loss of approx. 10%. This is due to two overlapping thermal processes as evidenced by the D-TG curve.
- 416-500 °C: a very important thermal process takes place which leads to a 79% weight loss. This process is due to the degradation /oxidation of the polymer. In the initial stages, this process is partially overlapped by the previous one.
- 501-600 °C: another process occurs which results in a weight loss of approx. 8%.

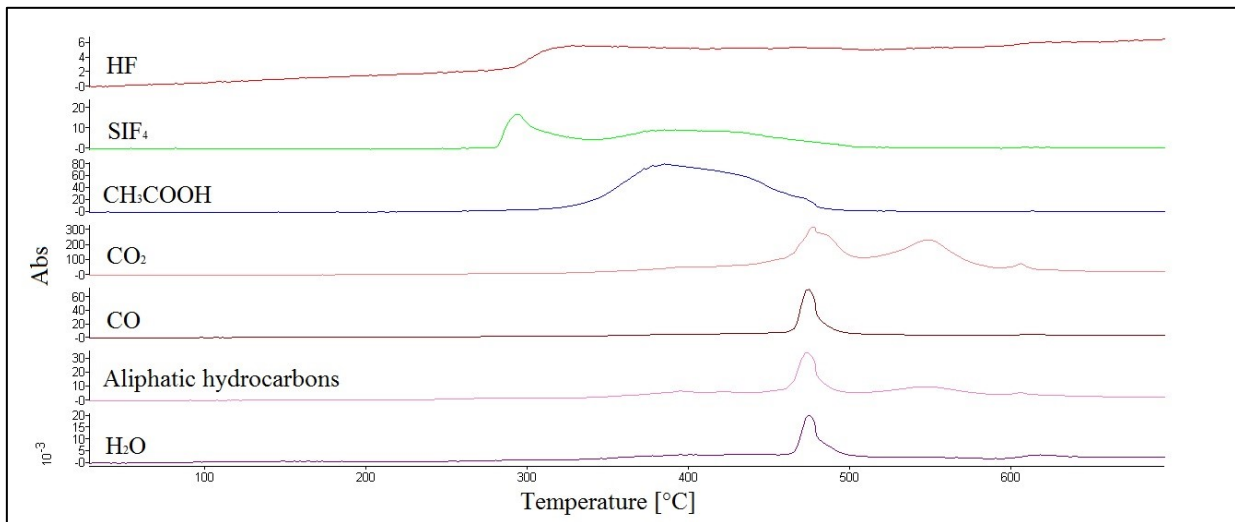


Fig. 4.30 FTIR thermogram of the gas released by the sample during heating in oxidant atmosphere.

Analysis of the gas released during heating allowed the identification of different species (Fig. 4.30). The FTIR analysis showed the release of acetic acid, hydrocarbons, CO₂, CO and H₂O. Moreover, the comparison with the spectra contained in the database has allowed to uniquely identify HF and with a high probability SiF₄ (Figure 4.31). SiF₄ is a volatile species that is formed by reaction of HF with SiO₂ (which probably derives from the quartz tube surrounding the furnace).

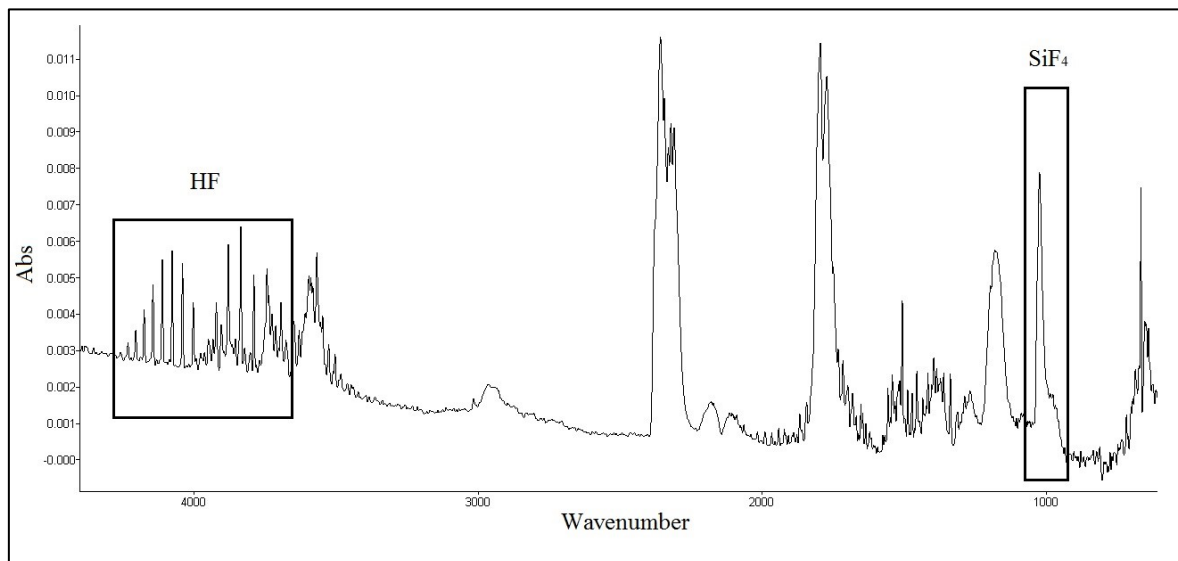


Fig. 4.31 Absorption spectrum of the gas released at 415°C with evidenced the peaks of HF and SiF₄.

After the identification of the compounds in the gases, the amount of the released species was estimated. In order to achieve this, it was convenient to separate the analysis of the two polymers (EVA and Tedlar).

From the results it appeared that Tedlar release HF between 280°C and 350°C that represent about 21% w/w of the sample weight whereas EVA releases acetic acid between 240°C and 400°C that represent about 22% w/w of the sample weight.

4.5.4 Test at TRL 5

After the study of the separation technique, some test were performed directly on 60-cell PV modules. In particular, different EOL PV panels were treated (some with broken glass and some or with unbroken glass before the treatment) in a 30m³ furnace.

The samples were introduced into the furnace at 520°C and different treatment times were tested (10, 15, 20, 30 and 60 min). It results that the polymeric combustion is completed in about 15 min. Moreover, it was found that, after the treatment, the quality of the obtained material strongly depends on the glass condition before the treatment.

In fact, the glass introduced into the furnace unbroken relaxed the internal stresses before breaking, and it was recovered in large pieces, up to 1m long, whereas the glass already broken was recovered in small pieces (average dimensions of 1 cm) typical of tempered glass break.

The different glasses behavior affected also the cells: in the first cases, almost all of them were unbroken whereas in the second ones the cells are recovered in small pieces (also smaller than 1cm). The small cell sizes can be explained by the polymer's tendency to contract (at ambient temperature) which forces the panel to flex, as it is not compensated by the glass because it is broken.

The comparison between the treated panels can be seen in Fig. 4.32.



Fig. 4.32 Two PV panels after the heating treatment: a, b) panel that have unbroken glass before the treatment; c, d,) panel which have the glass already broken before the treatment.

After the heating treatment, cells, ribbons and glass were separated.

In particular, while the unbroken cells were easily separated manually, for the broken cells two different techniques were tested.

In fact, it was verified that, although the glass was broken, if the panels was treated on a flat tray with the glass well resting on the surface, the cell pieces can be blown away with an air blade (Fig. 4.33).



Fig. 4.33 *Separation of cell pieces from the glass by air blowing.*

4.6 Hydrometallurgical treatments

After the cells recovery from the PV panels, different hydrometallurgical treatments were performed in order to recover silver and silicon from the cells. As anticipated, at the beginning the tests were performed on new cells and, after the treatment optimization, there were used the cells recovered from EOL PV panels.

4.6.2 Sodium hydroxide treatment

To remove aluminum, the cell was immersed 4h in a 40ml of 0,3M sodium hydroxide solution. After the treatment the aluminum backsheet was partially dissolved and partially detached from the cell as visible in Fig. 4.34 and known in literature [103].

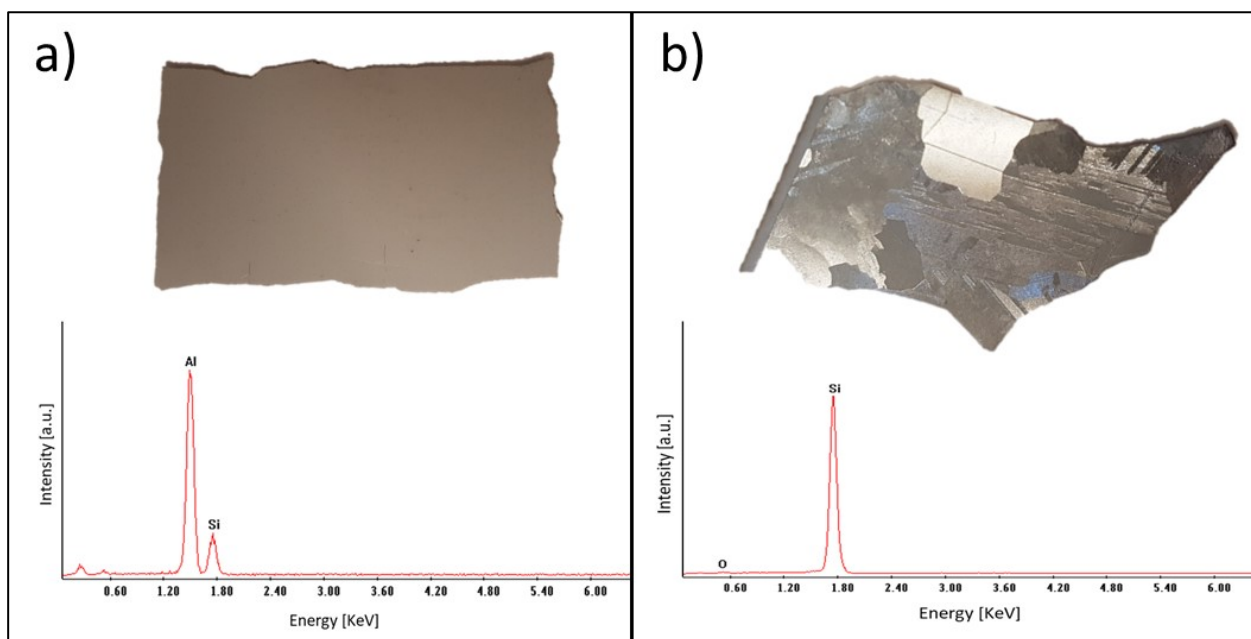


Fig. 4.34 Image of the silicon cell back-face and EDS spectrum before (a) and after (b) the treatment with sodium hydroxide solution.

ICP analysis of the solution (Tab.4.8) evidenced that the sodium hydroxide did not react with silicon and that only a small amount of silver was etched.

Ag	Si	Al
1.879	<6.055	303.2

Tab. 4.8 ICP analysis of the sodium hydroxide solution [ppm]

Different concentration (0,13 M; 0,31 M; 0,62M) and temperature (25°C; 40°C; 60°C) of the sodium hydroxide solution were tested and the effect of these parameters on aluminum dissolution was studied. The results are reported in Fig. 4.35.

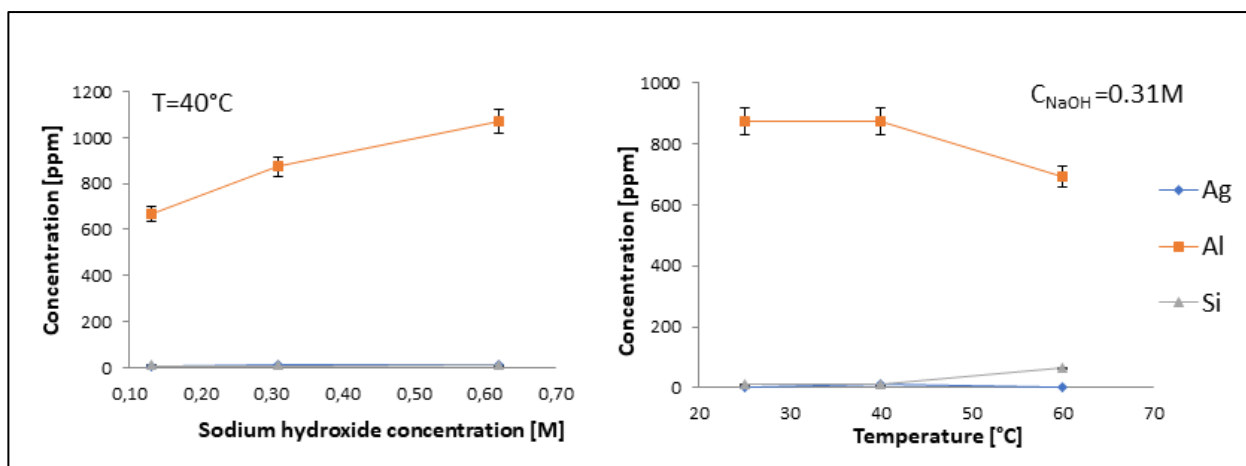


Fig. 4.35 ICP analysis of the sodium hydroxide solution with the effect of concentration and temperature.

From the testes it appeared that sodium hydroxide concentration strongly increase aluminum dissolution whereas temperature has not a great influence on the yield of the process.

After verifying the efficacy of hydrometallurgical treatment, the reagents consumption was evaluated.

To achieve this, 300ml of 0,6M sodium hydroxide solution at 40°C were used and different cells were successively treated into this solution.

From the first and second cells the detachment of the aluminum backsheet took place within 15 min, 30 min were required for the third cells and the fourth cell was not effectively treated.

After filtering the solid residue and adding new sodium hydroxide to the solution, the test was repeated but the solution seemed less efficacious and only 2,5 cells were effectively treated.

The lower yield in aluminum etching of the second treatment can be caused by the sodium alluminante in the solution, which is not present at the beginning of the first treatment and which prevent the completion of the reaction, that is:



As a consequence, it seems crucial to remove sodium alluminante from the solution in order to reuse it. Otherwise, instead of adding sodium hydroxide to it, it seems conveneint to use new solution.

In this case it can be estimated that for treating one PV panel (60 cells) there will be required 6L of solution 0,6M sodium hydroxide.

4.6.1 Nitric acid treatment

Nitric acid is able to leach silver through the reaction (Eq. 4.9)



First, to verify the efficacy of the treatment, a cell sample (0,42g) was immersed 1h in 40ml of 7,3 M nitric acid solution.

After the treatment XRF analysis was performed on the cell surface (Tab. 4.9).

Front-side			Back-side		
Element	% before treatment	% after treatment	Element	% before treatment	% after treatment
Si	97,73	97,83	Al	70,24	60,56
Al	1,586	1,608	Si	28,11	38,24
Mg	0,544	0,498	Mg	1,275	1,065
Ag	0,06152	0,00184	Pb	0,1567	0,02227
Pb	0,03452	0,00511	Ag	0,04395	0,00229

Tab. 4.9 XRF analysis on the cell surfaces before and after the nitric acid treatment.

As can be seen in Tab. 4.9, the silver was completely removed from the cell surfaces. This fact can be seen by observation with optical microscope of the cell surface before and after the treatment (Fig. 4.36).

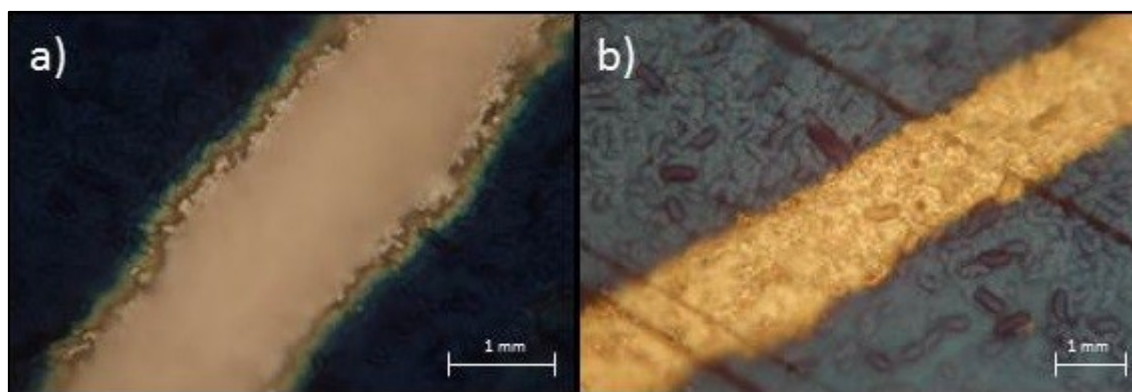


Fig. 4.36 Comparison at the optical microscope between the silver contacts of the photovoltaic cell before and after the treatment with nitric acid.

Moreover, ICP analysis of the solution was performed (Tab.4.10) revealing that aluminum and silicon are not strongly affected by the acid treatment.

Ag	Si	Al
675.8	2.122	31.4

Tab. 4.10 ICP analysis [ppm] of the nitric acid solution used to treat the silicon cells.

Different concentration (1,4M; 3,6M; 7,3M) and temperature (25°C; 40°C; 60°C) of the nitric acid solution were tested and the effect of these parameters on silver dissolution was studied.

The results are reported in Fig. 4.37.

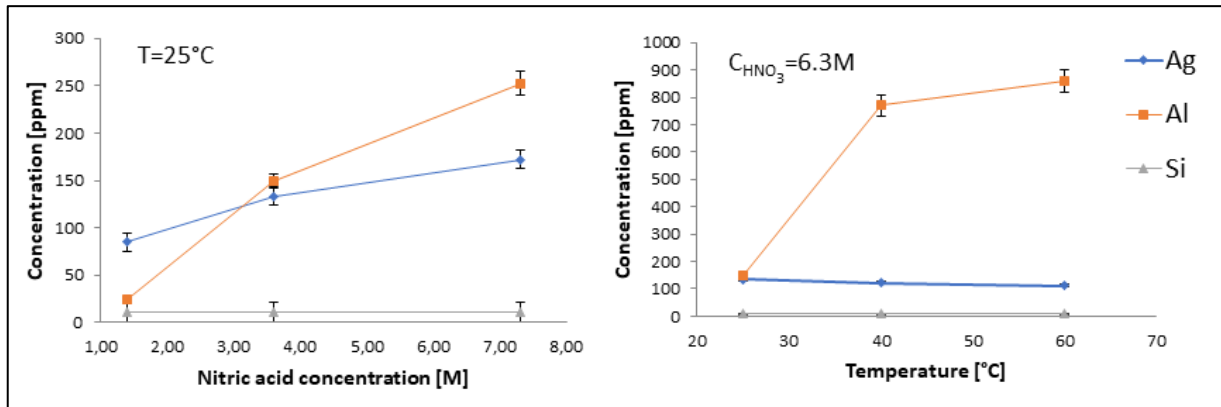


Fig. 4.37 ICP analysis of the nitric acid solution with the effect of concentration and temperature.

It can be observed that the nitric acid concentration increase the yield in the silver etching whereas the nitric acid temperature enhanced the dissolution of aluminum.

Moreover, it was observed that solution with high concentration of silver, together with the increase of temperature, can eventually produce the rapid dissolution of the aluminum: to prevent this, the treatment to remove aluminum can be previously performed.

After verifying the efficacy of hydrometallurgical treatment, the reagents consumption was evaluated.

In particular, 200 ml of 5 M HNO₃ solution were used and different cells, previously treated with sodium hydroxide solution (without aluminum backsheet), were successively treated in the solution.

Silver was effectively removed from fifteen cells within 2 min and the ICP analysis of the solution after each cell treated is reported in Fig. 4.38.

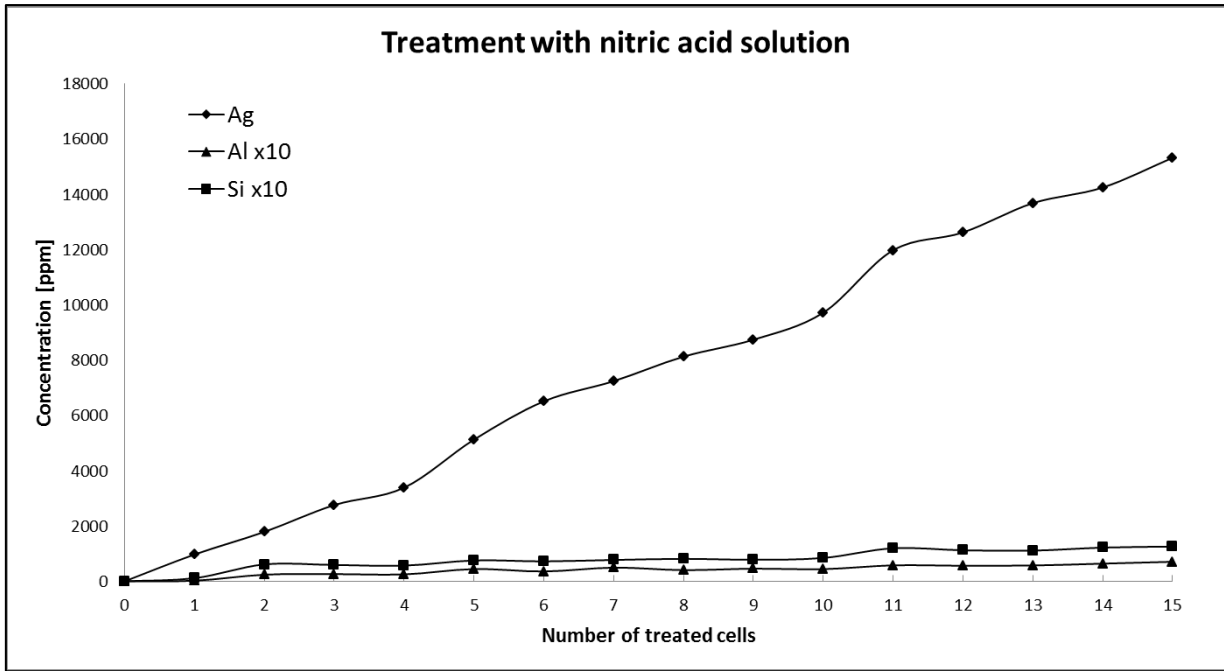


Fig. 4.38 ICP analysis of the nitric acid solution after the treatment of different cells.

As seems difficult to exhaust the solution through this method, this study was completed using pure silver. In particular, 10ml of the used solution were considered and it was possible to catch 3.98g of pure silver into this 10ml of solution. Considering that about 0.174g of Ag was estimated in each cell, it can be said that 3.98g corresponds to the amount of silver contained in $3.98g / 0.174g = 22.7$ cells.

From these considerations, it can be estimated that in order to treat one PV panel (60 cells) there will be required an amount of about 14 ml 5,1M nitric acid.

4.6.3 Test at TRL 5

After the optimization of the hydrometallurgical treatment parameters with PV cells coming directly from the production, there were performed some tests treating the cells coming from heating treatment described in 4.5.4.

Moreover, the tests were conducted with greater amount of material (Fig. 4.39).



Fig. 4.39 *The PV cells after the treatment with sodium hydroxide.*

In particular, four sodium hydroxide concentrations, different from the ones tested in 4.6.2, were studied at 40°C: 0,625M; 1,25M; 1,875M and 2,5M.

Best results were obtained using 1,875M solution and in this case, the detachment of aluminum from the cells was completed in about 40min.

Moreover, from these tests, it seems that are required 25L of solution (1,875M) for every kg of cells to treat.

4.7 Silver and Silicon recovery

4.7.1 Silver recovery

In this chapter the results of various methods of recovering metallic silver from the nitric acid solution will be described. Electrochemical and chemical techniques such as electrodeposition or Tollens reaction have been tested as well as heat-assisted techniques such as thermal reduction of silver oxide or chloride in the presence of reducing agents

4.7.1.2 Electrodeposition

In order of electrodeposit silver from the nitric acid solution a cyclic voltammetry was performed and compared with a cyclic voltammetry of nitric acid solution without silver (Fig. 4.40)

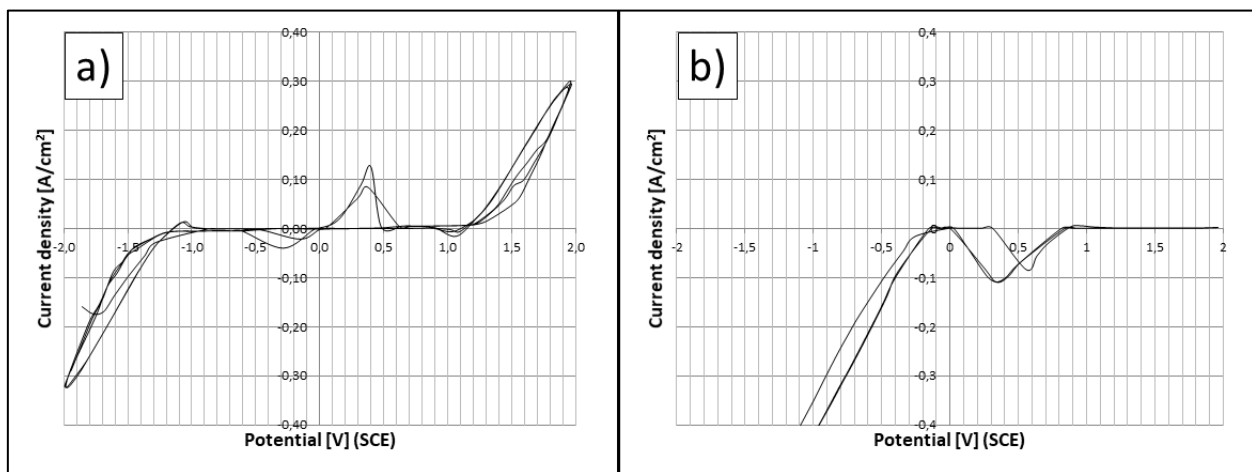


Fig. 4.40 Cyclic voltammetry on a) nitric acid solution with silver and b) nitric acid solution without silver.

Moreover, different depositions were tested on the solution using both as working electrode (WE) and counter electrode (CE) platinum wires.

At potential of -1,5 V it was possible to reduce silver on the electrode. However, silver recovery with this technique was very difficult because of the strong acidity of the solution (5,1M nitric acid). In fact, the deposit is rapidly etched by acid and it appeared non-homogenous and highly porous (Fig. 4.41).

In fact, a more adherent deposit was obtained only reducing the acidity of the solution at pH 4 (Fig. 4.42).



Fig. 4.41 SEM image of the deposit obtained by electrodeposition by a high acidity solution. It is interesting the particular hexagonal shape of silver crystals.

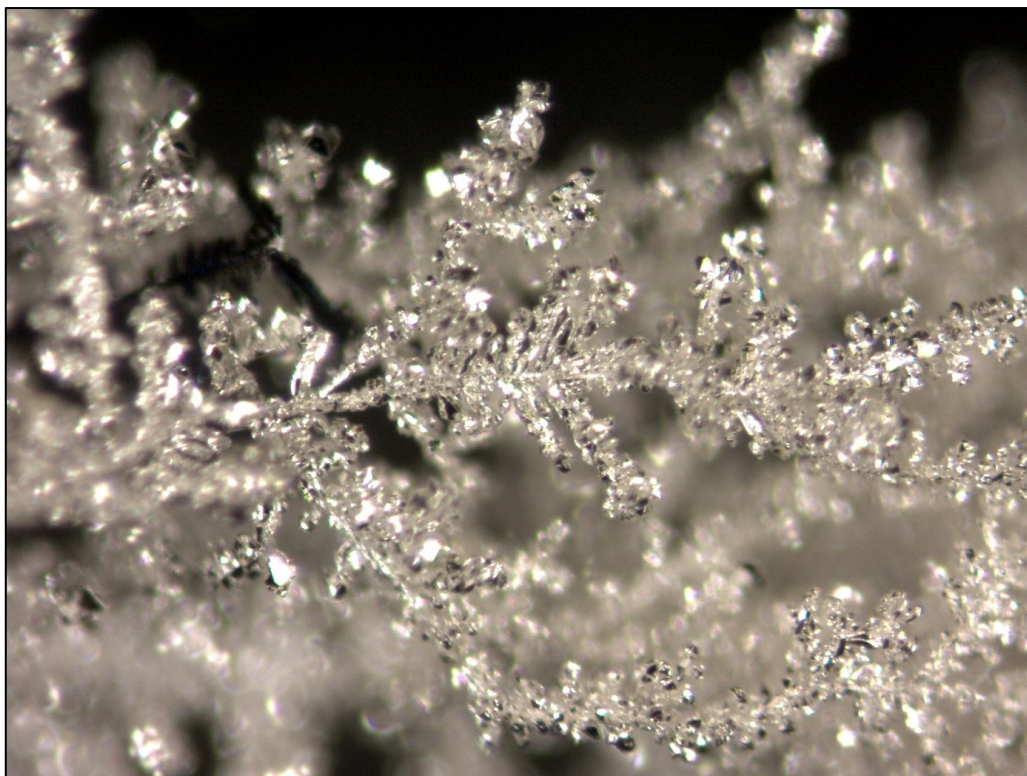


Fig. 4.42 Silver crystals obtained by electrodeposition from a nitric acid solution with pH 4.

4.7.1.2 Silver oxide precipitation

A possible way to recover silver from acid solution is converting silver nitrate into silver oxide Ag_2O and then obtain metallic silver by thermal reduction [104, 105].

A disadvantage of this method is the possible precipitation from the solution of other metallic oxides with silver oxide, but, as advantage, it can be seen from the Ellingham diagram (Fig. 4.43) that silver oxide spontaneously reduced to metallic silver at low temperature, higher than 468K. In fact, we can consider the reaction between silver and oxygen:

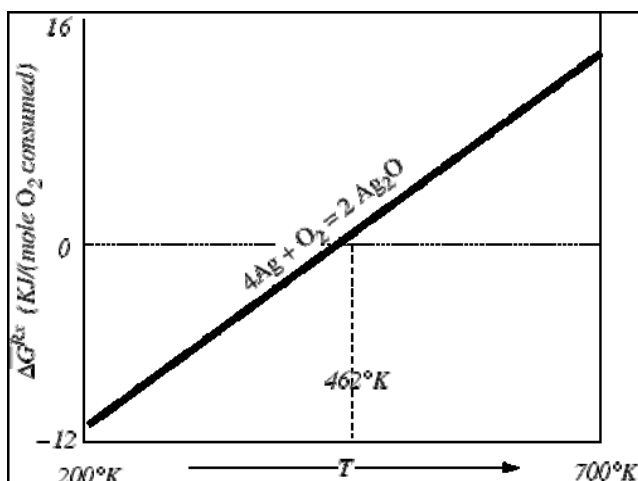


Fig. 4.43 Ellingham diagram with the reaction of silver and oxygen.

Compound	ΔH_f° (kJ/mol)	ΔG_f° (kJ/mol)	S° (J/mol·K)
Ag (s)	0	0	42.6
O ₂ (g)	0	0	205.2
Ag ₂ O (s)	-31.1	-11.2	121.3

Tab. 4.11 Standard enthalpy of formation, standard Gibbs free energy of formation and standard entropy of silver, oxygen and silver oxide.

From data in Tab. 4.11 [106], it is possible to calculate the standard state enthalpy (ΔH_{rxn}^0) and entropy (ΔS_{rxn}^0) changes for the reaction, which are -62.2 kJ and -0.133 kJ/K respectively. These values tell us that the reaction is exothermic and that the entropy of the reaction is negative. The decrease in entropy is to be expected when there are fewer moles of gaseous products than there were moles of gaseous reactants. The entropy and enthalpy terms are in opposition. The enthalpy term favors the reaction being spontaneous, but the entropy term favors the reaction being non-spontaneous. When the terms conflict in such a manner, the temperature at which the reaction occurs will determine the spontaneity. Eq. 4.11 will allow the standard Gibbs free energy (ΔG_{rxn}^0) of the reaction to be calculated.

$$\Delta G_{\text{rxn}}^0 = \Delta H_{\text{rxn}}^0 - T \Delta S_{\text{rxn}}^0 \quad (4.11)$$

Substituting the previously calculated values for the standard state enthalpy and entropy changes and the standard state temperature of 298 K into the previous equation yields:

$$\Delta G_{\text{rxn}}^0 = -62.2 \text{ kJ} - (298 \text{ K}) (-0.133 \text{ kJ/K})$$

$$\Delta G_{\text{rxn}}^0 = -22.6 \text{ kJ}$$

Since $\Delta G_{\text{rxn}}^0 < 0$, the reaction is spontaneous at room temperature. By rearranging Eq. 4.11 it is possible to determine at what temperature the reaction would be at equilibrium ($\Delta G_{\text{rxn}}^0 = 0$), even if it is not entirely accurate to use standard state thermodynamic quantities away from $T = 298 \text{ K}$, since they do have a temperature dependence to them.

$$T = \Delta H_{\text{rxn}}^0 / \Delta S_{\text{rxn}}^0$$

$$T = (-62.2 \text{ kJ}) / (-0.133 \text{ kJ/K})$$

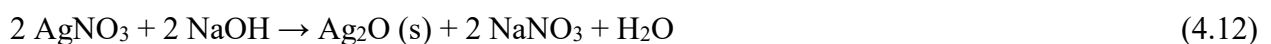
$$T = 468 \text{ K}$$

This is in accordance with Ellingham diagram (Fig. 4.43). For $T < 468 \text{ K}$ the reaction is spontaneous, for $T = 468 \text{ K}$ the reaction is at equilibrium and for $T > 468 \text{ K}$ the reaction would be non-spontaneous. Therefore, in order to reduce silver oxide, it is necessary to raise the temperature to above 468 K .

However, it is necessary to add to this value the activation energy for the reaction, which is 283.4 kJ/mol and so, as confirmed by experimental data available in literature, the reduction occurs between 623 and 673 K [105].

For the experiment there was used the 5.1 M nitric acid solution which was previously used to treat the panels, so it contains silver.

The solution was then basified by addition of a concentrated NaOH solution to obtain silver oxide according to the reaction:



After the reaction was completed the color change from transparent to black. The silver oxide was then recovered from the solution by centrifugation, washed with distilled water, dried and placed in a graphite crucible. The crucible was then treated in an oven at a temperature of $1150 \text{ }^\circ\text{C}$ for 1 h in an inert atmosphere of Argon. The obtained samples (Fig. 4.44) was observed at SEM, which confirmed that it was metallic silver.

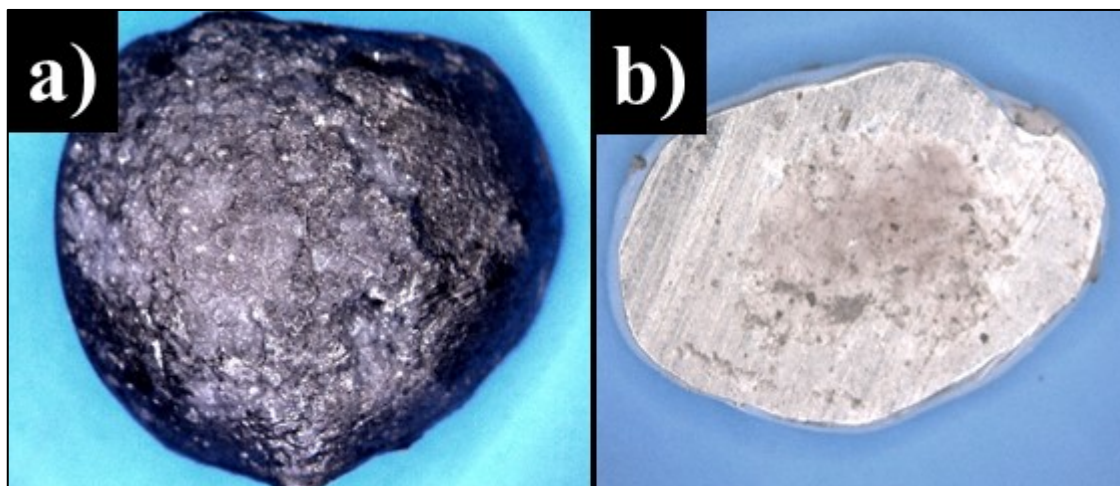


Fig. 4.44 a) The silver obtained from the silver oxide thermal reduction in argon at $1150 \text{ }^\circ\text{C}$ and b) section of the same.

4.7.1.2 Silver chloride precipitation

Silver chloride has a very low solubility in aqueous solutions and this can be used to recover silver from the nitric acid solution utilized to treat photovoltaic cells.

In fact, if NaCl is added to AgNO₃-containing solution, this produces the silver chloride precipitation, according to the reaction:



The silver chloride solubility product constant ($K_{sp} = 1.82 \cdot 10^{-10}$ at 25 ° C) is very low in aqueous solution:

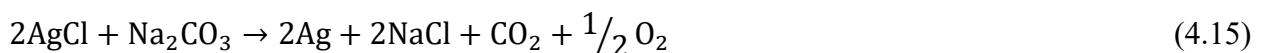


As a consequence, after NaCl addition to the 5.1M solution previously used to treat the cells, almost all the silver precipitated in AgCl form. Silver chloride is a salt characterized by a white color and gives the solution a milky appearance. After precipitation, AgCl was centrifuged and washed with distilled water.

Both one pyrometallurgical and one hydrometallurgical methods were tested to reduce silver chloride.

- Reduction of AgCl by pyrometallurgical method

From literature, it is possible to reduce AgCl by heating in presence of sodium carbonate, according to the reaction:



In order of verify the efficiency of this method to the recovered silver chloride, 1g of AgCl was placed in an alumina crucible with 1g of sodium carbonate and kept at 1150 ° C for one hour in Argon atmosphere. Thus, small metal spheres of variable diameter of about 1÷3 mm were obtained in a water-soluble salt (Fig. 4.45).

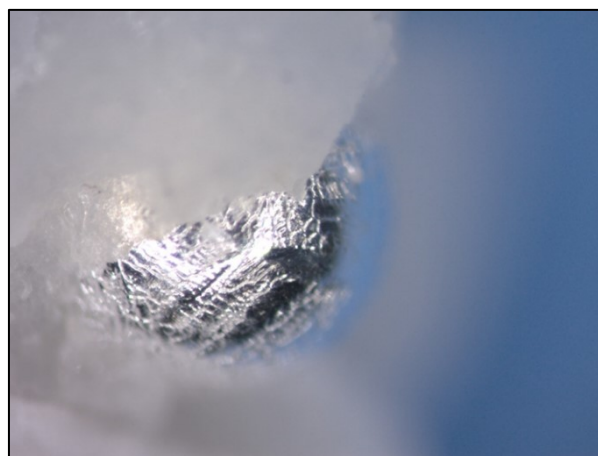


Fig. 4.45 The silver obtained from the silver chloride thermal reduction with sodium carbonate in argon at 1150 ° C.

However the reaction is completed also at lower temperature. In fact, the same test was repeated treating silver chloride with sodium carbonate at 650°C for one hour in air and it was obtained metallic silver with a sponge appearance (Fig. 4.46).

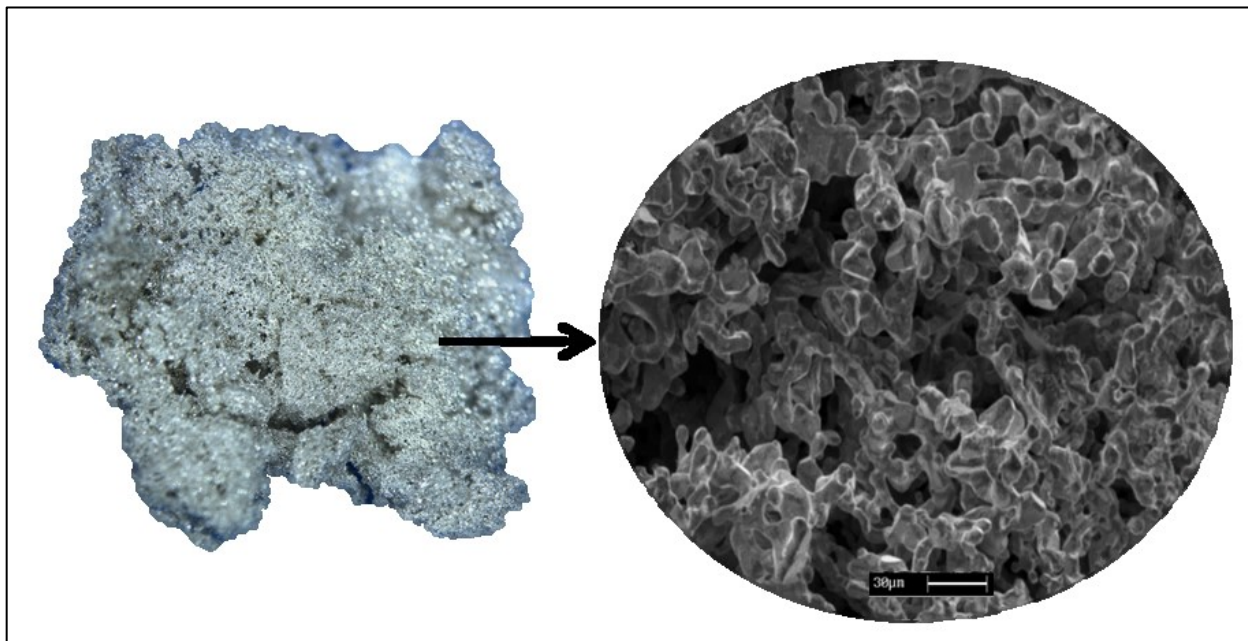


Fig. 4.46 *The silver obtained from the silver chloride thermal reduction with sodium carbonate in air at 650 ° C.*

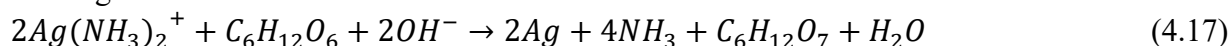
- Reduction of AgCl by hydrometallurgical method

Silver chloride reduction is possible also using hydrometallurgical method.

In order of dissolve silver chloride, it was first dissolved in ammonia, as diamminsilver (I) ion:



After silver chloride dissolution, silver can be reduced reacting with glucose aldehyde group, according with Tollens reaction:



This reaction, in fact, will be used also for silver nanoparticles synthesis in Chapter 6.5.

To verify the method, 1g AgCl, 22 ml of ammonia (30%) and 1.8g of glucose syrup in 5ml of water were used.

The solution was kept at 60°C until the silver was completely reduced, as confirmed by EDS spectrum reported in Fig. 4.47.

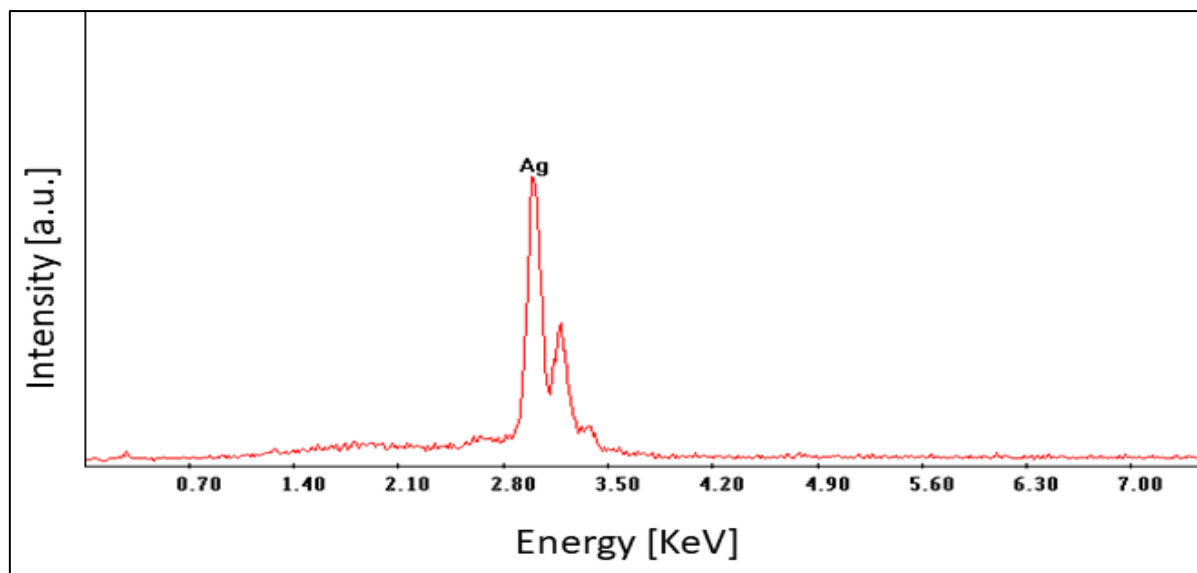


Fig. 4.47 The silver obtained from the silver chloride reduction with glucose syrup.

4.7.2 Silicon refining

As described in Chapter 4.2.4, for most silicon application, it is crucial its purity [107, 108]. Actually, the silicon recovered from the cells treated in according to Chapter 4.6, even if it's not polluted with other metals, still has antireflection layer (Si_3N_4) [109] and it is doped with P and B [110].

It is possible to remove the Si_3N_4 and P-doped layer using a chemical etching. Obviously, this method causes a loss of silicon.

In particular, a mixture containing 9ml of HF, 15 ml of HNO_3 and 9 ml of CH_3COOH was tested on 0,7g and 1cm^2 of silicon cell previously treated with nitric acid and soda, as described in Chapter 4.6.

This solution provokes the initial oxidation by HNO_3 of silicon to silica (SiO_2), which reacts with HF producing first SiF_4 and then SiF_6^{2-} . The reaction is:



The antireflection layer seems to be completely removed after 1 min. However, several treatment times were tested. The thickness of silicon cell was measured for each treatment time using SEM image analysis and the results are reported in Fig. 4.48.

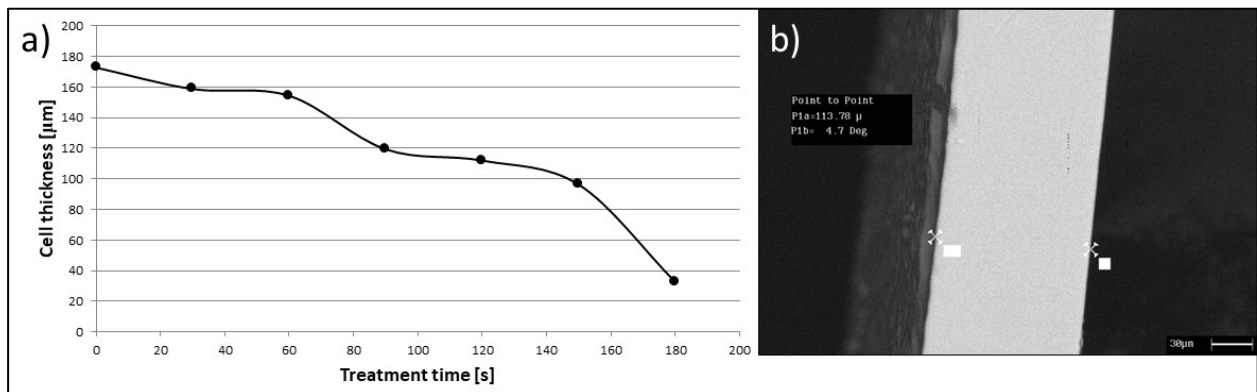


Fig. 4.48 a) the cell thickness dependence on treatment time and b) and example of measuring cell thickness using SEM image.

After the treatment, the removal of doped layer was verified with SIMS analysis and the results are reported in Fig. 4.49 and 4.50.

It was observed that both phosphorous-concentration in the front side and boron and aluminum concentration in the back-side were greatly reduced after 90s of treatment.

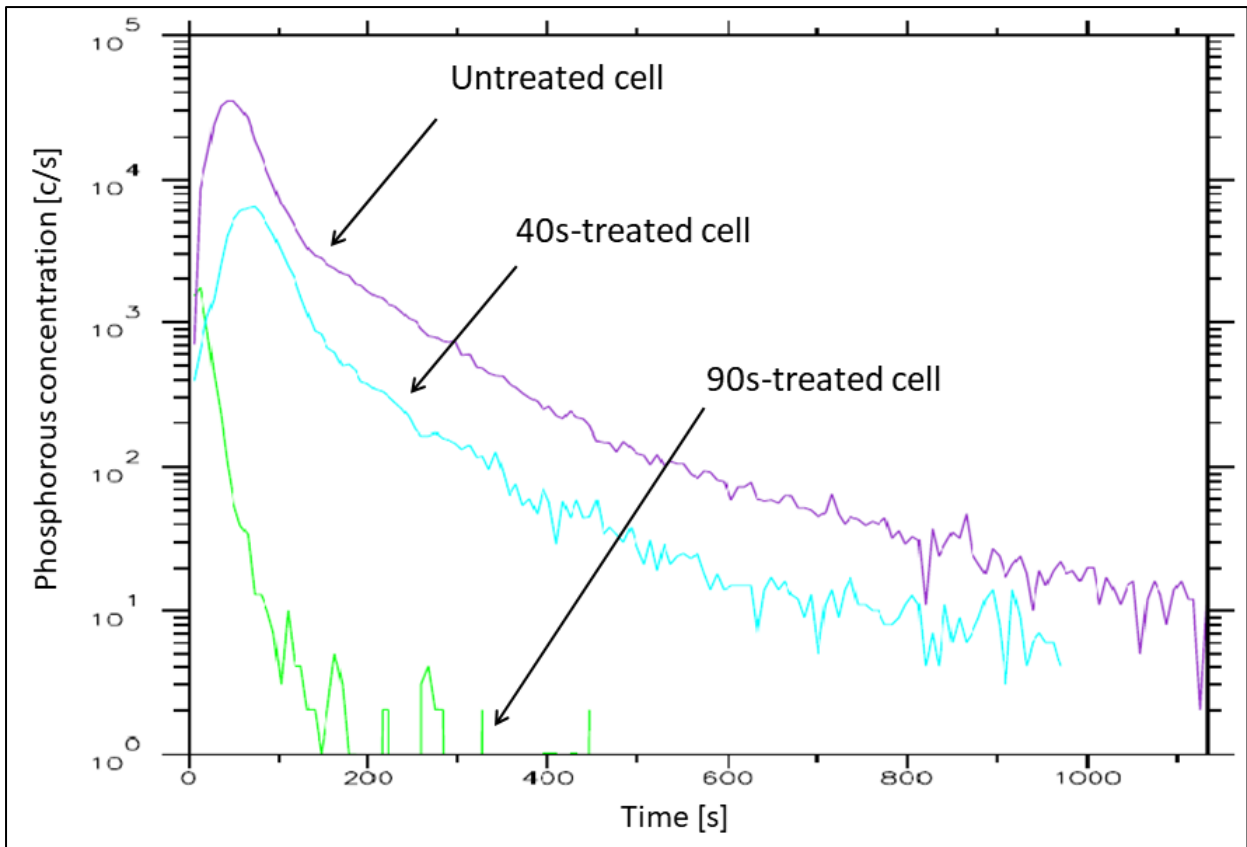


Fig. 4.49 SIMS analysis of the front side of the cell before the treatment with nitric-acetic-hydrofluoric acids and after two different treatment times.

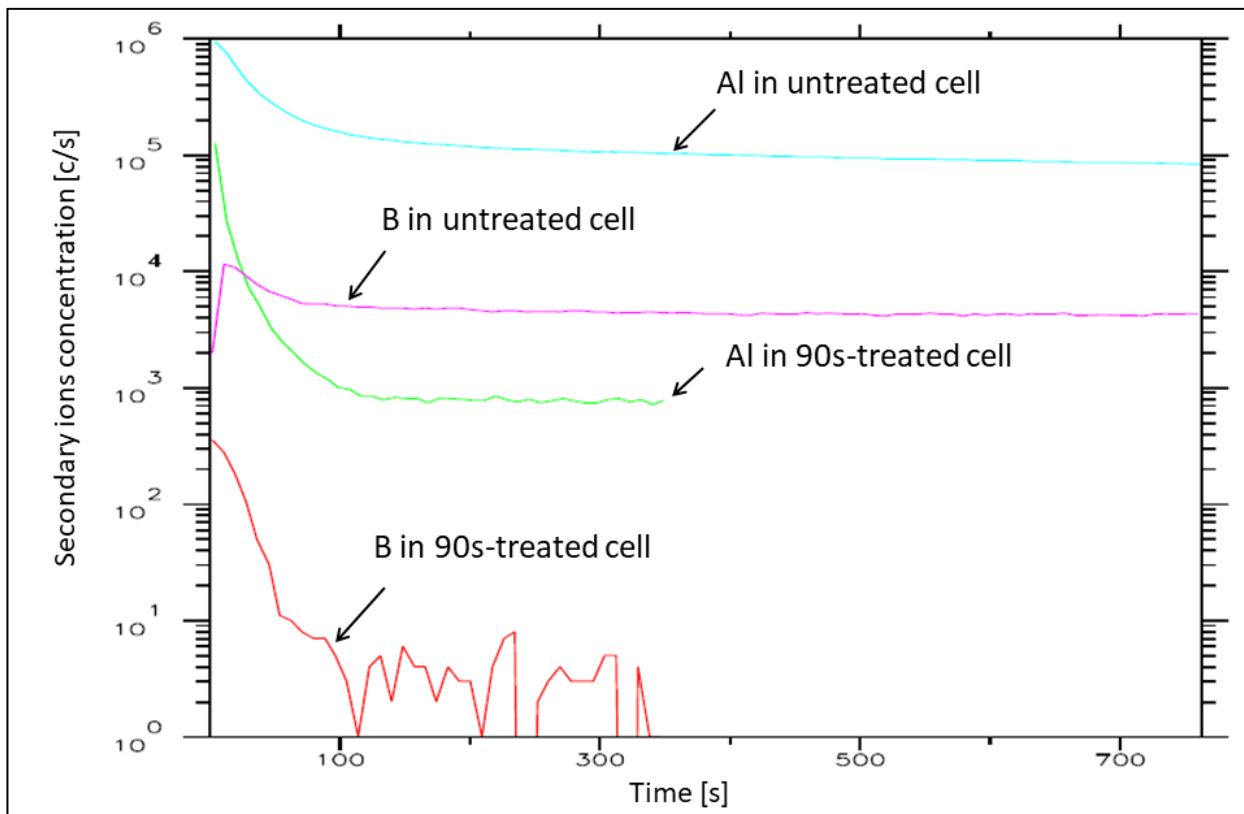


Fig. 4.50 SIMS analysis of the back side of the cell before the treatment with nitric-acetic-hydrofluoric acids and after 90s of treatment.

4.7.3 Test at TRL 5

4.7.3.1 Silver recovery

After the described studies for recovery and purification of silver and silicon, the examined techniques were applied on greater amount of material, in particular to the cells recovered (4.5.4) and chemically treated (4.6.3) in previous chapters.

30 g of cells (which it was estimated to contain ~0,5 g of silver) pre-treated with sodium hydroxide were immersed in 100ml of 7.3M nitric acid solution, then 10 ml of 12M hydrochloric acid was added and the precipitate powder was washed with deionized water and dried.

0,40415 g of silver chloride (which contain 0,3042 g of silver) were obtained. From these data it is possible to estimate that the silver chloride recovery yield is ~60%.

The relative low yield is due to the fact that a part of silver remains onto the ribbons after the heating treatment.

Moreover, silver chloride was then treated at 750 °C 1h with 1g of sodium carbonate, obtaining 0.28723g of silver. The yield of silver chloride reduction is therefore ~95%.

4.7.3.2 Silicon refining

To remove Si_3N_4 layer it was convenient, to make simpler the solution disposal, to use hydrofluoric acid solution without addition of acetic and nitric acid, as tested in Chapter 4.7.2.

Therefore, several hydrofluoric acid concentrations (2,8 M; 5,7M; 11,5 M; 23 M) at room temperature were tested and the time required to remove the antireflective layer is reported in Fig. 4.51.

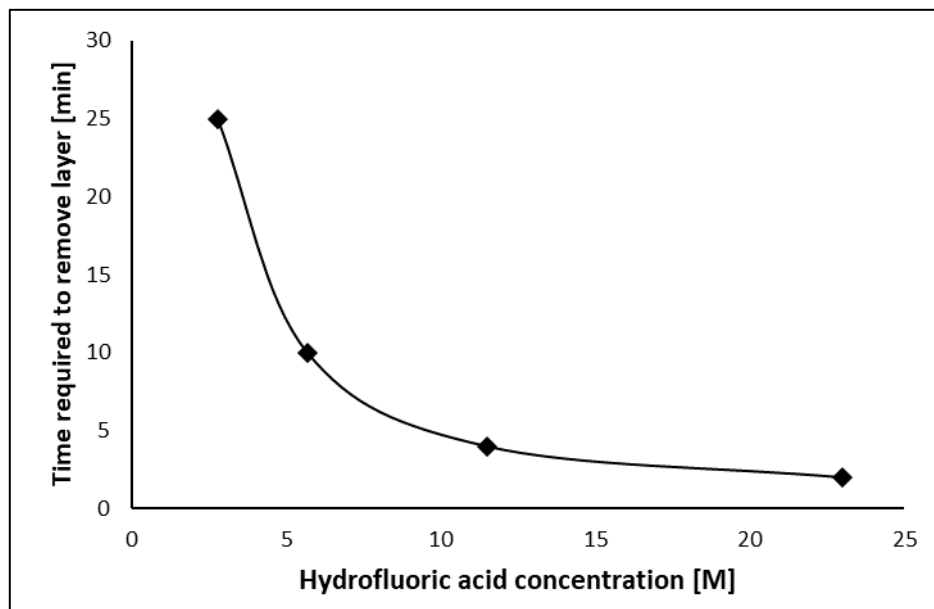


Fig. 4.51 Time required to remove Si_3N_4 layer as function of hydrofluoric acid concentration.

From these tests, it was decided that 5,7 M hydrofluoric acid solution represent the most convenient concentration to use it at TRL 7.

4.8 ReSiELP



Fig. 4.52 ReSiELP logo.

ReSiELP is a project that aims at recovering critical and precious as well as non-critical raw materials the largely available quantity of EOL PV waste.

ReSiELP proposes a circular economy with a product-centric zero-waste approach.

The ReSiELP consortium includes partners covering all sides of the knowledge triangle with expertise to deliver the proposed activities. For extraction and

recovery, University of Padova and Relight will be working hand in hand. University of Padova will provide planning of the plant and contribute to the purchase of equipment that will be installed at Relight. For purification, Bay Zoltan and Magyarmet will collaborate. Glass re-use in buildings, will be developed by Cetma and ITO. In recent years, Cetma and ITO were involved in national & European projects dealing with reuse of secondary raw materials in building products performing R&D activities with own resources. The project will be led by CEA, having experience in implementation of circular economy for PV, as demonstrated by Cabriss project. CEA will provide demonstrators of the recycled Si in term of fabricating and test mini modules and bifacial 60 cells modules. The project aims to implement a pilot case of circular economy, based on perfect complementary of partners and their roles.

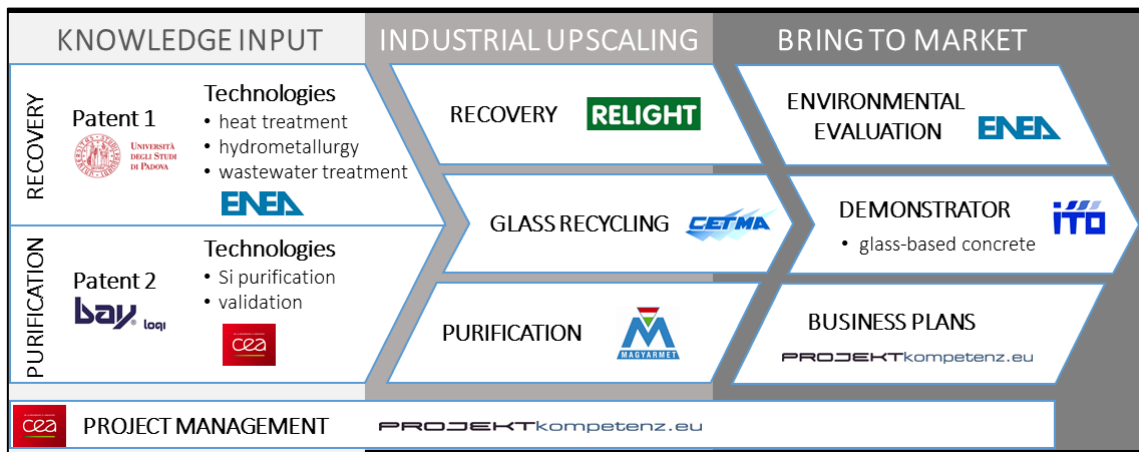


Fig. 4.53 An image of the ReSiELP partners complementarity.

The involved industries have the capability to match the expected PV panels incomes and to exploit market growth in Europe, attracting large industries and creating spin-offs to sell the technology.

The objectives of the project in fact are:

- To patent the new technology and to license it to foreign companies
- To realize, after the end of the project of TRL 9 plant in Relight
- To found a spin-off to sell the acquired technology and know-how

4.8.1 Recovery process workflow

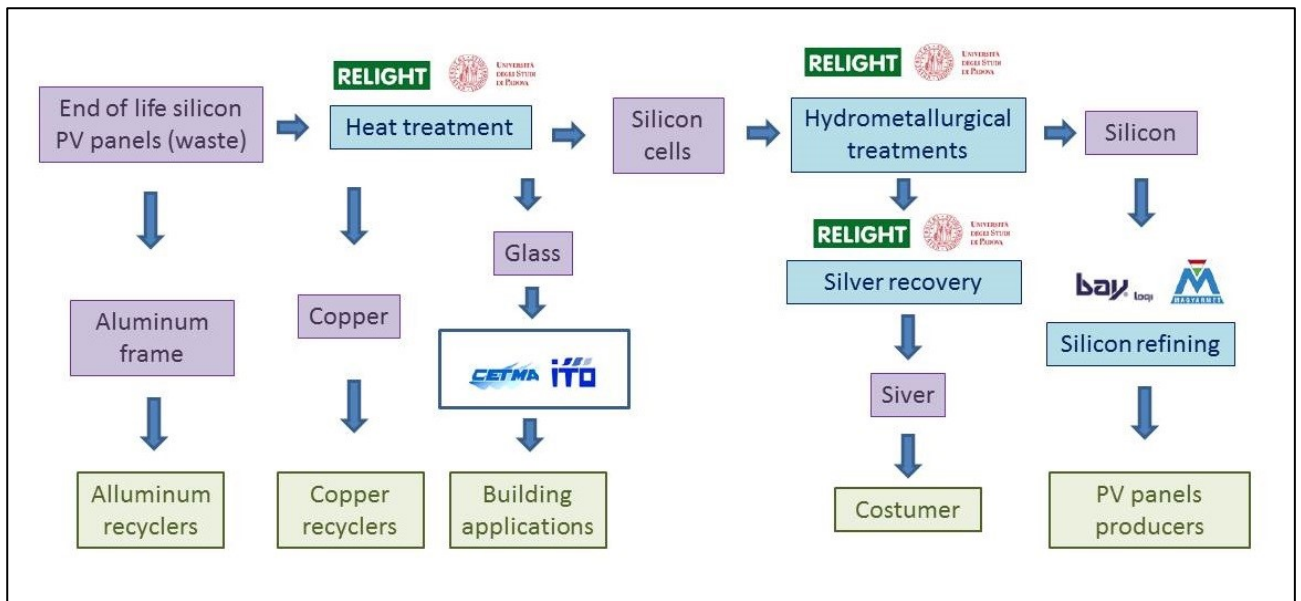


Fig. 4.54 Scheme of the ReSiELP recovery and purification line.

ReSiELP process, showed in Fig. 4.54, comprise different parts.

First, the EOL PV panels are collected by Relight and submitted to heat and hydrometallurgical treatments that will be performed in new plant designed by Unipd and Relight.

From the process different raw material will be recovered.

In particular copper, aluminum and silver will be directly placed on the market. The recovered silicon will be purified in the new plant of Bay Zoltan and Magyarmet whereas Cetma/ITO will use the glass in their existing plants.

4.8.2 Recovery line design

The recovery line, which will produce raw material (glass, aluminum, copper ribbons, silver and silicon) from the EOL PV panels will be placed in Milano, Italy. In particular, the equipment will be installed in Relight, who has a dedicated space of 12x12m².

The layout of the plant is showed in Fig. 4.55.

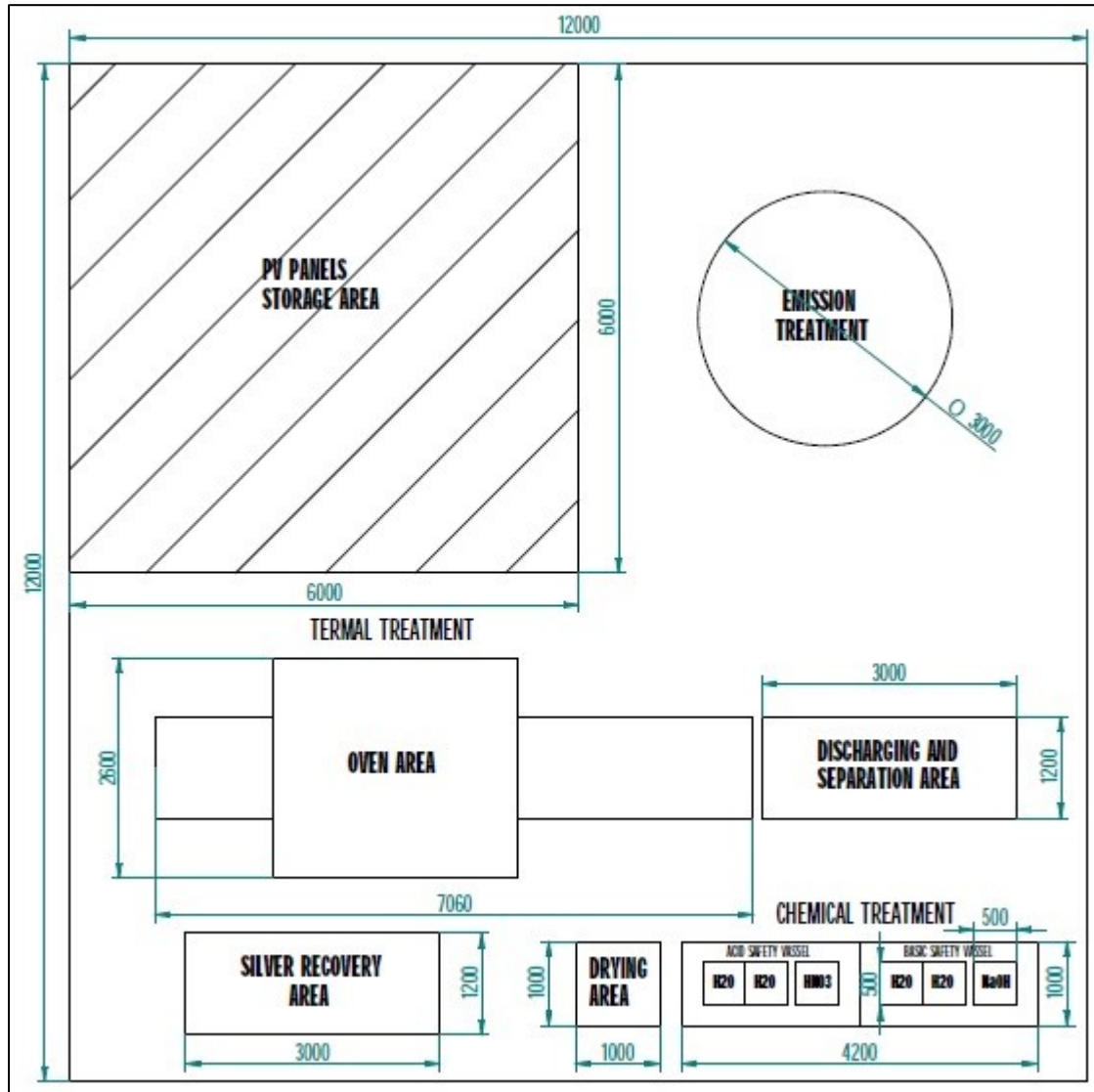


Fig. 4.55 Layout of the plant.

Facilities will be provided to make the plant up and running. Also waste treatment were considered. Even if all recovery line will be in the same place, for clarity, it is divided into the three points here described.

After the recovery the purity of the recovered materials will be verified with the instrument in University of Padova (SEM equipped with EDS, ICP-OES) and some analyses, in particular concerning the purity of silicon, will be made in collaboration with CEA or Bay Zoltan.

4.8.2.1 Design of heating treatment and material separation

The first part of the recovery process comprises the removal of aluminum frame and power optimizers.

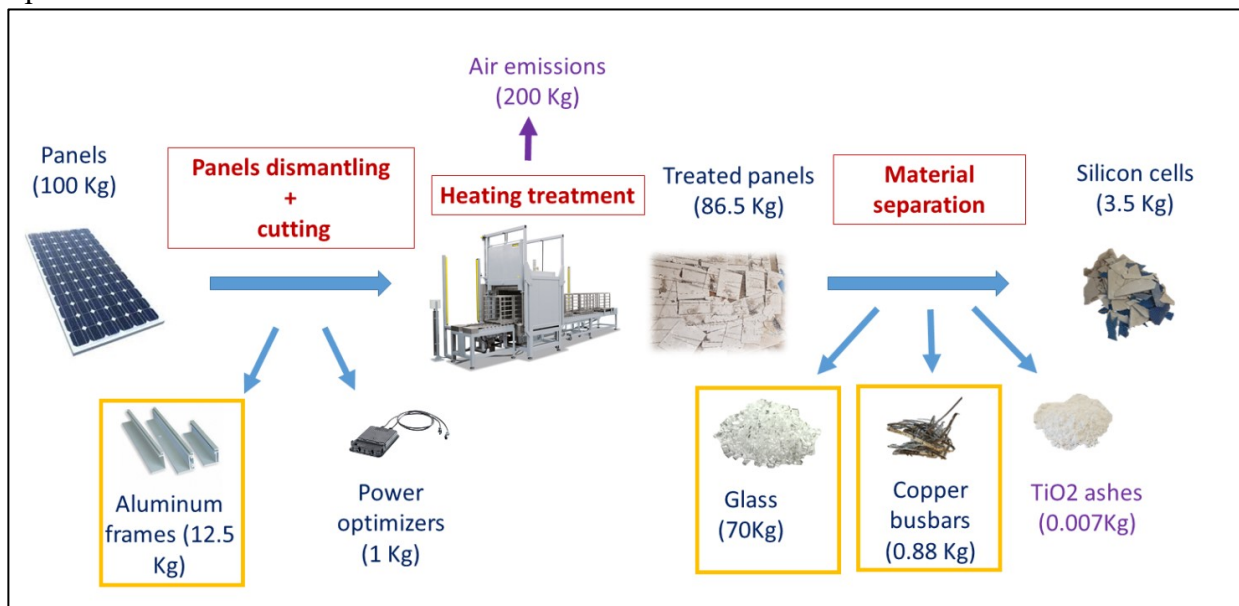


Fig. 4.56 Scheme of the thermal treatment and material separation.

This step will be performed manually by Relight operators. However, it must be pointed out that sometimes the PV panels are collected without these parts: in this case this step is not necessary. After the dismantling, the panels are cut into two parts: in fact, the oven was design to treat halves of panels in order of reducing the oven size. The cutting process will be performed by Relight operators, as the company is specialized in this kind of works.

The panels are then placed on the furnace loading rolls which move them inside the chamber.

The panels will stay in the furnace at about 530°C for about 15 min with an air flow of 320m³/h. After this treatment, which will remove all the polymeric parts (EVA and Tedlar), the rolls will move them outside in a cooling place and, after, in a place where they are collected.

In fact, the furnace with that technical requirements was designed and purchased and the layout is shown in Fig. 4.57.

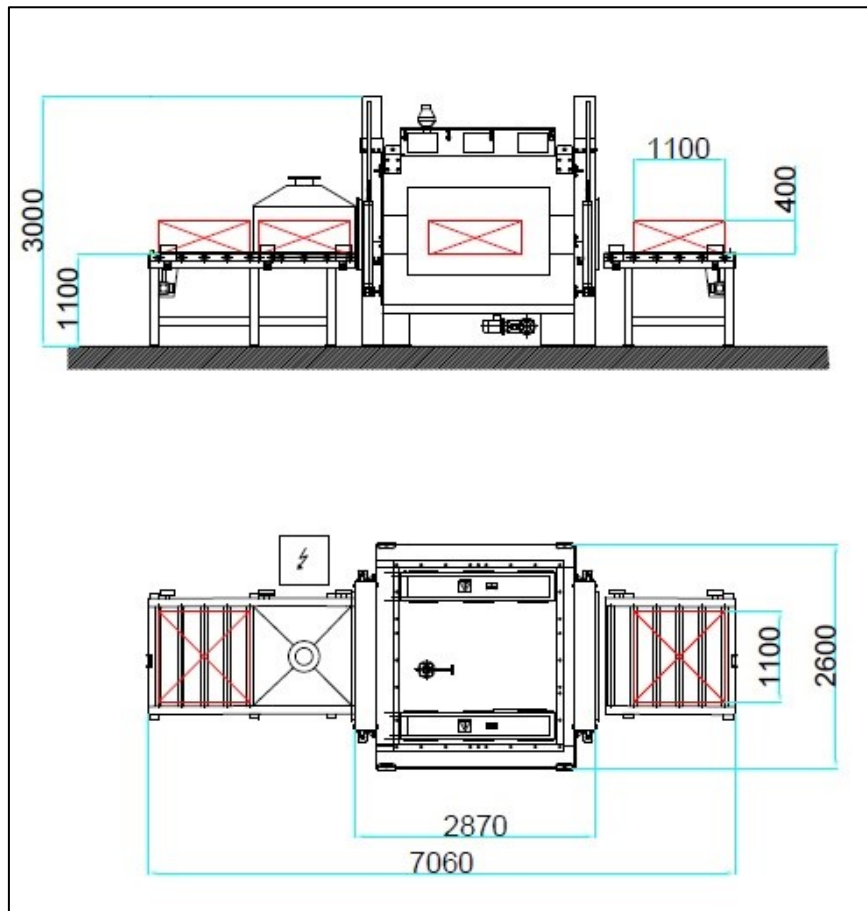


Fig. 4.57 Layout of the designed and purchased furnace for the EOL PV panels heating treatment.

4.8.2.2 Design of hydrometallurgical treatments

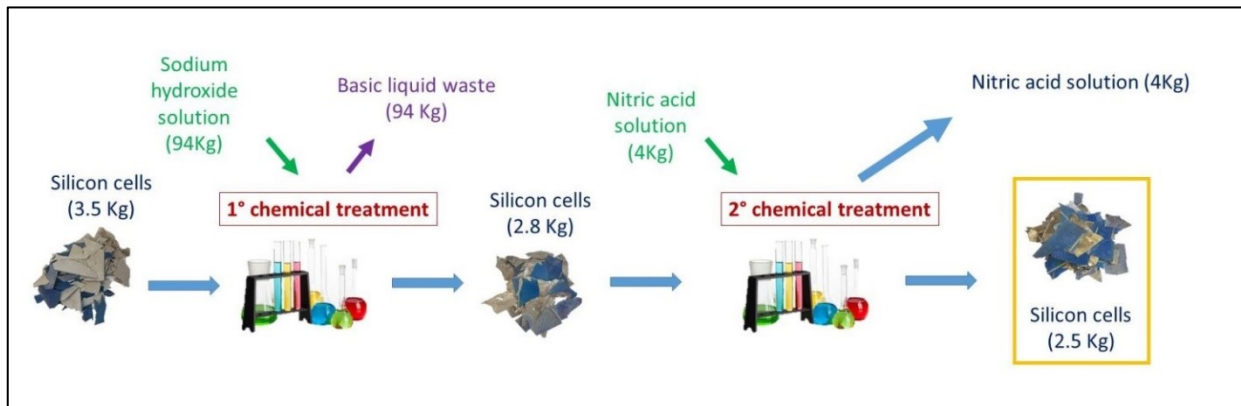


Fig. 4.58 Scheme of the hydrometallurgical treatments.

• 1° chemical treatment

After the silicon cells are separated from the other components of the PV panels, they are subjected to two hydrometallurgical treatments: a first with a basic solution to remove aluminum from the back side and a second one to remove silver contacts from the front side of the cell.

In details, the first one is performed by introducing the material into a sodium hydroxide solution (7.5g/l) for one hour in order to completely remove the aluminum. The solution will be kept at 40°C.

The treatment will be performed by introducing a basket containing the cells into one tank reactor (Fig. 4.59) containing the basic solution. After the treatment, the material is washed in two adjacent tanks with water.

Moreover, the sodium hydroxide solution will be continuously recirculated and filtered to remove the unreacted aluminum pieces, so recovering aluminum and reducing reagent consumption.

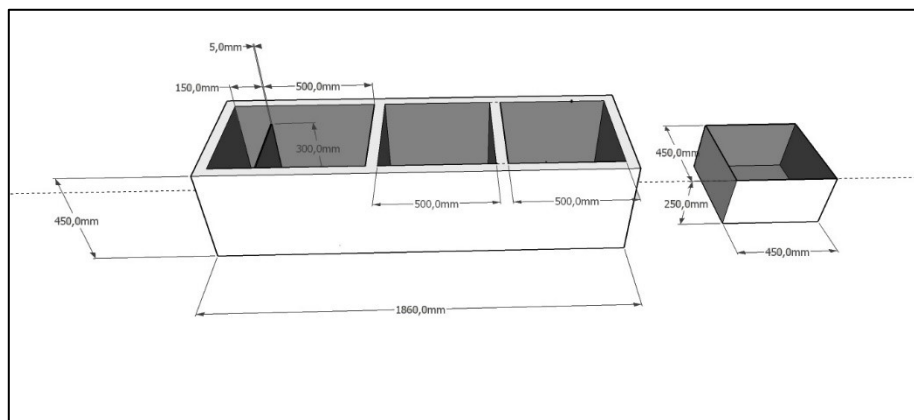


Fig. 4.59 First design of the reactor tank for the first hydrometallurgical treatment

- **2° chemical treatment**

The second chemical treatment will be performed with nitric acid solution (30%) for few minutes in order to completely remove silver contacts from the silicon wafers.

Also in this case the treatment will be performed introducing a basket containing the cells into one tank reactor (Fig. 4.60) containing the acid solution and, after the treatment, the material will be washed into two adjacent tanks with water.

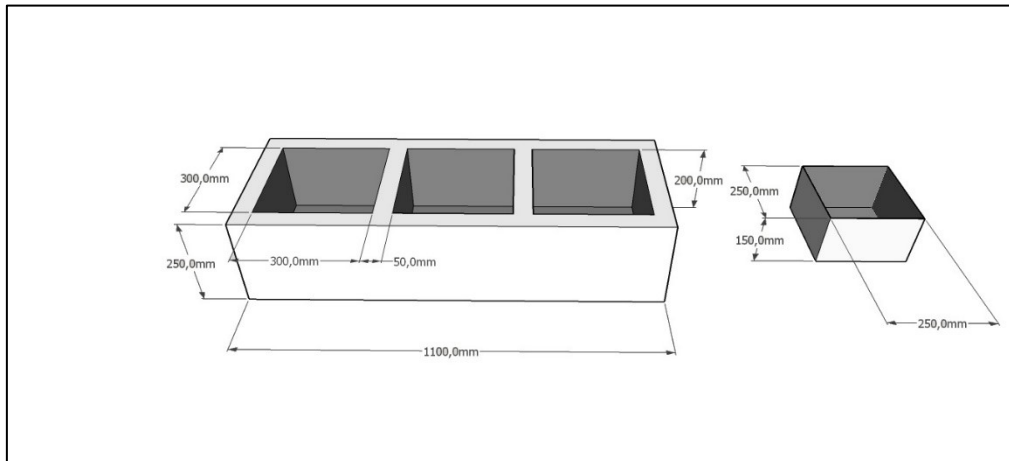


Fig. 4.60 First design of the reactor tank for the second hydrometallurgical treatment.

For both chemical treatments, specific reactor will be design, comprising temperature control of the solution, gas stirring for moving the wafers, containment tank, loading dosing pump and automated system to move the baskets. Moreover, a water demineralizer will be bought as demineralized water will be used.

Before nitric acid solution disposal, the recovery of silver from the solution will be performed.

To achieve this, sodium chloride will be added directly into the acid solution. The solution will be filtered, recovering the silver chloride, with a dedicated basket and washed.

After the recovery, silver chloride will be reduced to metallic silver by heating treatment in presence of sodium carbonate. The heating treatment, that consist of keeping the material at 700°C for one hour, will be performed in a small furnace

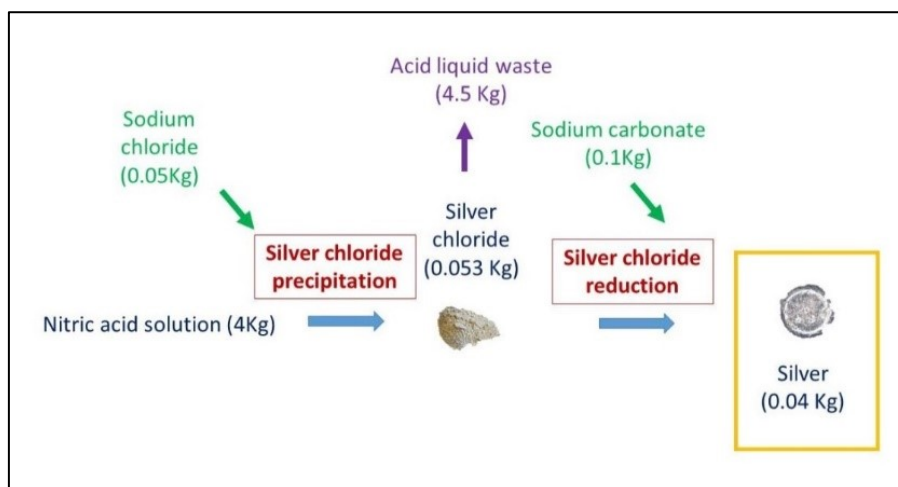


Fig. 4.61 Scheme of the silver recovery from acid solution.

4.8.2 Design of gas treatment

Using the gases analysis performed (Chapter 4.5.3), the off-gases flown and composition of the recovery plant were estimated in order to design the proper treatment equipment.

4.8.2.1 Amount of polymer

First of all, it was estimated the amount of polymer that will be burn during the heating treatment. Considering that the oven will treat $12\text{m}^2/\text{h}$ ($\sim 150\text{Kg}/\text{h}$) of PV panels, the amount of polymer was calculated.

A. It was considered that in a 60-cell panel ($1,6\text{m}^2$), that weights 20Kg , the polymeric fraction is $12,5\%$ (2% Tedlar and $10,5\%$ EVA). This means $0,25\text{ Kg}/\text{m}^2$ of Tedlar and $1,31\text{ Kg}/\text{m}^2$ of EVA, that is $3\text{Kg}/\text{h}$ of Tedlar and $15,7\text{ Kg}/\text{h}$ of EVA.

B. A more accurate estimation was made considering the material given by CEA. In particular:

- **EVA**

The EVA 33% from CEA was $0,9\text{mm}$ thick and weights $0,8\text{ Kg}/\text{m}^2$ ($0,89\text{ Kg}/\text{m}^3$).

- **Tedlar**

The Tedlar from CEA was $0,35\text{mm}$ thick and weights $0,475\text{ Kg}/\text{m}^2$ ($1,36\text{Kg}/\text{m}^3$).

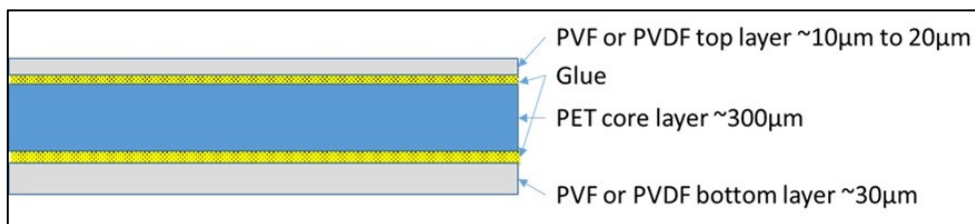


Fig. 4.62 Image of Tedlar structure.

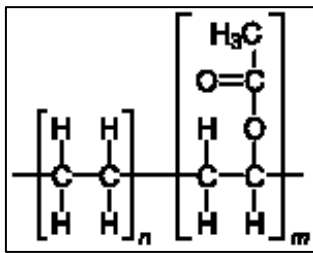
However, these data are a bit old (2012 documentation) and might be not completely accurate since PVF prices are very high. So these layers tend to become thinner and thinner.

This estimation seems more accurate than A, as the thickness of EVA + Tedlar measured is $1,3\text{mm}$. The amount of polymer is so $1,275\text{Kg}/\text{m}^2$.

Considering the two estimations, the value $1,5\text{ Kg}/\text{m}^2$ was considered

4.8.2.2 Required air

EVA typically used for PV panels contains 33% of acetate and 67% of ethylene (reduced to 22-78% for new polymer)



• Vinyl acetate is a monomer of PM = 86uma composed of 4C 6H 2O, and requires 9 Oxygen (144uma) to burn completely, so 1 Kg of VA requires 1,674 Kg of oxygen, that are contained in 7,2 Kg of air (23,2 %Wt).

Fig. 4.63 Formula of EVA

• Ethylene is a monomer of PM = 28uma composed of 2C 4H, and requires 6 Oxygen (96uma) to burn completely, so 1 kg of ethylene requires 3.429 Kg of oxygen, corresponding to 14,715 Kg of air.

As ethylene requires more air to burn it is more secure to consider that all polymeric part is made of only this kind of plastic.

For each treatment of about 15 minutes, about 63 Kg of air or (density 1,225 Kg/m³) 61 m³. This represent 250 kg/h, that is about 204 m³/h. Considering that oven chamber is ~5m³, this allows to obtain an air excess of 20 m³/h. However, estimating an excess of air of 15%, the required air flow should be 235 m³/h.

4.8.2.3 Off-gasses composition

The concentration in the off-gasses produced, were estimated prudently considering the air flown of 204 m³/h so as the concentration are higher.

- CO₂

The amount of carbon dioxide was estimated with stoichiometric consideration.

Also in this case, the cautionary estimation was made considering that all the polymeric fraction is PE. As the combustion of every kg of PE produces 3,143 Kg of CO₂, we can consider a production of 56,5 Kg/h of CO₂.

- CO

It was not possible to make a precise estimate, but it can be said that the CO should be very low. CO formation occurs above all at elevated T (> 1000 ° C) and in the absence of excess air. With an excess of 15% and much lower temperature, CO formation should be very limited.

For the next concentration calculation, the amount of CO₂ produced was not considered, so even in this case, the real concentrations will be lower than these:

- **HF**

The amount of produced hydrofluoric acid is 21% of the amount of Tedlar, so 0,63Kg/h of HF.

The concentration in gasses will be **3,09 mg/L**.

- **Acetic acid**

The amount of produced acetic acid is 22% of the amount of EVA, so 3,45Kg/h.

The concentration in gasses will be **16,93 mg/L**.

- **Aldehydes/ketones**

A mixture of aldehydes and ketones is released when plastic is between 400 and 500 °C, but the amount cannot be estimated.

- **Metals**

The metals concentrations in the gas were estimated using data from literature [111]. In particular, concentration of Al samples (subtracted of the amount of blank test).

Al	Cr	Cu	As	Cd	Pb	Fe	Sn	Zn	In	Ni
171,79	4,2	3,53	0,43	8,84	176,89	16,43	494,66	63,19	1,79	0,59

Tab. 4.12 Metals [μg] contained in 110 g of PV panel.

From these data, considering to treat 150Kg/h and air flown of 204 m³/h the estimation is reported in Tab. 4.13.

Al	Cr	Cu	As	Cd	Pb	Fe	Sn	Zn	In	Ni
1,123	0,028	0,021	0,003	0,059	1,179	0,102	3,307	0,393	0,012	0,003

Tab. 4.13 Estimated metal concentrations [$\mu\text{g/l}$] in off-gasses.

- **NO_x, SO_x and HCl** are not present.

- **Powders (TiO₂)**

From literature, the polymer loaded typically has a thickness of 178 μm and is charged at 35% TiO₂ [112], however, from our tests, the Tedlar recovered from panels given by Relight had 15.6% of ashes (TiO₂). From UniTo analysis the solid residue of Tedlar is 3%. It seems so that the amount is not constant. It's possible to estimate a 10% of ashes from Tedlar combustion, that is 0,3Kg/h. If we suppose that all powders will goes into the gasses, the concentration in gasses will be **1,5 mg/L**.

4.8.3 Timeline

The timeline for the building of recovery line is reported in Fig. 4.64.

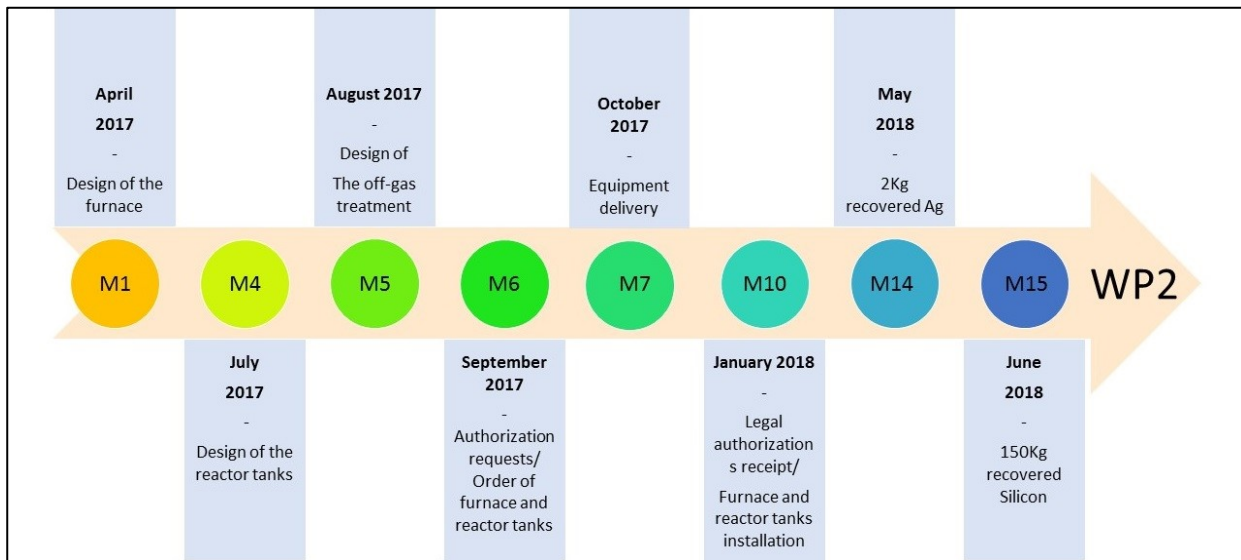


Fig. 4.64 *Timeline of the new plant building*

Chapter 5

Other resources recovery

As described in Chapter 1, the interest in strategic metals and rare earth (Rare Earth Elements, REE) has grown considerably in recent years. Strategic metals find innumerable applications in the industry and they are fundamental to the development and production of technological devices. In particular, in this chapter, two topics will be treated: first, the recovery of Tantalum from Ta₂O₅-based condensers and in the second part, the recovery of Neodymium from permanent magnets Nd₂Fe₁₄B.

A method for recovering tantalum was studied by means of a thermal treatment coupled with hydrometallurgical processes. The use of hydrofluoric acid allows obtaining silica-free tantalum fluoride. This represents an advantage, because silica is very difficult to separate from tantalum oxide. This separation treatment can represent a substitute for the sieving process described in the literature, which has the defect of causing the loss of high quantities of raw material.

The objectives of the second study was the optimization of recovery processes to improve the purity of the resulting materials, a crucial property in optic of reusing of the same.

Thus, the purity of the neodymium salts was increased by adding to the hydrometallurgical process employed in the literature an ammonia treatment, which allowed to significantly reducing the iron present in the double salt of neodymium and sodium recovered.

Moreover, this new treatment makes easier to control process parameters.

5.1 Recovery of Tantalum pentoxide from out of use capacitors

Recent trends in reducing the size of electronic devices, such as laptop computers and mobile phones, have accelerated the demand for high-performance tantalum capacitors. As compared to other capacitors, tantalum capacitor has the largest capacity per unit volume and is thermally stable. With such superior characteristics, the production volume of tantalum capacitor has dramatically increased in the last 10 years. Nevertheless, tantalum is a scarce resource in the earth's crust, and therefore, has a limited production volume. Currently, only about 2000 ton of tantalum is produced annually in the world, and about 40% of the world Ta production is used for capacitors.

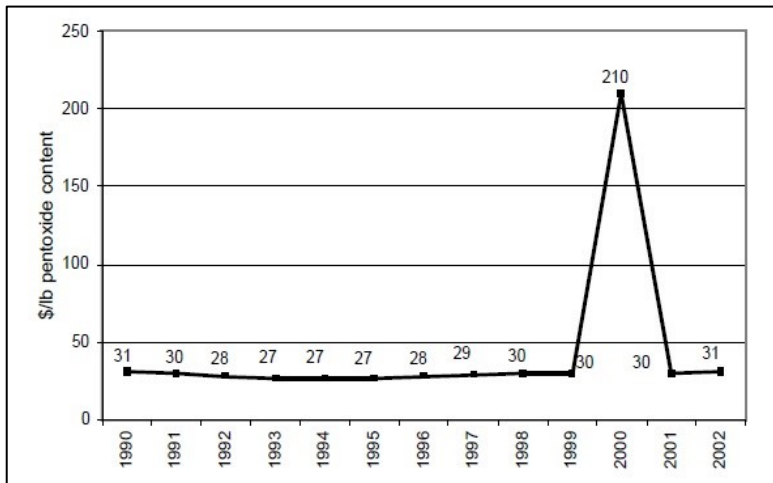


Fig. 5.1. Average year-end prices for tantalite, 1990 to 2002 (based on USD/lb Ta_2O_5 content)

In the year 2000, the balance between the demand and supply of tantalum ore collapsed due to a strong demand from the market, and the price of the ore jumped by about six times and tantalum capacitor manufacturers encountered a material crisis [113].

Particular attention was devoted to disruptive effects that this world shortage in tantalum had in Democratic Republic of Congo.

In fact, congolese gold miners switched to tantalite, farmers left their fields to mine, youths aged 12-18 were forced into labor as an 'Army of Development' under military supervision, Rwandan prisoners were used and a wholesale invasion to exploit the resources in the national parks commenced [114].

In order to avoid the profound crisis in supply, it is particularly important for Tantalum the recovery from waste.

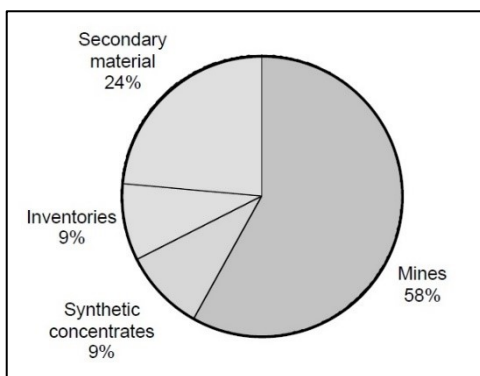


Fig. 5.2. Sources of tantalum, 2012.

There is a range of processes for the recovery from off-specification batches of capacitor production [113, 115, 116, 117]. Most of the established recycling processes utilize mechanical milling and sorting processes and acid leaching to separate tantalum from the other parts of the capacitor. The focus is set on recovering pure tantalum powder directly from the scrap.

From statistical data, it is known that every German citizen discard about 0.6 g of tantalum year, (i.e., 48 t), into the residual waste stream fed [118] predominantly to waste incineration plants. On top, additional amounts find their

way through separate collection systems, e.g., for electronic scrap, into the overall waste stream. This so-called post-consumer scrap is a promising source for tantalum, too. Furthermore, the recycling can be particularly important if we consider that tantalum ore always contains considerable amount of niobium, and a large amount of energy is required to remove niobium. This is because niobium and tantalum are related elements and have similar chemical characteristics. On the other hand, the tantalum used in capacitors is free of niobium, and therefore, capacitor scraps can be considered as high quality resources of tantalum. However, tantalum capacitors are not yet recovered from scrap printed circuit boards (PCB), which constitute their main application area [119].

5.1.2 Tantalum condensers

The structure of a tantalum condenser is shown in Fig. 5.3 [120].

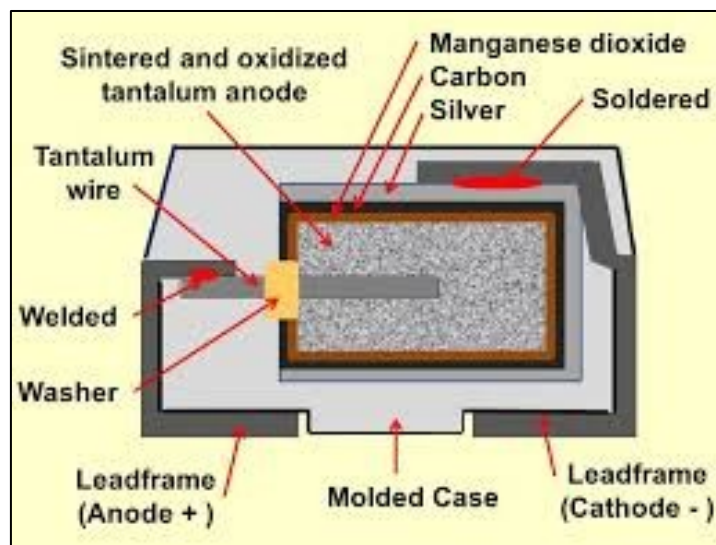


Fig. 5.3. Construction of a typical SMD tantalum electrolytic chip capacitor with solid electrolyte.

Tantalum condenser is roughly divided into three components: terminals, a package made of fireproof epoxy resin, and a sintered tantalum electrode. The terminal is made of iron, nickel, or copper. The fireproof epoxy resin is a polymer in which SiO_2 powder is added to enhance its thermal durability. The sintered tantalum electrode is made of fine tantalum powder and other trace elements, and it contains 90% or higher tantalum. Silver paste and graphite are daubed on the surface of the electrode as a cathode layer.

It is rational to remove the sintered tantalum electrode from the capacitor before chemical treatment, because tantalum exists only in the sintered tantalum electrode at a very high concentration.

Moreover, as the epoxy resin covers the tantalum electrode very tightly, it is necessary to remove this resin before mechanical and chemical treatment [113].

5.1.3 Characterization

First of all, three types of capacitors, showed in Fig. 5.4, were recovered from electronic cards.



Fig. 5.4. *The three type of tantalum capacitors analyzed.*

The capacitors were mounted and polished to evidence the internal contacts and dielectric. Successively the samples were analyzed with the stereomicroscope and the images are reported in Fig. 5.6.

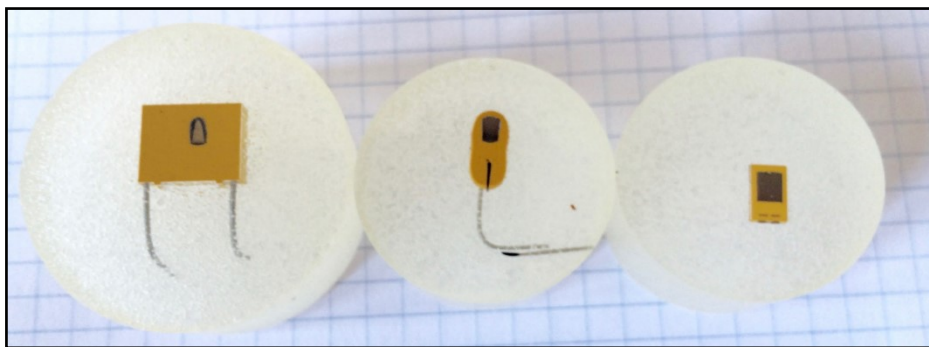


Fig. 5.5. *The analyzed tantalum capacitors after mounting.*

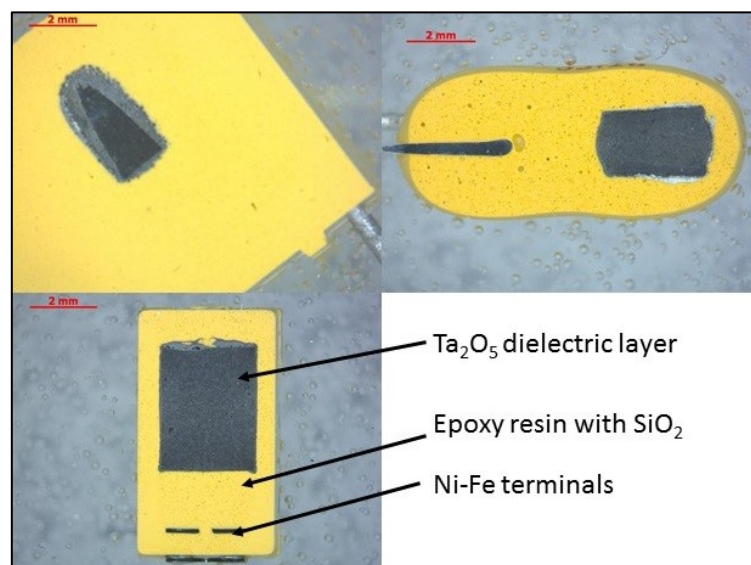


Fig. 5.6. *Stereomicroscope images of the three type of tantalum capacitors analyzed.*

From the analysis, it can be seen the structure of the tantalum condenser: the tantalum pentoxide dielectric layer is surrounded by the epoxy resin.

The samples were then observed at SEM and the images are reported in Fig. 5.7, where it was confirmed the presence of tantalum pentoxide sintered powder as dielectric.

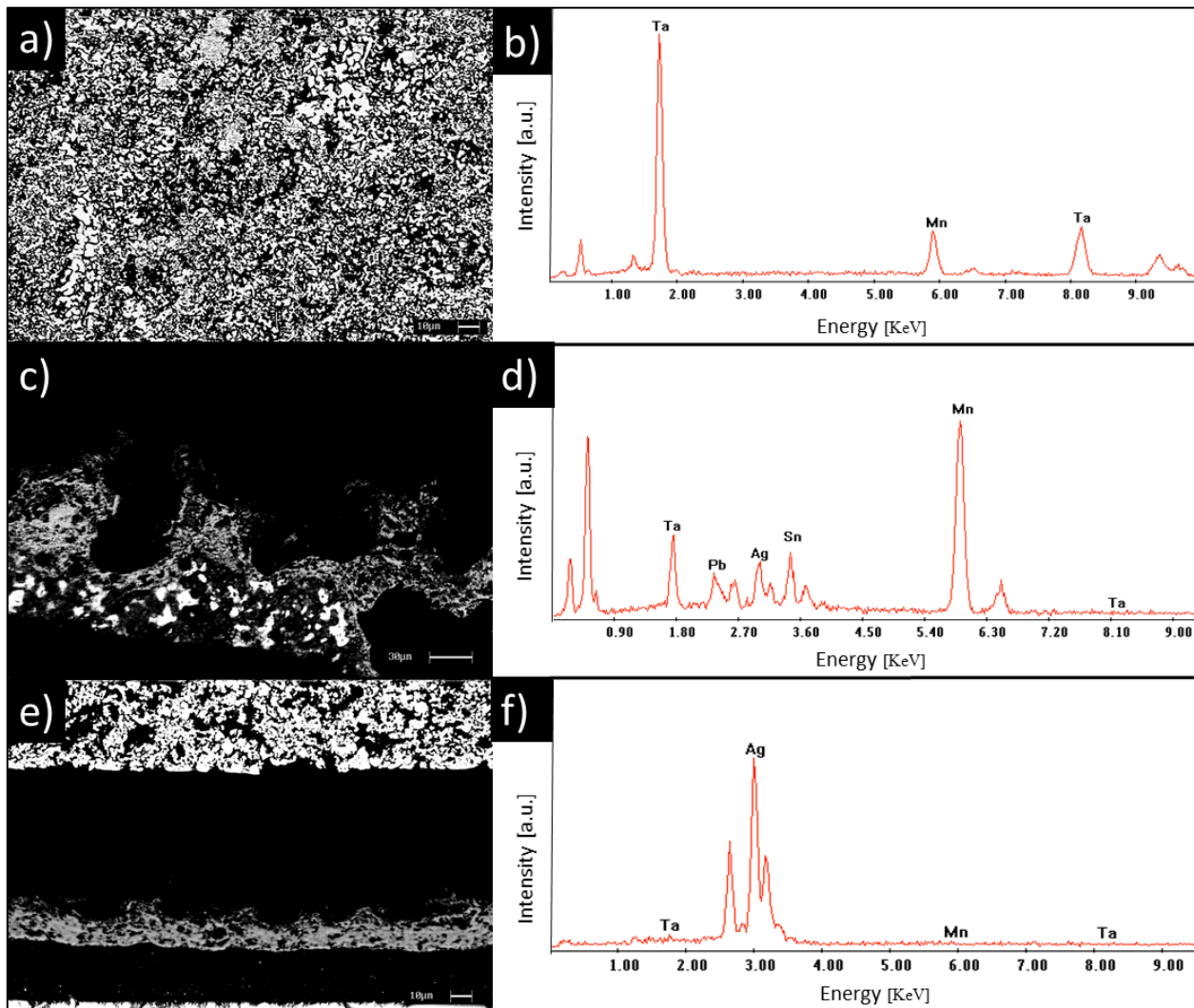


Fig. 5.7. SEM images and corresponding EDS spectra of different parts of Tantalum capacitors: Ta₂O₅ dielectric as sintered powder (a, b), MnO₂ cathode (c, d) and silver used to connect MnO₂ to the terminal (e, f).

5.1.4 Heating treatment, grinding, magnetic separation

The outer polymeric fraction is made up of an epoxy resin with SiO_2 , which increase its thermal stability and properties. While working in electronic equipment, in fact, the capacitors may reach high temperatures and in the event of malfunctions or electrical short-circuits this property is necessary.

To remove the epoxy resin, four types of condensers were treated at 1000°C for one hour into alumina containers (Fig. 5.8).

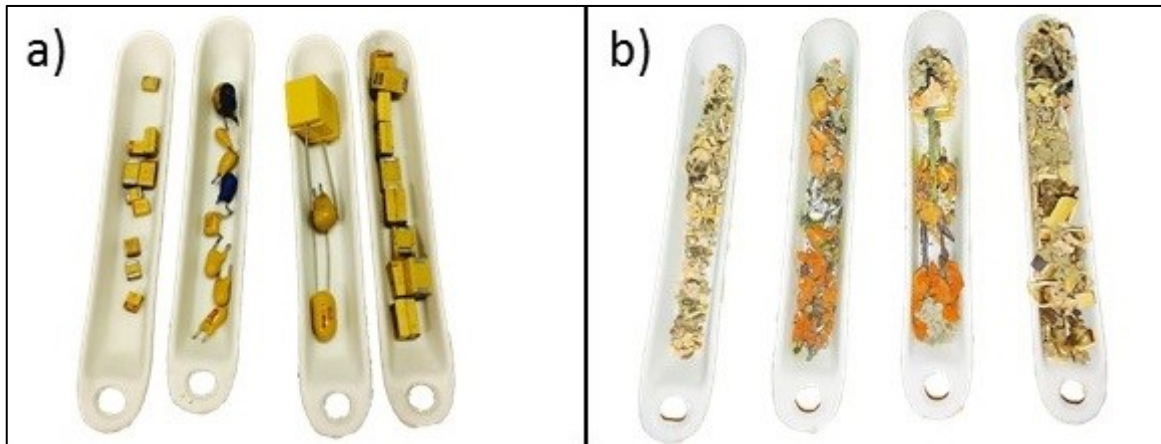


Fig. 5.8. images of the different Tantalum condensers before (a) and after (b) the heating treatment.

Successively the heat-treated samples were grinded (Fig. 5.9a) and contacts and metallic parts magnetically separated. The EDS spectrum of the non-magnetic fraction is reported in Fig. 5.9b.

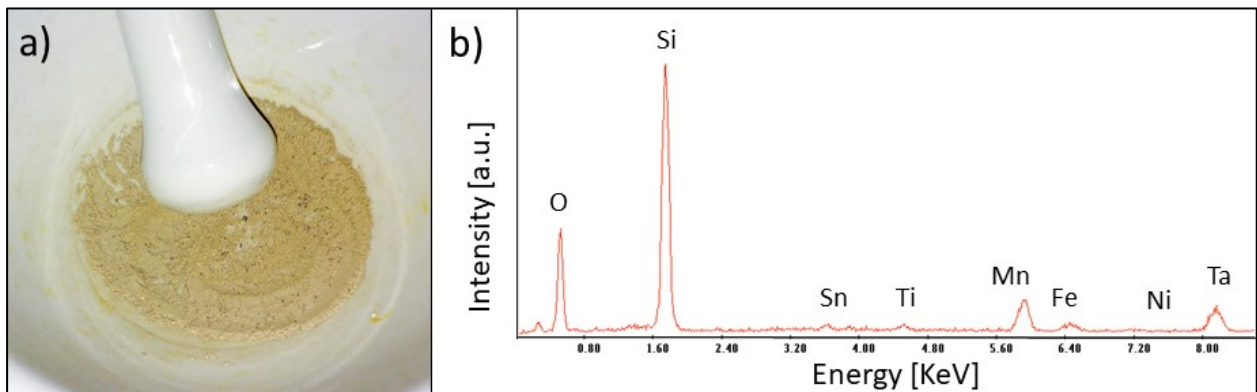


Fig. 5.9. a) powder obtained from the heat-treated capacitors and b) EDS spectrum of the nonmagnetic fraction.

5.1.5 Chemical treatments

5.1.3.1 Hydrochloric acid

After magnetic separation, there were still metals like iron, nickel, manganese, tin, lead, antimony and silver (Fig. 5.9b). In order to remove these metals, it was performed a treatment with 6M HCl solution using liquid/solid ratio of 10ml/g. The sample was then immersed in the solution at 90 °C for 1 hour. After the treatment, the powder was washed with deionized water, dried and analyzed at SEM (Fig. 5.10).

From Fig. 5.10b it can be seen that most of metals impurities were removed.

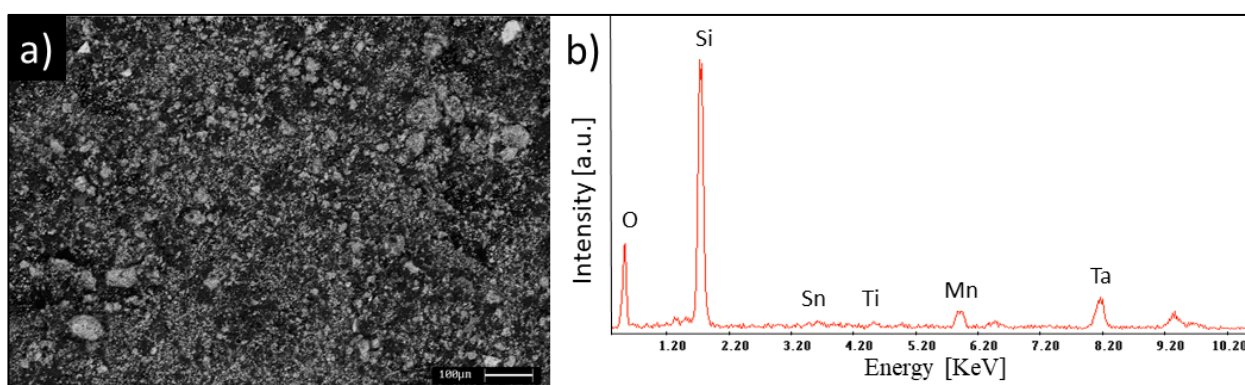


Fig. 5.10. SEM image and EDS spectrum of the powder after hydrochloric acid treatment.

5.1.3.2 Hydrofluoric acid

In order to separate the Silica from the Tantalum pentoxide, a sodium hydroxide solution was tested to react with the silica but it resulted not very efficacious. Therefore, hydrofluoric acid treatment was performed.

In fact, hydrofluoric acid reacts with the silica by the reaction:



And, in excess of HF, also:



Moreover the acid reacts also with tantalum oxide:



The test was performed adding to 1,48g of the obtained powder 18 ml of concentrated hydrofluoric acid (70%) in a platinum crucible.

The temperature was 130 °C to completely evaporate the silicon fluoride and the remaining acid. In fact, silicon fluoride is a volatile compound with a boiling temperature of -65°C whereas tantalum fluoride has a boiling temperature of 229.5°C.

By increasing the temperature, the silicon fluoride should evaporate leaving only tantalum fluoride in the crucible. The residue was then analyzed and the results are reported in Fig. 5.11.

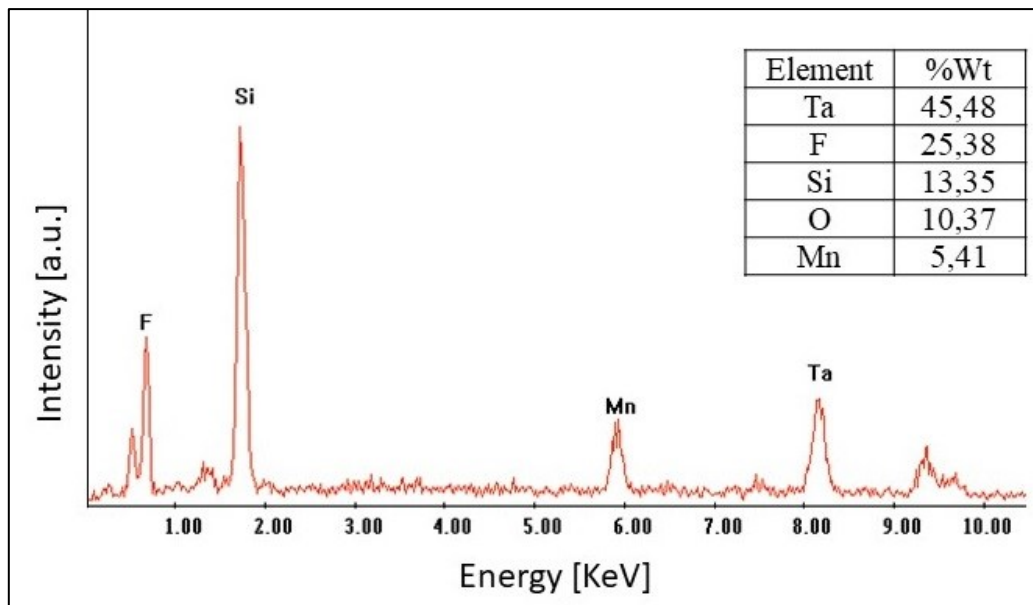


Fig. 5.11. EDS spectrum and semi- quantitative analysis of the powder after hydrofluoric acid treatment.

From the analysis, it seems that the concentration of tantalum in the solid residue increased, even if there is still silica. In particular, in the solid residue it results that the water-soluble part contains more than 50% tantalum (Tab. 5.1).

Element	%Wt
Ta	58,21
F	21,24
O	10,99
Mn	6,31
Si	3,25

Tab. 5.1. EDS semi- quantitative analysis of the water-soluble part of the powder.

5.2 Recovery of neodymium from permanent magnets

Neodymium is a soft silvery metal that can be found in everyday life objects and its main application concerns NdFeB magnets, which are used in numerous household appliances such as washing machines, dryers, computer hard drives, electric or hybrid vehicles etc.

In fact, neodymium-iron-boron permanent magnet materials are of considerable current interest because there is the potential of higher energy product than SmCo₅ or Sm₂TM₁₇ (TM= transition metal) type rare-earth cobalt magnets at significantly lower materials cost. Nd is about 15 times more plentiful and correspondingly lower priced than Sm, and Fe is far less costly than Co. The important magnetic phase, Nd₂Fe₁₄B, with a room-temperature saturation magnetization of -16 kG, makes a maximum energy product of >60 MGOe possible [121].

A Neodymium problem is that it loses significantly magnetic force with high temperatures. This was partly overcome by the addition of other rare earths such as dysprosium and praseodymium. Many neodymium magnets are used in electric motors of hybrid vehicles which can operate up to 200°C. The 10% bulk disproof allows magnets to operate at those temperatures.

The importance of neodymium demand is evidenced by the estimation that in 2010 the worldwide Neodymium production was 45,000 tons [122].

Unfortunately, neodymium tops many of the critical element lists, due to several reasons. First, difficulties encountered in scaling up the production of rare earth elements (often produced as byproducts during the mining of other metals) combined with the sharp increase in demand for technologies depending on these rare earth elements led to a short-lived scarcity crisis in 2011. Second, China currently wields a near-monopoly over rare earth production, with a global 86% market share. In the past years, China has implemented export quotas for rare earths, forcing companies to move the production of neodymium magnet containing products to China in order to secure access to raw materials. Additionally, the use of rare earths has often been criticized for the environmental impacts related to the mining and purification processes.

Given the above reasons, one would expect that recycling of neodymium would have taken high flight in recent years.

However, this is not the case, prompting Reck and Graedel [123] to point to the “seemingly bizarre situation of spending large amounts of technology, time, energy, and money to acquire scarce metals from the mines, and then throwing them away after a single use”.

This is especially true in light of the fact that recycling can play an important role in keeping the rare earth market in balance. Because rare earths occur as a group and are thus mined together, increasing primary production to meet an increase in demand for one of the rare earths can cause a supply glut in the other rare earths [124].

In literature, different recycling techniques for NdFeB magnets are described and they can be divided in pyrometallurgical or hydrometallurgical ones.

Among the pyrometallurgical there are: casting, extraction by liquid metals and formation of glass slag.

Most elegant would be the first one, direct melting, where the magnet is melted and directly reprocessed into NdFeB flakes, so it can be further used in the traditional NdFeB production process. However, neodymium magnets are usually covered with a Nickel and Copper-based protective layer. Although the nickel coating of the HDD magnets is reported to initially not have any negative effects on magnet performance, repeated recycling would lead to a high nickel content, which not only would degrade magnetic performance but also constitute a waste of the nickel fraction [124].

In the other hand, in the formation of glass slag process, magnetic scrap is selectively oxidized to produce an iron-based alloy and a slag containing the rare earths. These are recovered from the slag through leaching and separation. However, although various other pyrometallurgical routes are known [125], they all have in common that they require large amounts of energy for the melting of the material.

Among the hydrometallurgical methods, there is the extraction by ionic liquids, which separate and extract rare earth from other metal elements with a filter membrane.

Another important hydrometallurgical method is the selective leaching designed by Lyman and Palmer [126].

This method involves dissolution of the ground scrap in a H_2SO_4 solution with pH lower than 1. The pH is then increased to 1.5 with sodium or potassium hydroxide: this provokes the precipitation of a neodymium-sodium or neodymium-potassium sulphate. After separation from iron, neodymium can be treated with hydrofluoric acid to form neodymium fluoride, used for production of new NdFeB magnets.

The boron in the sulfuric acid solution is generally converted by further raising the pH in zinc or calcium borate.

Finally, an interesting process is hydrogen decrepitation. The magnets are immersed in hydrogen gas, which causes them to disintegrate into small particles. Because the nickel coating does not react to hydrogen in the same manner, it can be removed through sieving. The powder can be directly reprocessed into new magnets because the particle size in the powder is almost equivalent to the particle size after jet-milling in primary magnet production.

The first part of the work was dedicated to verify if hydrogen decrepitation is possible also through an electrolytic cell.

The second part of the work was focused on the neodymium salts recovery from hydrometallurgical solutions with high purity.

5.2.1 NdFeB magnets

Considerable technological interest has centered on $\text{Nd}_2\text{Fe}_{14}\text{B}$ because of its excellent intrinsic properties [$(\text{BH})^*_{\text{max}} \sim 64 \text{ MGOe}$, $H_a \sim 73\text{kOe}$] and economic advantages over samarium-cobalt materials. Practical magnets with energy products in the 40-50 MGOe range, values significantly larger than any previously attained (Fig. 5.12) have been prepared from melt-spun and sintered

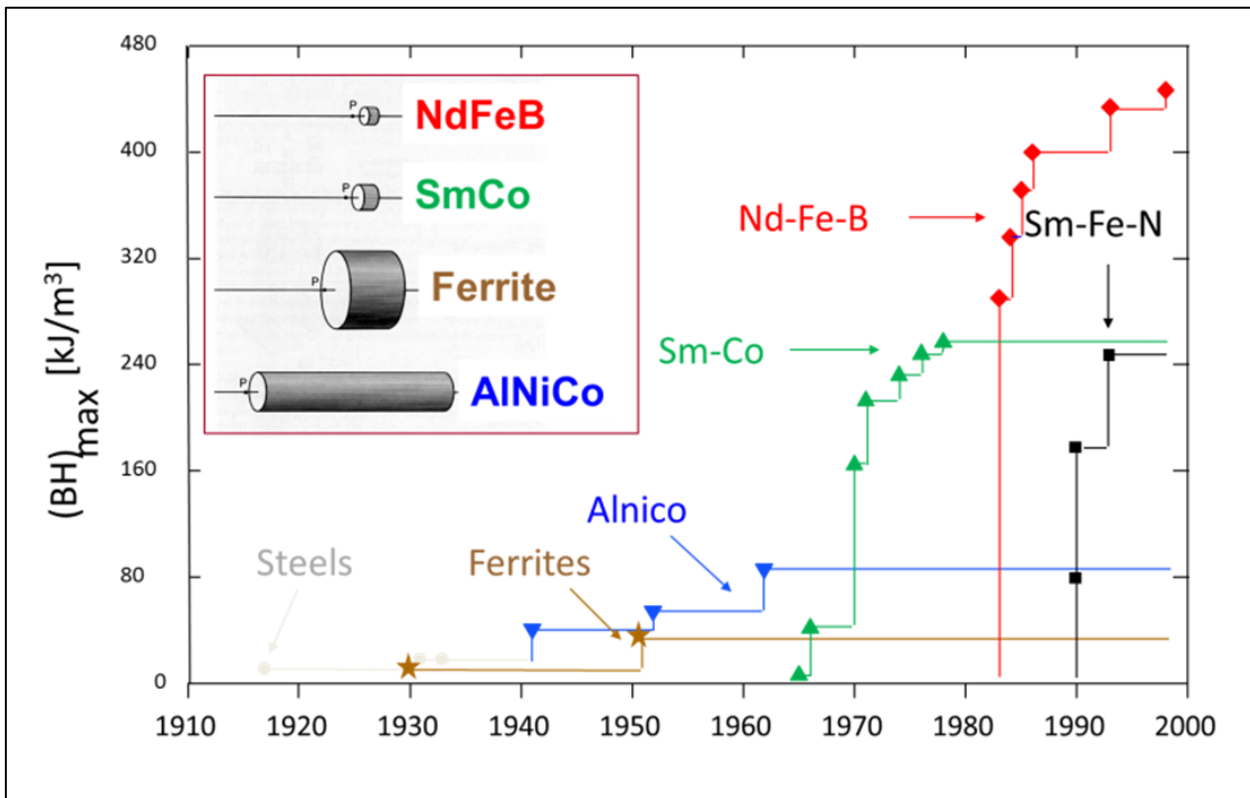


Fig. 5.12. Development of energy density in permanent magnets [64].

alloys, and large-scale production programs employing both approaches have been implemented. The spectrum of applications for NdFeB magnets continues to expand [127].

The production of these magnets begins with the alloy preparation. Neodymium, Iron, Boron and other additives are measured according to the preferred element composition and melted into alloy inside a vacuum induction furnace.

After the melting step, the obtained alloy is pulverized into fine powders that are several microns in size. In order to avoid oxidation, the small powders are protected by nitrogen and argon.

Successively, the powders are pressed into shape in a magnetic field to obtain a preferred magnetization direction. Through this process, magnetic anisotropy is achieved.



Fig. 5.12. *NdFeB magnets before the sinterization process.*

Two methods of pressing exist: perpendicular pressing in a perpendicular magnetic field and parallel pressing in a parallel field. Given a certain grade of magnet, the perpendicular pressed magnet will have a higher performance than the parallel pressed one. However, ring magnets must be pressed with the parallel method. In fact, the neodymium iron boron powder are typically pressed into a basic form (mostly cylinder or cuboid-shaped) (Fig. 5.12). The pressed working

piece receives heat treated in a sintering furnace. Through this process the magnet's volume is reduced by about 50%.

Then, the raw magnets are sawn or rotated until they have the desired size and shape (disc, rod, block, sphere, etc.) (Fig. 13a).

Thereafter, the raw magnets are galvanically coated, normally with a layer of nickel (Fig. 13b).

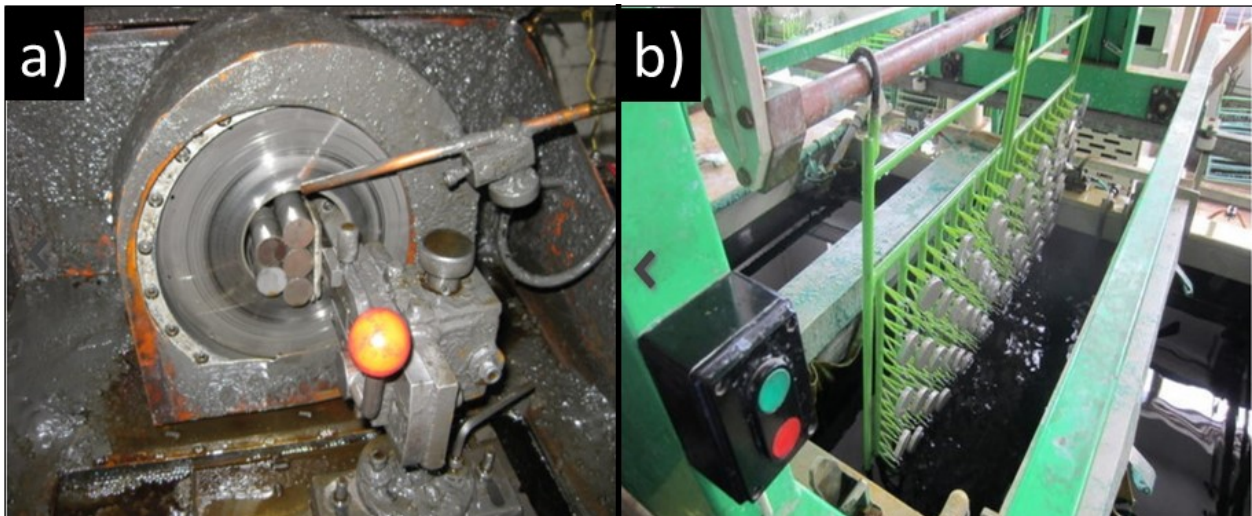


Fig. 5.13. a) *NdFeB magnets sawing* b) *Nickel electrodeposition on the NdFeB magnets.*

Without this coating, magnets would quickly oxidize and disintegrate into grey dust.

Most neodymium magnets have a nickel copper nickel coating.

Now the finished magnets are placed in a magnet coil, through which a strong electrical current is shot for one millisecond. This coil produces a strong magnetic field and the super magnets are being magnetized [128, 129].

5.2.2 Characterization

Two types of neodymium magnets were used for the tests.

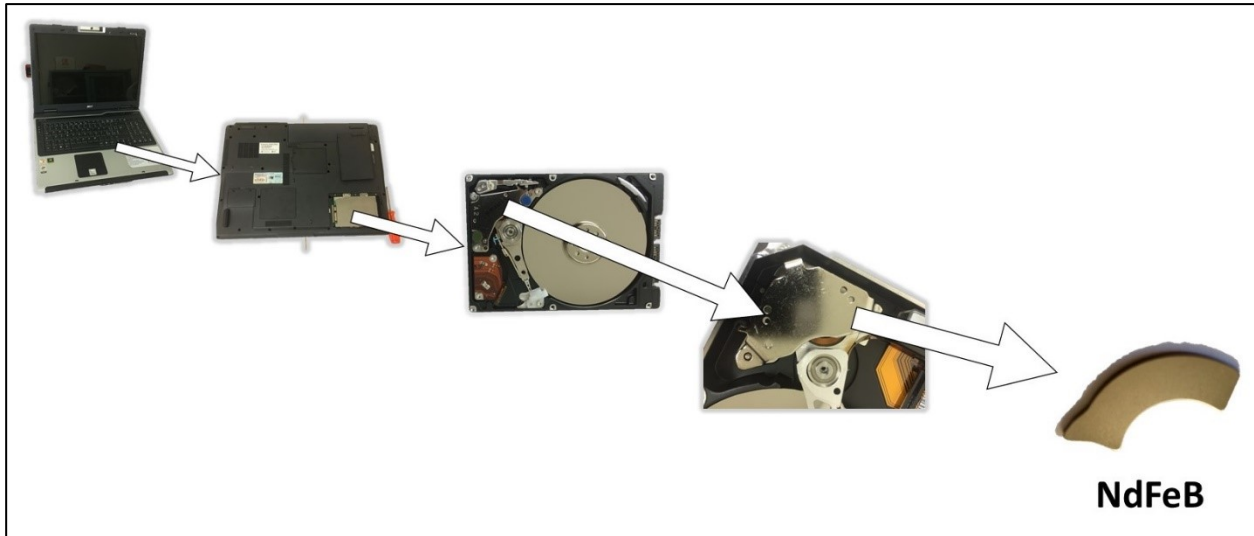


Fig. 5.14. *The recovery of NdFeB magnet form the hard disk of end of life PC.*

The first is generally used is used in drive actuators of the hard disk in computers and was recovered from end-of-life PC as shown in Fig. 5.14.

The other magnets used for the experiments is typically used in household appliances, i.e. in washing machines and is shown in Fig. 5.15.



Fig. 5.15. *The NdFeB magnet typically used in washing machine.*

After recovery of the magnets, the cross section was analyzed with optical and electronic microscope (Fig. 5.16).

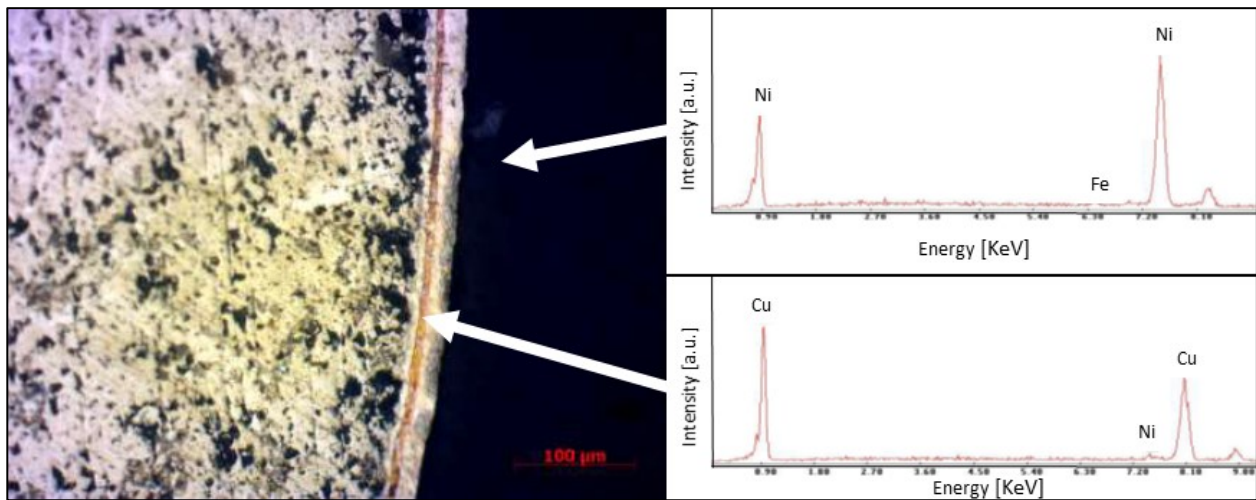


Fig. 5.16. Optical Microscope image of the cross section of one magnet EDS spectra of the layers in the coating of the magnet.

From analysis it results that the magnets are composed by a synthesized NdFeB powder (Fig.5.17), coated with three layers (with total thickness of $25\div 30\mu\text{m}$) constituted of nickel, copper and nickel. The SEM image of sintered powder, in particular, evidenced two phases: one with high concentrations of neodymium and one constituted mainly of iron.

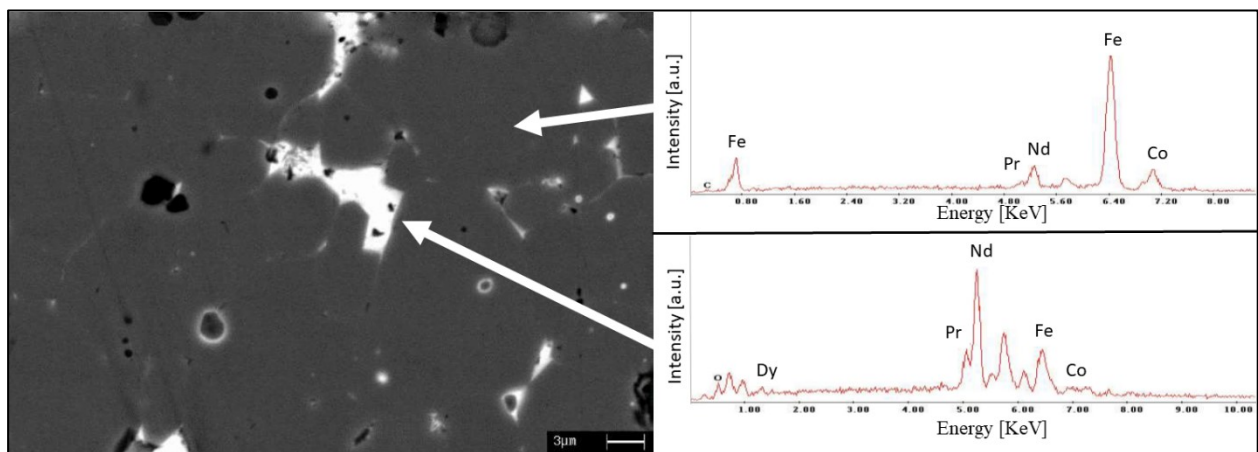


Fig. 5.17. BSE image of the NdFeB magnet with EDS spectra of different parts identified.

5.2.3 Test for “electrolytic decriptation”

As mentioned, a possible solution to recover Nd from magnets is Hydrogen decriptation. By this technique, the hydrogen penetrates in the sintered material and reacts with the matrix forming hydrides. The involved local increase in volume breaks and almost pulverize the material. This phenomenon is already used for magnets recovery and the technique involves high-pressure gaseous hydrogen flow into a sealed chamber [130]. The advantage of this method is that after the treatment only sieving is required to separate the NdFeB powder from the coating but involves the risks due to the use of gaseous hydrogen. In fact, a gas leakage would be very dangerous as it can easily cause explosions.

Therefore, an “electrolytic decriptation” was tested, using the magnet as cathode and reducing hydrogen onto its surface.

A H₂SO₄ solution at pH 5 semi-saturated with Na₂SO₄ to minimize oxygen solubility and reduce the risk of oxidation of the precipitates was used as electrolyte. Platinum electrode was used as anode and the treatments time was 90 min keeping a constant current density of -0.014 A/cm².

During the experiment, as hydrogen bubbles formed on magnet surface, small magnets pieces violently detached from the surface, suggesting that the decriptation occurs.

The detached material was isolated from the solution and analyzed with XRD (Fig. 5.18). From the analysis, it results to be a Neodymium-Iron-Boron hydride, confirming that the decriptation occurred. Nevertheless, this process is still too low for industrial applications and further studied would be required to developed this technique.

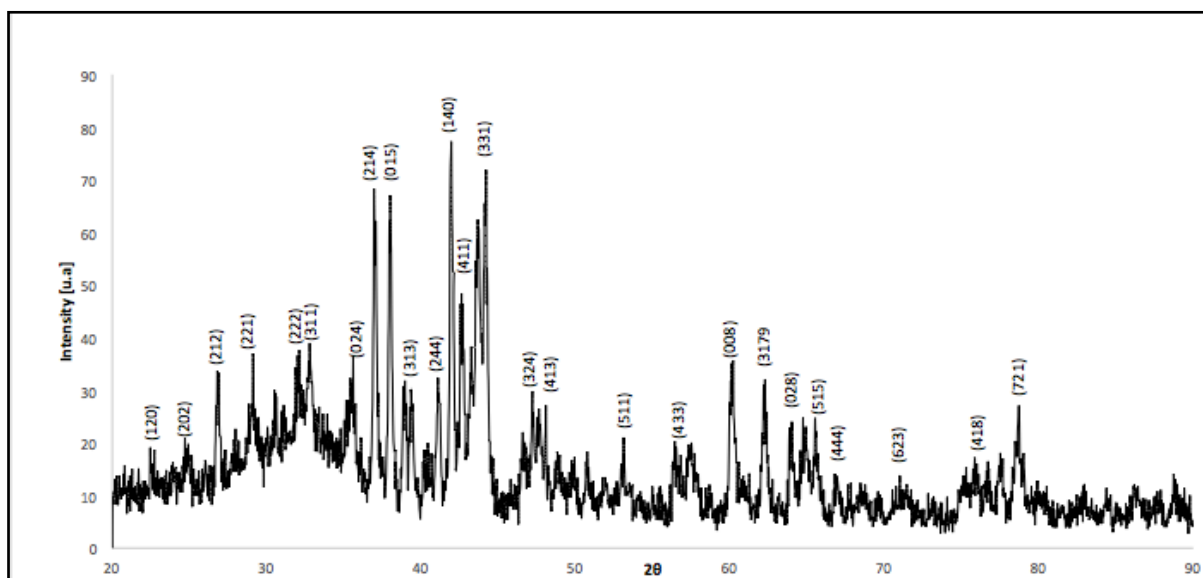


Fig. 5.18. XRD spectrum of Nd₂Fe₁₄BH_{1.86} obtained from “electrolytic decriptation” test.

5.2.4 Neodymium recovery

In this part, Neodymium was recovered as $\text{NaNd}(\text{SO}_4)_2$ through the hydrometallurgical method described in 5.2.1 [126].

In particular, a further step using ammonia was introduced in order of increasing the purity of the obtained salt. The two processes are shown in Fig. 5.19.

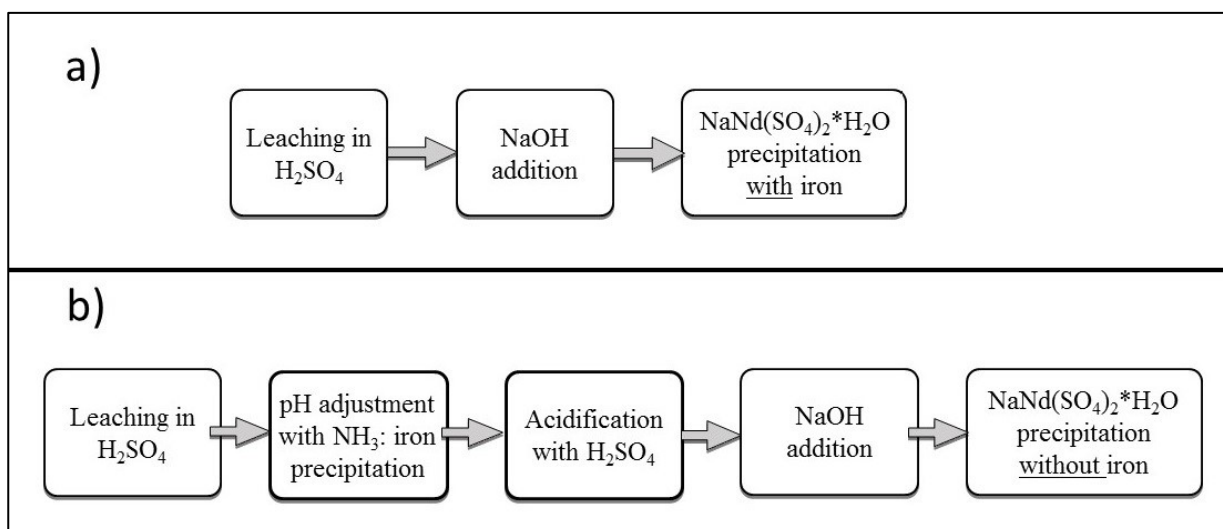


Fig. 5.19. Scheme of the processes to recover Neodymium salts: a) method found in literature; b) process modified to increase purity of the recovered salt.

6 g of magnet was leached in 60 ml of 2M H₂SO₄ solution. The obtained solution was then separated into two equal parts of 30 ml each. The first was used as a comparison and there was added NaOH causing the neodymium salt precipitation.

The other fraction of solution, before NaOH addition and neodymium salt recovery, was treated with NH₃.



Fig. 5.20. The Neodymium salt precipitated from the solution.

In the first case, the pH was increased with NaOH to 1.5 and the precipitated neodymium salt (Fig. 5.20) was isolated, washed and analyzed with SEM. EDS spectrum is reported in Fig. 5.23a.

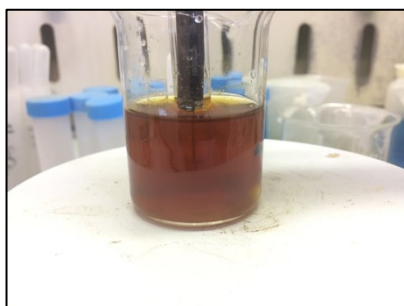


Fig. 5.21. The iron hydroxide (goethite) precipitated from the solution.

After neodymium precipitation, iron can be recovered from the solution. In this case, pH is further increased with NaOH addition to 5 causing the precipitation of a brown gelatinous substance composed of a ferrous hydroxide called goethite (Fig. 5.21). The precipitate in fact, was analyzed with XRD, which confirmed its composition (Fig. 5.22).

The recovered goethite was used for the synthesis of iron nanoparticles described in Chapter 6.6.

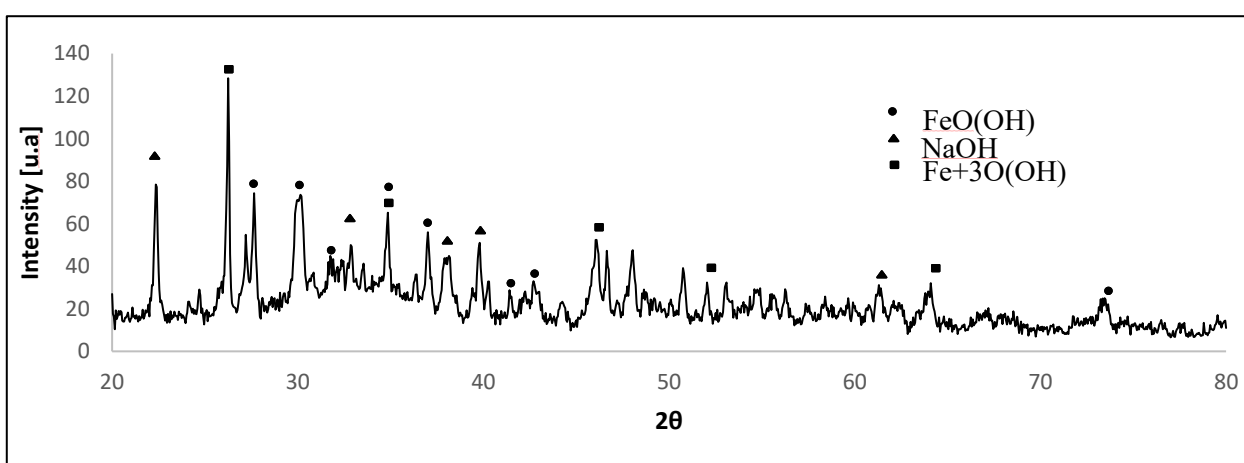


Fig. 5.22. XRD spectrum of the precipitated goethite.

As shown in Fig. 5.23a, the recovered neodymium salts contain iron impurities. To reduce such impurities, the ammonia treatment was introduced.

The pH of sulfuric acid solution was raised to 7 by ammonia addition causing ferrous hydroxides to precipitate before neodymium salt.

The precipitate was separated by centrifugation, washed with deionized water, dried and analyzed. After that pH was adjusted to 0 with H₂SO₄ addition and then NaOH was added increasing pH to 1.5 and recovering neodymium salt. The EDS spectrum is reported in Fig. 5.23b and the semi-quantitative analysis in Tab. 5. 2. Moreover XRD is reported in Fig. 5.24.

Process	O	Na	S	Pr	Nd	Fe	Dy
a	48,46	7,64	14,72	4,09	14,59	8,12	2,38
b	39,44	10,72	15,74	6,22	22,49	1,74	3,61

Tab. 5.2. Semi quantitative analysis of the neodymium salts recovered with literature (a) and modified method (b).

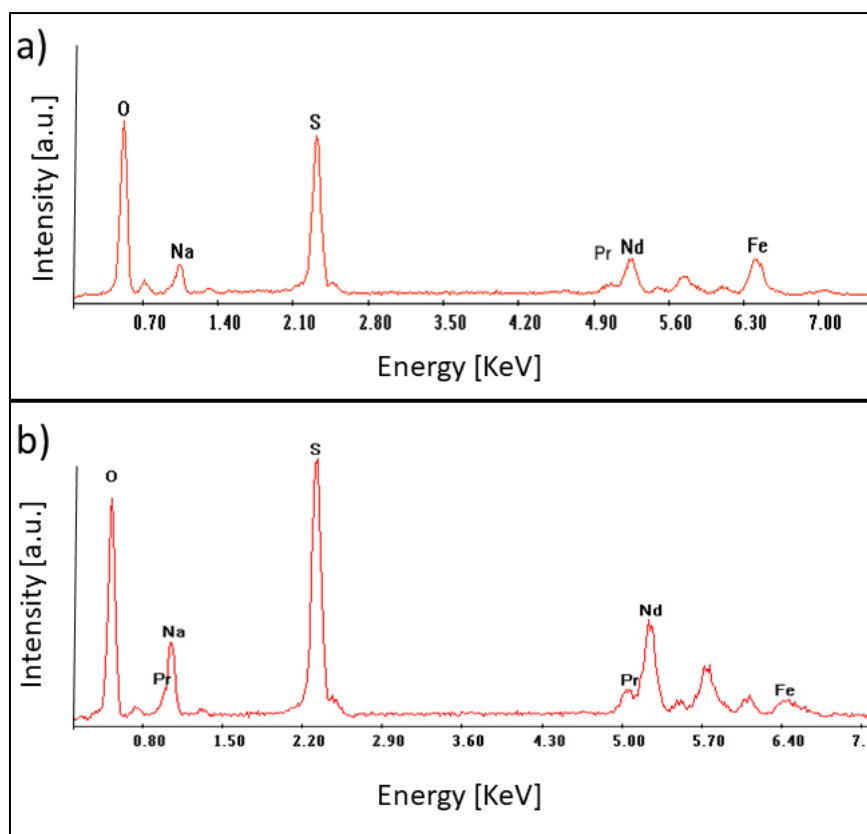


Fig. 5.23. EDS spectra of the recovered neodymium salts obtained with literature (a) and modified method (b).

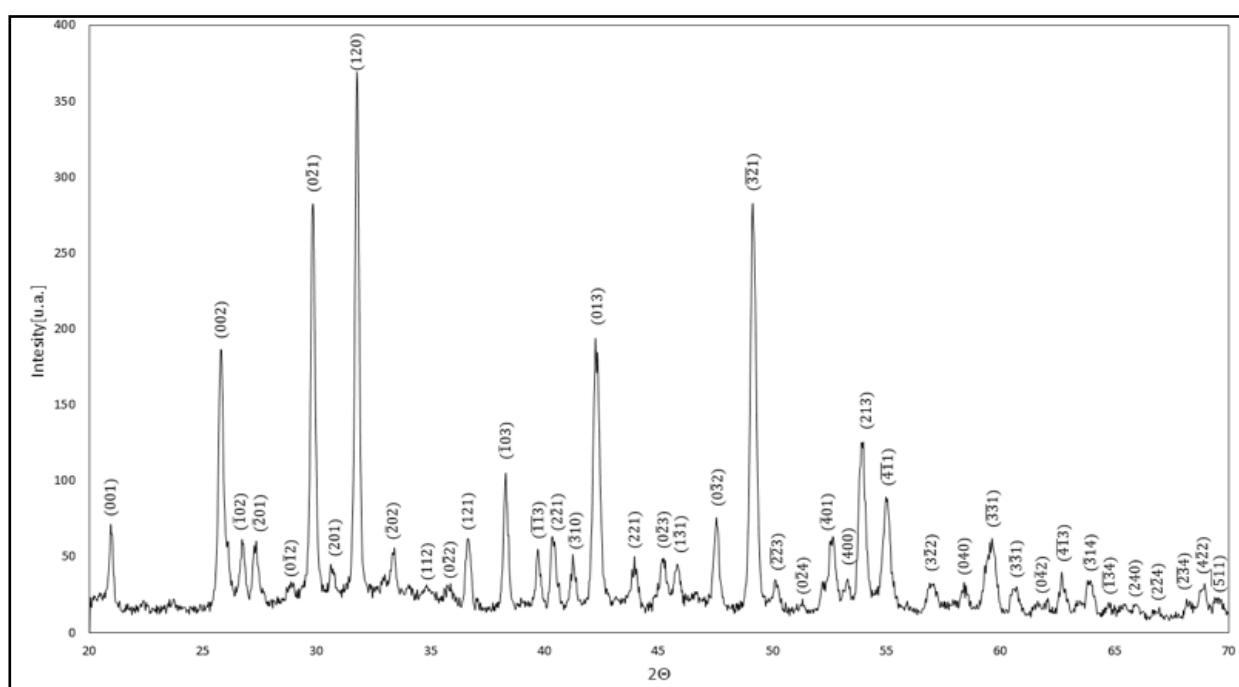


Fig. 5.24. XRD spectrum of the recovered neodymium salt.

5.3 Concluding remarks

In this chapter two resource recovery from wastes were studied. First tantalum was recovered from capacitors.

In this case a method was studied using hydrofluoric acid which allows eliminating almost all silica from the sample by avoiding the waste of raw material by sieving. The recovered material has a very high percentage of Ta. However, further studies may lead to techniques for obtaining tantalum metal or TaO₅ oxide from the fluoride.

The neodymium recovery from permanent magnets was then studied. In particular electrolytic decriptation was tested.

Moreover, the hydrometallurgical treatment known in literature was modified introducing an ammonia treatment which increase the purity of the recovered neodymium-sodium sulfate.

Chapter 6

Green synthesis of nanoparticles from e-waste

In recent years, many attempts have been made to recover metals from electric and electronic wastes; these in fact contain significant amounts of precious metals like gold, palladium, and silver, along with a high amount of copper, silicon, aluminum, tin etc. [131].

By proposing new processes that allow to recover metals as nanoparticles a further benefit could be achieved, beside the intrinsic value of the metals.

As a matter of fact, nanoparticles exhibit very interesting and promising properties in comparison with the corresponding bulk material counterparts [132]. In fact, nanoparticles possess particular properties due to the high surface/bulk ratio and often exhibit size-dependent properties that are profoundly different from the corresponding bulk material counterparts. Size-dependent characteristics of interest include optical, magnetic, catalytic, thermodynamic, electrochemical, and electrical transport properties [133].

Nanoparticles can be produced essentially by two ways: top down and bottom up approach. The first consists in reducing the dimensions of a materials to the nano-scale thanks to operations like milling or cyclic cooling; This way, consisting essentially in a mechanical grinding, produces nanoparticles that usually have wide dimensional distribution, different morphologies and could contain also impurities coming from the equipment. Some materials, with particular thermal properties, can be instead reduced into nanoparticles with successive thermal shocks.

The most applied approach is actually the bottom up, that comprises different physical or chemical methods, as is visible in Fig. 6.1, and the most improved is the liquid/liquid methods.

In particular, the most often used method for synthesis of metallic nanoparticles is the chemical reduction method, which deals with the reduction using reducing agents like sodium borohydride or sodium citrate.

Moreover, metal nanoparticles, independently how they have been synthesized, need to be stabilized by a “protective layer”. In the case of synthesis without stabilizing agent the protective layer is made by the electric double layer (electrostatic stabilization), which gives stable dispersion but very diluted. With such kind of stabilization, it is very difficult to extract the particles and disperse them in another solvent. It is necessary to use polymers as steric capping agent for obtaining colloidal solution with higher concentration, and for extracting the nanoparticles. The capping agent not only provides a barrier among the nanoparticles, which prevent their further

aggregation, but it is also very important because it can influence the morphology of the nanoparticles [134].

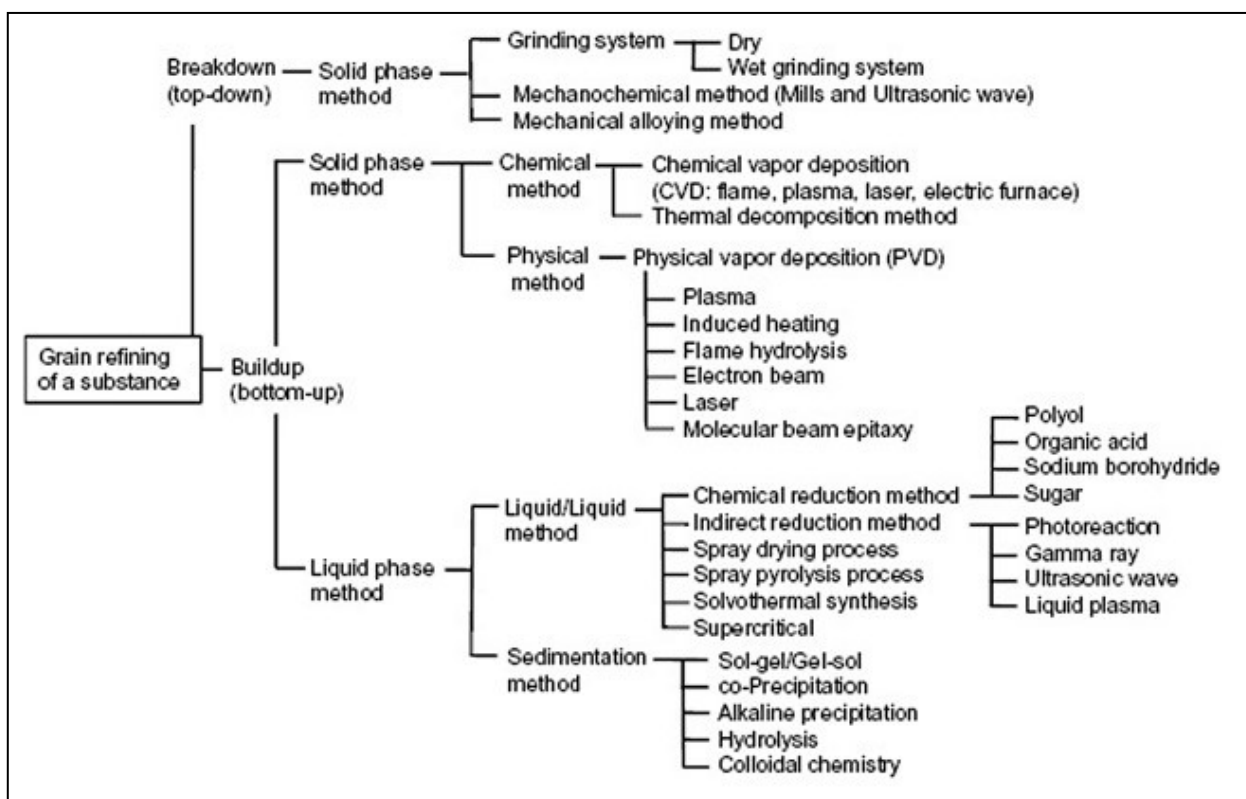


Fig. 6.1 The exiting processes for the synthesis of nanoparticles.

Moreover, processes environmentally friendly should be preferred to limit both the use of energy and the dispersion of pollutants in the environment. In fact, since the publication of the work of Paul Anastas and John C. Warner, finding ways to minimize the environmental impact, where possible, is considered an urgent topic in the field of chemical research [135], as described in Chapter 1.3. The green chemistry principles can be very successfully applied to the nanoparticles synthesis especially for the choice of non-toxic reaction components, the atom efficiency, the E-factor, the control of the exposure pathway and the waste management.

However, the challenge was to develop processes for the synthesis of nanoparticles using as raw material the leaching solution of electronic scraps: all the processes available in literature start from single reagents with high purity.

Moreover, in this chapter also the effect of ultrasound and microwaves will be discussed, as their green value is known in chemistry [136, 137]. In fact, it seems that both these two techniques are able to reduce the dimensions of the particles, due to two different effects: when using ultrasound, the phenomenon of micro-cavitations (Chapter 1.4) occurs, whereas localized “hotspot” heating characterizes the microwaves assistance [138, 139, 140].

Different nanoparticles were synthesized from wastes: tin oxide, copper, cuprous oxide, silver, gold and iron.

In order to synthesize tin oxide, silver, copper and copper oxide nanoparticles, as raw material was used the pre-treatment nitric solution used for treating PCBs described in Chapter 3.

In this case, first a precursor of tin oxide was precipitated from the nitric acid solution by three different techniques: i) conventional heating; ii) microwave irradiation; and iii) ultrasound treatment. Secondly, this precursor was transformed into tin oxide nanoparticles by heat treatment in a furnace.

After that, hydrochloric acid was added to the nitric acid solution to induce the precipitation of silver chloride. Silver chloride was reduced to metallic silver nanoparticles in an ammonia solution using glucose syrup as both reducing and capping agent. The reduction reaction was carried out using: i) conventional heating; ii) microwave irradiation and; iii) ultrasound treatment.

After tin and silver recovery from the acid solution, copper was precipitated from the solution by cementation with iron powder. From the recovered metallic copper, both copper and cuprous oxide nanoparticles can be synthesized.

Copper and cuprous oxide nanoparticles have been synthesized dissolving the recovered metallic copper in nitric acid and reducing it respectively with L-ascorbic acid or glucose with two different methods.

These processes are shown in Fig. 6.2. Moreover, gold nanoparticles were synthesized using as raw material PCBs even though in this case the process was different from the one previously described.

The PCBs were treated with nitric acid before grinding because most of the gold is located on the surface of the board (as shown in Chapter 3). The recovered gold was then dissolved by leaching in aqua regia. After pH correction, gold was reduced with L-ascorbic acid. Furthermore, some experiment to perform Brust synthesis using the aqua regia solution as raw material were performed.

Finally, as preliminary work, iron nanoparticles were synthesized from iron hydroxide precipitated in the form of goethite by the sulfuric acid solution used for treating permanent magnets described in Chapter 5. As reducing agents for iron there were used sodium borohydride and eugenol, a natural reducing agent directly extracted from the cloves.

The processes for gold and iron nanoparticles synthesis are shown in Fig. 6.3.

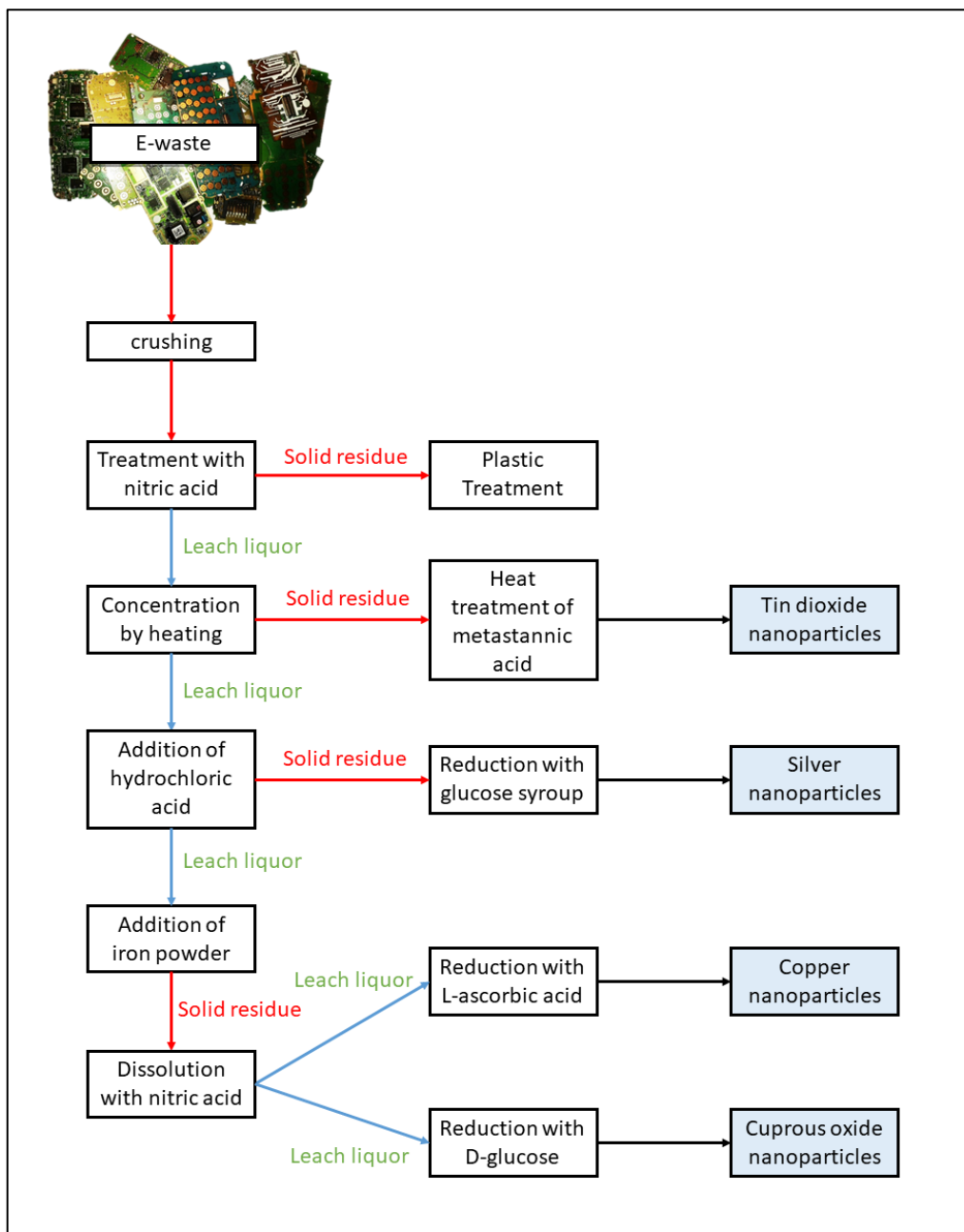


Fig. 6.2 Scheme of the process for the synthesis of tin oxide, silver, copper and cuprous oxide nanoparticles from wastes.

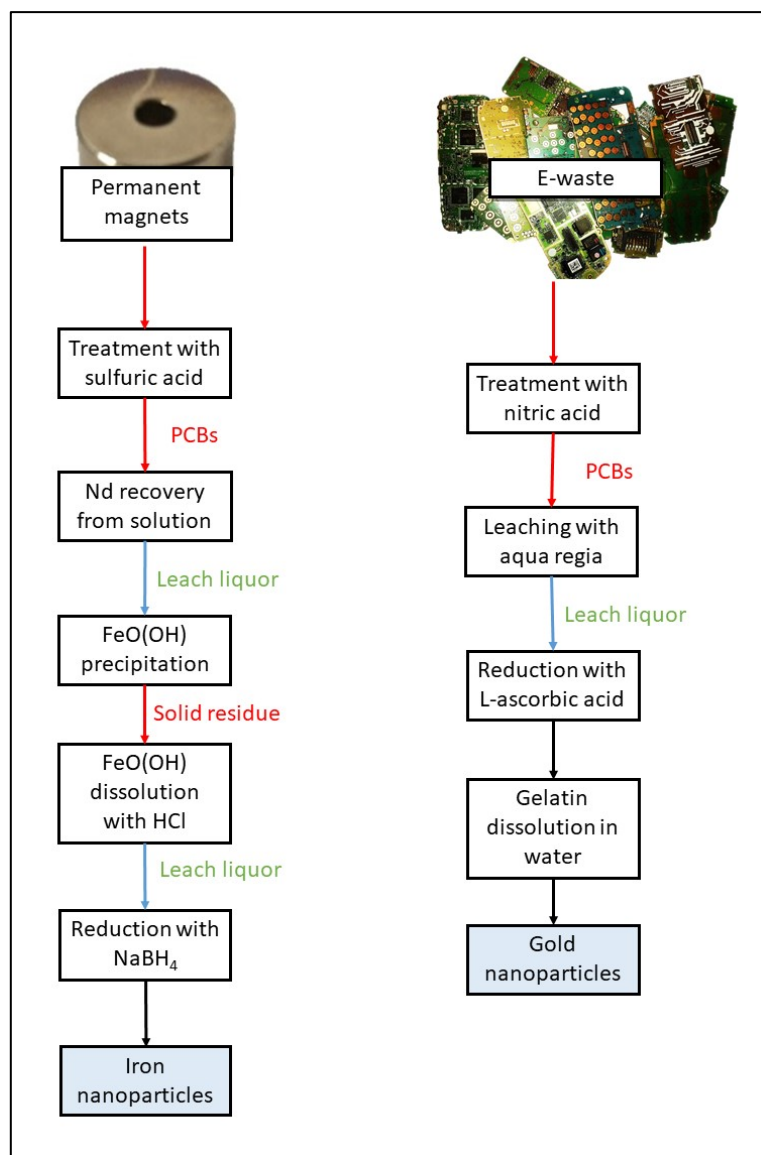


Fig. 6.3 Scheme of the process for the synthesis of iron and gold nanoparticle from wastes.

6.1 Tin oxide nanoparticles



Fig. 6.4 The synthesized tin oxide nanoparticles.

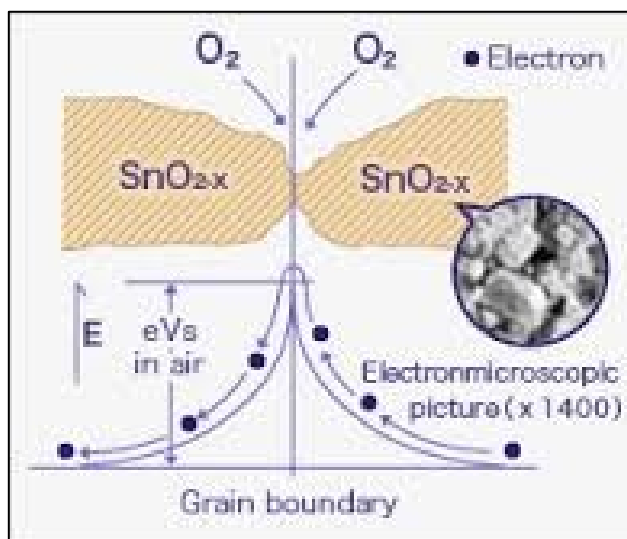


Fig. 6.5 SnO_2 nanoparticles can find application in gas sensor (to detect CO and O_2).

Tin oxide is an important n-type wide-energy-gap semiconductor and, due to its properties, tin oxide nanoparticles are interesting for the applications in gas sensors (Fig. 6.5). The SnO_2 can also find applications as optical electronic devices, transistors, electrode for dye-sensitized solar cells etc. [141, 142].

Several methods have been developed to synthesize SnO_2 nanostructures, e.g. hydrothermal methods, chemical vapor deposition, thermal evaporation of oxide powders, sol-gel method and thermal decomposition [141, 142, 143, 144].

Compared to existing processes used to synthesize SnO_2 nanoparticles, the method adopted in this work proposes the following new approaches: i) as raw material the electronic waste leaching solution coming from WEEE treatments, and ii) the process assistance of ultrasound or microwave irradiation.

This process can be interesting as there is huge amount of tin in e-waste.

In fact, tin and tin alloys are used in the electronic boards to solder the electronic components. In Fig. 6.6 are shown two electronic scraps and the SEM backscattered images of two different types of tin-based solders found in the electronic scraps. One (Fig. 6.6a) was constituted only by tin (Fig. 6.6c) and showed a typical dendritic structure, whereas the other one (Fig. 6.6b) by an alloy of tin and lead (Fig. 6.6d and 6.6e) with a eutectic microstructure.

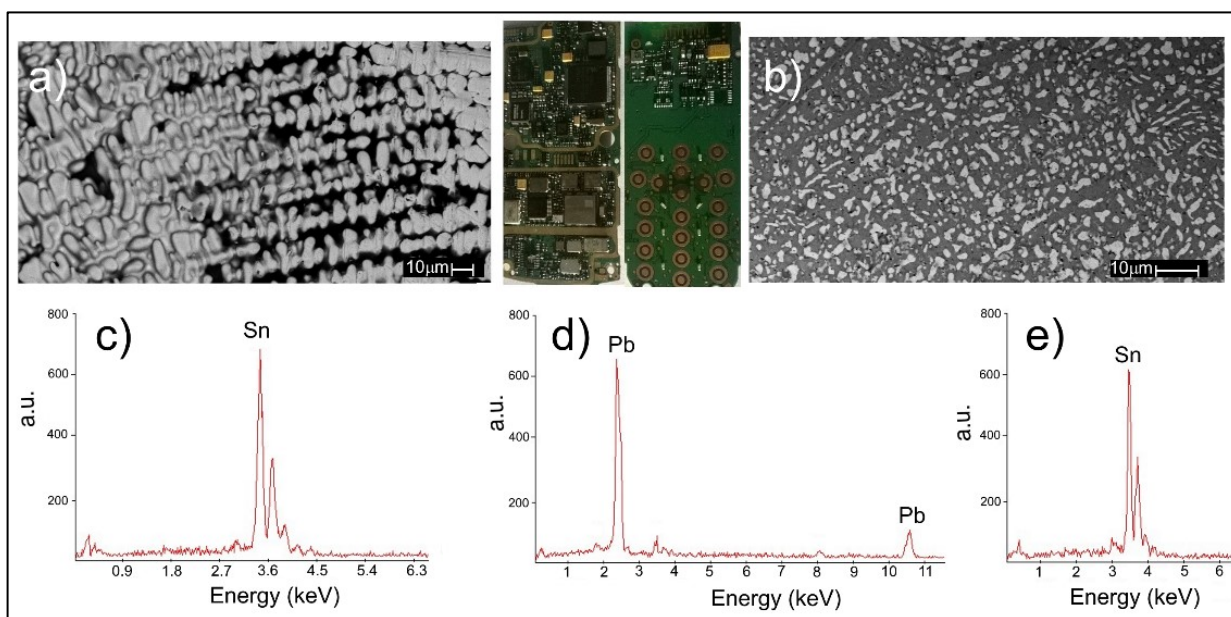


Fig. 6.6 Electronic scrap of end of life mobile phones and the SEM-BSE images of the microstructure of two different solders components with EDS spectra.

6.1.1 Synthesis

The solutions coming from the pre-treatment of end-of-life mobile phone scraps were used as raw material. In Fig. 6.2 the scheme of the whole process is represented. The pre-treatment consisted in the leaching of the crushed electronic scraps by 7 M nitric acid solution for two hours at 60°C. After the pre-treatment most of the metals in the electronic scraps were extracted, whereas gold remained in the solid residue. The resulting solution contained mainly Cu, Ni, Fe, Sn, Ag, Al, Cr, Zn, and Mg. The composition of a representative leaching solution used in this study is reported in Tab. 6.1. The concentration of Sn was about 1200 ppm.

The first step of the process consisted in the precipitation of metastannic acid (hydrated tin oxide), which is a precursor of SnO₂. The precipitation occurred during volume reduction by evaporation of the solution. The evaporation was achieved by three different experimental methods: conventional heating at 85°C for 6 hours, ultrasound irradiation for 1 hour, microwave irradiation for 15 minutes. All three experiments were performed to obtain a reduction of 90% in volume.

The low frequency (20 kHz) ultrasound was generated by titanium probe. Microwaves were supplied by a microwave oven working at 500 W. The precipitated powders were characterized with SEM with XRD. FT-IR analysis was performed to verify the presence of metastannic acid.

The metastannic acid powders were treated in a furnace at different temperatures (200, 400, 600°C) for 2 hours to induce the decomposition of metastannic acid in tin dioxide and water. The treated powders were characterized by XRD and TEM.

6.1.2 Characterization

The use of microwave or ultrasound irradiation reduced the particle size of the powder precipitated during the volume reduction, as shown by SEM analysis (Fig. 6.7).

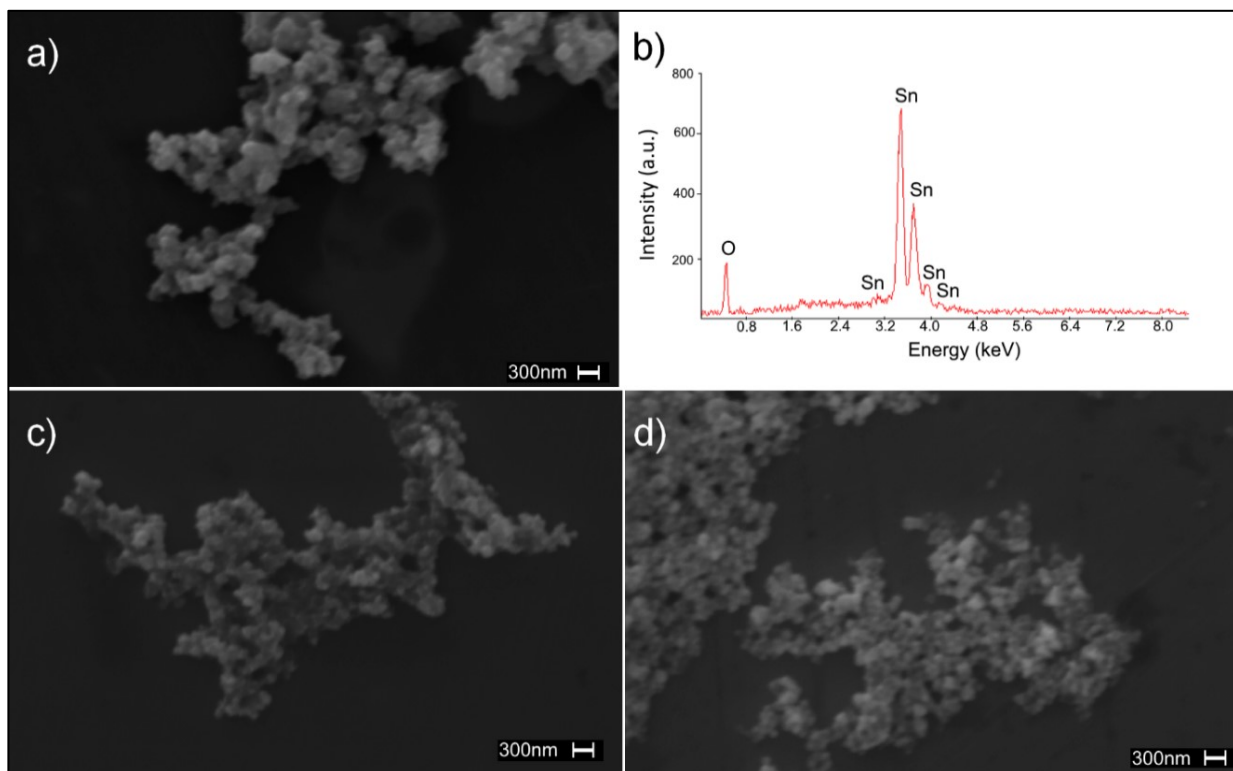


Fig. 6.7 SEM-SE images of powder obtained with: a) conventional heating; c) microwaves; d) ultrasound. In b) EDS spectrum of the powder (extended area in correspondence of the particles).

The powders were in the form of agglomerates and composed by Sn and O, suggesting the presence of metastannic acid (Fig. 6.7). The agglomerates obtained by conventional heating contained particles with an average size of about 400 nm, whereas the ones produced by microwaves or ultrasound contained particles with an average size of 200 nm and 150 nm, respectively. The ICP analysis showed that about 95% of Sn was recovered (Tab. 6.1, Tab. 6.2).

Cu	P	Ni	Fe	Ca	Mg	Pb	Al	S
15960	1211	1879	1123	453	89	839	198	86
Sn	Co	Si	Na	Zn	B	Ba	Cr	Ag
1190	30	22	21	115	14	560	10	543

Tab. 6.1 Elemental composition of the nitric acid solution after the treatment of PCBs in ppm.

Cu	P	Ni	Fe	Ca	Mg	Pb	Al	S
15988	1198	1788	1098	398	79	1115	187	80
Sn	Co	Si	Na	Zn	B	Ba	Cr	Ag
30	32	18	23	110	12	712	9	530

Tab. 6.2 Elemental composition of the nitric acid solution after tin removal by evaporation in ppm.

FT-IR analysis was performed to check the presence of metastannic acid (Fig. 6.8). The FT-IR

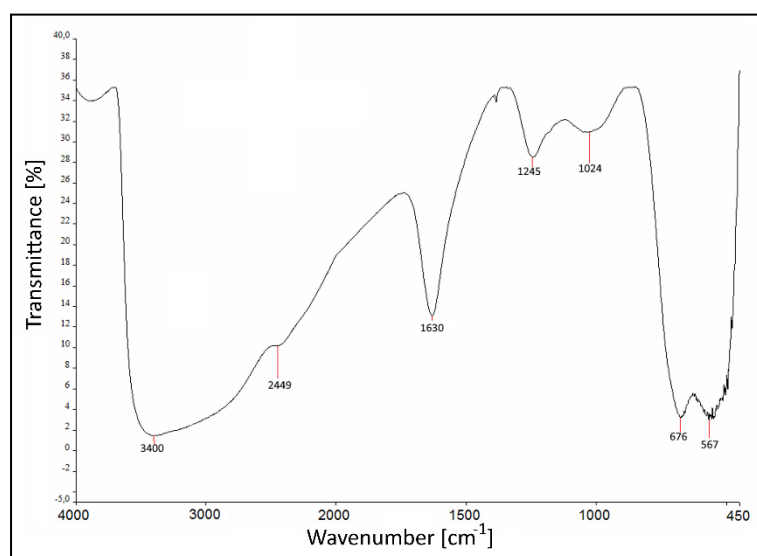


Fig. 6.8 FT-IR spectrum of the powder.

spectrum shows a strong vibration from 3500 to 2500 cm^{-1} , indicating the presence of water and Sn-OH groups (OH stretching). The peak at 1630-1626 cm^{-1} can be assigned to the OH bending of water molecules. The vibration at 554-535 cm^{-1} is related to the terminal oxygen vibration of Sn-OH, and the peak at 672-663 cm^{-1} is attributable to oxo-bridge functional groups (Sn-O-Sn). Therefore, the precipitate was metastannic acid (H_2SnO_3).

The concentration by evaporation of a nitric acid solution in which tin has

been oxidized, caused the precipitation of a hydrated tin oxide, called metastannic acid (H_2SnO_3), as described in Equation 6.1:



The XRD analysis showed broad peaks that were attributed to the presence of SnO_2 in form of amorphous metastannic acid (Fig. 6.8). The following heat treatments at 200°C and 400°C induced a partial crystallization of the metastannic acid, whereas the complete transformation into SnO_2 occurred at 600°C, as shown in Fig. 6.9. The peaks of the sample treated at 600°C were indexed and attributed to SnO_2 in cassiterite form, with tetragonal crystal system (ICSD n. 98-000-9163).

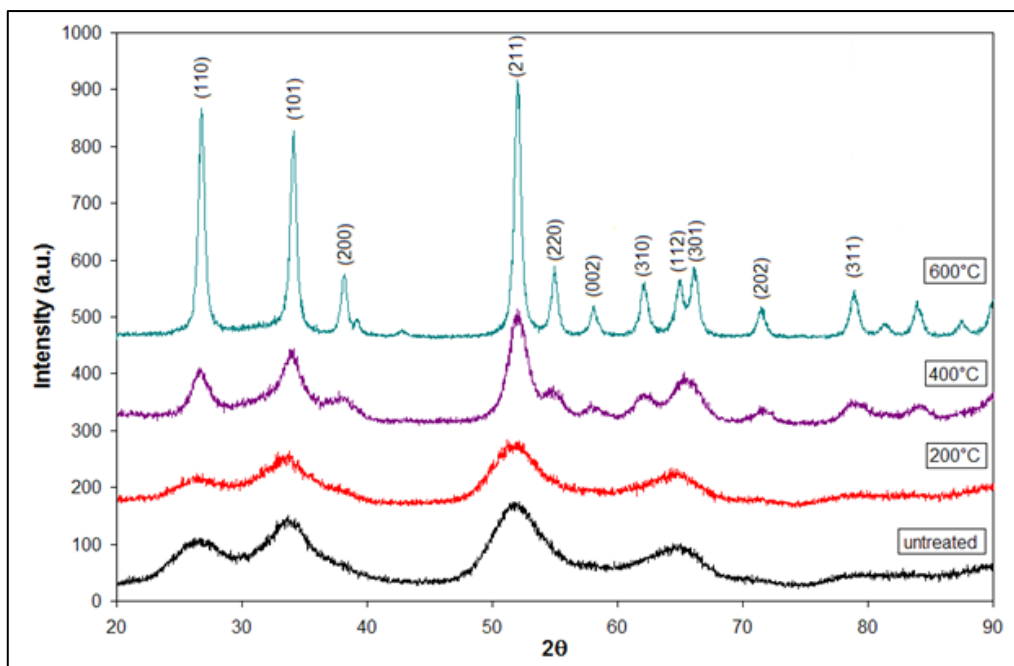


Fig. 6.9 XRD patterns of the powder before and after the heat treatments.

TEM analysis of the thermal treated powders at 600°C are shown in Fig. 6.10. The powders were composed by nanoparticles with a spherical shape. The evaporation method, with which the precursor was previously precipitated, influenced the size of the particles. As a matter of fact, an average size of 15 nm was measured for the nanoparticles whose precursor was obtained by conventional heating (Fig. 6.10a); whereas an average size of 8 nm was estimated for the nanoparticles with the precursor produced by ultrasound or microwave (Fig. 6.10b, c).

The selected area electron diffraction analysis was carried out, and the indexing of diffraction patterns confirmed that these nanoparticles were SnO₂.

In comparison with conventional heating, the use of microwave and ultrasound during the precipitation of metastannic acid can reduce the reaction time and produce nanoparticles of SnO₂ of smaller size.

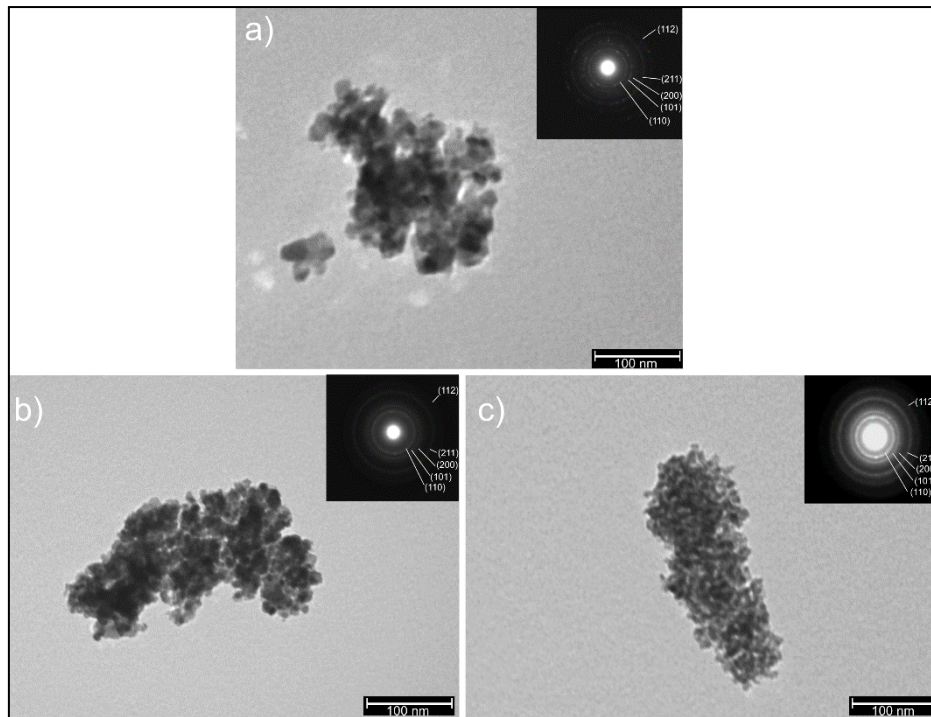


Fig. 6.10 TEM images and SAED of SnO₂ nanoparticles obtained with the metastannic produced by: a) conventional heating; b) microwaves; c) ultrasound.

6.2 Silver nanoparticles



Fig. 6.11 *The synthesized silver nanoparticles.*



Fig. 6.12 *Example of Silver nanoparticles application: toothpaste.*

Silver nanoparticles are among the most studied nanoparticles because of their particular properties, and their quite simpler and more known synthesis process in comparison with other metallic nanoparticles. In fact, the synthesis of a citrate-stabilized silver colloid was reported by M. C. Lea over 125 years ago, in 1889 [145].

In addition, colloidal silver shows good conductivity, chemical stability, catalytic and antibacterial activity [146] thus finding applications in different fields, such as antibacterial, antistatic, and cryogenic superconducting materials. In particular, the antimicrobial action of silver nanoparticles raises a particular interest (Fig. 6.12). In fact, silver ions and their related compounds have low toxicity toward animal cells but present a high toxicity to microorganisms like bacteria and fungi [147]. This effect is extended to silver nanoparticles, which have high potential for releasing silver ions because the high surface per mass of silver influences the solubility and dissolution kinetics of silver which are function of silver metal size. Many studies has been carried out about the effects of both size and shape on antibacterial efficacy [148, 149]. It seems that Ag NPs of size 25 nm possessed the highest antibacterial activity. This effect is exploited for coating of medical devices and in particular wound dressing with the silver nanoparticles [150].

Several works have been carried out on the green synthesis of Ag NPs. Y. Park and al. wrote an interesting review about the use of polysaccharides and phyto-chemicals as reducing and capping agents [151]. Extracts from bio-organisms may act both as reducing and capping agents in Ag NPs synthesis. The reduction of Ag⁺ ions by combinations of biomolecules found in these extracts such as enzymes/proteins, amino acids, polysaccharides, and vitamins is environmentally friendly, yet

chemically complex [152]. Rowel et al. instead analyzed the green synthesis with plants extracts, bacteria or fungi [153].

However, the most frequently applied method for the synthesis of silver nanoparticles is the chemical reduction in organic solvents or water. Typically the method consists of reducing silver nitrate with borohydride, citrate, ascorbate, and elemental hydrogen [146, 154, 155].

For the synthesis of Ag nanoparticles, the novelty of the proposed method consisted in using at the same time: i) electronic waste leaching solution as raw material; ii) the reduction of silver chloride with glucose in water; and iii) the assistance of microwave or ultrasound irradiation during the glucose reduction. In this respect, silver chloride represented an innovation in the synthesis of silver nanoparticles, as silver nitrate is generally used as raw material [156, 157, 158, 159].

6.2.1 Synthesis

The liquid residue coming from the tin recovery was brought to the initial volume by adding deionized water and the elemental composition is shown in Tab. 6.2.

The solutions, as revealed from ICP analysis, contained a lot of different metals, in particular copper, iron and nickel. The amount of silver was about 500 ppm.

Moreover, the solution was strongly acid. Therefore, although many ways of recovery of silver are

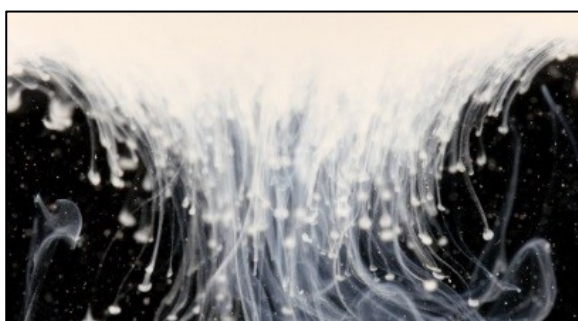


Fig. 6.13 Example of precipitation of silver chloride.

possible (for example cementation with less noble metals or electrodeposition), the most efficient and selective method is the precipitation into silver chloride form. Chlorides in fact can be easily added to the solution as hydrochloric acid. Without introducing others metals ions into the solution, this acid rapidly induced the precipitation of silver chloride due to the low solubility of this salt.

The experiments for the recovery of silver were performed in a 1000 ml Pyrex-glass containing 500

ml solution, to which 10 ml hydrochloric acid 37% was added to precipitate of silver chloride.

The salt precipitated with an average size of about 4 μm (Fig. 6.14a).

For the synthesis of the silver nanoparticles, 15 mg silver chloride was dissolved in 15 ml ammonia solution (30%) in a 200 ml Pyrex-glass, to which was added 150 ml water and then 20 g glucose syrup. The solution obtained was heated by three different methods to promote the reduction: conventional heating at 50°C for 1 hour, ultrasound irradiation for 10 minutes (maximum temperature 50°C), and microwaves irradiation for 10 minutes (maximum temperature 100°C).

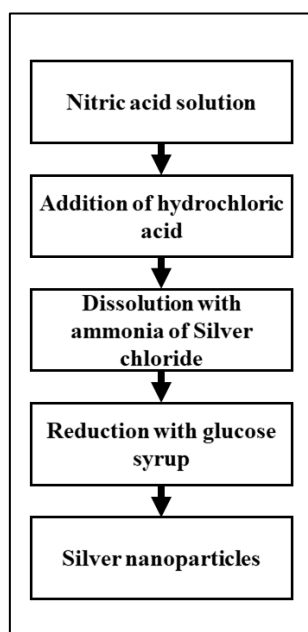


Fig. 6.14 Process for the synthesis of silver nanoparticles.

6.2.2 Characterization

The ICP analysis showed that about 95% silver was recovered after the precipitation of the chloride salt.

Cu	P	Ni	Fe	Ca	Mg	Pb	Al	S
15216	974	1560	986	217	43	1027	153	130
Sn	Co	Si	Na	Zn	B	Ba	Cr	Ag
26	16	18	20	60	10	647	8	12

Tab. 6.3 Elemental composition of the nitric acid solution after tin and silver removal. This solution was successively used for copper and cuprous oxide nanoparticles synthesis.

The irradiation of microwaves during the addition of HCl promoted the reduction of silver chloride size and a powder with particles lower than 1 μm was obtained (Fig. 6.15c).

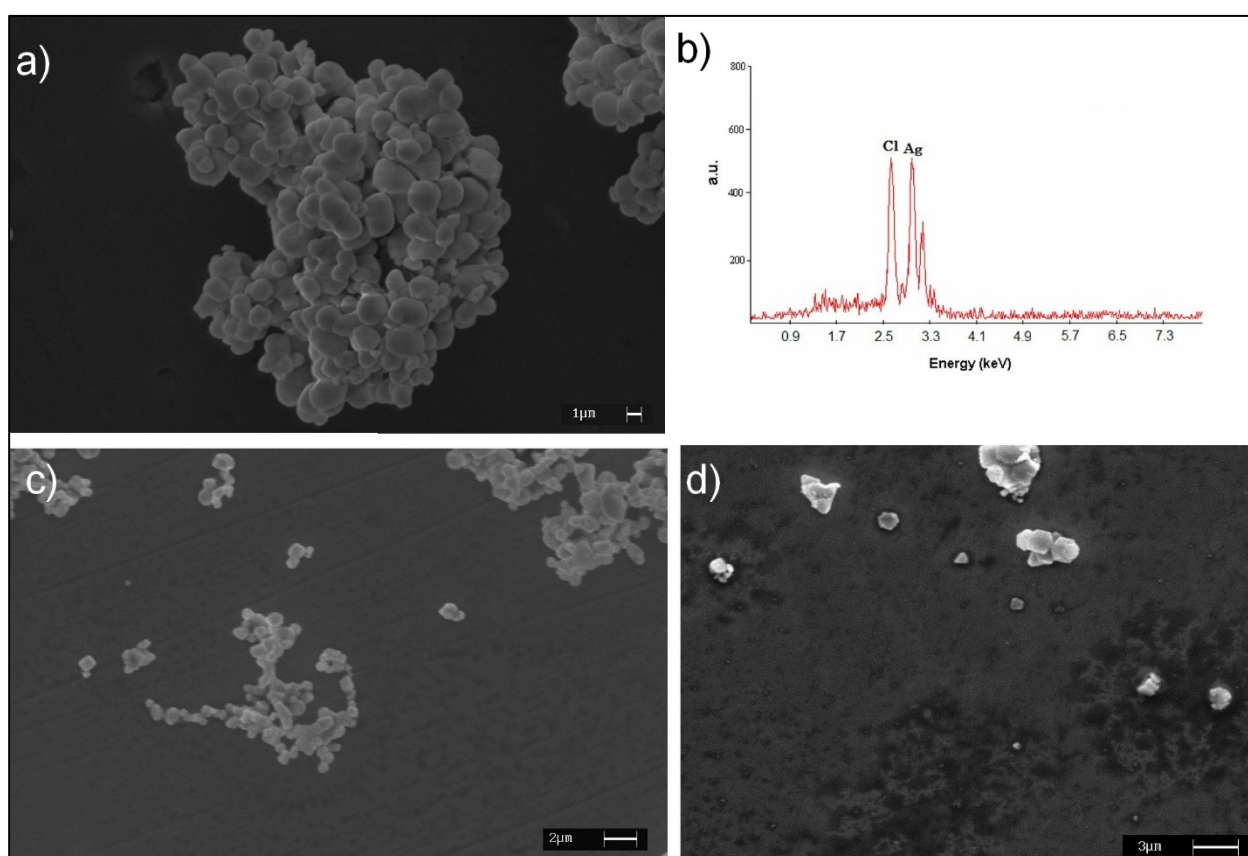


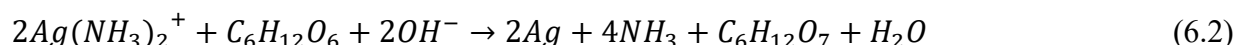
Fig. 6.15 SEM images of silver chloride precipitated after addition of HCl and EDS spectrum of silver chloride (extended area in correspondence of the powder). Precipitation with: a) conventional method; c) microwave assistance; d) ultrasound assistance.

The use of ultrasound seemed to be not more efficient in decreasing the size of the precipitate, as it shown in Fig. 6.15d.

Silver chloride, contrary to the silver nitrate, is not soluble in the water, and therefore, it was necessary to find another solvent where dissolve it to synthesize silver nanoparticles in aqueous solution. It was chosen ammonia as solvent.

The following step involved the use of glucose syrup as reducing agent to reduce silver chloride dissolved in ammonia solution to metallic silver. In this reaction (Equation 6.2), Tollens' reagent is the alkaline solution of silver (Ag^+) ion complexed with ammonia (NH_3), which keeps the Ag^+ ion in solution and sugar with an aldehyde functional group, is used as the reducing agent.

When Tollens' reagent oxidizes the aldehyde group, the Ag^+ ion is reduced to free silver (Ag).



The synthesis of metallic silver was performed by adding glucose syrup and by heating the solution for 1 hour at 50°C . Instead of using conventional heating, the solution with glucose syrup was treated for 10 minutes with microwaves or ultrasound. At the end of the three treatments, the solution changed color and became dark yellow, suggesting that the reaction occurred. The three solutions were analyzed by UV-spectroscopy and the absorption intensity at 420 nm confirmed the presence of silver nanoparticles (Fig. 6.16a). The solution obtained using conventional heating showed a positive shift of the peak, indicating an increase in the nanoparticle's size or in their agglomeration [160].

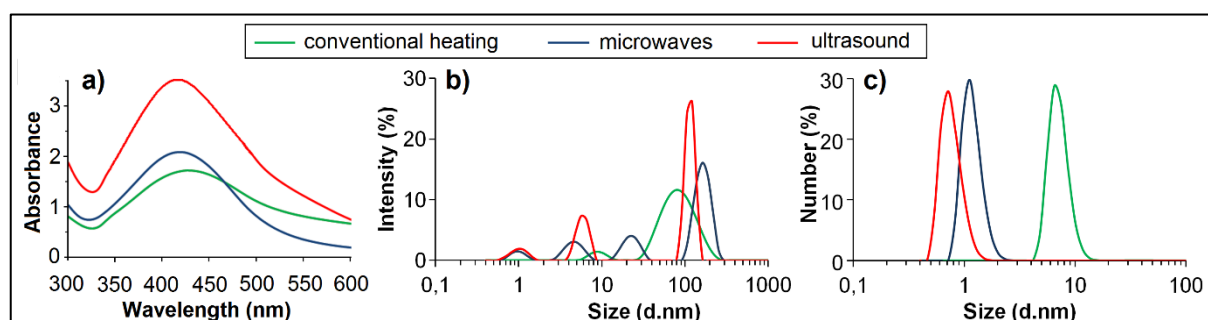


Fig. 6.16 a) UV absorption spectra; b) size distribution by intensity of the nanoparticle solutions; c) size distribution of the nanoparticle solutions by number.

The diffraction laser analysis showed that the three methods produced nanoparticles with a size between 0.7 nm and 200 nm (Fig. 6.16b). However, the analysis of size distribution showed that the average size of the nanoparticles was about 7 nm for conventional heating, 1 nm for microwaves, and 0.7 nm for ultrasound (Fig. 6.16c).

TEM analysis showed that the nanoparticles were spherical and had different sizes, between 0.7 and 80 nm, with the presence of agglomerates of 150-200 nm.

The selected area electron diffraction was carried out and the indexing of diffraction patterns confirmed that these nanoparticles were metallic silver (JCPDS No. 1-1167) (Fig. 6.17a, 6.17c, 6.17e).

The nanoparticles obtained with conventional heating had an average size of about 7 nm (Fig. 6.17b), whereas the majority of nanoparticles produced with microwaves or ultrasound were

smaller and showed a mean size of about 1 nm and 0.7 nm, respectively, in agreement with the diffraction laser analysis results (Fig. 6.17d, 6.17f).

Among the three proposed methods, conventional heating and ultrasound showed higher yield in the production of Ag nanoparticles (about 90% versus 60% for microwaves).

The 100°C temperature during the silver reduction with microwaves induced the evaporation of ammonia, thus preventing the complete reduction of the salt in metallic silver.

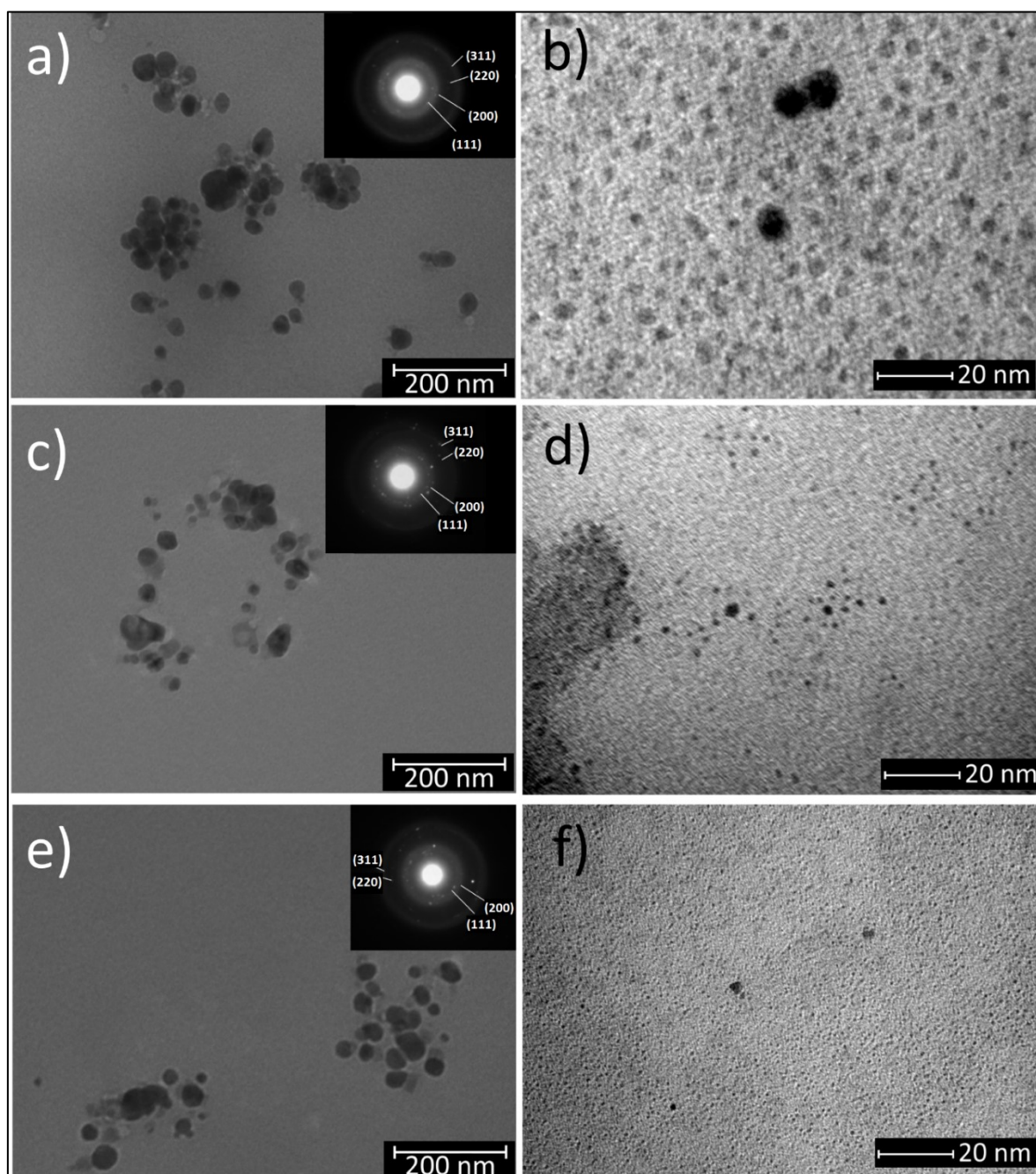


Fig. 6.17 TEM bright field images and SAED of silver nanoparticles obtained with: a), b) conventional heating; c), d) microwaves; e), f) ultrasound.

6.3 Copper nanoparticles



Fig. 6.18 The synthesized Cu nanoparticles.

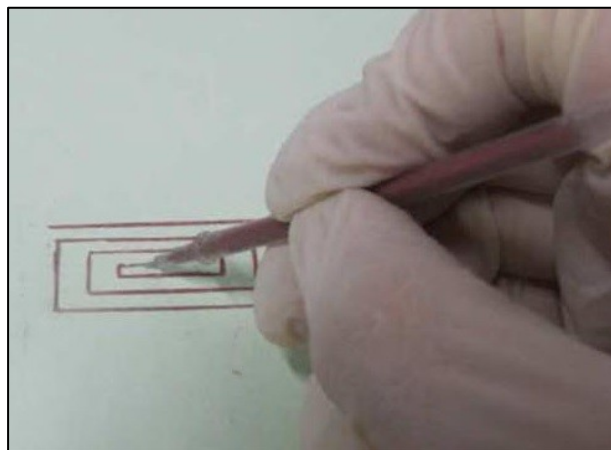


Fig. 6.19 Cu nanoparticles are applied as conductive inks in “flexible electronics”

Interest in Cu nanoparticles has increased recently due to their application in catalysis [161], thermal dissipation fluids, optical and magnetic devices, metal injection molding, flexible electronics (Fig. 6.19), and as antifungal and antimicrobial agents [162].

Several methods have been suggested to produce them [163, 164, 165, 166, 167, 168, 169, 170, 171, 172]. In particular, physical methods can be used, such as pulsed laser ablation, vacuum vapor deposition, pulsed wire discharge, thermal decomposition, and mechanical milling [173, 174, 175, 176, 177, 178, 179]. Alternative chemical methods include chemical reduction, microemulsion techniques, sonochemical reduction, electrochemical, photoirradiation, microwave assisted, and hydrothermal synthesis [180, 181]. As far as chemical reduction concerns, Cu salt can be reduced by a reducing agent, such as sodium borohydride, hydrazine, ascorbate, polyol, isopropyl alcohol with cetyltrimethylammonium bromide (CTAB), or glucose [182]. The most widely used capping agent is polyvinylpyrrolidone, although oleic acid, carboxylic acids (glycolic acid, lactic acid, acetic acid, etc.) poly(allylamine), and polyethylene glycol are amongst other capping agents that are commonly employed [183].

In this study, different process parameters, namely, the effect of ultrasound, reducing agents and capping agents, were investigated, where L-ascorbic acid and sodium borohydride were used as reducing agents. In order to make the process environmentally friendly, the synthesis was performed in aqueous solutions, in ambient conditions, and exposed to air. The nanoparticles were characterized with SEM, TEM, XRD, UV-spectroscopy, and by using laser diffraction particle size analyzer. Results show that, using L-ascorbic acid as reducing agents, the use of ultrasound leads to the production of Cu nanoparticles, with a reaction time of 10 min, compared with a time of several hours when performing the synthesis without ultrasound. The nanoparticles produced by this method have dimensions of approximately 5 nm and remain stable in the solutions for days.

6.3.2 Copper cementation

After tin and silver removal from nitric acid solution, as explained in previous paragraphs (the composition of the solution is shown in Table 6.3), copper was removed from the solution by cementation with iron (Equation 6.3).



Iron powder was added directly to the solution until copper stops precipitating (1,26g of Fe in 100ml of acid solution).

ICP analysis of the solution confirmed that there was recovered about 2/3 of the copper from the acid liquor (Tab. 6.4).

	Cu [ppm]	Fe [ppm]
Before cementation	15216	986
After cementation	5892	30093

Tab. 6.4 Elemental composition of the nitric acid solution in ppm.

The precipitated powder was separated by filtration and then washed three times with deionized water and analyzed by SEM, EDS, and ICP.

Figure 6.20 shows the SEM image of the Cu powder and the corresponding EDS spectrum. The powder was constituted by an agglomeration of particles of about 1 μm .

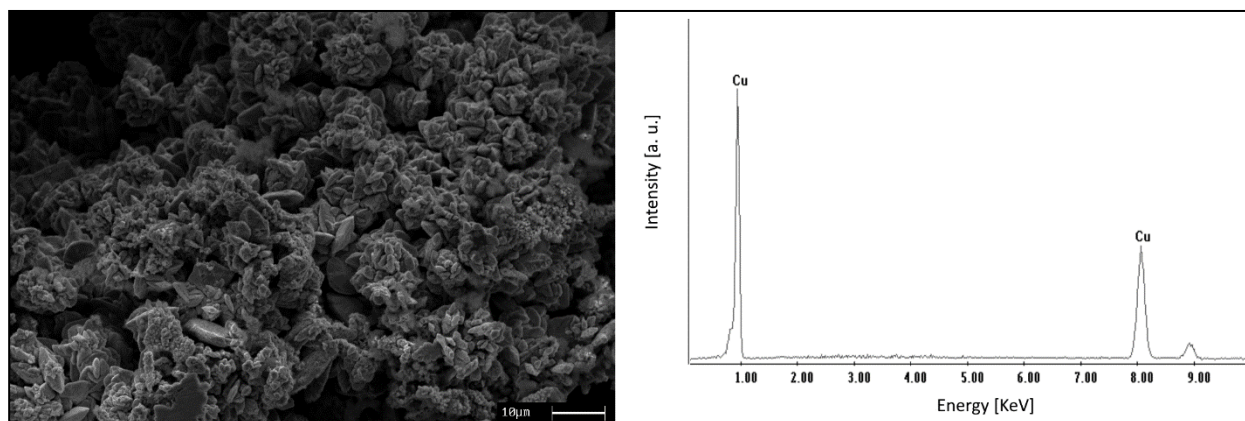


Fig. 6.20 SEM image and EDS spectrum of the precipitated Cu powder.

From EDS analysis, the powder was found to be composed of Cu without the presence of other elements. The ICP analysis confirmed the purity of the Cu. In order to achieve the synthesis of Cu nanoparticles, the powder was used to prepare a solution containing Cu salt.

In particular, 0.0263 g of the Cu powder was dissolved in 100 μl of nitric acid, after which 40 ml of water was added to the solution. The acid solution was neutralized with a 10 ml solution 0.6 m of sodium hydroxide. Two different reducing agents were tested: L-acid ascorbic (8 g/l) and sodium borohydride (0.1 g/l). The effects of ultrasound on the sizes of the nanoparticles, on the reaction time and on the yield were investigated.

The powder obtained was characterized by SEM and by XRD. The size and the structure of the powder were characterized by TEM. For TEM observation, the powder was dispersed in isopropyl alcohol and sonicated for 1 min. The particle size distribution was analyzed by laser light scattering. Moreover, UV spectroscopy was performed and solutions were analyzed by ICP spectrometer.

6.3.3 Synthesis with L-ascorbic acid

When using L-ascorbic acid, ultrasound assistance was found to reduce the reaction time, as shown in Fig. 6.22. The Cu reduction with ultrasound assistance was completed within 10 min, whereas in literature the process required approximately 17 h with conventional heating at 80°C [180]. The UV-vis absorption spectrum of the solution treated under ultrasound for 5 min had a peak at 580 nm, confirming that the Cu nanoparticles were produced (Fig. 6.21a), in agreement with the literature [184, 185].

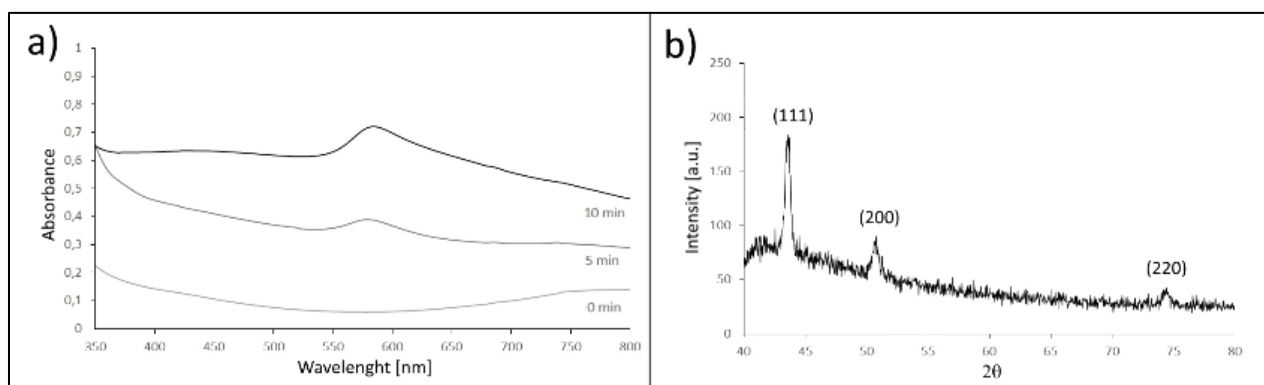


Fig. 6.21 UV-vis absorption a) and XRD b) spectra of the Cu nanoparticles solution synthesized with L-ascorbic acid and ultrasound irradiation for 10 min.

After 10 min, the peak became more pronounced, suggesting that the complete reaction occurred after this time. The XRD analysis performed on the nanoparticles obtained after a reaction time of 10 min is shown in Fig. 6.21b. The peaks were attributed to the Cu (ICSD n. 98-005-3247). The images of changing in color during the reaction are visible in Fig. 6.22.

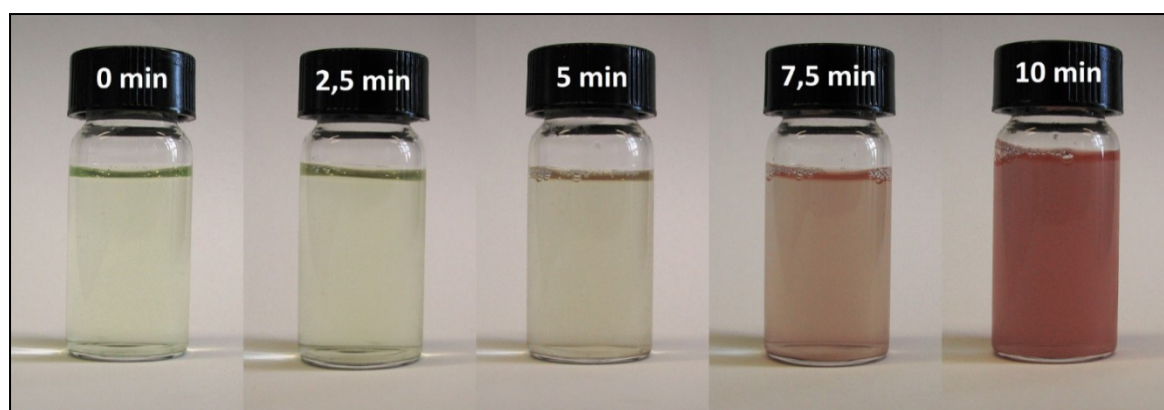


Fig. 6.22 Solution with reduced Cu after 10 min of sonication using L-ascorbic acid as a reducing agent.

Meanwhile, SEM images of the powders obtained with and without ultrasound are shown in Fig. 6.23. As can be seen, the mean size of the particles produced without ultrasound is shown to be approximately 1 μm (Fig. 6.23b), whereas the particles produced with ultrasound were smaller than 100 nm (Fig. 6.23a).

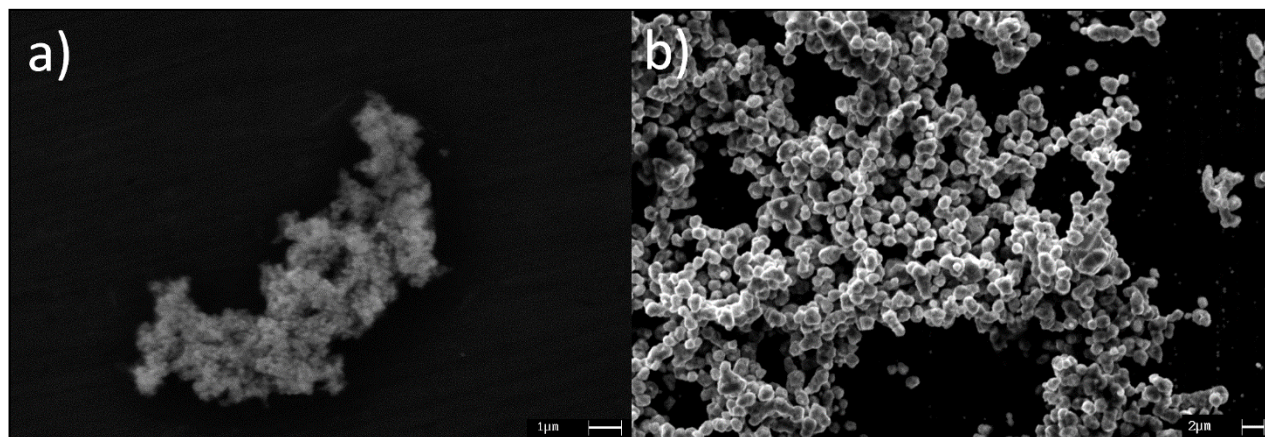


Fig. 6.23 SEM images of powder obtained using L-ascorbic acid a) without ultrasound and b) with ultrasound.

Using laser diffraction analysis, we find that the dimensions of the nanoparticles produced using L-ascorbic acid with ultrasound irradiation were approximately 5 nm and TEM analysis showed that nanoparticles with diameter of about 5–7 nm were present (Fig. 6.24).

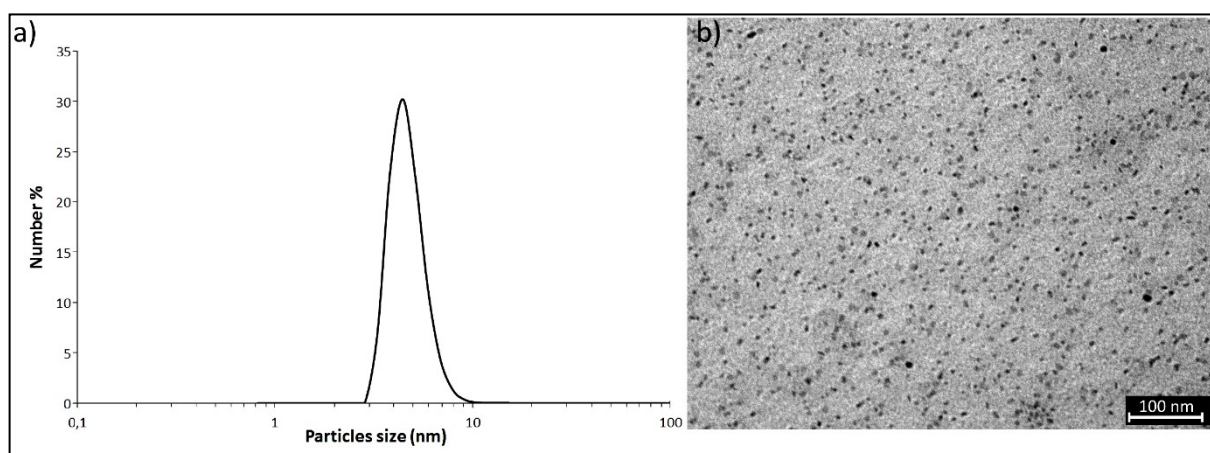


Fig. 6.24 Malvern analysis of the powder with (a) ultrasound and (b) TEM bright field image of the powder obtained with ultrasound, using L-ascorbic acid as reducing agent.

Moreover, we verified that ultrasound increased the yield of the reaction. In particular, two more concentrated solutions containing 20 g/l Cu nitrate and 40 g/l of L-ascorbic acid, respectively, without any capping agent, were prepared. One was heated for 1 h at 80°C, whereas the other one was treated with ultrasound for 10 min. In the first case, using conventional heating, 0.01499 g of Cu powder precipitated, whereas in the second case, using ultrasound irradiation, 0.07608 g of Cu powder precipitated. Therefore, the yield obtained with ultrasound assistance was approximately 5 times higher, but took less time to produce (Fig. 6.25).

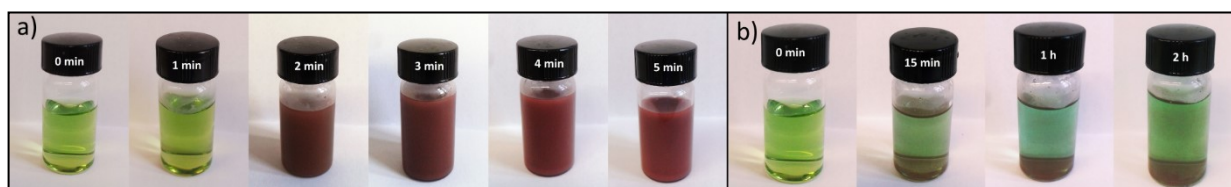


Fig. 6.25 Comparison between the reaction carried out a) with ultrasound and b) without ultrasound, using L-ascorbic acid.

6.3.4 Synthesis with sodium borohydride

For comparison, the synthesis of Cu nanoparticles was also performed with sodium borohydride, both without and with the assistance of ultrasound. With this reducing agent the reaction occurred within a shorter time relative to L-ascorbic acid, and heating was not required in the reaction without ultrasound. However, it was observed that nanoparticles dissolved after 6 h, whereas the nanoparticles produced with L-ascorbic acid remained stable for weeks.

The UV spectroscopy analysis confirmed that Cu nanoparticles were produced, and the characteristic peak at 580 was observed. Meanwhile, SEM images of the powders obtained with and without ultrasound are shown in Fig. 6.26, where agglomerates of nanoparticles smaller than 300 nm are visible.

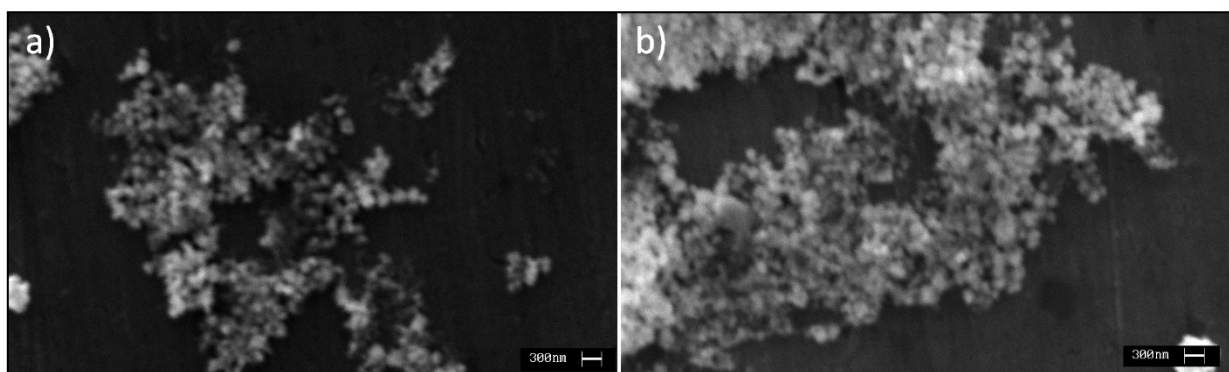


Fig. 6.26 SEM images of the nanoparticles obtained a) with ultrasound and b) without ultrasound, using NaBH_4 as a reducing agent.

The Malvern analysis showed that nanoparticles obtained with ultrasound had a particle size of approximately 6 nm, whereas the nanoparticles produced without ultrasound were characterized by a mean size of about 15 nm (Fig. 6.27).

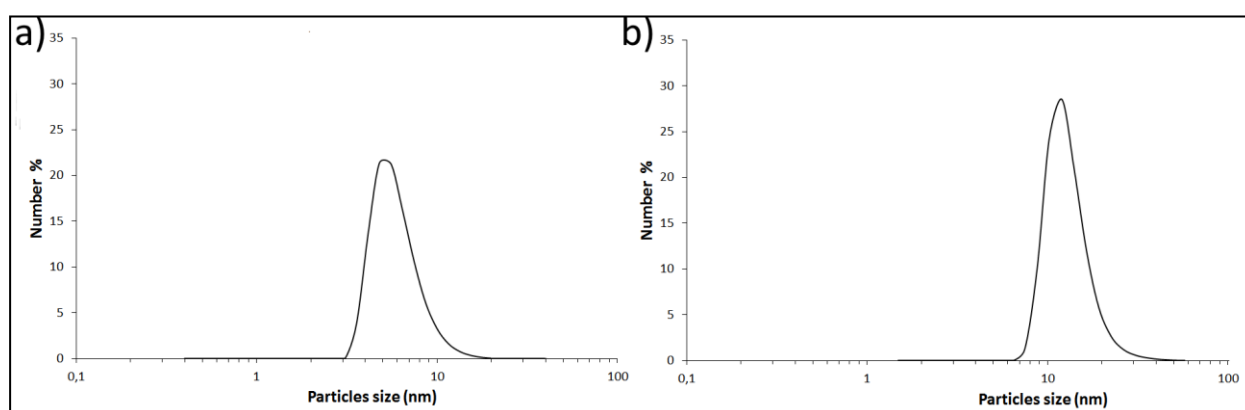


Fig. 6.27 Malvern analysis of the powder using NaBH_4 as reducing agent a) with ultrasound and b) without ultrasound.

The analysis carried out with TEM showed that the nanoparticles produced with the assistance of ultrasound had a size of about 7 nm, whereas the ones produced without ultrasound were larger, with sizes ranging between 10 and 20 nm, thus confirming the results of the Malvern analysis (Fig. 6.28).

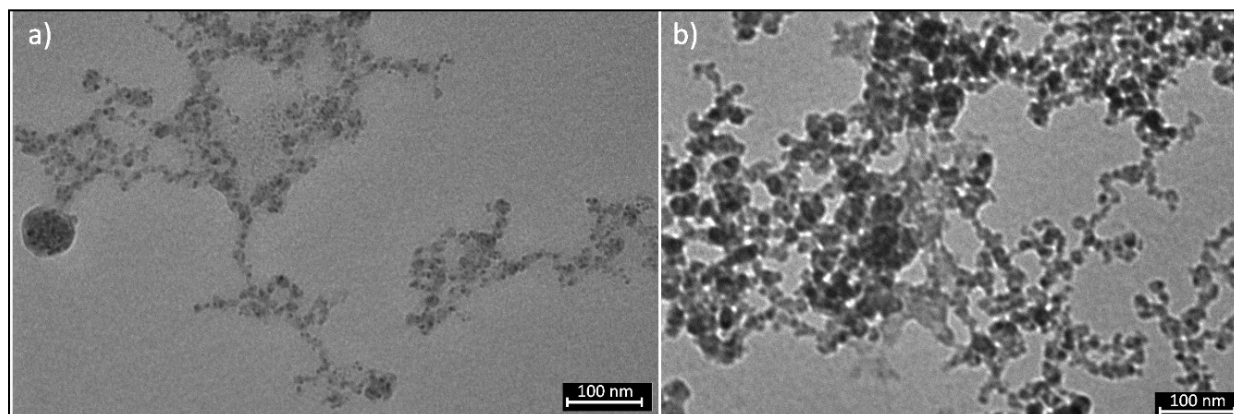


Fig. 6.28 TEM bright field images of the powder obtained a) with ultrasound and b) without ultrasound, using L-ascorbic acid as a reducing agent.

6.4 Copper oxide nanoparticles

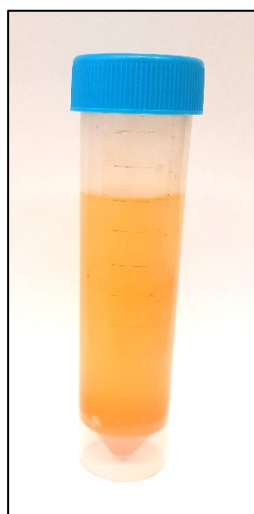


Fig. 6.29 The synthesized Cu_2O nanoparticles.

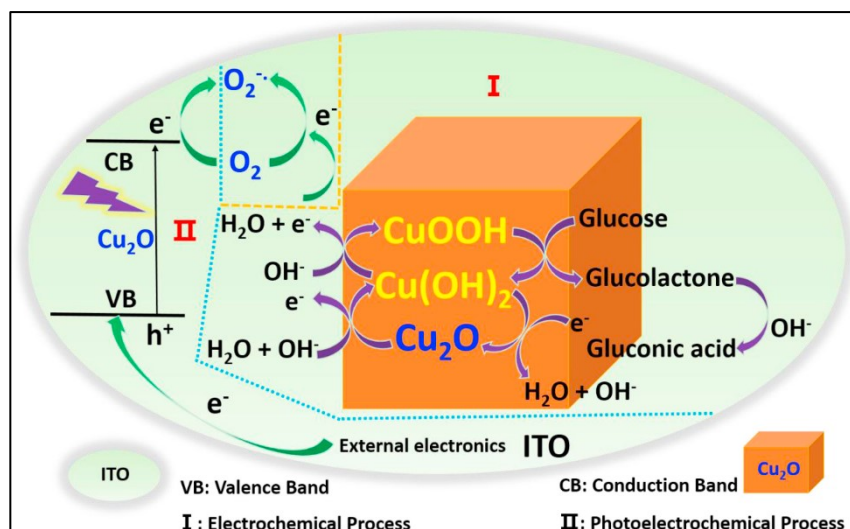


Fig. 6.30 Cu_2O can be used for non-enzymatic and oxygen-sensitive photo electrochemical sensing of glucose.

Among the numerous transition metal semiconducting oxides, cuprous oxide (Cu_2O) is of intense interests and has been extensively investigated for its distinctive properties. Cu_2O is a reddish p-type semiconductor with a direct bandgap of 2.0–2.2 eV, which has been researched previously for application in solar energy converting devices. It has the potential to form a solar cell with circuit voltage by combination with a suitable n-type semiconductor.

For this reason, Cu_2O was studied as a potential material for low-cost photovoltaic power generation as it has a theoretical solar cell conversion efficiency of 18%.

Even though Cu_2O is one of the oldest semiconducting materials known to solid-state physicists, not much technological improvement has been achieved. As a testimony to this, the highest conversion efficiency using Cu_2O solar cells to date is below 2%. Techniques of doping Cu_2O , to obtain n-type material, do not exist so that homojunction cells of Cu_2O cannot be fabricated. Present research is geared towards Schottky barrier and heterojunction solar cells of Cu_2O [186]. The major attraction of Cu_2O is that it has low toxicity and good environmental acceptability, is inexpensive, plentiful and readily available. Moreover, Cu_2O has been widely exploited for use in the fields of photo catalyst, sensors (Fig. 6.30 [187]) solar energy conversion, antifouling coatings, photoelectrode in electrochemical cells and water-splitting materials. The water-splitting activity of Cu_2O , especially under visible light irradiation, has been the focus of many debates. It was reported that Cu_2O films had gas sensing activity at 200 °C. Cu_2O has been successfully synthesized by many methods including electrolysis, reduction of cupric salts or copper oxide, thermal oxidation, hydrothermal production and γ -irradiation. Considering the potential applications of copper-based materials, many kinds of morphologies have been reported, such as wires, monodisperse nanotubes, octahedral nanocages, hollow nanospheres, and so forth.

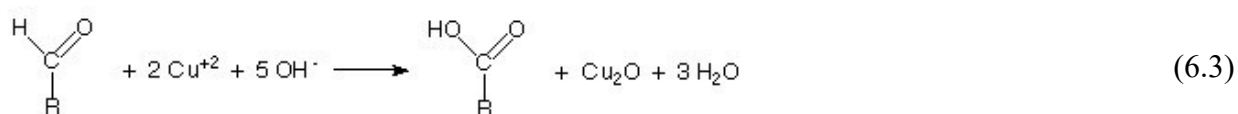
For example, it's possible to use a solvothermal method in N, N-dimethylformamide (DMF) at 150-180 °C for 20-40 h to get hollow Cu₂O nanospheres. It was found the formation process of Cu₂O hollow spheres included formation of CuO nanocrystals, aggregation of primary CuO nanocrystals, and the reductive transformation to Cu₂O [188].

Monodisperse Cu₂O or CuO nanospheres which can form three-dimensional self-assembly patterns should have potential usage on gas sensors because they have sufficient surface area and interspaces for gas absorption [189].

6.4.1 Synthesis

In a typical experiment, the proper amount of precursor was dissolved, together with D-glucose in 50ml of solution. In particular, two precursors were tested for Cu₂O nanoparticles synthesis: copper nitrate and copper acetate. Copper acetate is typically used for the synthesis [190], but also copper nitrate was successfully tested [191] and in particular it was selected in order to apply the process also to the copper recovered from PCBs as performed in Chapter 6.3 for copper nanoparticles synthesis.

The solution was then heated at 80°C or put under ultrasound irradiation. To start the reaction 1.6 ml of 1.1M NaOH solution was added. In fact, in basic solutions, D-glucose can be oxidized into D-gluconic acid thus reducing Cu(II) into Cu(I), according to Benedict's reactions [192]:



Moreover, in order to enhance the effect of ultrasound, in some test the basic solution was added dropwise during the sonication (0,2 ml/min). After the synthesis was completed, the particles were isolated by centrifugation, washed and preserved in acetone.

Different parameters were studied, in particular the kind of precursor (copper nitrate or acetate), precursor concentration (5, 10 and 20 mM), D-glucose concentration (0.05, 0.1; 0.2 M) and the effect of ultrasound. For each test, the particles were observed at SEM and the average diameter was calculated by image analysis.

6.4.2 Characterization

First the particles were characterized with SEM, which shows the highly spherical shape as well as the EDS analysis the copper oxide composition (Fig. 6.31).

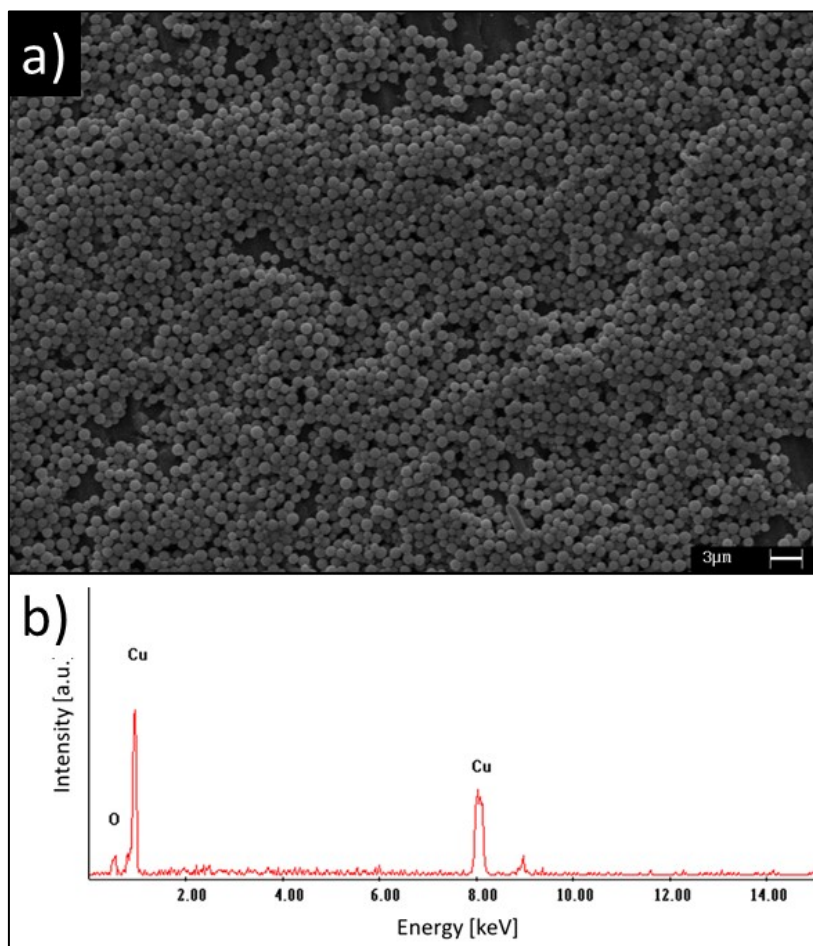


Fig. 6.31 SEM images (a) and EDS spectrum (b) of the Cu_2O particles.

Moreover, XRD analysis was performed to confirm that the particles were composed of Cu_2O (Fig. 6.32b).

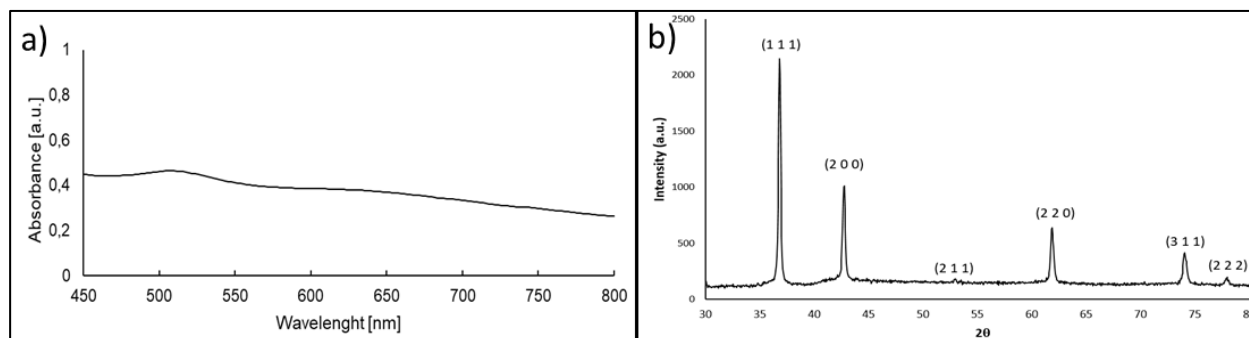


Fig. 6.32 UV absorption (a) and XRD (b) of the Cu_2O particles.

In particular, UV absorption analysis (Fig. 6.32a) showed a not very high peak at ~510 nm that is different from the nanoparticles, which have an obvious absorption edge at ~550 nm consistent with the Cu₂O band gap energy. This fact was explained by Zhang et al. and it is mainly due to, the Cu₂O nanoparticles aggregation in nanospheres, which have increased size and uniformity, and then produce a superimposition of the visible light scattering on the absorption of as-prepared nanospheres spectra [189].

The perfectly spherical shape was verified with TEM analysis and it is reported in Fig. 6.33.

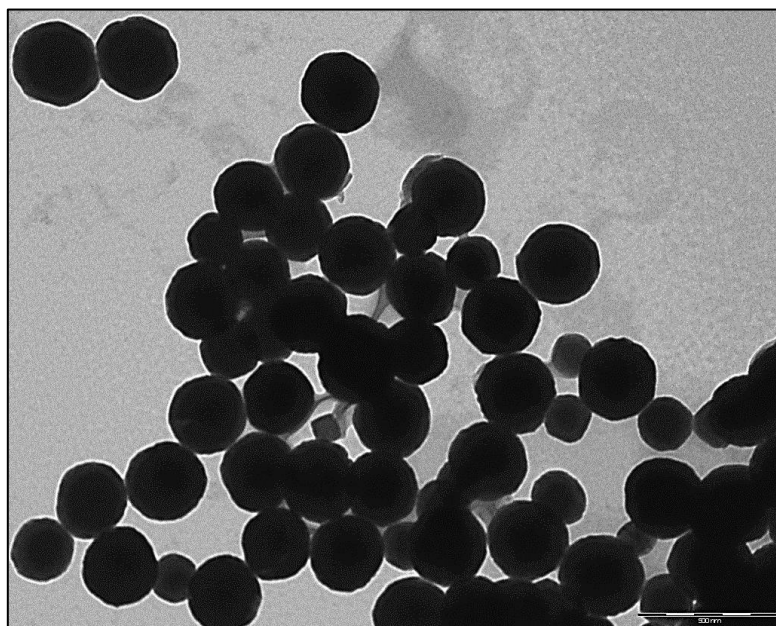


Fig. 6.33 TEM image of the Cu₂O particles.

From SEM analysis results, that use of copper acetate caused the reduction of the particles dimensions in comparison with copper nitrate. Moreover, an increase in copper nitrate concentration seems to increase particles dimensions, whereas using copper acetate 10mM the smallest particles were obtained (Fig. 6.34).

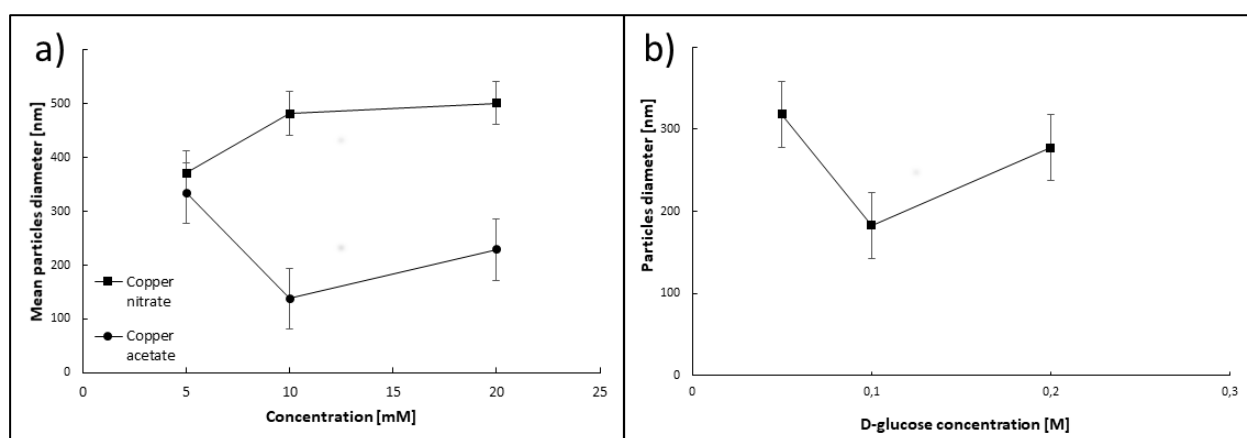


Fig. 6.34 Effect of precursor concentration (a) and of D-glucose concentration on the size of the Cu₂O particles.

However, the most relevant effect was due to ultrasound irradiation. In fact, (Fig. 6.35), ultrasound assistance greatly reduced the size of the synthesized particles.

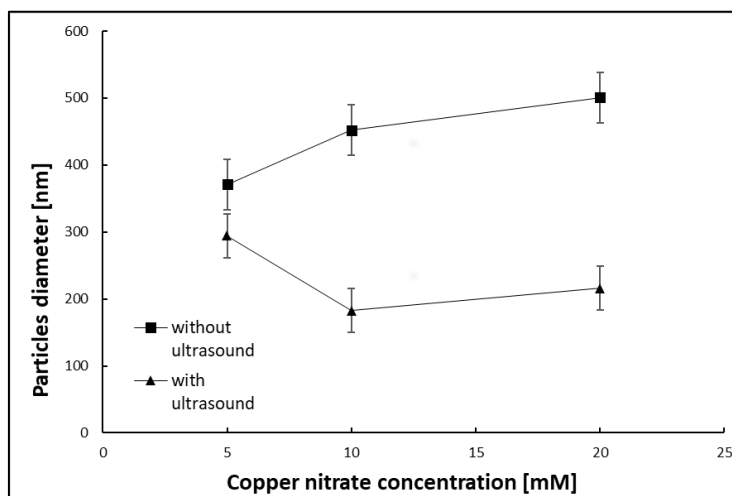


Fig. 6.35 Effect of ultrasound assistance on the size of the Cu_2O particles.

In particular, using copper nitrate 20mM, the mean diameter of the particles was ~ 500 nm without the ultrasound and ~ 200 nm with the ultrasound (Fig. 6.36).

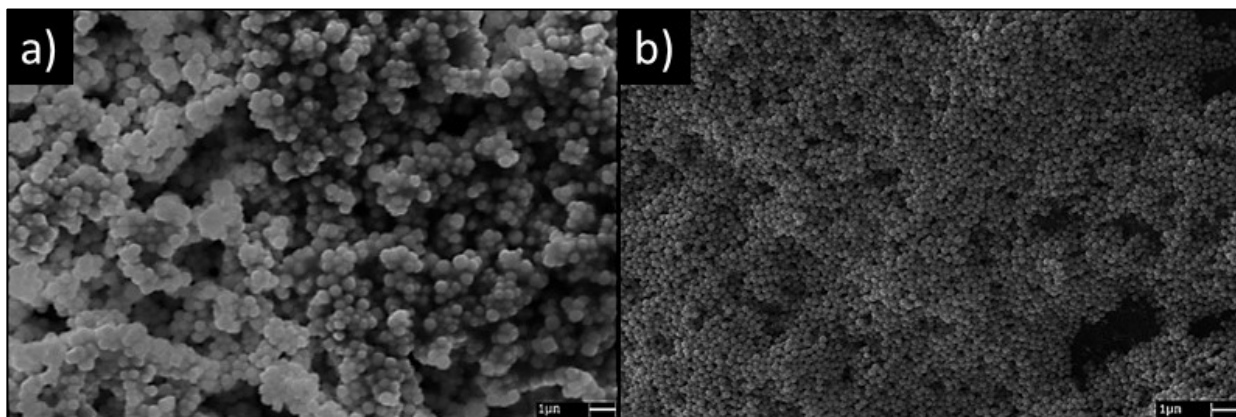


Fig. 6.36 SEM images of the Cu_2O particles obtained using 20mM copper nitrate without (a) and with (b) ultrasound assistance.

Moreover, both in copper nitrate and in copper acetate tests, ultrasound reduced the reaction time and the synthesis was completed respectively in 30 minutes without ultrasound and in 8 minutes with the ultrasound.

It was also observed how the size of the particles depends on the manner of sodium hydroxide solution was added. The addition of 0.2 ml of NaOH each minute during sonication, compared with the addition of the same amount (1.6 ml) at the beginning of the same, allows to accentuate the effect of the ultrasounds by reducing the particle size.

6.5 Gold nanoparticles

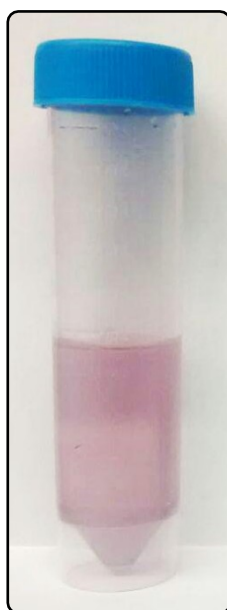


Fig. 6.37 The synthesized gold nanoparticles.

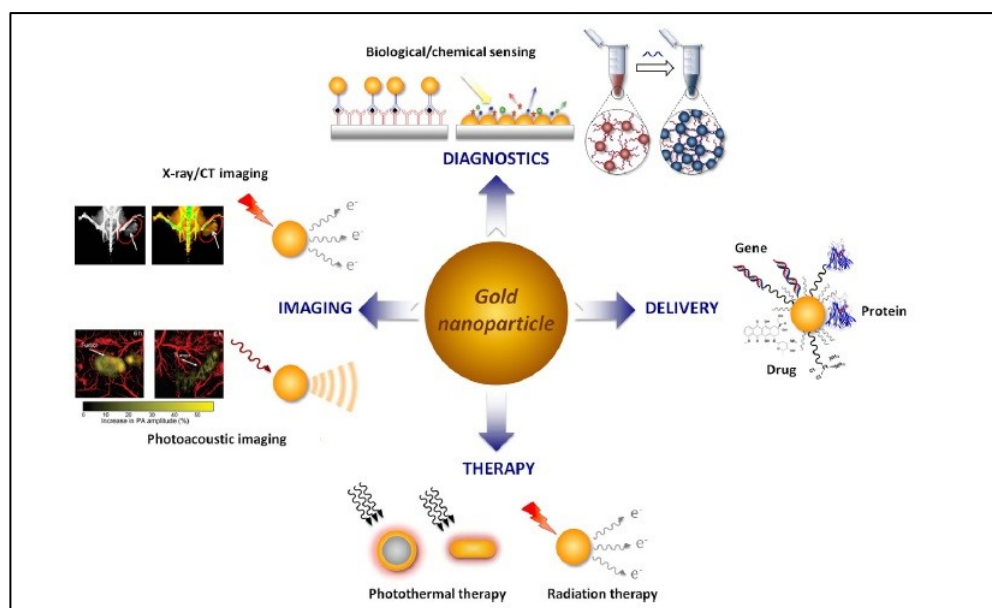


Fig. 6.38 Biomedical applications of AuNPs. Owing to their unique physico-chemical, optical and electronic properties, AuNPs have been exploited for a wide range of applications in diagnostics, imaging, delivery, and therapy.

Gold nanoparticles (AuNPs), which have been known for 2500 years, are the subject of an exponentially increasing number of reports and are full of promises for optical, electronic, magnetic, catalytic, and biomedical applications in the 21st century, using the “bottom-up” approach with the hybrid organic-inorganic and biological inorganic building blocks derived therefrom. From the fascination produced by the more or less virtual medical uses of soluble gold in the past millenaries, it remains at least that AuNPs are completely biocompatible. The reasons for the present excitement in AuNP research are also the stability of AuNPs, the extraordinary diversity of their modes of preparations (including biosynthetic modes and template synthesis) involving ceramics, glasses, polymers, ligands, surfaces, films, oxides, zeolites, biomolecules, and bio organisms, and their essential properties and role in nanoscience and future nanotechnology. The classic Turkevitch-Frens synthesis with citrate stabilizer is practical and still very much used to prepare precursors. However, the stabilization of AuNPs by alkane thiolate and various functional thiolate ligands forming very stable, relatively monodisperse materials and the two-phase Schiffrin synthesis have been a breakthrough. These facile syntheses have been shown to be particularly favorable for easy manipulations, such as place-exchange reactions and extensive physical characterizations, formation of superlattices and crystals, and rich molecular chemistry. For instance, multiple redox states (up to 15) of AuNP-alkanethiolate were beautifully characterized at room temperature as charge injection in the core is quantized, and 2D and 3D AuNP superlattices are now common, easily controlled assemblies that use supramolecular principles and are characterized by spectacular imaging and microscopy techniques. Fascinating

aspects are the optoelectronic properties of AuNPs related to the surface plasmon absorption, reflecting the collective oscillation of the conducting electrons of the gold core, a feature relevant to the quantum size effect. Nonlinear optic applications of AuNPs are also rapidly growing. The combination of this photonics discipline with biology and medicine has already been demonstrated by the seminal work on AuNP-DNA assemblies and is very promising for future biomolecular manipulations and applications, such as labeling, detection, and transfer of drugs, including genetic materials. Electronic conduction correlated with single-electron tunneling is a possible basis for future nanoelectronics digital circuits in connection with self-assembled monolayers, although the quantized capacitance involved will require ultrapure AuNP materials. Excellent sensory and environmental devices are becoming available by tuning the spectroscopy, fluorescence, luminescence, and electrochemical characteristics of AuNPs with those of substrates including DNA, sugars, and other biological molecules or systems. Another promising electrochemical field that has just started to develop is that of AuNP ultramicroelectrodes.

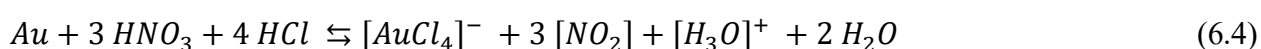
Thus, it is becoming possible to control molecules at a resolution well below that offered by photolithography. In particular, DNA is a candidate for this task because of its excellent specificity in base pairing, and it can be easily addressed at the nanoscale for applications in biosensing and bionanotechnology (Fig. 6.38 [193]). Finally, although bulk gold is well known for being inert, the reactivity of the gold cores in AuNPs has recently proven very useful in catalytic applications, even at subambient temperatures, and the field of AuNP-catalyzed CO and methanol oxidation and O₂ reduction is now also developing at a rapid rate. Here again, the variety of synthetic possibilities using AuNP components and the understanding of the AuNP nanostructures and their role on the catalytic events is a key toward future applications. In conclusion, an extraordinary variety of structures, properties, and applications is available for AuNPs and will motivate fundamental studies and applications in connection with those of other molecular, inorganic, and biological nanomaterial components in interdisciplinary research involving chemistry, physics, biology, and medicine [194].

6.5.1 Synthesis with L-ascorbic acid

As mentioned, the synthesis of gold nanoparticles was achieved using a method different from that described in Chapter 3.

As a matter of fact, the test performed in order of obtaining gold nanoparticles from thiourea solution mentioned in Chapter 3 were unsuccessful. As a consequence, gold leaching was performed in this case using aqua regia.

Moreover, as the gold is located on the surface of the board (as shown in Chapter 3), the PCBs were treated in nitric acid without grinding. After this treatment, the detachment of the gold was obtained. The gold was recovered as solid residue by filtration of the solution in the form of gold powder. The powder of gold was dissolved by leaching in aqua regia, according to Eq. 6.4:



With this method (Fig. 6.39) it was possible to obtain a solution containing only gold (and traces of tin).

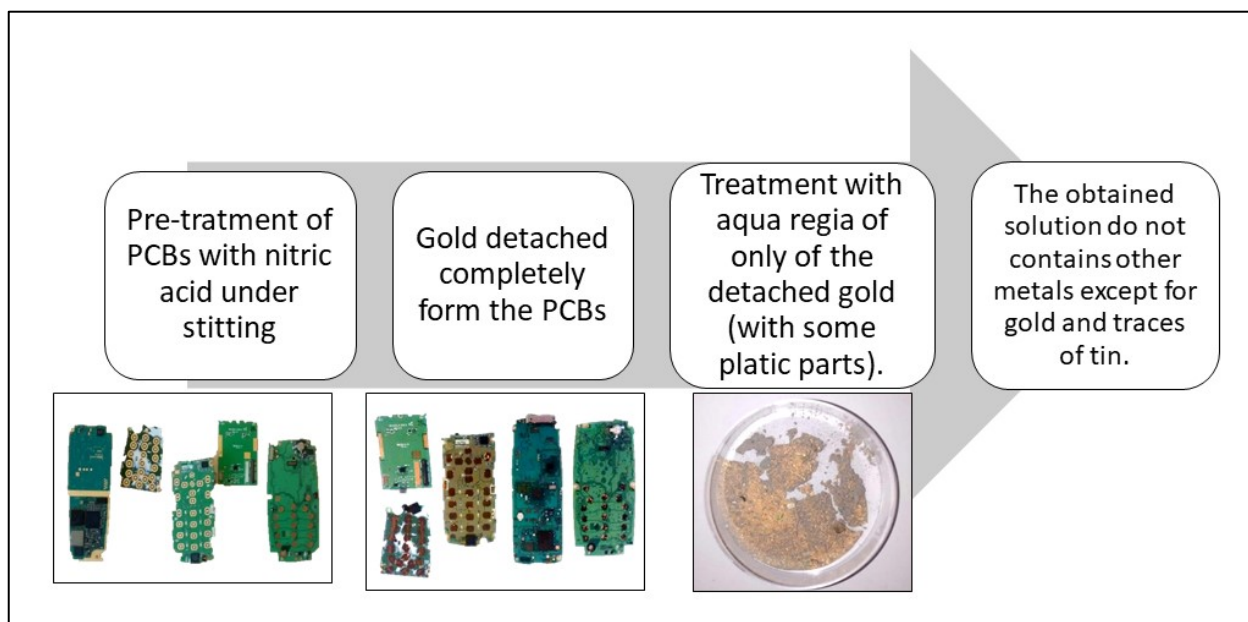


Fig. 6.39 The process to obtain the aqua regia solution from PCBs

In fact, after the treatment of the whole PCBs in aqua regia (Fig. 6.40a), even if the solution neutralizing caused the precipitation of most metals (Fig. 6.40b), they are not completely removed and interfere with the synthesis of gold nanoparticles. In particular, after the synthesis silver chloride was found with the reduced gold (Fig. 6.40c).

Using the method described in Fig. 6.39 instead, only tin dioxide (with a small amount of gold) precipitated from the solution when pH was increased to 7, as visible in Fig. 6.41

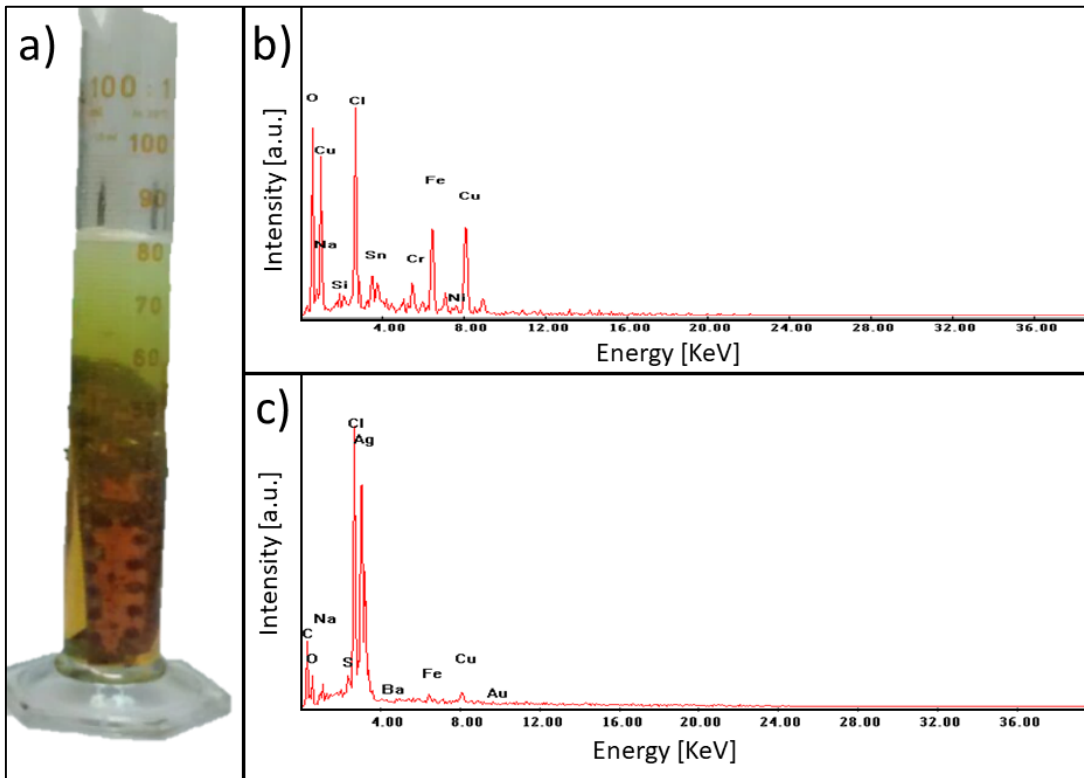


Fig. 6.40 a) Treatment of PCB in aqua regia; b) metals precipitated from the solution when pH is adjusted to 7; c) Silver chloride detected with gold nanoparticles after the synthesis.

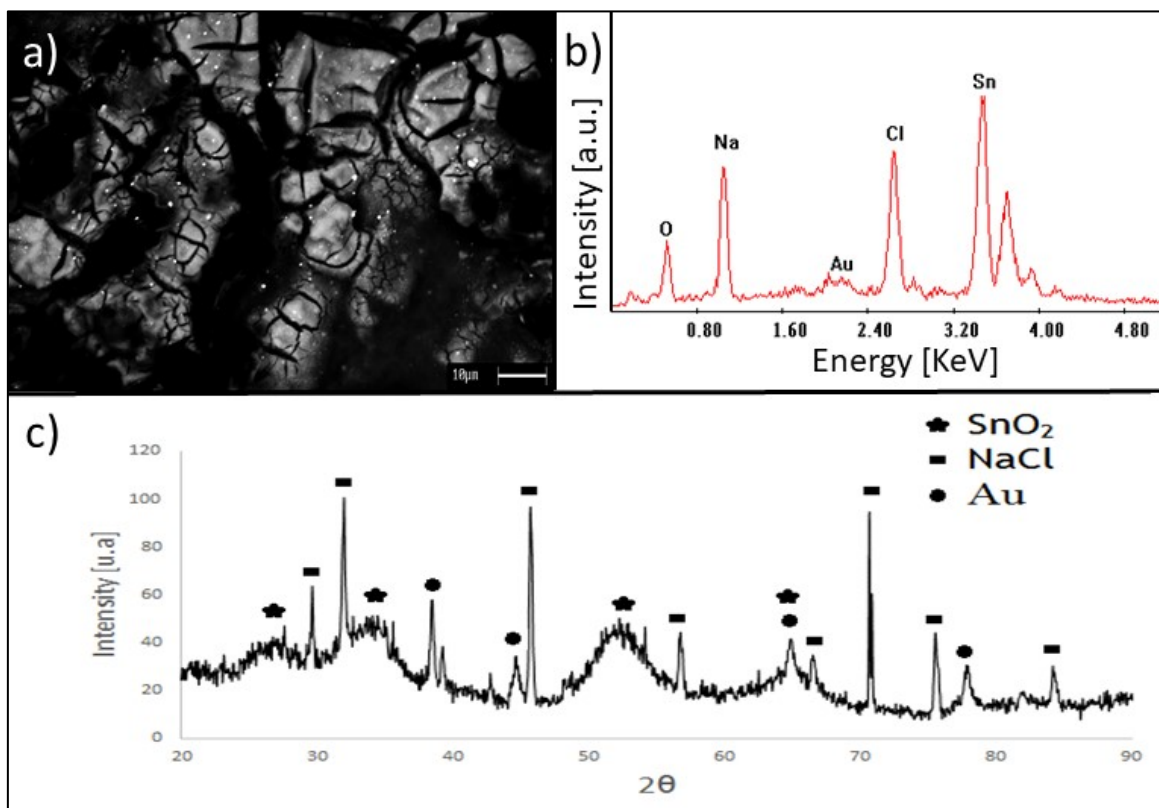
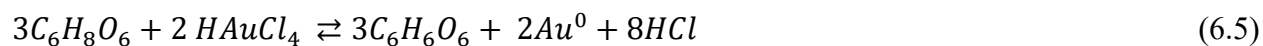


Fig. 6.41 SEM image (a), EDS (b) and XRD (c) spectra of the solid residue after pH correction to 7.

In fact, after 30min a proper quantity of gold was completely dissolved in aqua regia and the pH of the solution was adjusted to 7 by addition of ammonia or sodium hydroxide. The obtained solution was 1,22 mM of gold. Subsequently, even if glucose was tested as reducing agent, it resulted inefficacious and it was preferred L- ascorbic acid to reduce gold according to the reaction 6.5 [195]:



Moreover, gelatin (3,125g/l) was tested as stabilizer. The gold nanoparticles were separated from the solution by centrifugation. Successively, the nanoparticles were separated from the liquid and dispersed into water solution. The nanoparticles were characterized with UV-Vis absorption spectroscopy (UV-Vis-AS), SEM, LSD and TEM.

6.5.2 Characterization

The colour of the neutralized aqua regia solution containing the gold ions changed from yellow to light red after the addition of the ascorbic acid, suggesting the reduction of gold ions to metal gold nanoparticles occurred. The UV-vis absorption spectra with the main absorption peak at 550 nm confirmed the presence of gold nanoparticles (Fig. 6.42a) [196]. The average size of the particles was investigated by the Laser diffraction of the solution, and an average size of 100 nm resulted (Fig. 6.42b).

The SEM image of the gold nanoparticles is shown in Fig. 6.43a, where it possible to observe that they were constituted by agglomerates with a spherical shape and size lower than 100 nm. The EDS analysis showed that the nanoparticles were composed by gold.

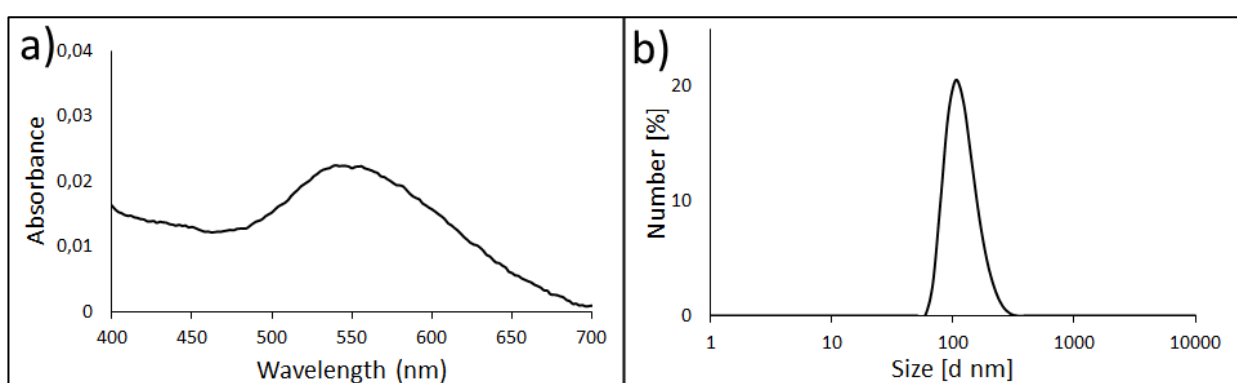


Fig. 6.42 UV-vis absorption spectrum (a) and LSD (b) of gold nanoparticles.

TEM analysis showed that their dimension was about 80 nm (Fig. 6.42b).

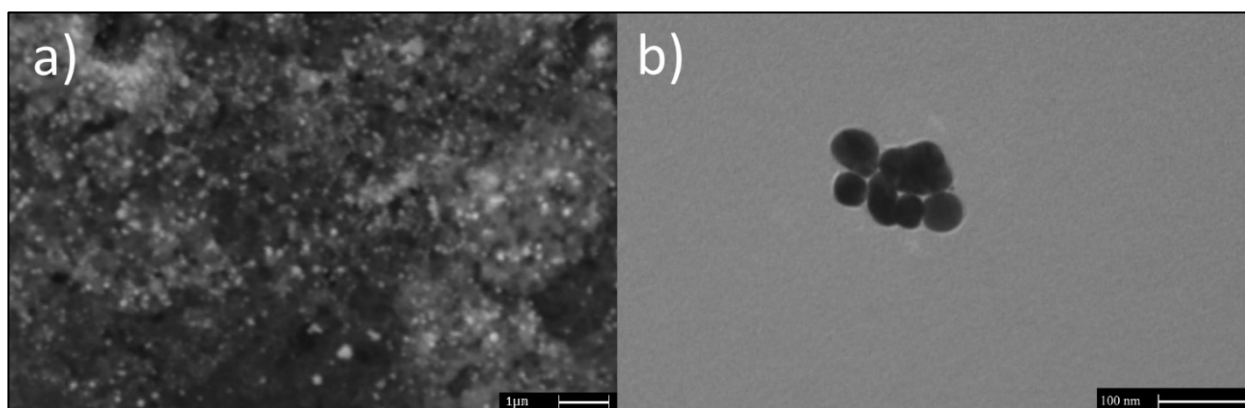


Fig. 6.42 SEM image (a) and TEM image (b) of gold nanoparticles.

6.5.2 Brust Synthesis

The Brust-Schiffrin method for AuNP synthesis, published in 1994, has had a considerable impact on the overall field in less than a decade, because it allowed, for the first time, a simple synthesis of thermally stable and air-stable AuNPs with reduced dispersity and controlled size (diameter between 1.5 and 5.2 nm). Indeed, these AuNPs can be repeatedly isolated and redissolved in common organic solvents without irreversible aggregation or decomposition, and they can be easily handled and functionalized just as stable organic and molecular compounds. The technique of synthesis is inspired by Faraday's two-phase system and uses the thiol ligands that strongly bind gold due to the soft character of both Au and S. AuCl_4^- is transferred to toluene using tetraoctylammonium bromide as the phase-transfer reagent and reduced by NaBH_4 in the presence of dodecanethiol, as shown in Fig. 6.43 [194].

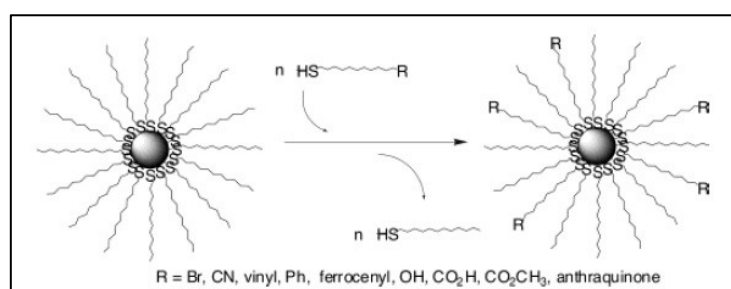
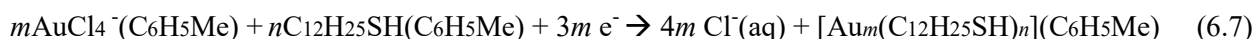


Fig. 6.43 General scheme for the ligand-exchange reaction

The organic phase changes color from orange to deep brown within a few seconds upon addition of NaBH_4 :



The TEM photographs of this synthesis showed that the diameters were in the range 1-3 nm, with a maximum in the particle size distribution at 2.0-2.5 nm, with a preponderance of cuboctahedral and icosahedral structures. Larger thiol/gold mole ratios give smaller average core sizes, and fast reductant addition and cooled solutions produced smaller, more monodisperse particles. A higher abundance of small core sizes (≤ 2 nm) is obtained by quenching the reaction immediately following reduction or by using sterically bulky ligands. Brust et al. extended this synthesis to p-mercaptophenol-stabilized AuNPs in a single-phase system [197], which opened an avenue to the synthesis of AuNPs stabilized by a variety of functional thiol ligands. Subsequently, many publications appeared describing the use of the Brust-Schiffrin procedure for the synthesis of other stable AuNPs, also sometimes called monolayer-protected clusters (MPCs), of this kind that contained functional thiols. The proportion thiol: AuCl_4^- used in the synthesis controls the size of the AuNPs (for instance, a 1:6 ratio leads to the maximum average core diameter of 5.2 nm, i.e., ca. 2951 Au atoms and ca. 371 thiolate ligands; core diameter dispersity of $\sim \pm 10\%$).

Brust synthesis was performed as shown in Fig. 6.44.

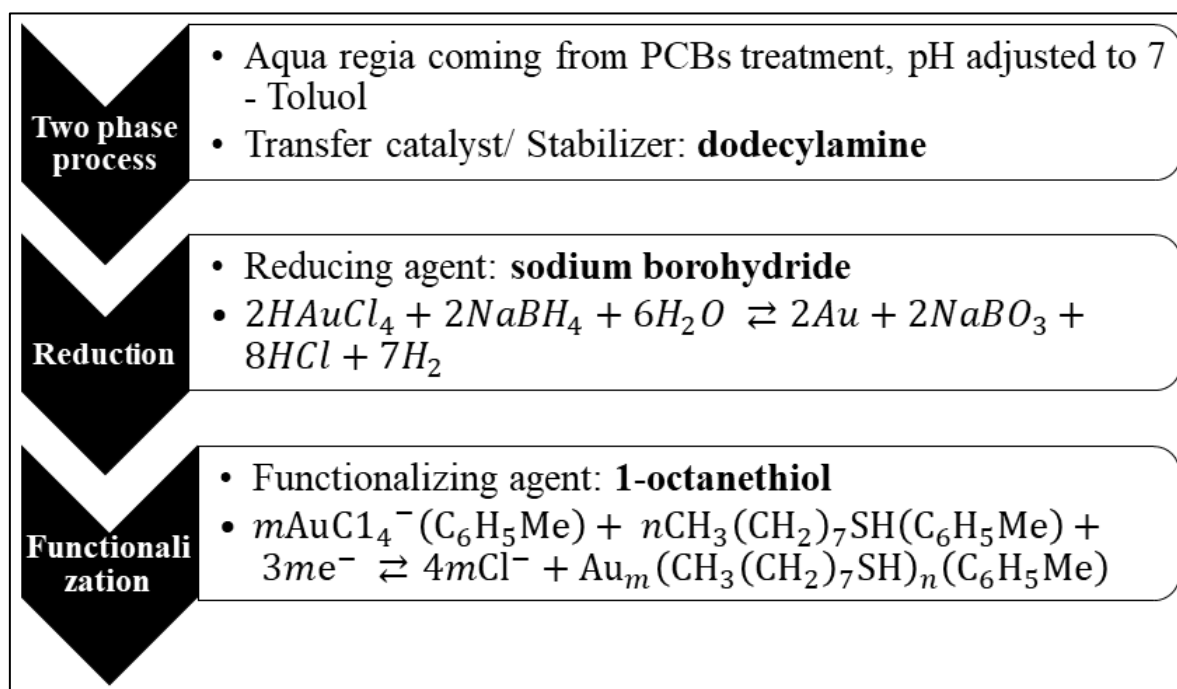


Fig. 6.44 Process used for Brust synthesis

The preliminary test allowed to synthesized gold nanoparticles thiol-functionalized, with diameter of ~100nm, as shown in Fig. 6.45. At first, synthesis was difficult because of the presence of other metals in aqua regia solution, which, however, precipitate after pH correction and applying production method described in Fig. 6.39. However, the high dimensions (in comparison with few nanometers expected) are probably due to low control of gold concentration in aqua regia solution.

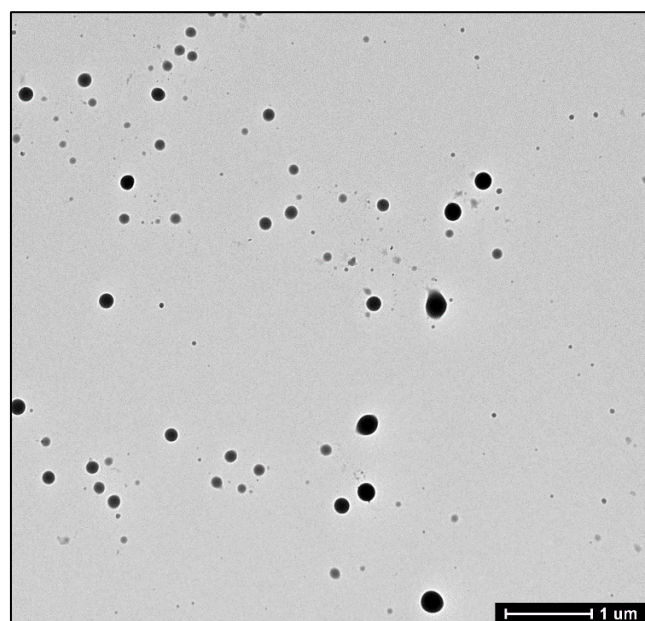


Fig. 6.45 TEM images of gold nanoparticles obtained with Brust synthesis.

6.6 Iron nanoparticles



Fig. 6.46 The synthesized zero-valent iron nanoparticles.

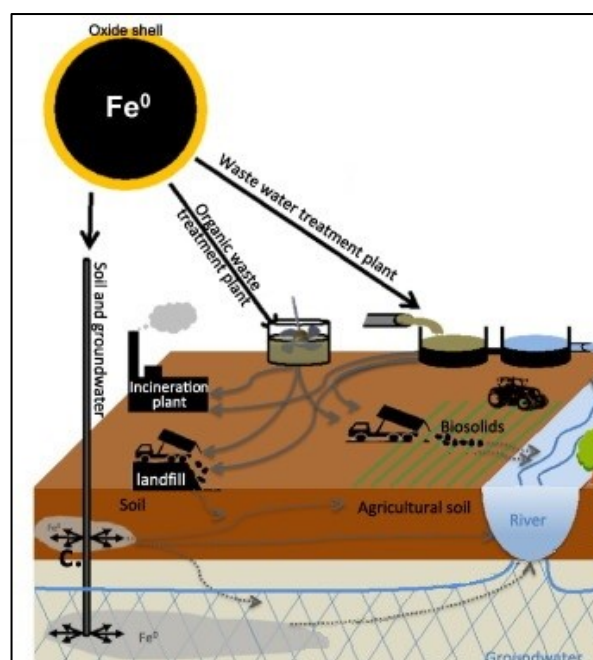


Fig. 6.47 Application of zero-valent iron nanoparticles in soil remediation.

In recent years, iron nanoparticles, amongst other metallic nanoparticles, have received much attention for their potential application to the treatment of contaminated soils and waters (Fig. 6.47 [198]). In fact, one of the most important nanomaterials studied for soil and groundwater purification is Fe [199], as it covers the broadest range of environmental contaminants such as halogenated organics, pesticides, arsenic, nitrate, and heavy metals.

Moreover, the high surface area to volume ratio and high surface energy means that iron nanoparticles offer a greater reactivity than the surfaces of bulk scrap metal or iron filings/granules commonly used for remediation purposes in permeable reactive barriers, injection, etc.

The remediation mechanism depends on the nature of the contaminant but, in all cases, it is driven by the oxidation of Fe(0). In the case of chlorinated organics, the mechanism of reactivity for iron is similar to the mechanism of corrosion and involves the generation of electrons, which, in turn, reduces the organic species through dichlorination and their transformation to relatively innocuous species. To date, iron nanoparticles have been shown to be effective remediators of a range of contaminants including chlorinated organics and inorganic anions. In addition, FeNP have also been shown to successfully remediate solutions contaminated with a range of metals, including Pb, Cr, Cu, As, Ni, Zn, Cd and Ag. In particular, for waters containing heavy metals, decontamination occurs via sorption and/or reduction onto the surface of the iron. It has repeatedly

been demonstrated that iron nanoparticles degrade contaminants more rapidly than the aforementioned forms of zero-valent iron [200].

Several types of iron nanoparticles are already available in the market. However, the development of sustainable and responsible zero-valent iron nanoparticle production and a better information exchange with the remediation industry should be promoted.

Usually, the production of zerovalent iron involves the use of $\text{FeCl}_2 \cdot 4\text{H}_2\text{O}$ and NaBH_4 , where NaBH_4 acts as a reducing agent of Fe^{3+} to produce zero-valent iron [201, 202].

In the preliminary study summarized in this Chapter, zero-valent iron nanoparticles are synthesized using as raw material goethite precipitated during permanent magnets treatment described in Chapter 5.2.

The iron hydroxide (goethite) was first dissolved in hydrochloric acid solution and successively reduced to zero-valent iron with ultrasound assistance. The synthesis was performed using two different reducing agents: sodium borohydride and eugenol.

Sodium borohydride is a strong reducing agent typically used for this kind of synthesis. In order of making the process greener was tested also eugenol, which is compound which can be derived from various plant species including cloves (*Syzygium aromaticum* or *Eugenia Caryophyllata*) [203].

6.6.1 Synthesis with sodium borohydride

Firstly, the use of NaBH_4 for nanoparticles synthesis was tested.

After dissolving 3g of FeOOH , without being dehydrated, in 100ml 0.5M HCl , 10ml of solution 0.1M NaBH_4 was added dropwise under ultrasound irradiation, for 2 min. In fact, ultrasounds inhibit particles growth and aggregation, as explained in Chapter 1.4.

The solution turned from yellow to black color (Fig. 6.48), and the black powder was separated by centrifugation. After the complete reaction, the powder was washed three times with ethanol and then held in a vacuum chamber.

The EDS spectrum of solid residue (Fig. 6.49) shows the presence of iron, even if there is also oxygen, probably due to sample oxidation before the SEM observation.

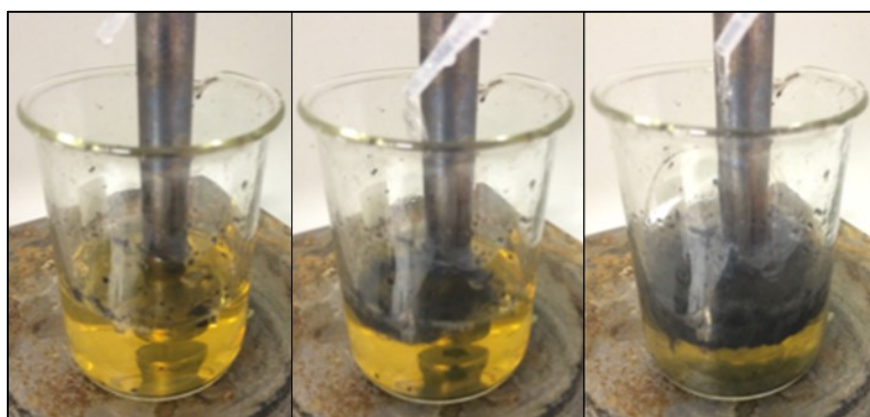


Fig. 6.48 Iron reduction due to sodium borohydride addition.

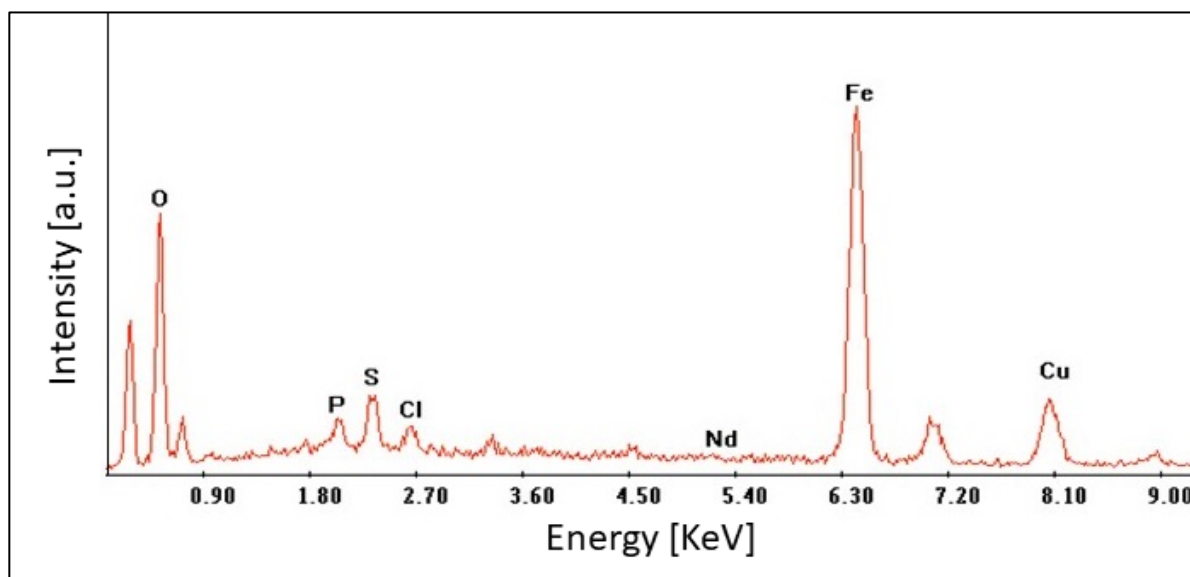


Fig. 6.49 EDS spectrum of nanoparticles synthesized with NaBH_4

The X-ray diffraction analysis showed the presence of iron oxides (Fig. 6.50).

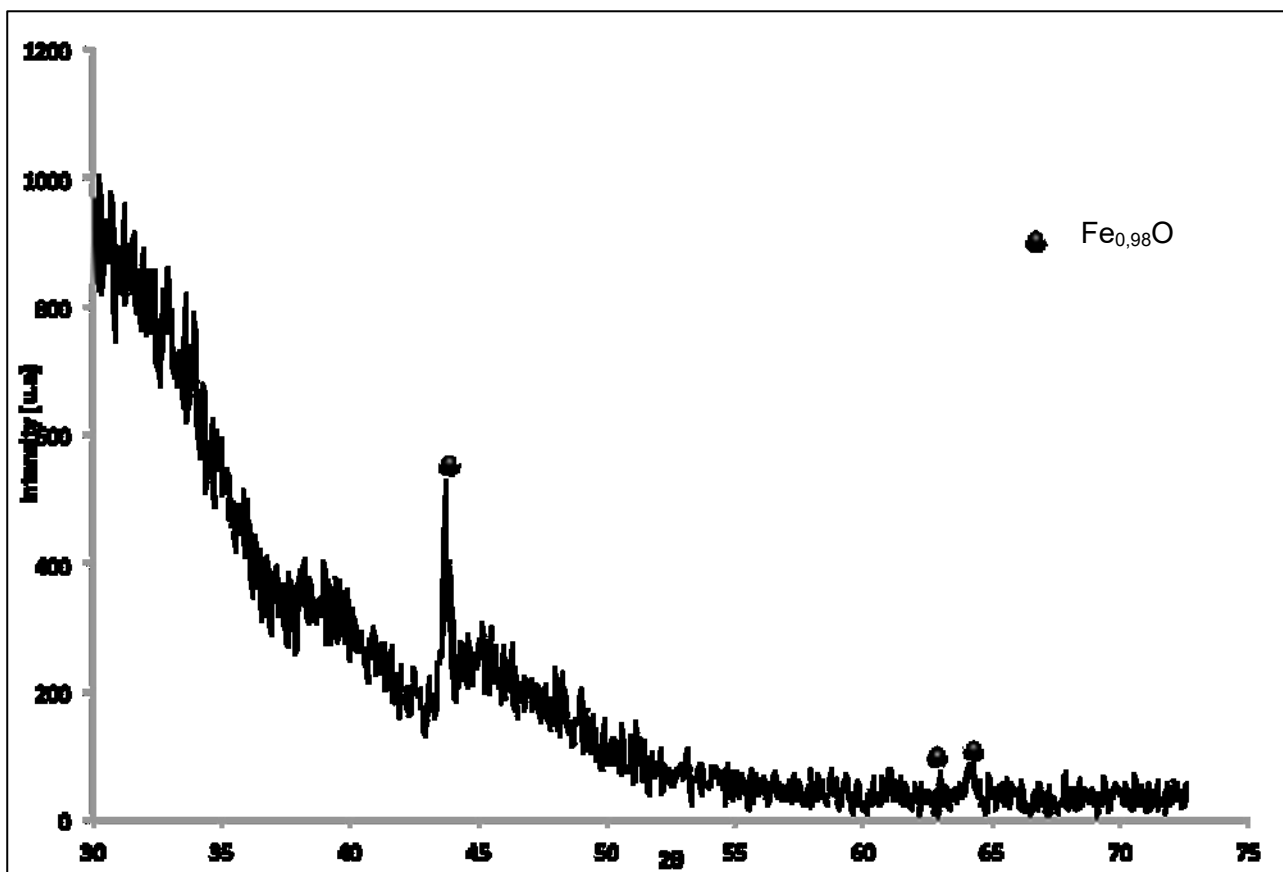


Fig. 6.50 XRD spectrum of nanoparticles synthesized with NaBH_4

The sample was also observed with TEM, which showed particles of about 50nm (Fig. 6.51).

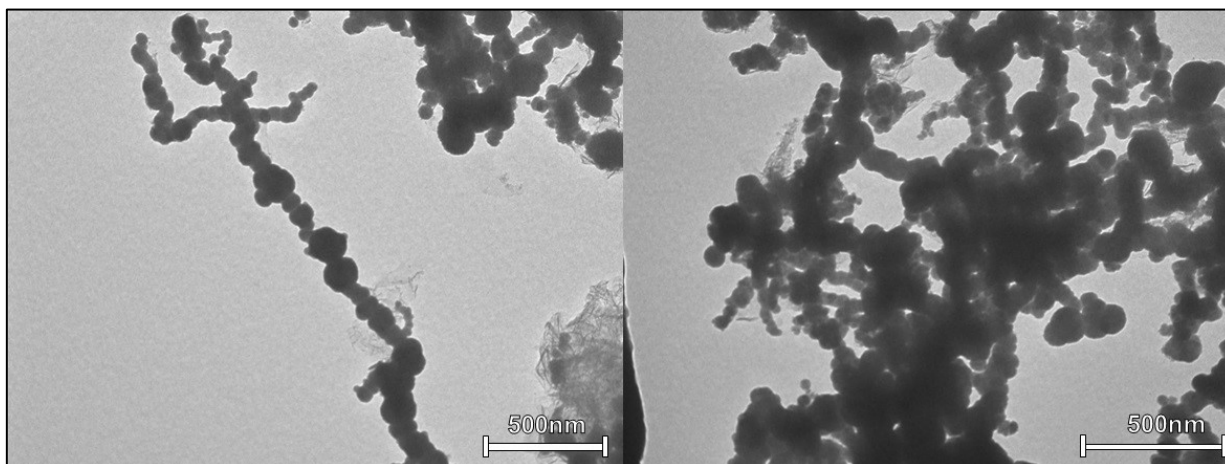


Fig. 6.51 TEM image of the nanoparticles synthesized with NaBH_4

6.6.2 Synthesis with eugenol



Fig. 6.52 Cloves (*Syzygium aromaticum*) and the preparation for eugenol extraction.

For the synthesis with eugenol, first the compound was extracted directly from cloves.

There were used 2g of dried cloves, after they've been crushed with pestle (Fig. 6.52). The treatment reported in the literature [122] involves the infusion into deionized water at 70-80°C for 3 min and the filtration of the solution. It is important not to exceed the prescribed temperature to avoid degrading the reducing agent. Moreover, the solution thus obtained needs to be used just after the preparation, otherwise it will not be reactive.

As raw material, it was used the same solution tested with sodium borohydride (0.5M HCl solution with goethite) and the same procedure.

The characterization of particles synthesized with eugenol was first performed with UV analysis. From the results (Fig. 6.53) there were visible two peaks at 216nm and 268nm, which confirm the presence of iron nanoparticles in the solution.

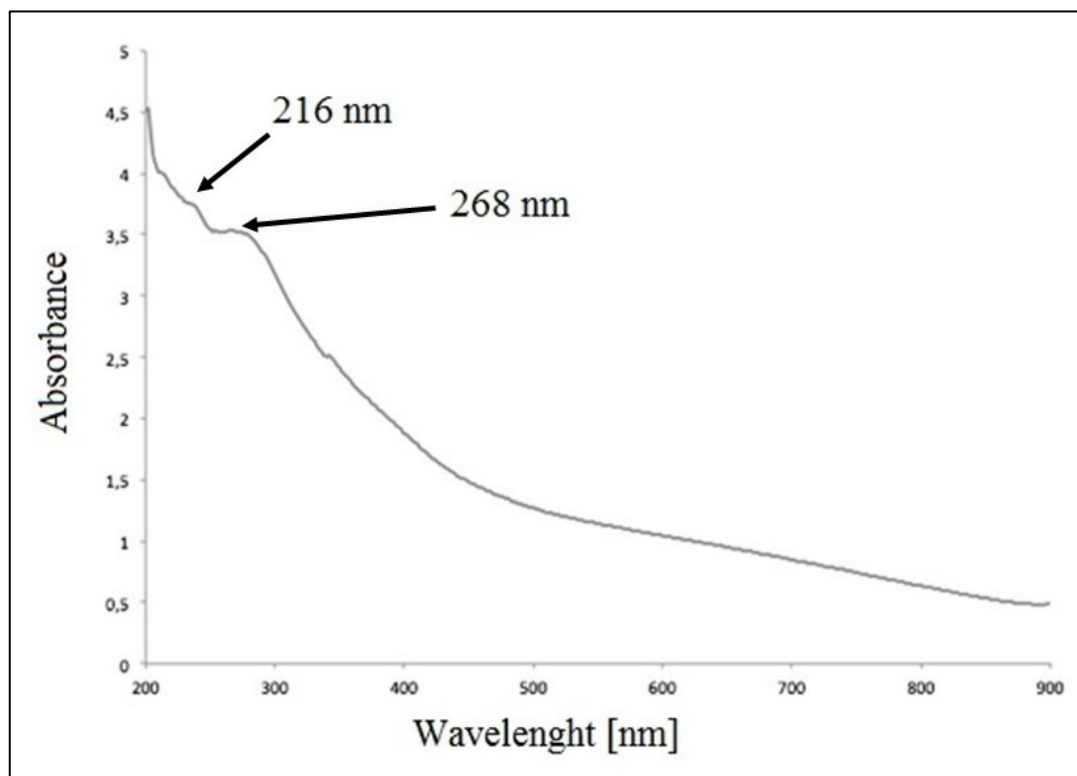


Fig. 6.53 UV absorption spectrum of the solution with the nanoparticles synthesized with eugenol.

TEM analysis showed the particles surrounded by organic substance, probably reducing agent residue (Fig. 6.54).

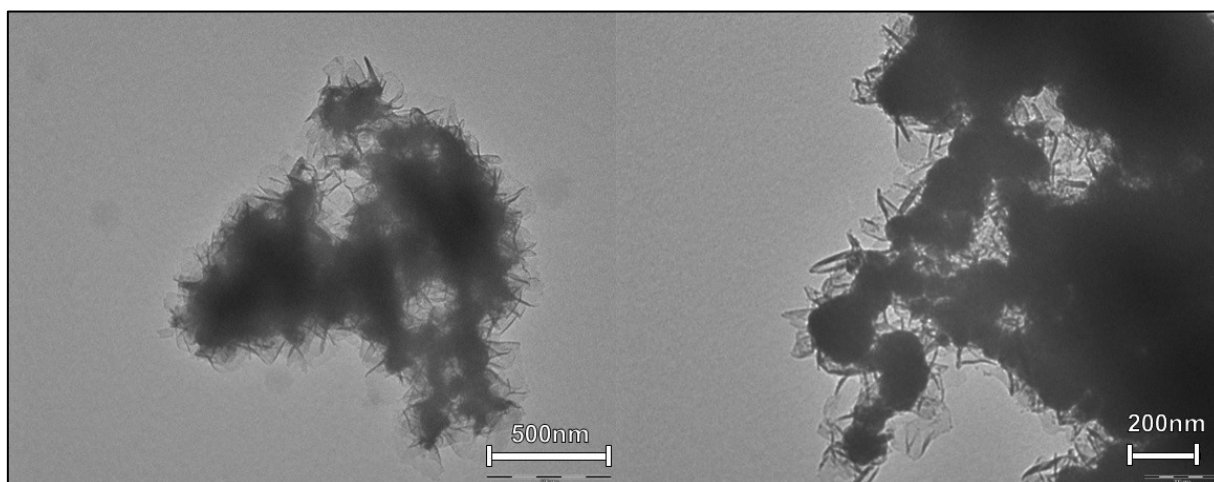


Fig. 6.54 TEM images of the nanoparticles synthesized with eugenol.

6.7 Concluding Remarks

In this chapter, the syntheses of different kind of nanoparticles were studied.

First as raw material it was used the nitric acid solution obtained from the leaching of PCBs of end-of-life mobile phones (Chapter 3).

In particular, tin oxide was precipitated from the solution using heating treatment and microwave or ultrasound assistance and SnO₂ nanoparticles produced had a size smaller than 10 nm.

Successively, silver was recovered from the solution causing precipitation of silver chloride and reducing it to metallic silver with Tollens reaction. The Ag nanoparticles obtained with conventional heating had a size of about 7 nm, whereas the ones synthesized using microwaves and ultrasound were about 2 nm and 0.7 nm, respectively.

Copper was finally recovered from the solution by cementation with iron powder. The recovered copper was used to synthesize copper and cuprous oxide nanoparticles.

For copper nanoparticles synthesis the use of L-ascorbic acid in water solution was investigated. It was interesting to notice that in this case the use of ultrasound reduced both the reaction time and the mean size of the nanoparticles. Specifically, copper nanoparticles with a mean size of about 5 nm were obtained with ultrasound, whereas without ultrasound the reaction took several hours and the final powder produced had a mean size of 1 μm.

Furthermore, the use of L-ascorbic acid as a reducing agent with ultrasound allowed for the production of Cu nanoparticles with a size that can be comparable to nanoparticles produced with sodium borohydride, the typical reducing agent used for nanoparticles synthesis.

In order of synthesize cuprous oxide nanoparticles D-glucose was used as reducing agent and also the ultrasound assistance allows the production of nanoparticles with dimensions less than 150nm. A method for the synthesis of gold nanoparticles from the gold coming from PCBs was also developed and gold nanoparticles with dimensions of about 100nm were synthesized. Moreover, the Brust synthesis using the same raw material was tested and also in this case the synthesis succeeded even if dimensions are of about 100nm instead of few nanometers typically obtained.

Finally, zero-valent iron nanoparticles were successfully synthesized using as raw material the goethite coming from the treatment of permanent magnets to recover Neodymium (Chapter 5).

Eugenol was tested as reducing agent and compared with sodium borohydride. The synthesized nanoparticles were very polydisperse with dimensions less than 200nm. However, further studies are required for the optimization of this synthesis, in particular avoiding particles oxidation and the presence of organics residue on the particles when eugenol is used.

In conclusion, different nanoparticles were synthesized using e-waste as raw material. Even if the proposed processes can be further studied, high-purity nanoparticles were obtained. This proved that, besides the intrinsic value of the recovered metals, a further value could be achieved by recovering them in the form of nanoparticles, which is possible to synthesize directly from hydrometallurgical solutions.

Chapter 7

Application of recovered metals

In this Chapter the applications of the recovered metals are studied, in particular copper and silver. In detail, silver or copper powder were successfully introduced inside Plasma Electrolytic Oxidation (PEO) coating.

PEO is a quite new process which allows creating porous ceramic layer on metallic substrates. This coating can improve not only corrosion resistance, but also other surfaces properties, mainly the wear resistance. The process is similar if compared with traditional anodizing but works at higher potentials, above the dielectric breakdown of the oxide formed on the surface. During the treatment, micro-discharges are formed and they produce the growth of the oxide ceramic film [204, 205, 206, 207, 208]. Considering the process divided in different stages, as reported in literature [209], conventional anodizing stop at stage II instead in the PEO process also stage III (sparking stage) and IV (micro-arc stage) occur. Comparing the two different processes, PEO is characterized by a lot of advantages: the used electrolytes are more environmental friendly, the obtained coatings are characterized by increased mechanical and corrosion properties, and coatings are composed not only of predominant substrate oxides but also of more complex oxides that contain the elements present in the electrolyte [205]. Moreover, it is possible to incorporate into the coating different types of particles in order to functionalize the coating and confer or increase some properties. Moreover, it is possible to incorporate into the coating different types of particles in order to functionalize the coating and to confer or to increase some properties. The possibility to include into the coating, particles that were suspended in the electrolyte without modifying the coating formation process is a peculiarity of the PEO process, and it can be used for different purposes, as extensively explained by Lu et al. [210] .

In this chapter, silver particles were incorporated into the coating to produce samples characterized by antifungal and antimicrobial activity. This fact could be very interesting for future application of PEO coated objects in furniture and fixtures of hospitals and in general in the medical field. In addition, copper particles were incorporated in order to increase antifouling properties. The antifouling test, performed both in estuarine and sea water for different times up to one month, confirm the antifouling effect.

7.1 Antibacterial and antifungal effect of silver powder in PEO coating

Plasma electrolytic oxidation (PEO), also called ‘Microarc Oxidation’ (MAO) is a relatively new surface modification technique that is arising an increasing interest in producing oxide ceramic coatings on light alloys such as aluminum, titanium or magnesium. PEO treatment can enhance the corrosion and wear resistance properties of these metals, or confers various other functional properties including anti-friction, thermal protection, optical and dielectric. Furthermore, PEO can be used as a pre-treatment to provide load support for top layers [204, 211]. PEO is derived from conventional anodizing [212, 213], but it shows many advantages such as higher anticorrosion and wear resistance performances of the coatings, more environmental friendly electrolytes and the possibility to include into the coating particles coming from the electrolyte [214]. PEO of metals is a complex process that combines oxide film formation, dissolution and dielectric breakdown: the sample, as anode, is immersed in an electrolyte and it works with high voltages and current densities inside a tank that is the cathode [215, 216]. Due to the high voltage that needs to be above the dielectric breakdown potential of the oxide layer, there are persistent anodic micro-discharges on the surface during the PEO treatment. These short-lived micro-discharges are the key of the process; they move randomly over the processed surface and produce the growth of an oxide ceramic coating [217].

In literature it has been already studied the possibility to incorporate particles inside the PEO coating, typically in order to increase the wear and corrosion resistance of the obtained layer [218, 219, 220, 221]. However, up to now, studies concerning the addition into PEO coating of silver particles to obtain antimicrobial activity have never been reported in literature and this is the real novelty of this work.



Fig. 7.1 Application of silver as antimicrobial agent.

The antimicrobial and disinfectant effect of silver is well known in literature [222, 223, 224, 225, 226, 227, 228]. Several mechanisms of interaction between silver and bacteria have been proposed. In particular, considering the one commonly accepted, silver ions cross the cell-membrane through a membrane transporter and their presence inside of the cell inhibit several functions in the cell and eventually cause cell death. Moreover, the addition of silver particles and nanoparticles in various types of coatings is described extensively in literature and allows to obtain an antimicrobial effect on various components without the use of detergents [229, 230, 231, 232, 233, 234].

Also the antifungal activity of silver is well known and in literature a lot of studies regarding this subject can be found [235, 236, 237, 238, 239, 240, 241]. There also can be found detailed studies of the antifungal action of silver on *C. Albicans*, where it is stated that the silver particles produce the disruption and create pores in the cell membrane potential that cause ion leakage, ultrastructural changes and induce apoptosis [242, 243]. Also the production on silver-containing coating with antifungal activity is reported in literature: Wojcietszak et al. [244] reported the production of magnetron sputtered Ti-Ag and Nb-Ag coatings with antifungal activity and Kamikawa et al. [245] reported the use of a polymeric silver containing coating with fungicidal activity against *Candida*.

However, no studies regarding the antifungal or antimicrobial effect of PEO coated specimens can be found in literature.

In this Chapter, silver particles were innovatively added into the PEO coating produced on AA7075. The properties of the obtained coating were studied and in particular there were tested both its antimicrobial and antifungal activity. The test were conducted comparing the silver-containing sample with the untreated alloy, the conventionally anodized samples and the samples PEO coated without silver particles.

The developed treatment could be very useful in the production of support devices (tray, furniture, etc.) used in hospitals or for other medical purposes because these particles can give antimicrobial and antifungal properties to the coated specimen without the use of detergents or additives.

7.1.1 Production of PEO coatings

Samples of 7075 aluminum alloy were used as substrate for coatings. The nominal composition of the alloy is reported in Tab. 7.1.

Al%	Mg%	Zn%	Cu%	Others%
90.7	3.1	4.1	0.9	1.2

Tab. 7.1 Chemical composition of 7075 alloy.

Before performing the PEO treatment, all the samples were polished following standard metallographic technique and degreased with acetone in an ultrasound bath. The electrolyte used in the PEO process was constituted by an alkaline aqueous solution containing 25 g/L of sodium silicate, 2.5 g/L of sodium hydroxide and two different quantities of silver particles, as described below.

7.1.1.1 Silver particles production

The production of the silver particles was performed using as raw material silver chloride coming from the acid pre-treatment of electronic scraps, as described in Chapter 6.2.1.

The reduction process was similar to that used for silver nanoparticles synthesis but higher concentration were used. The silver chloride, after washing, was dissolved in ammonia solution (30%) to which glucose syrup was added and then heated at 50°C for 1 h.

The precipitated powder was constituted by silver particles; a SEM image and EDS analysis of this particles are reported in Fig.7.2.

After washing with deionized water, this powder was added directly to the PEO solution.

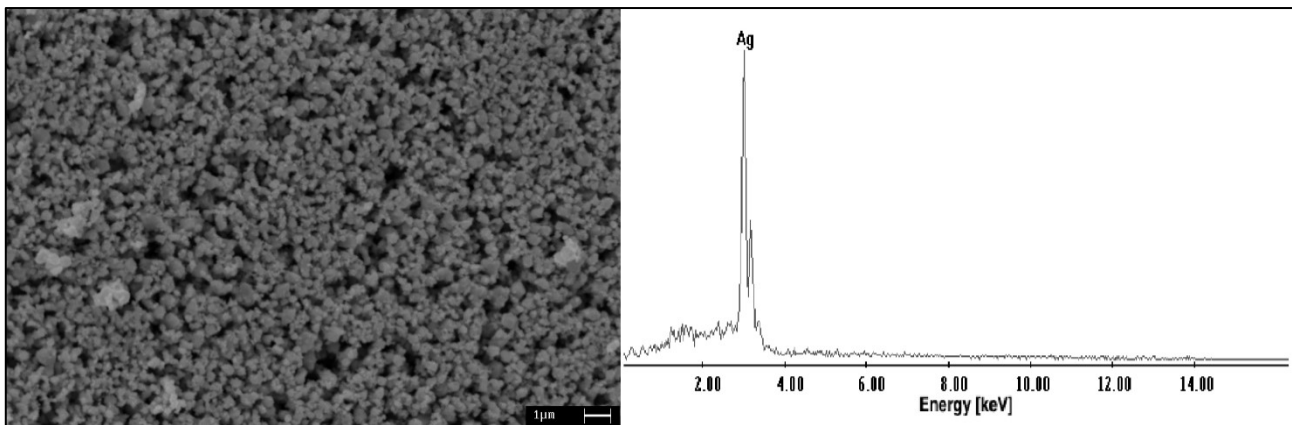


Fig. 7.2 SEM image and EDS analysis of the silver powder produced and added to the PEO electrolyte.

Moreover, as reported before, two different cases with different quantities of silver particles were studied:

- PEO Ag low: 110 g of silver particles obtained using as raw material 160 mg of AgCl
- PEO Ag high: 220 g of silver particles obtained using as raw material 320 mg of AgCl

7.1.1.2 PEO treatment and characterization methods

The plasma electrolytic oxidation process was carried out using a TDK-Lambda DC power supply of 400V/8A capacity. During the treatment, the aluminum alloy was the anode whereas the cathode was a carbon steel mesh immersed in the electrolyte. The treatments were performed for 4 min keeping a constant current density of 0.3 A/cm². After the PEO treatment, the samples were washed with deionized water and ethanol and dried with compressed air.

The PEO samples obtained in the solution with silver particles were compared with an untreated sample, a sample PEO treated without silver particles and a traditional anodized one. The traditional anodizing was obtained using a current density of 0.016 A/cm² for 25 min in a solution of sulfuric acid (20%) and using a lead cathode. The temperature of the electrolyte was maintained constant at 18 °C with the connection to a thermostatic bath. Also a conventional anodizing with silver particles addition in the electrolyte was tested.

After the PEO coating, a final sealing treatment was carried out in some samples in order to increase their corrosion properties. As a matter of fact, the surface of the PEO coating are usually porous and a sealing treatment is necessary. The sealing treatment was performed immersing the samples for 15 minutes in boiling water with a suspension of silver particles.

Summarizing, the following surface treatments were tested: i) PEO in silicate solution; ii) PEO in silicate solution with two different amounts of silver particles, “PEO Ag low” and “PEO Ag high”; iii) anodizing; iv) anodizing with silver particles. The samples obtained with PEO in silicate solution with silver particles were also subjected to a sealing treatment.

The surfaces of the different samples were observed with stereo-microscope in order to evaluate the external appearance of the samples. The cross-sections of the layers instead, after the cutting operations, were mounted in epoxy resin and polished with standard metallographic technique. Both the surface and the cross-section of treated samples were examined with SEM, to evaluate the morphological features, the thickness of the coating and the elemental composition.

The phase analysis and the crystallinity of the coatings was carried out with Diffractometer described in Chapter 2.9 operated at 40 kV and 30 mA.

XPS analysis were run using spectrometer described in Chapter 2.12, using standard Al K_α radiation (1486.6 eV) working at 250 W. The working pressure was $< 5 \cdot 10^{-8}$ Pa. The spectrometer was calibrated by assuming the binding energy (BE) of the Au4f_{7/2} line at 83.9 eV with respect to the Fermi level. The standard deviation for the BE values was 0.15 eV. The reported BE were corrected for the charging effects, assigning, in the outer layers where contamination carbon is still present, to the C1s line of carbon the BE value of 284.6 eV [246]. Survey scans (187.85 pass energy, 1 eV/step, 25 ms per step) were obtained in the 0 - 1300 eV range. The atomic composition, after a Shirley type background subtraction [58], was evaluated using sensitivity factors supplied by Perkin [59]. The assignments of the peaks were carried out by using the values reported in the reference handbook [59], in the NIST XPS Database [247, 248]

7.1.2 Surface Characterization

The surface of all the treated samples, PEO and anodized ones, were observed at the stereo microscope and the results are shown in Fig.7.3.

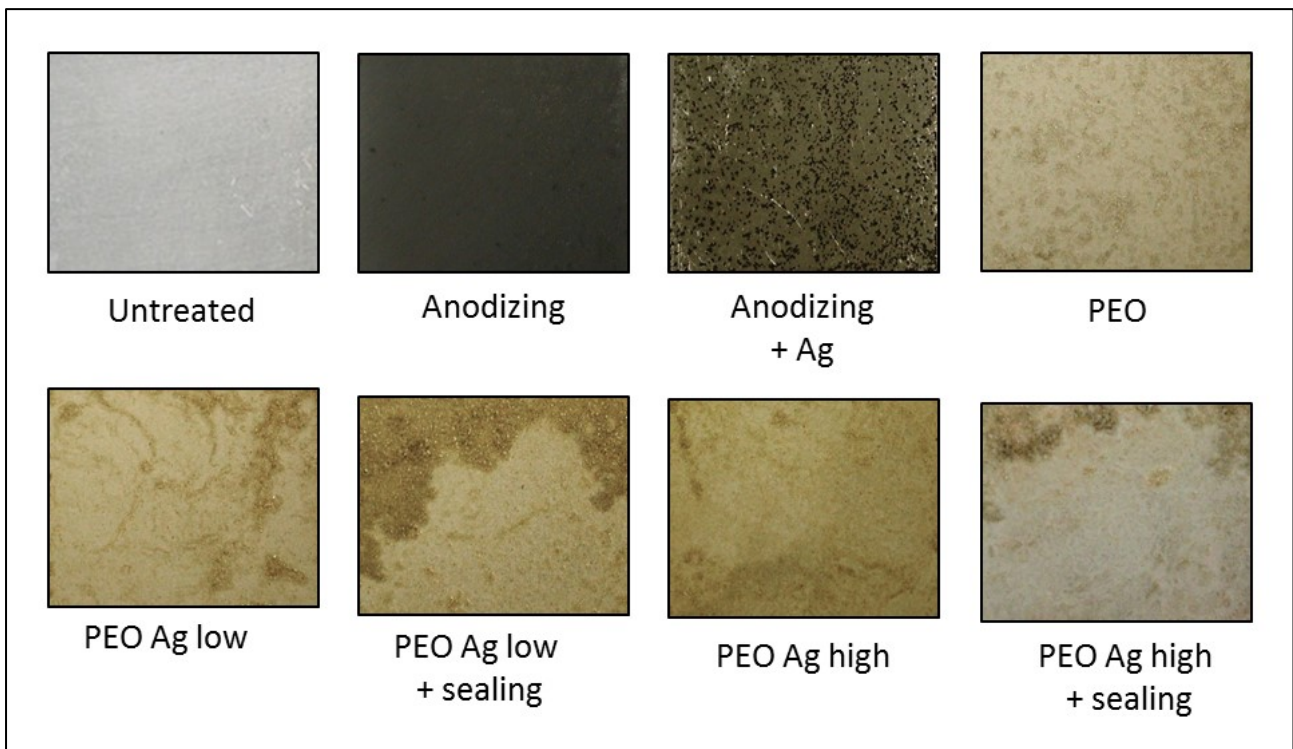


Fig. 7.3 Stereo Microscope images of the surfaces of the different samples.

It can be observed the typical light gray-brown color of PEO treated sample and the dark grey color of the anodized one. The presence of the silver particles changed the color of the PEO coating, especially in the case of the highest concentration of Ag: the surface was dark brown and after the sealing treatment it became gray. Moreover, it can be observed that the oxide layer has not formed on the sample subjected to anodizing with silver particles in the electrolyte, and pitting corrosion occurred. This fact can be explained with the interferences caused by the silver particles in the discharge phenomena during the anodizing process, a process notoriously more difficult to control than PEO [211].

All the samples were observed at the electron microscope in order to verify quality of the coating and verify the presence of silver in the coating. In Fig. 7.4 are reported the surfaces and the cross sections of the sample treated respectively with the conventional PEO process and with traditional anodizing.

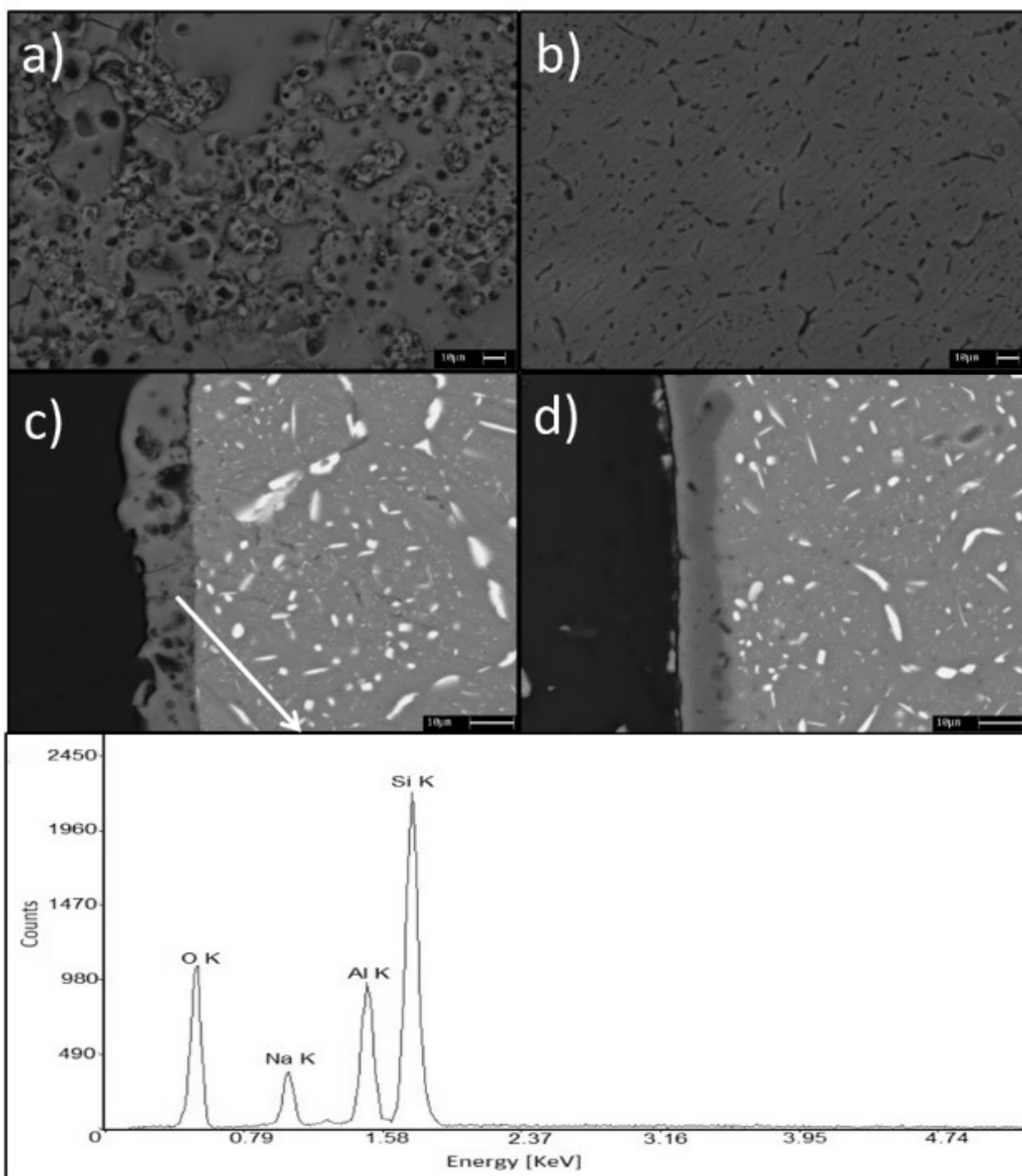


Fig. 7.4 SEM images (BSE electrons) of the surface of the sample PEO treated without silver particles in the electrolyte (a) and of the sample conventionally anodized SEM images (b) and images of their cross sections (b,c) with EDS composition of the PEO coating.

Considering the cross section of the PEO sample (Fig. 7.4 c), it can be observed a uniform and compact oxide coating with an average thickness of about 11 μm . Also the adhesion between the coating and the substrate seems good but pores and micro cracks are clearly visible. The surface of the sample (Fig. 7.4 a) is the typical of PEO coatings with a lot of pores and micro-cracks [249, 250, 251]. The anodized sample, instead, exhibited the conventional morphology of this type of coating with an average thickness of about 9 μm and the presence of pores on the surface. The composition of the PEO coating obtained on 7075 AA, reported in the EDS analysis in the same figure, is in accordance with the composition of the substrate and of the electrolyte. In particular, it can be observed that the coating was mainly composed by aluminum and silicon oxides, but there is also the presence of sodium oxide, as reported in the semi-quantitative analysis in Tab 7.2.

O%	Na%	Al%	Si%
36.6	7.2	17.7	38.5

Tab. 7.2 EDS semi-quantitative analysis of the PEO coating

The SEM micrographs of the surfaces and the cross sections of the two PEO sample obtained with the two solutions containing Ag, sample “PEO Ag low” and of the sample “PEO Ag high” are reported in Fig. 7.5.

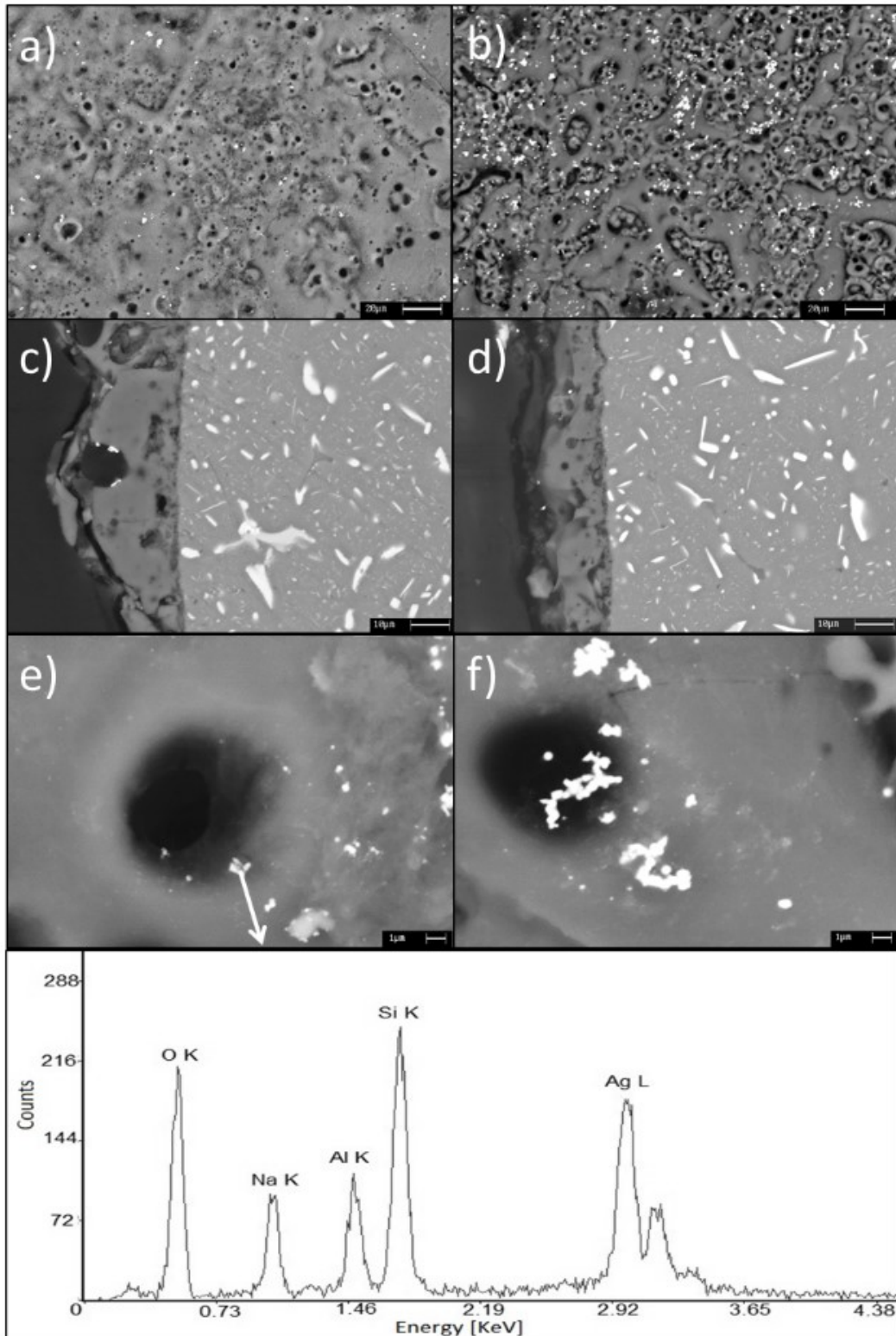


Fig. 7.5 SEM images (BSE electrons) of the surface, at two magnification (a, e), and cross section (c) of the sample “PEO Ag low” and of the surface, at two magnification (b, f), and cross section (d) of the sample “PEO Ag high” with EDS micro-analysis of the silver particle in the pore.

It can be observed that the presence of silver particles in the electrolyte seems to have not influenced the formation of the oxide ceramic coating. In fact, both the protective layers obtained with two amounts of silver particles were adherent to the substrate and homogeneous and the surfaces of the samples showed the typical porous morphology of PEO coatings. The possibility to incorporate into the coating particles that were suspended in the electrolyte without modifying the formation process of the coating is a peculiarity of the PEO process, and it can be used for different purposes as extensively explained by Lu et al. [210]. The observation in backscattered electron (BSE) mode allowed to characterize the distribution of silver on the surface because it is a heavier element and thus appears brighter in the image. The EDS (Fig.7.4) analysis performed in correspondence of the lighter zones indicated a high presence of silver (the EDS spot has a diameter of 1 μm and therefore also the surrounding zone was considered in analysis).

From the images, it can be observed that the distribution of the silver particles on the surface of the sample is not uniform and that they were concentrated in the proximity of pores. The cross section of the coatings, evidenced that silver particles were present also inside the pores.

Comparing the surface of the samples obtained with “PEO Ag low” and “PEO Ag high”, the presence of larger agglomerates of silver particles resulted on the surface obtained with “PEO Ag high” as can be observed in Fig. 7.5 e and Fig.7.5 f (SEM image of the surfaces obtained at higher magnifications).

The sealing of the pores that characterized the PEO coatings is always necessary if the specimen needs good corrosion resistance, as in medical applications. In fact, without this final treatment, no protection against galvanic corrosion can be obtained by the oxide ceramic coating on the surface. In the devices used in the medical applications, corrosion is not allowed so, in these cases, the sealing treatment must be performed. In this work, a treatment of sealing in boiling water for 15 min was performed on sample “PEO Ag low” and sample “PEO Ag high”. Moreover, silver particles were added in the boiling water solution in order to produce a sealing treatment with silver particles.

After the sealing treatment, in order of studying its effects, the surfaces and the cross sections of the coatings were observed with SEM. The results are reported in Fig.7.6.

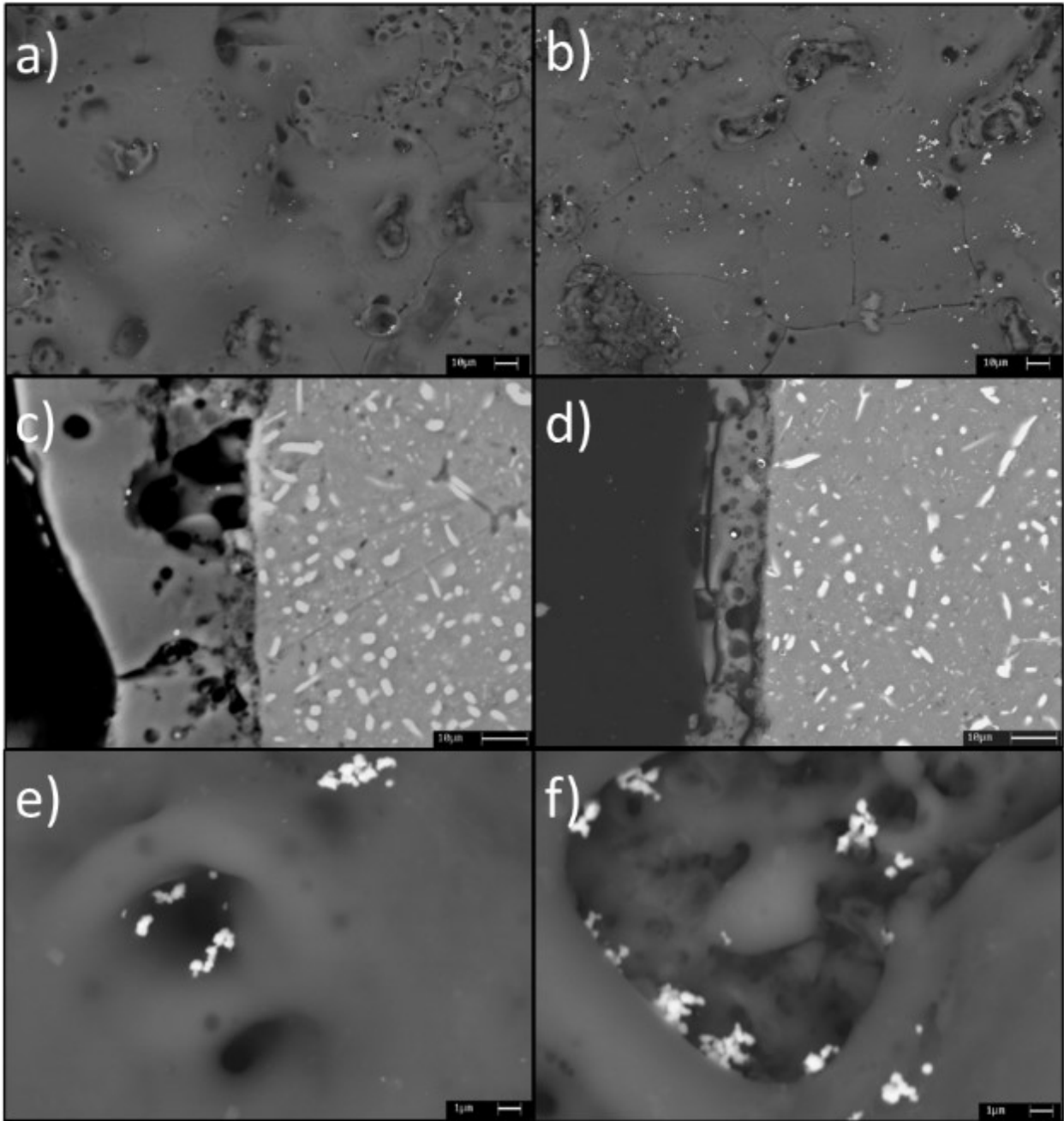


Fig. 7.6 BSE-SEM images of the surface, at two magnification (a,e), and cross section (c) of the sample “PEO Ag low” after the sealing treatment and of the surface, at two magnification (b, f), and cross section (d) of the sample “PEO Ag high” after the sealing treatment.

As it can be seen, after the sealing treatment the coating remained adherent to the substrate and the pores were sealed, increasing barrier effect of the oxide layer. The sealing of the pores was more marked in sample “PEO Ag high”. The presence of silver on the surface was noticeably reduced after the sealing treatment, and the images taken at higher magnification (Fig. 7.6) evidenced that agglomerates of silver were present inside the pores. As expected, the quantity of silver is higher in the sample “PEO Ag high + sealing” (Fig.7.6 b) than in the sample “PEO Ag low + sealing” (Fig.7.6 a).

X-ray diffraction (XRD) analysis were performed on the sample “PEO Ag high” in order to identify the different phases of the coating. The results are reported in Fig.7.7.

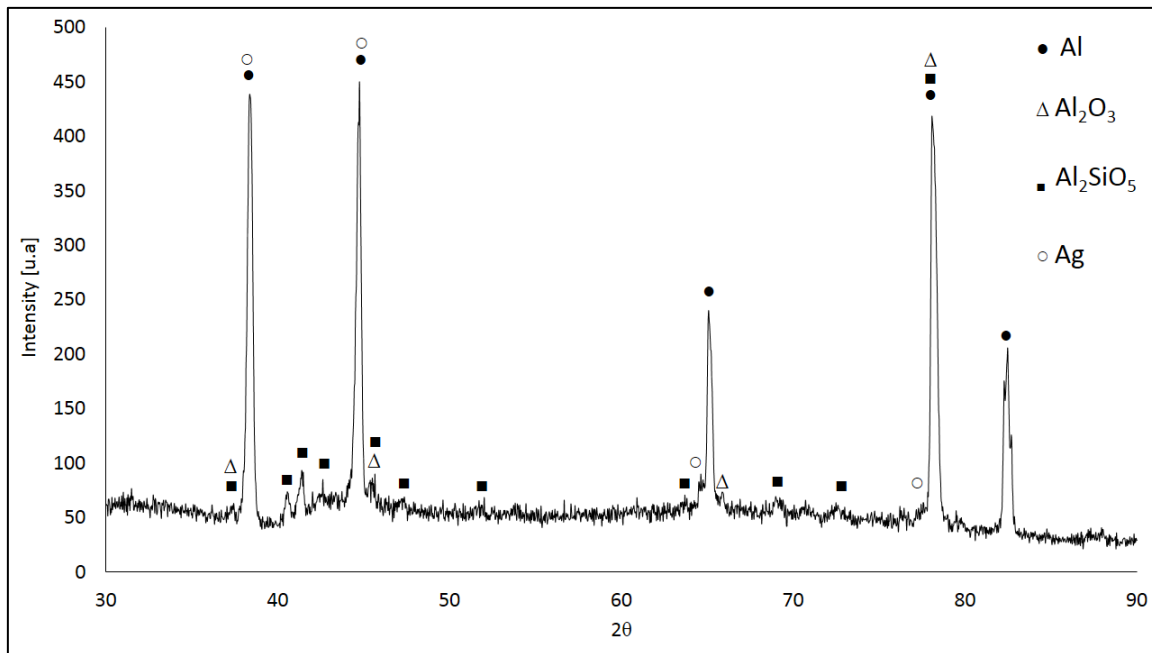


Fig. 7.7 XRD diffraction pattern of the PEO treated sample high silver

The diffraction pattern was also compared with the one obtained on the sample with the treatment without silver particles, reported in [252].

Both analysis showed the peaks of Al_2O_3 and Al_2SiO_5 in accordance with the composition of the alloy and of the electrolyte used in the PEO process. In the sample “PEO Ag high”, also the peaks of Ag were present. The presence of the Al peaks was due to the diffraction from the substrate.

XPS analysis (without sputtering) was performed on the surface of the “PEO Ag high + sealing” sample and the results were compared with those obtained with the PEO treated sample. The survey spectra of the samples are shown in Fig. 7.8.

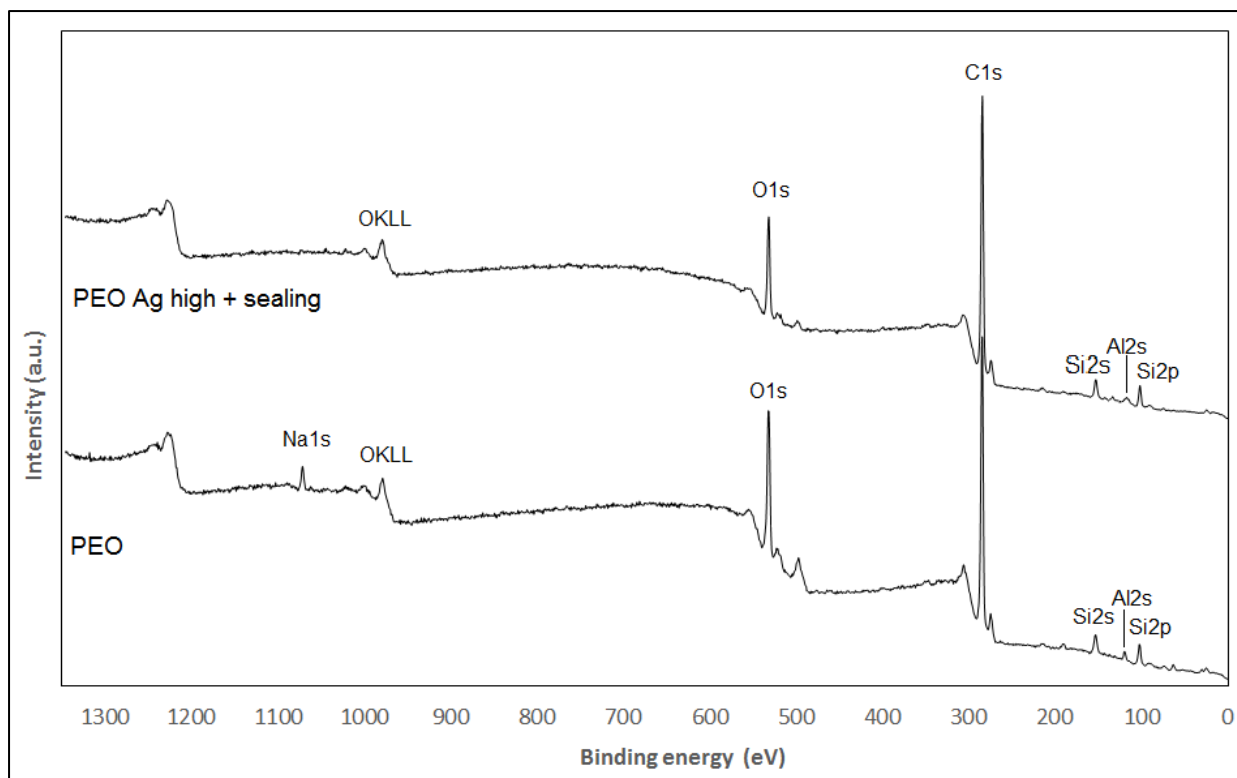


Fig. 7.8 Survey spectra of PEO sample and of “PEO Ag high + sealing” sample.

From the collected spectrum of the main photoelectron lines, the atomic percentages of the elements present in the external surface of the coating were calculated. The surface of the PEO sample resulted to be principally constituted by O, Si, Na and Al, whereas the surface of the PEO Ag sample by O, Si and Al. The presence of C is ascribable to contamination.

The results of the quantitative analysis are reported in Table 7.3.

Element	C	O	Na	Mg	Al	Si	Zn	Ag
Region	C1s	O1s	Na1s	Mg2s	Al2p	Si2p	Zn2p3/2	
PEO	32.9	45.7	4.3	1.1	3.2	12.4	0.4	-
PEO Ag high + sealing	77.8	13.7	0.2	0.8	1.7	5.3	0.2	0.3

Tab. 7.3 Quantitative XPS analysis of the external layer formed on the samples (Wt%).

A more detailed XPS characterization of AA7075 sample PEO treated with an alkaline aqueous solution containing 25 g/L of sodium silicate and 2.5 g/L of sodium hydroxide was already studied [252] and is not reported. The surface resulted mainly constituted by Al_2SiO_5 , Al_2O_3 , $(\text{SiO}_2)_{0.7}(\text{Na}_2\text{O})_{0.3}$.

The high resolution O1s spectra of the “PEO Ag high + sealing” sample is shown in Fig. 7.9 a. Oxygen spectra can be deconvoluted in two main components: the peak located at 531.8 eV BE corresponding to the metal hydroxides and to aluminosilicate compounds, whereas the peak at 532.7 eV to silicate compounds [253]. The high resolution Si2p peak of the “PEO Ag high + sealing” sample is shown in Fig. 7.9 b, and the peak located at 102.2 eV BE was attributed to silicate compounds, whereas the other one at 102.7 suggested the presence of aluminosilicate compounds [253, 59]. The high resolution peak Al2p peak is shown in Fig. 7.9 c. The main peak

located at 74.7 eV BE is consistent with aluminosilicate [253]. The high resolution Ag3d region is shown in Fig. 7.9d, where it is possible to observe the two components 3d_{5/2} and 3d_{3/2} at 368.2 and 374.2 eV BE, respectively. These values indicated the presence of metallic Ag [59].

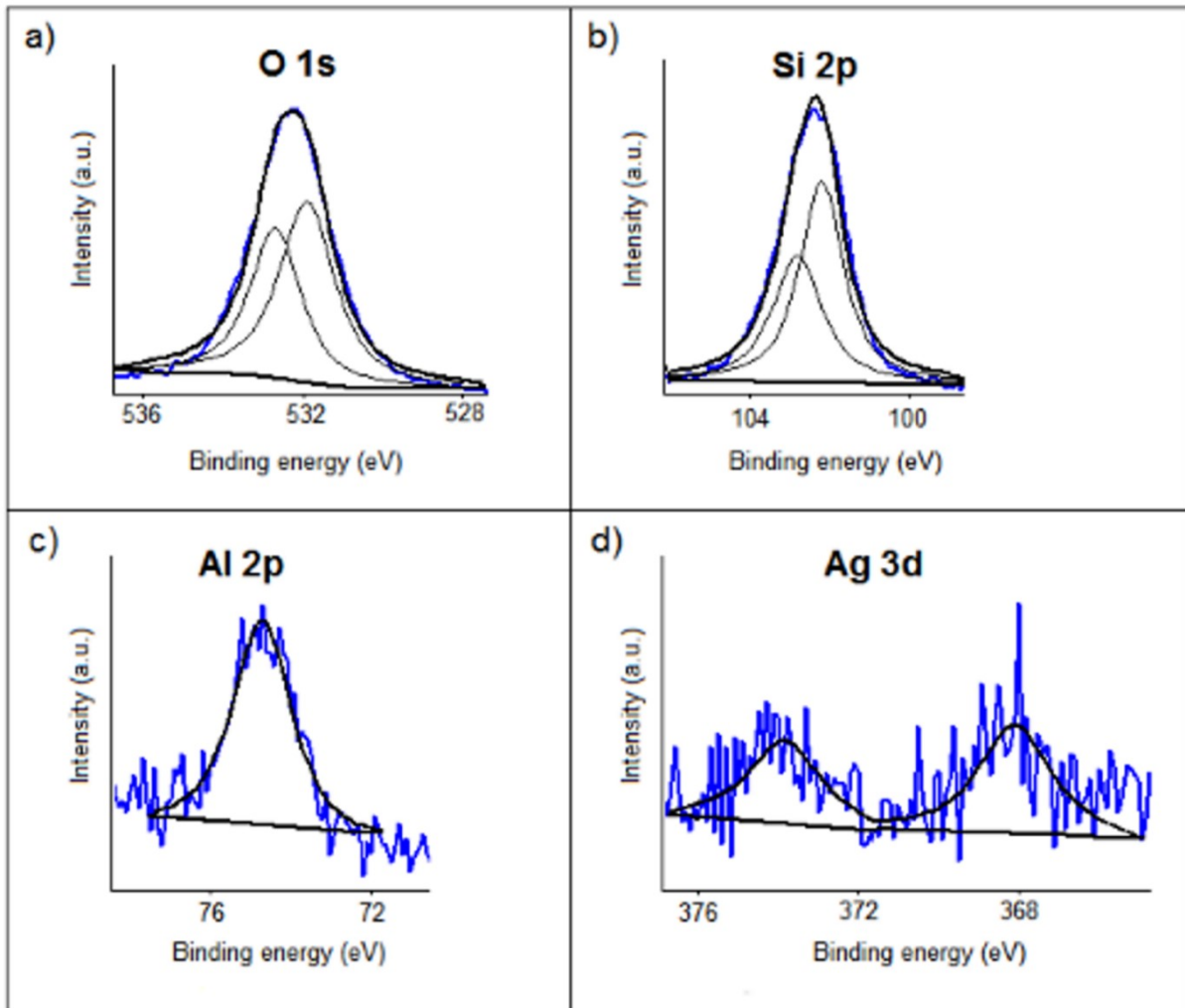


Fig. 7.9 XPS high resolution spectra of the sample “PEO Ag high + sealing” sample.

7.1.3 Corrosion Resistance

In order to evaluate the effect of the different treatments on the corrosion resistance of the various samples, potentiodynamic polarization tests were performed in an electrolyte that simulate an aggressive environment containing both chlorides and sulfates. Potentiodynamic tests were performed in a solution containing 0.1 M sodium sulfate and 0.05 M sodium chloride, with potentiostat described in Chapter 2.5, using a saturated calomel electrode as reference electrode (SCE) and a platinum electrode as counter electrode with a scan rate of 0.5 mVs⁻¹. The corrosion resistance of the different samples was compared to evaluate if the addition of silver particles produce a decrease in the corrosion resistance. The potentiodynamic polarization plots of the different samples are reported in Fig. 7.10 and the corrosion current densities and corrosion potentials, extrapolated from the curves, are summarized in Table 7.4.

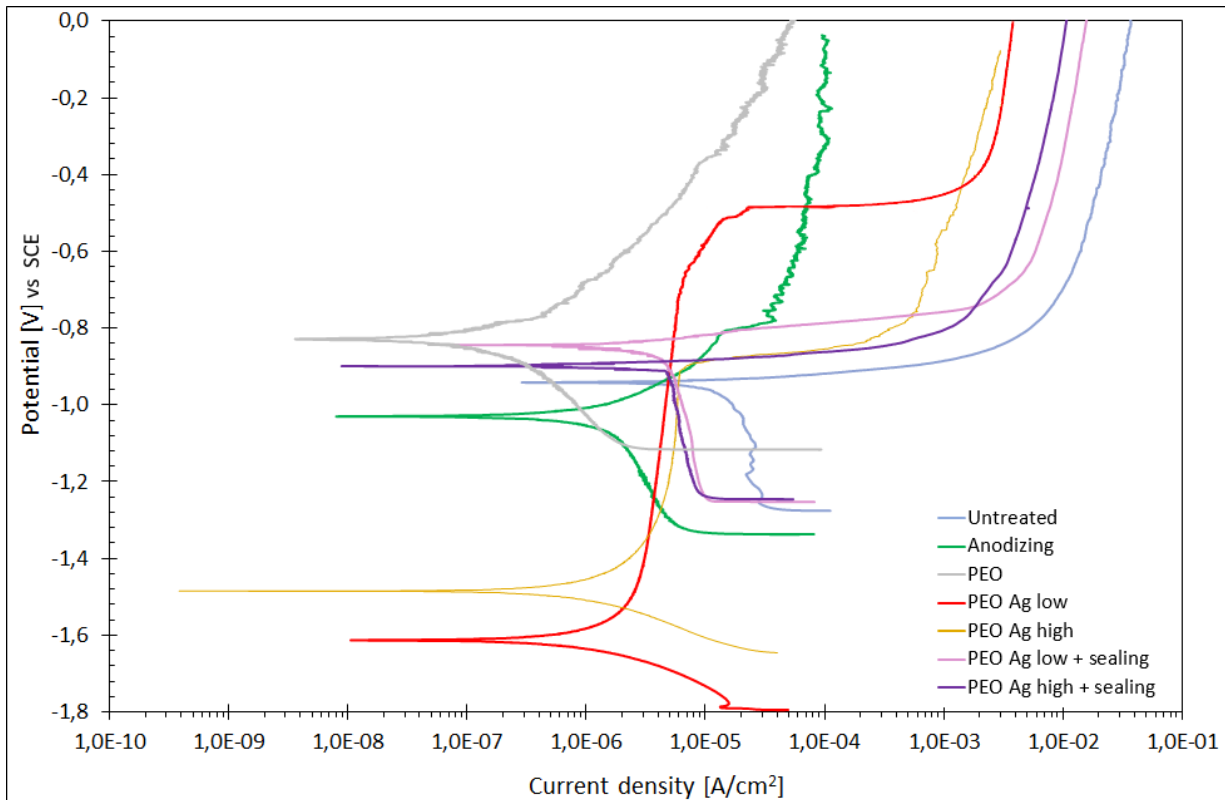


Fig. 7.10 Potentiodynamic polarization plot for the different samples (test electrolyte: 0.1M Na₂SO₄ + 0.05M NaCl)

	E_{corr} [V]	I_{corr} [A/cm²]
Untreated	-0.9	1.5x10 ⁻⁵
PEO (No Silver)	-0.86	1.5x10 ⁻⁷
Anodized	-1.4	1x10 ⁻⁶
PEO Ag low	-1.62	1x10 ⁻⁶
PEO Ag high	-1.48	1x10 ⁻⁶
PEO Ag low + sealing	-0.92	3.5x10 ⁻⁶
PEO Ag high + sealing	-0.86	3x10 ⁻⁶

Tab. 7.4 Corrosion potentials and corrosion current densities for the different samples.

It can be observed that the sample with the best corrosion performance was the one treated with PEO process without silver particles in the electrolyte. In fact, this sample showed the higher value of corrosion potential (that indicates the nobility of the sample) and the lower value of corrosion current density, directly connected with the corrosion rate through the Faraday law. In detail, the corrosion current density of the sample PEO treated without silver particles in the electrolyte was about two orders of magnitude lower than the untreated sample. The conventionally anodized sample was characterized by a corrosion behavior intermediate between the untreated sample and the PEO coated sample; this in accordance with the well-known fact that the PEO coatings shows improved corrosion resistance than the conventionally anodization coatings [254]. Focusing on the samples treated with silver particles in the electrolyte, it can be observed that the presence of silver caused a remarkable decrease in the corrosion potential in comparison with the sample treated without these particles. This fact is confirmed both in sample “PEO Ag low” and sample “PEO Ag high”, and it was related to the local galvanic couple that is formed between the silver and aluminum, causing galvanic corrosion. Also the current density increases of about one order of magnitude in the samples treated with silver particles than those of PEO treated without silver particles but, nevertheless, it remains one order of magnitude lower if compared with the untreated one. This behavior was due to the high difference in the potentials scale between silver and aluminum that strongly favored the corrosion phenomena. The sealing treatment allowed to reduce the problems connected to galvanic corrosion enhancing the corrosion potential of the samples: in fact, the samples after the sealing treatment were characterized by a corrosion potential similar to the sample treated without silver particles. Moreover, the corrosion current densities remain one order lower than untreated sample.

The addition of silver particles during the PEO process caused a general decrease in the corrosion properties in comparison with PEO samples but, after the sealing treatment, the susceptibility of corrosion decreased. In detail, the corrosion resistance of the samples containing silver particles after sealing remains lower than the one of the sample PEO treated without silver particles but it is remarkably higher than the one of untreated sample and comparable with the one of the conventionally anodized.

7.1.4 Antimicrobial Activity

Two bacteria, gram-negative *Escherichia Coli* and gram-positive *Staphylococcus Aureus* were selected for the antimicrobial tests. At first, all samples (in triplicate, for a total of 21 surfaces) were cleaned with alcohol and treated under the Germicidal lamp for 2 h. Bacterial colonies of 18-20 h were diluted in nutrient broth containing 0.4 % Agar. A suspension of 50 µl of Agar was distributed on the surfaces to be tested and incubate at 35 °C for 3 h in humidified atmosphere to prevent drying of inocula. The surfaces were washed with 10 ml of phosphate buffer with pH between 6,8 and 7,2, according to the standard BS ISO 22196:2011, in physiological saline and serially diluted, always in phosphate buffer. Of each dilution 250 µl were included in triplicate, in Tryptic soy agar (TSA) kept molten at 47 °C. After solidification, the plates with TSA were incubated at 35 °C for 24-48 h and then the number of colonies was counted and the mean values reported. The data have been compared with reference samples and the antimicrobial activity of the different surfaces was established by comparing the initial number of UFC of *E. coli* and *S. aureus* to the number of bacterial colonies after the incubation in contact with the different surfaces.

The antimicrobial activity was evaluated counting the number of bacteria after 3 h of exposition to the treated surface. In particular, the antibacterial properties were evaluated comparing the different PEO treated surfaces containing silver particles with other two surfaces: one untreated and one PEO treated without silver particles. The tests were performed in triplicate in order to assure good reproducibility. Two different bacteria were used: a gram-positive (*Staphylococcus Aureus*) and a gram-negative (*Escherichia Coli*) in order to compare two different types for whom silver shows its action [149, 255, 256].

The results of the counting of the colonies of *Escherichia Coli* and the slides with the bacteria after 3h of exposure can be observed in Fig. 7.11.

From the results it can be observed that the contact with the surfaces of the untreated and the conventionally anodized samples do not produce any significant effect in term of decrease of the density of bacterial colonies, in fact only a reduction comparable with the experimental error was recorded. The contact with the PEO coating without silver produce a decrease of about one order of magnitude in the density of bacterial colonies probably due to the alkaline environment which formed when the broth with the bacteria goes in contact with the treated surface. All the samples treated with silver particles in the electrolyte showed a very efficacious antimicrobial effect: in fact, after 3h all the *E. Coli* died when in contact with the treated surface. This fact is in accordance with the high antimicrobial effect of silver for this bacterium [255] that, however, in these tests appeared remarkably higher than in literature [222] due to the high amount of silver contained in the coating. The different quantity of silver particles and the sealing treatment did not influence the results. However, the sealed samples should be preferred due to the better corrosion resistance previously verified.

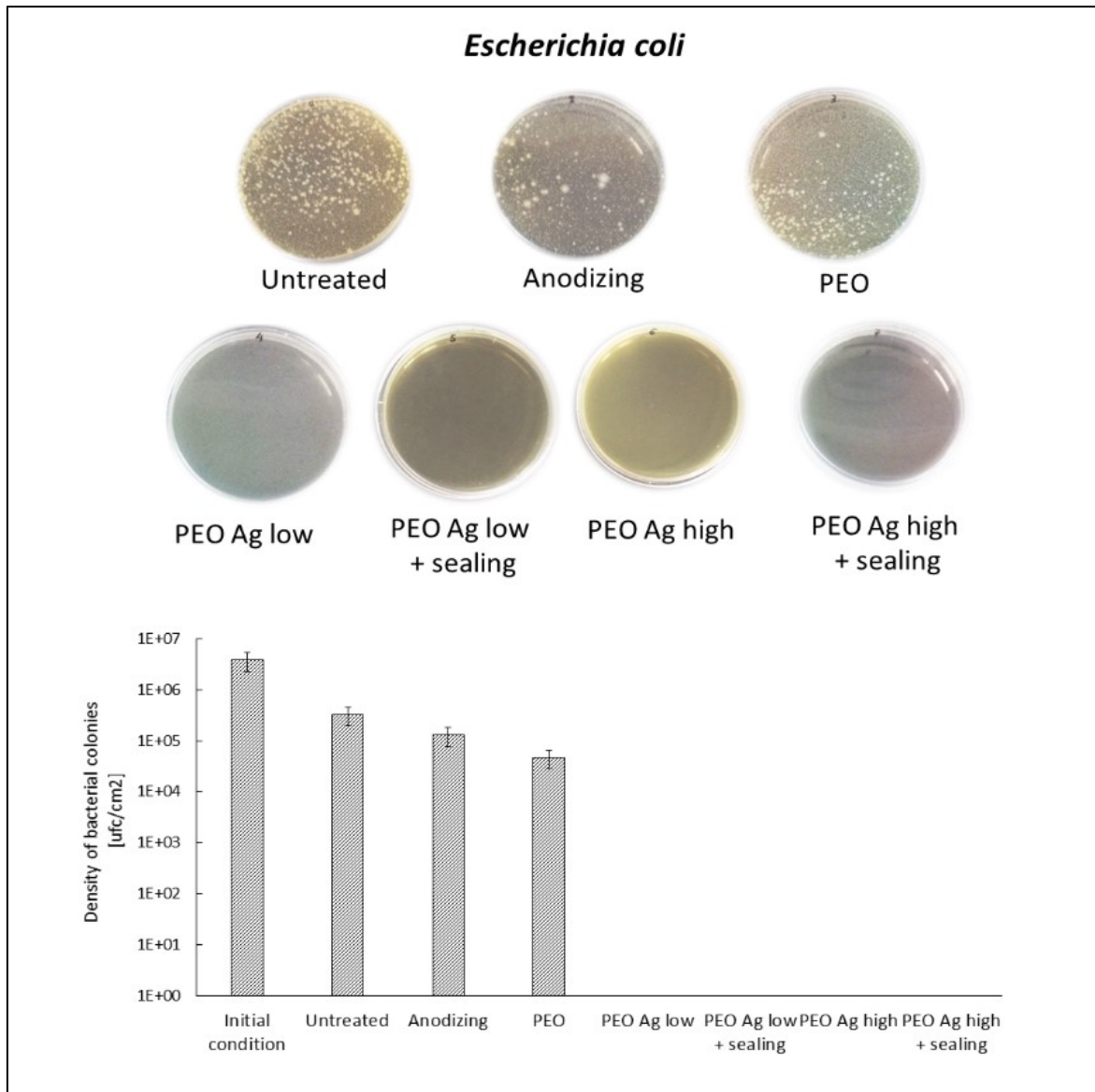


Fig. 7.11 Counting of *E. Coli* and images of the slides with the bacteria colonies after 3h of exposition to the different surfaces.

The effect of the coating on the activity of *S. Aureus* was evaluated in the same way as for *E. Coli* and the results of the counting and the slides with the bacteria after 3h of exposition can be observed in Fig. 7.12. The results substantially confirmed the ones obtained for *E. Coli*. In fact, the contact with the conventionally anodized and the untreated sample do not produce antimicrobial effect whereas the contact with the PEO treated surface without silver particles produce a reduction of about one order of magnitude in the density of the bacterial colonies.

Also for *S. Aureus* the presence of silver induced a remarkable increase in the antimicrobial effect given by the surfaces. In fact, silver can interact both with DNA, respiratory chain dehydrogenase and proteome of *S. aureus* cells [257]. However, in this case a density between 10^1 and 10^3 of bacterial colonies can be observed also after 3h of exposition with the coatings containing silver particles unlike the case of *E. Coli*. Furthermore, some differences between the different silver-containing samples can be observed: without the sealing treatment, an increase in the antimicrobial effect with the increase of silver can be observed, in accordance with the literature where is reported that the antimicrobial activity is strongly linked with the silver content [258, 259]. Nevertheless, after the sealing treatment the behavior of the samples “PEO Ag low” and “PEO Ag high” was substantially the same.

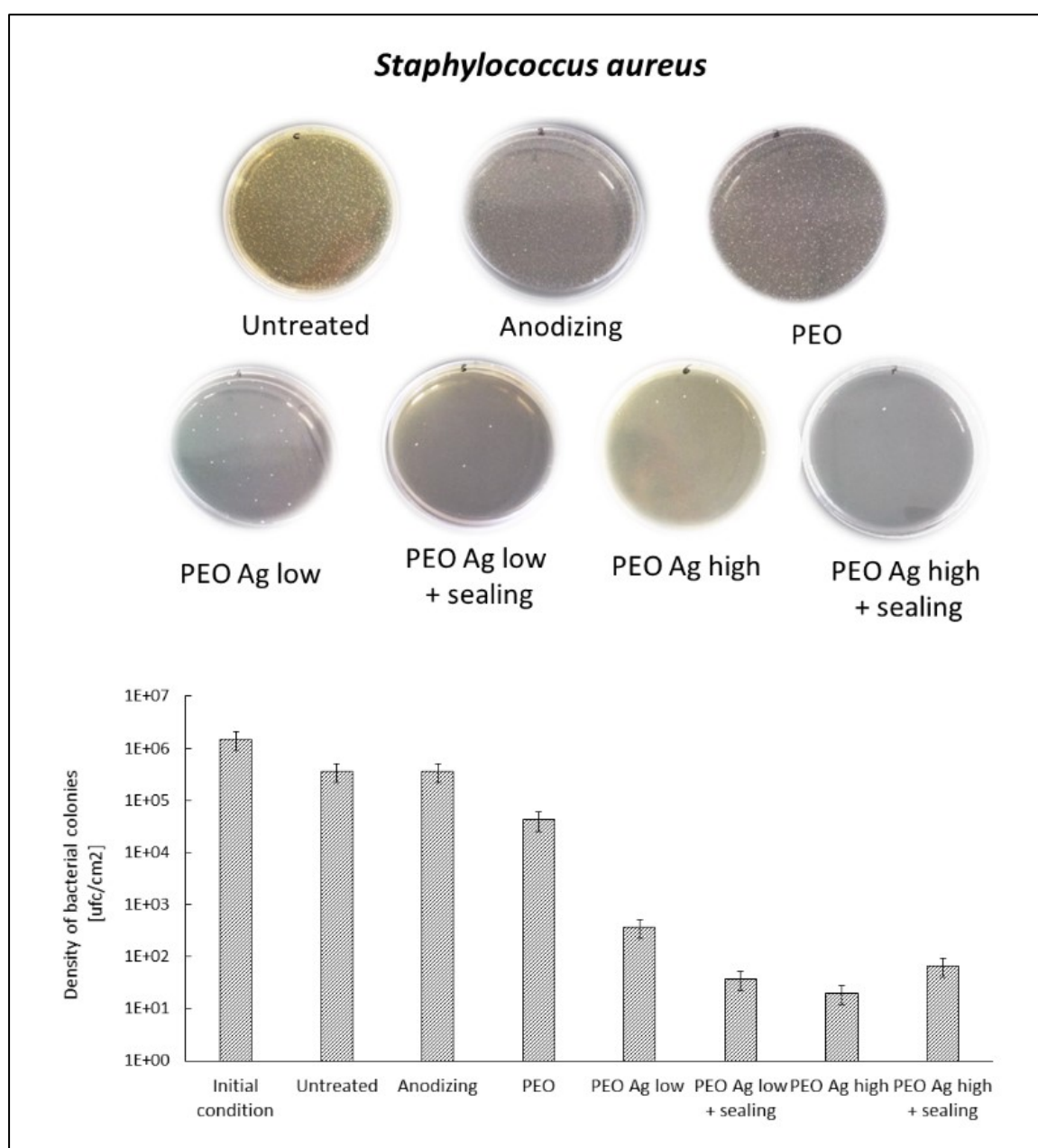


Fig. 7.12 Counting of *S. Aureus* and images of the slides with the bacteria colonies after 3h of exposition to the different surfaces.

7.1.5 Antifungal Activity

The fungicidal tests were performed using *Candida Albicans*, a typical pathogenic fungus. At first, all samples (in triplicate) were cleaned with alcohol and treated under the Germicidal lamp for 2 hours. Subsequently, a solution was prepared diluting 1:500 of nutrient broth containing 107-108 cells/ml and 0.4% Agar. 50 μ l of this solution, kept in liquid state at 46°C, were then distributed on 2.5 cm² of the surface of each sample. The solution was incubated at 35°C for different times in humidified atmosphere to prevent drying of inocula. After 0, 2 and 4 hours, the survived cells were dispersed in 10 ml of Phosphate Buffer Saline (PBS) with pH 7.4. The suspensions were then serially diluted in PBS and 50 μ l were inoculated in Saboraud 2% Glucose Agar. After the incubation for 48h at 30°C, the number of colonies was counted and the average values reported. In particular, considering the antifungal effect, the number of fungi colonies is reported in Fig. 7.13.

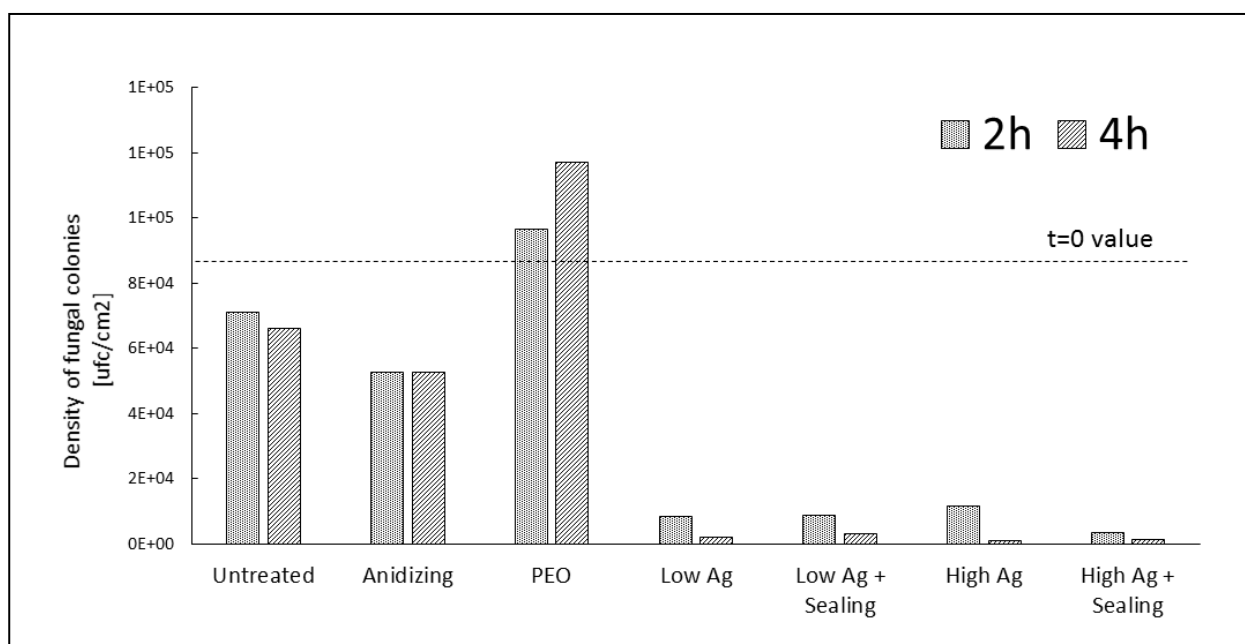


Fig. 7.13 Graph with the *Candida Albicans* survived cells counts after the two different times of incubation in contact with the surfaces.

As can be seen in the figure, the untreated sample seemed to slightly reduce the number of colonies over time and this fact can be explained with the release of aluminum ions in the nutrient broth. Probably due to the same reason, also the anodizing treatment exhibited small fungicidal effect. Interesting results were instead showed by the PEO treated samples. In fact, the ceramic coating, due both to the fact that it prevented the aluminum ions release and that it is a ceramic and porous layer, caused an increase in the cells number. Moreover, as expected, all silver containing PEO coatings showed high fungicidal effect, confirming the efficacy of silver ions against this kind of fungus.

Considering these coating, the colonies number decreased over time and great colonies reduction (more than one order of magnitude) can be seen just keeping the fungi in contact with the surfaces for two hours. There were no significant differences between the two tested quantities of silver and best results were obtained with "High Ag + Sealing".





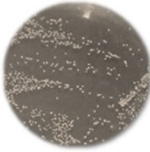

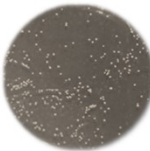


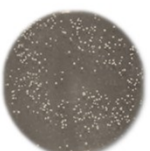

Initial condition		
Treatment:	2h	4h
PEO		
Low Ag		
Low Ag + Sealing		
High Ag		
High Ag + Sealing		

Fig. 7.14 Image of the *Candida Albicans* colonies after the different times on PEO coated samples.

7.1.6 Concluding remarks

In this work, the effect of the addition of silver particles in the electrolyte used to produce PEO coatings on AA7075 is explored. The particles did not influence the mechanism of formation of the oxide coating that resulted adherent, uniform, homogeneous on the surface of all the PEO treated samples and mainly constituted by aluminum and silicon oxides. This fact is interesting because, on the other hand, the simply addition of the particles to the electrolyte during the conventional anodizing process prevented the formation of a good-quality coating. The distribution of the silver particles was uniform and their presence was detected also inside in the pores. The samples containing silver particles exhibited a decrease in the corrosion resistance if compared with the sample PEO treated without silver particles and this fact can be explained with the galvanic couple formed between silver and aluminum. However, the sealing treatment in boiling water allow to obtain coatings with improved corrosion resistance, if compared with untreated sample.

The antimicrobial activity of the coated samples was verified both with *E. Coli* and *S. Aureus* bacteria. In both cases, after 3 h of contact of the bacteria with the surfaces, on the untreated and the anodized samples a reduction of the bacterial colonies wasn't detected, whereas on the sample PEO treated without silver particles a reduction of about one order of magnitude in the density of bacterial colonies was found. The presence of the silver particles in the PEO coatings, however, remarkably increased the antimicrobial effect. Regarding *E. Coli* bacteria, all the bacteria died after 3h in contact with the coatings containing silver particles, regardless the different amounts of silver or the sealing treatment. With *S. Aureus* bacteria, the antimicrobial effects were slightly lower, nevertheless a reduction of 5 order of magnitude in the density of bacterial colonies was obtained for the silver-containing coatings.

Moreover, the obtained samples are characterized by high fungicidal activity: in fact, all the PEO coated samples containing Ag produce the death of almost all the fungi (*Candida Albicans*) after four hours of contact.

The procedure described in this work so allows to produce coated aluminum alloys with good corrosion resistance and high antifungal and antimicrobial activity.

7.2 Antifouling effect of copper powder in PEO coating

The appearance of aluminum alloys as an alternative material in boat and ship constructions is related to the 1960's [260] and, since then, aluminum is recognized as an advantageous material in shipbuilding by marine engineers and naval architects. In particular, it finds application in small boats as police or patrol boats, fishing vessels, fire boats or fast passenger vessels as catamarans (up to 400 passengers) in Europe, North America and especially in Asia [261]. The lightweight, superior mechanical properties and corrosion resistance of aluminum alloys has dictated their use in many of these applications. Using aluminum, naval architects can design ships and boats with high-speed capability, long life, high payloads and low maintenance costs, as well as a high recycle value [262]. The low density of aluminum, combined with high strength, toughness, and corrosion resistance, allow vessel designers to achieve weight savings of 15-20% over steel or composite designs [263, 264]. Weight savings equate to higher speed, increasingly demanded for vessels such as ferries, patrol boats, military craft, hydrofoils, fishing vessels, cargo vessels, leisure craft, and work boats. The weight saving improves the ship stability allowing design of narrower ships [265]. However, aluminum structures in marine environment suffer of some corrosion problems especially connected with fouling [266].

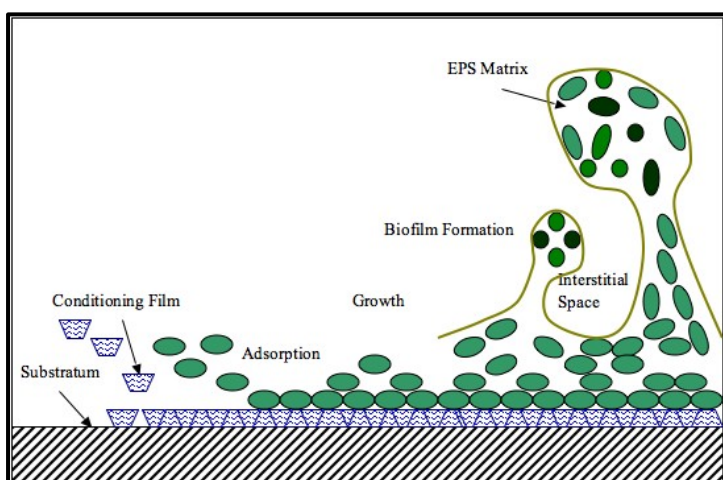


Fig. 7.15 Scheme of biofouling growth on the substratum.

Biofouling (accumulation of organisms) is a common problem on man-made objects submerged in the waters throughout the world [267]. The biofouling growth on a substratum in the aquatic environment is a complex process which consists in an initial biofilm formation (constituted by bacteria and microalgae) followed by settlement of invertebrate larvae and algal spores (Fig.7.14) [268, 269]. Biofouling on submerged surfaces in the marine environment has

considerable ecological and economical importance besides particularly serious implications for shipping, offshore aquaculture, and coastal industries [270, 271, 272]. The effects are mainly due to the loss of productivity in aquaculture [273] or increased costs of fuel to shipping (Fig. 7.16), as well as the costs associated with ongoing prevention, management and control [274, 275].

Therefore, the use of antifouling coatings in the marine environment has a long history. In particular, often are produced organic coatings containing metallic species that work as antifouling species [276, 277]. As metallic compounds with antifouling properties are typically used silver and copper among the 18 compounds currently employed worldwide [278]. Organic coatings containing silver, as well as silver nanocomposites, are already produced in literature for their

antifouling properties [279, 230, 280, 281]. Elementary silver, in detail, is believed to function antimicrobial either as a release system for silver ions or as contact-active material [282]. Also copper containing organic coatings are already described in literature and the mechanism of action of copper as antifouling compound is the same if compared with the one of silver [283, 284, 285, 286].

Nowadays, one of the most promising techniques to produce coatings that can improve the corrosion resistance of aluminum alloys is the plasma electrolytic oxidation (PEO) described in Chapter 7.1. However, no works in literature do exist regarding the anti-fouling properties of PEO coated samples even though, as reported above, the use of aluminum alloys in marine environments is widespread.

In this chapter, the antifouling properties of different PEO coatings produced on aluminum alloys were studied in estuarine water. In particular, coatings without additives and coatings containing silver or copper particles, incorporated in the PEO coatings directly during the production process, were tested. As a comparison were also tested untreated samples with different substrates, a conventionally anodized sample and a sample with a commercial antifouling painting.



Fig. 7.16 *Example of fouling colonization of a vessel* [64].

7.2.1 Production of PEO coatings

The different coatings were produced on 7075 aluminum alloy and its nominal composition is reported in Tab. 7.1.

Before PEO treatment, the samples were polished following standard metallographic techniques and then degreased using acetone through ultrasound. The PEO electrolyte was constituted by an aqueous alkaline solution with 5 g/l of NaOH and 25 g/l of Na₂SiO₃.

The plasma electrolytic oxidation process was carried out using a TDK-Lambda DC power supply of 300 V/8A capacity. During the treatment, the sample worked as anode and the cathode was a zincified steel mesh immersed in the electrolyte. The treatments were performed maintaining the constant current, letting the potential free to vary. The current density used was 0.3 A/cm² and the treatment lasted 5 minutes.

Among the coated samples tested for the comparison, some were anodized. For this treatment, it was used a current density of 0.016 A/cm² for 25 min in a solution of sulfuric acid 20% using a lead cathode. The temperature of the electrolyte was maintained constant at 18°C by a thermostatic bath. Other samples were painted: painting was performed sandblasting the samples and laying on the samples first one primer coat of epoxy resin and then two coats of white antifouling painting.

7.2.1.1 Silver/copper particles production

Silver powder was synthesized as described in Chapter 7.1.1.1 whereas copper powder was synthesized using the process described in Chapter 6.3.3 but using higher concentrations. In particular copper particles used for every PEO treatment were synthesized using 14g of copper nitrate trihydrate and 24g of ascorbic acid in 300ml of water.

The average dimension of the obtained powders was 0.5 μm and 3 μm respectively, as can be observed in Figure 7.17.

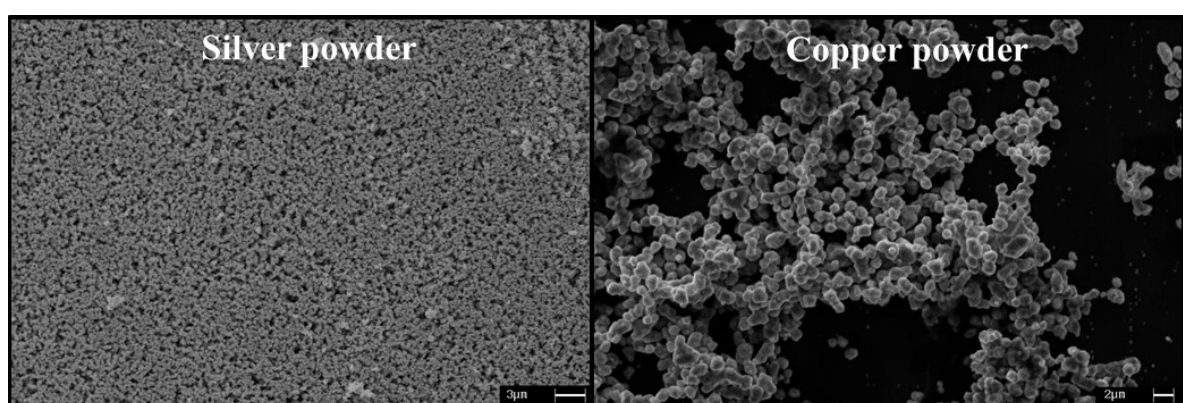


Fig. 7.17 Images of the silver and copper powders.

7.2.1.2 PEO treatment and characterization methods

These powders were added directly into the electrolyte during the treatments. PEO treatment was performed using the same solution and the parameters described in Chapter 7.1.1.2.

Moreover, on the PEO treated samples, a sealing treatment was performed by immersing the samples into boiling water for 15 min.

The samples with copper or silver powders into the coatings were sealed using water added with other copper or silver powders, in order to increasing the amount of particles on the surfaces of the coatings.

After all the samples were coated, the samples were first washed with deionized water and ethanol and dried with compressed air. The cross-sections of the treated samples were then cut and mounted in epoxy resin and polished with standard metallographic technique. Both the surface and the cross-section of treated samples were examined by SEM, to evaluate the morphological features, the thickness of the coating and the elemental composition.

7.2.1.3 Antifouling tests procedure

After the characterization, four samples for seven different treatments conditions were prepared to perform the test for the evaluation of the antifouling properties of the coatings. During the test, all of them were completely 40 cm depth immersed in the river Piave.

This river, in northern Italy, springs in the Alps and flows southeast into the Adriatic Sea. The sampling site selected for the test (45.582065 N; 12.652398 E) is near to the river mouth, where the river is deeper and tidal action is present. However, the test was performed in late spring, when the river flow is enough to prevent the ascent of the salt wedge. Every week one series of samples was collected so up to four week. Moreover, the water pH and temperature were measured at every sampling. The test site and physical data are reported in Fig. 7.18. Fouling colonization was investigated both by stereomicroscope observation and SEM analyses. Moreover, to estimate the most common species, samples were scraped and observed at the light microscope. Antifouling tests were performed also in seawater. For this test, different samples were prepared. In addition to PEO coated and PEO coated with copper powder, there were tested some painted samples and some samples painted after PEO treatment.

Moreover, some samples were scratched to verify the corrosion and antifouling properties in the case that the coating was damaged. The procedure was analogous to that used for the test in estuarine water and the test site and physical data are reported in Fig. 7.19.



Fig. 7.18 Image of the place selected for the antifouling tests with the samples immersed in the estuarine water. In the table on the bottom left are reported the pH and temperature values recorded at the four sampling times.



Fig. 7.19 Image of the place selected for the antifouling tests with the samples immersed in the seawater. In the table on the bottom left are reported the pH and temperature values recorded at the four sampling times.

7.2.2 Surface Characterization

The PEO coating without additives was produced at high current densities and short treatment times and the complete characterization of the PEO treated sample can be found in [252]. The stereomicroscope observation of the surfaces of the samples treated with silver and copper particles in the electrolyte can be observed in Fig. 7.20. The particles incorporated inside the oxide ceramic coating can be observed. Moreover, the coating seems to be not influenced by the presence of the particles and resulted continuous and homogeneous with the typical grey color of the PEO coatings produced on aluminum alloys.

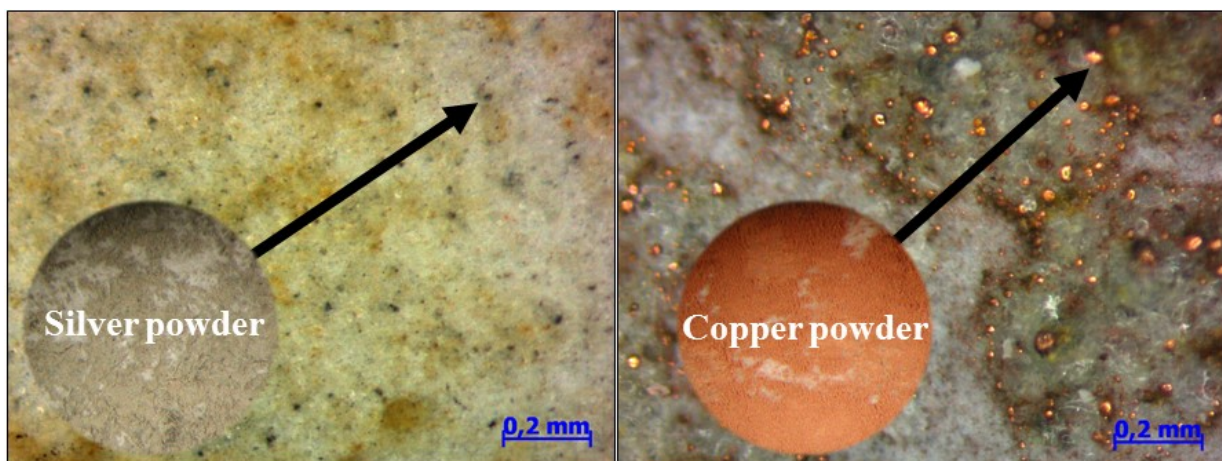


Fig. 7.20 Image of the two PEO coating obtained with silver and copper powder. The particles are clearly visible on the surfaces.

The EDS analysis at SEM of the coatings containing silver or copper particles revealed the presence of particles both on the surface and inside of the pores characterizing PEO coatings (Fig. 7.21).

As observed in Chapter 7.1.2, the presence of the particles into the electrolyte seems not to influence the formation and the morphology of the coatings, that is almost the same if compared with that obtained without particles. From SEM analysis, it can be observed the typical surface of PEO coatings, rich of pores and micro-cracks (Fig. 7.21a and 7.21c) and the thickness of the coatings is between 45 and 50 μm (Fig. 7.21b and 7.21d). Analysis of the cross section of the samples highlight also the typical double layer structure of PEO coatings, with an inner thin and dense layer, called also barrier layer, and an external porous layer, called technological layer [205]. Moreover, from the surface observation, the pores result partially sealed by the sealing treatment in boiling water. EDS analysis of the white spots, observed at SEM in backscattered electron mode, reveals that these spots correspond to the silver (Fig. 7.21b) and copper particles (Fig. 7.21d).

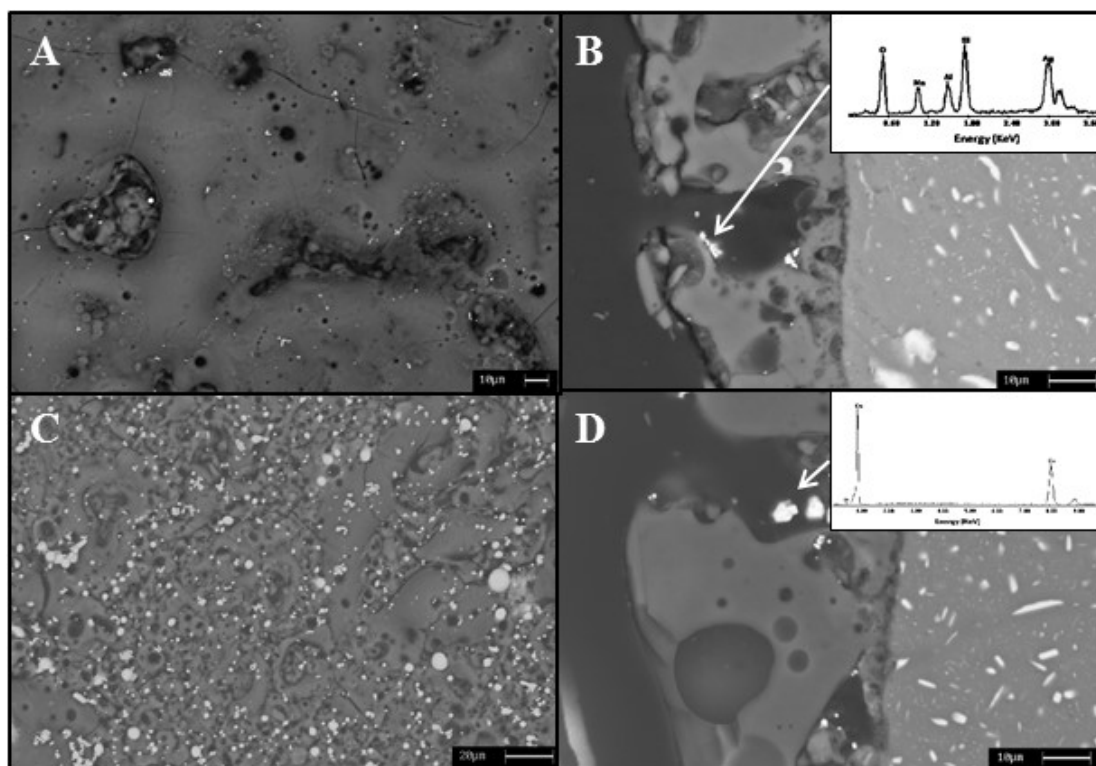


Fig. 7.21 Image of the surface and section of the two PEO coatings obtained with silver and copper powders. A) surface of sample with silver; B) section of sample with silver; C) surfaces of sample with copper; D) section of sample with copper.

From the semi-quantitative EDS analysis, performed on the cross section of the samples, in areas without the particles (Tab. 7.5), the coating results mainly composed by aluminum and silicon compounds with oxygen. Moreover, the composition of the coating is not influenced by the presence of the particles and it is in accordance with the composition of the electrolyte and substrate.

Sample	O%	Al%	Si%
PEO	38	22	40
PEO + Silver	44	18	38
PEO + Copper	41	20	39

Tab. 7.5 EDS semi-quantitative analysis performed on the cross section of the samples.

X-ray diffraction (XRD) analyses were performed on the samples containing silver or copper particles in order to identify the different phases of the coating. The results are reported in Fig. 7.22. The diffraction pattern was also compared with that obtained on the sample treated without silver or copper particles, reported in [252].

Both analyses showed the peaks of Al_2O_3 and Al_2SiO_5 in agreement with the composition of the alloy and the electrolyte of the PEO process. In the sample PEO+ Silver, also the peaks of Ag were

present whereas the peaks of Cu are present in the case of the sample PEO + Copper. The presence of the Al peaks was due to the diffraction from the substrate.

Corrosion tests showed results similar to the one obtained with silver addition to the substrate (Fig. 7.23). In fact, the decrease in corrosion potential and the increase in corrosion current density caused by the powder addition can be overcome using a sealing treatment.

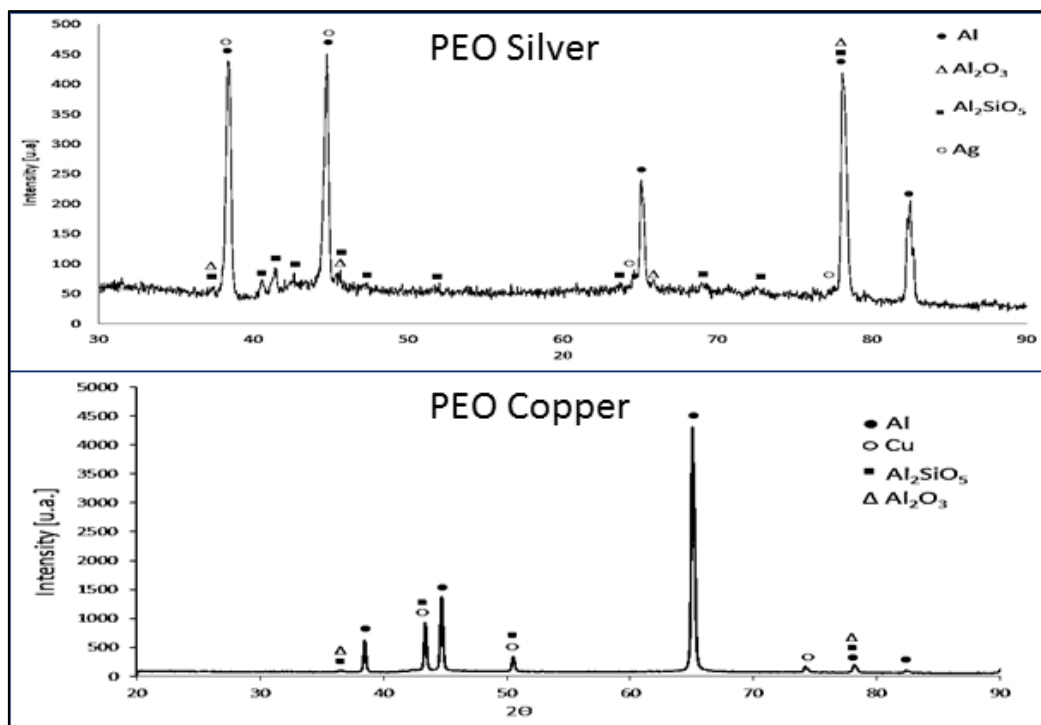


Fig. 7.22 XRD diffraction patterns of the samples PEO treated with silver particles in the electrolyte (above) and with copper particle in the electrolyte (bottom).

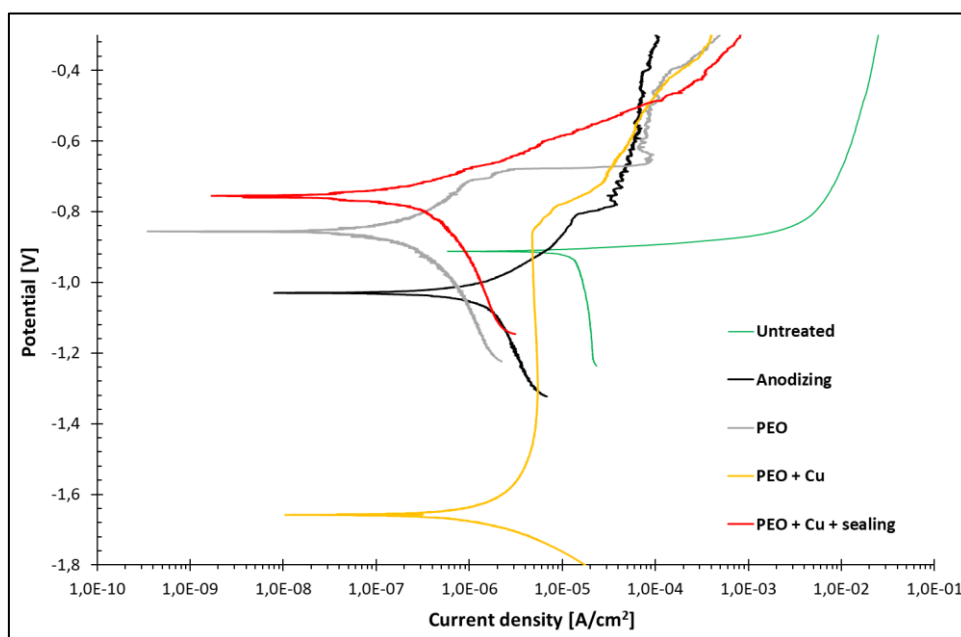


Fig. 7.23 Potentiodynamic polarization plot for the different samples (test electrolyte: 0.1M Na₂SO₄ + 0.05M NaCl).

7.2.3 SVET Analysis

SVET was applied to verify if the Cu microparticles present in the PEO coating could induce the corrosion of the adjacent aluminium alloy matrix due to the formation of local galvanic couplings. The procedure is described in Chapter 2.13.

Fig. 7.24 presents the cross-section of the PEO-coated sample after the SVET test and the corresponding SVET maps obtained between 30 and 110 min of immersion. First, it can be seen that the alloy is subjected to a local anodic attack, as depicted by the arrows in Fig. 7.24(b).

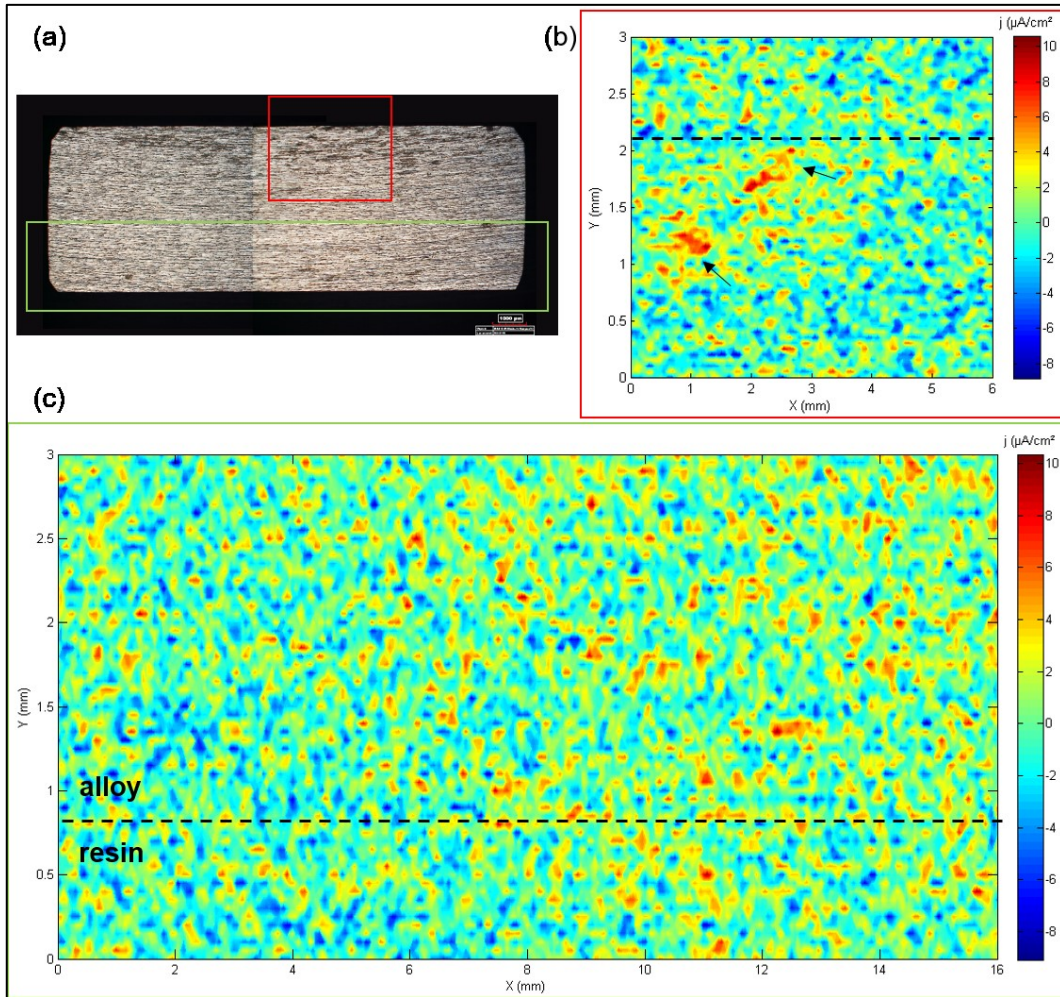


Fig. 7.24 (a) the resulting cross-section of the PEO-coated AA7075 after 3 h of immersion in 12.00 mM NaCl electrolyte. The corresponding time-dependent current density maps obtained by SVET (c) from 30 to 80 min and (b) from 80 to 110 min of exposure. The dashed lines indicate represent the alloy/resin interface.

This result illustrates the susceptibility of the alloy to localised corrosion due to the presence of intermetallics. The centres of anodic activity seemed to develop at random locations, as suggested by the different performed scans (not presented here). The corresponding cathodic activity appears spread over the entire alloy surface and cannot be assessed with precision. From the scan performed along the entire inferior border (Fig. 7.24(c)), no significant electrochemical activity could be observed on the alloy part. In fact, the spatial resolution of SVET is often not great enough to detect local activity arising from individual intermetallics/pits [287, 288]. For that reason, the spatial assignment of corrosion in such systems is a matter of probability. In other words, as localised corrosion events are time-dependent, the probe scanning over a certain point can only detect activities that take place there at that exact moment.

The sample comprising the PEO coating doped with Cu microparticles presented similar results (Fig. 7.25).

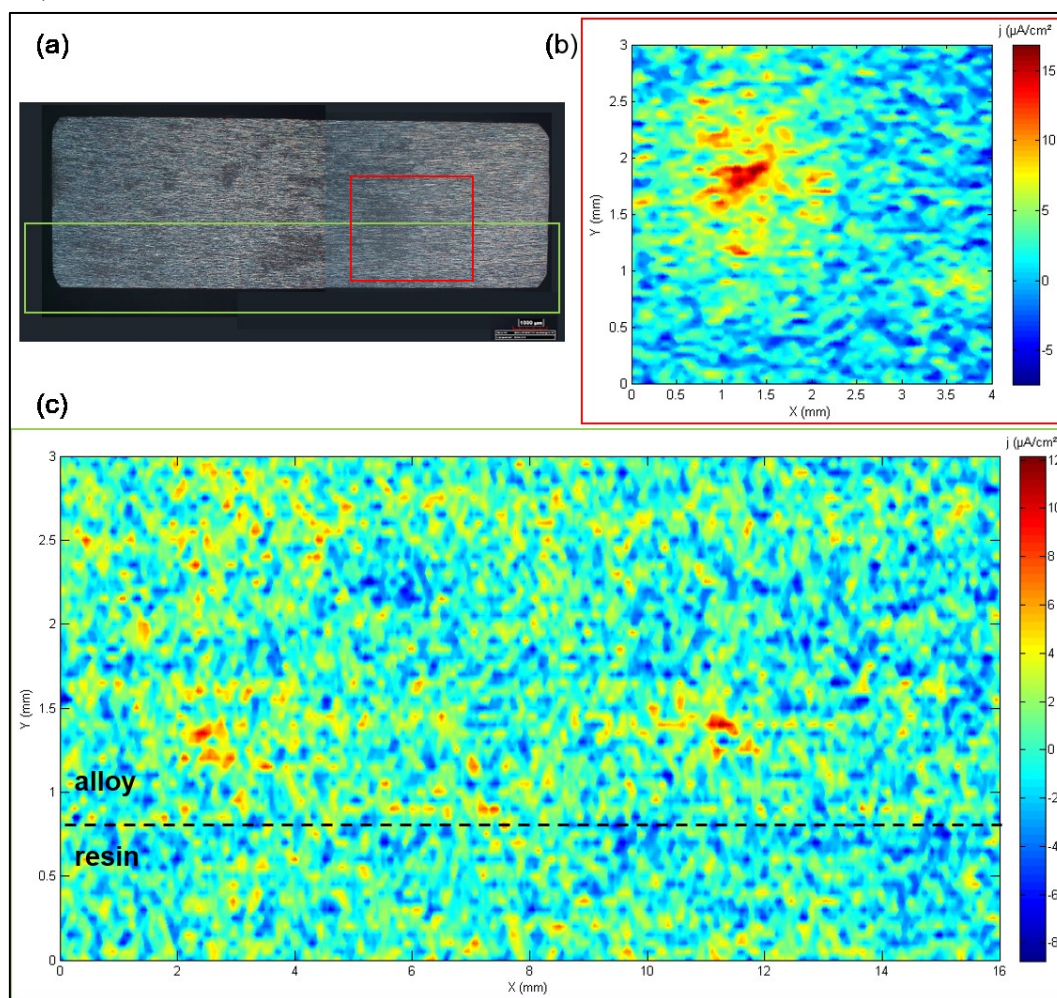


Fig. 7.25 (a) the resulting cross-section of the PEO + Cu particles-coated AA7075 after 3 h of immersion in 12.00 mM NaCl electrolyte. The corresponding time-dependent current density maps obtained by SVET (c) from 30 to 80 min and (b) from 110 to 120 min of exposure.

The SVET map obtained from the centre of the alloy (Fig. 7.25(b)) once again indicates the occurrence of anodic attack. In this case, the scan performed along the border (Fig. 7.25(c)) could eventually depict clear centres of anodic activity. In general, these centres appear to be established in space and time randomly. The difference in the intensity of the anodic peaks observed between Fig. 7.24 and Fig. 7.25 is not necessarily reflective of distinct corrosion rates. Once again, localised phenomena measured by SVET cannot be quantitatively compared, as the probe is necessarily losing information while scanning the surface in a point-by-point fashion. In conclusion, for both coated systems, SVET was able to highlight the behaviour of an alloy prone to localised corrosion. Furthermore, galvanic coupling between the Cu microparticles from the PEO coating and the Al matrix does not seem to be the driving force for the corrosion of the alloy. Otherwise, the anodic activity should be preferentially located near the borders of the matrix, next to the referred PEO coating. It is worth mentioning that these SVET outcomes does not prove a complete absence of local galvanic coupling related to the coating doped with Cu. Instead, they prove that the anodic attacks induced by the alloy constituent intermetallics are considerably stronger than an eventual galvanic corrosion process promoted by the PEO coating.

7.2.4 Antifouling properties in estuarine water

The photographic and stereomicroscopic images of the samples during the antifouling test are shown in Fig 7.26.

As it can be observed, aluminum alloy samples after 28 days exhibit the presence of white oxide spots on the surfaces, as expected in absence of any protective coating. This white spots are in fact due to corrosion phenomena on the aluminum surface. Moreover, as predictable, the oxidation is more remarkable in the case of sand blasting of the surface, since a greater area is exposed to the water.

The colonization by the foulers is also quite similar between them: in fact, even if on one hand the surface roughness facilitates adhesion of the organisms, on the other hand the higher oxidation prevents the settlement, probably due to the substrate dissolution and the release of aluminum ions. In particular, these two samples show significantly the presence of algae since the third week of immersion. As far as the vanished sample concerned, the commercial antifouling painting resulted to have great antifouling and anticorrosive effects, since the surface does not change after the four weeks of immersion and no trace of foulers nor corrosion was detected. The antifouling painting used was a so called "hard" bottom paint and it is typically applied to fast ships. It differs from other kind of paintings, like abrasive ones, whose coating gradually wear away releasing the biocide, and as a consequence its antimicrobial activity is caused only by chemical action. In fact, it contains copper oxide particle as biocide. In the case of its application to aluminum alloys, a primer under the paint is necessary in order to avoid galvanic couple and rapid corrosion of the less noble metal. The presence of the biocide inside the paint together with the smoothness of the surface allows to the sample to have, among with the tested ones, the greatest antifouling effect.

Considering the next three treated samples: anodizing, PEO coating and PEO coating with silver, the three samples colonization was similar and significantly high, with of a lot of different species. In particular it seems that, despite the improved corrosion resistance of these samples in comparison with untreated aluminum alloy, their ceramic coatings offers a substrate more favorable to the settlement of the foulers, because of its chemical inertness and roughness. This fact is also connected with the porosity of the PEO surface because the pores are ideal zones for the colonization of different species, indeed are reported in literature the use of PEO coating as substrate for cell growth [289]. Also the presence of silver, commonly considered a strong antifouling agent seem to not influence the antifouling effect of the coating that resulted very poor. This fact can be linked with the quantity of silver inside of coating that have a strong relevance in the antifouling effect of this metal and that is probably not enough in our case to produce an appreciable effect. In detail, for all these treated samples, after two weeks of immersion the presence of colonization can be clearly detected and after three and four weeks the surface is completely colonized by a lot of types of organisms.

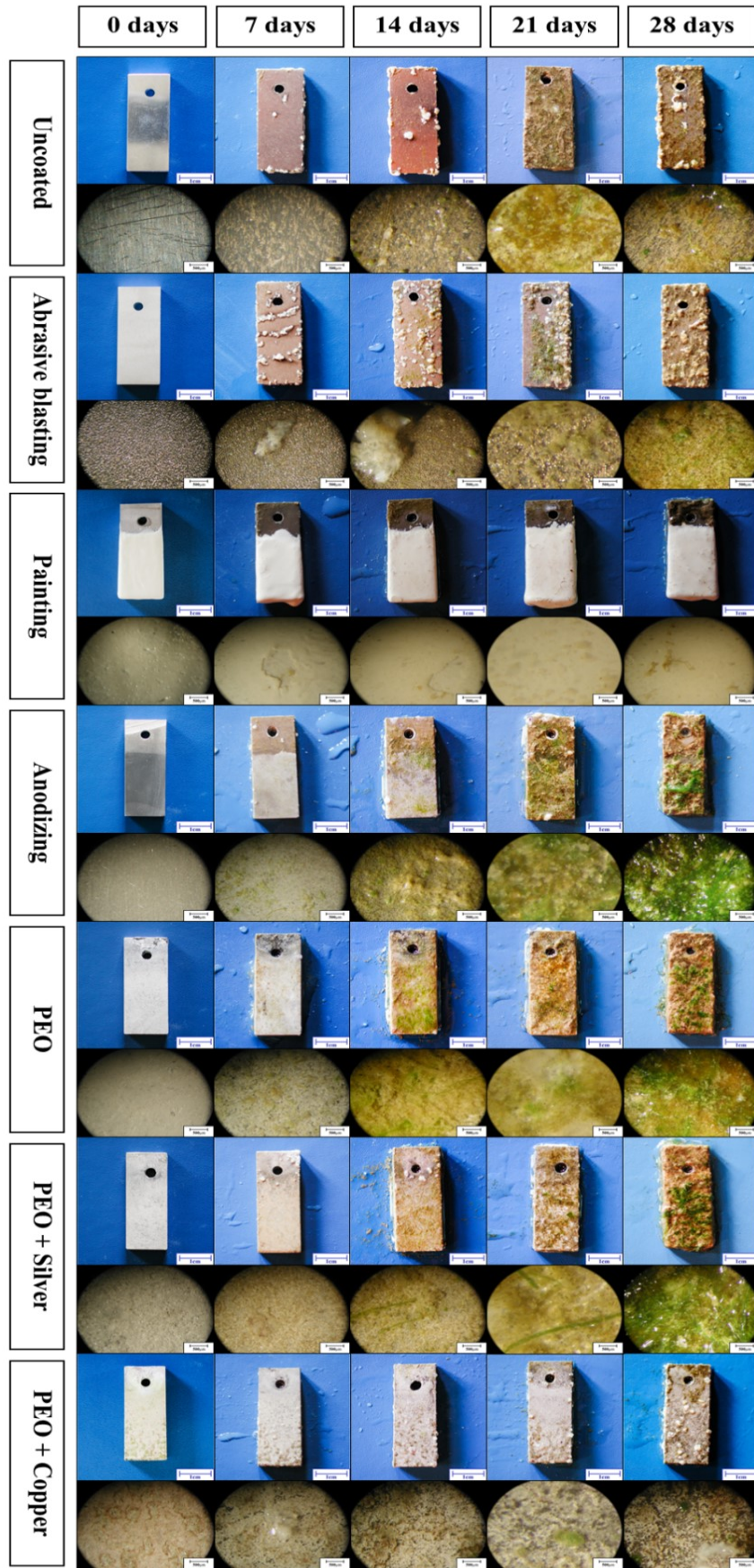


Fig. 7.26 Image of the samples used for the antifouling test in estuarine water.

However, the presence of the coating remarkably increases the corrosion resistance of the samples in fact no white oxide spots are detected both in the anodized and PEO coated samples.

Very interesting results were indeed found observing the sample treated with PEO with copper powder. Copper powder exhibited a remarkable antifouling effect on this samples. In fact, only in the third week the presence of organisms can be observed and at the end of the analysis the species present on the sample surface are clearly less than for the other treated samples. The corrosion phenomena are, as on the other treated samples, significantly less than the untreated samples. The samples treated with PEO that contain copper particles seem so the most promising to produce a surface with good antifouling properties and corrosion resistance, useful for example as substrate for commercial paintings. In this way, in fact, the presence of cracks in the painting will not be deleterious for the aluminum substrate both in term of corrosion and antifouling resistance.

Moreover, microscopic analysis of the samples was performed, counting the number of different organisms on the surfaces in order to better estimate the colonization. In particular, in Tab. 7.6 it is reported the abundance of the organisms distinguished between diatoms and chlorophycean filaments.

	7 days	14 days	21 days	28 days
Uncoated	D	D + C	C + DDD	CC + DDD
Abrasive Blasting	-	DD	DDD	DDD + CC
Painting	-	-	-	-
Anodizing	DD	DDD + C	DD + CC	DD + CCC
PEO	DDD	DDD + CCC	DD + CC	DDD + CCC
PEO + Silver	DD	DDD + CC	DD + C	DD + CCC
PEO + Copper	D	D	D	DD + C

Tab. 7.6 Fouling colonization in all tested samples during 4 weeks. *D* = Diatoms; *C* = Chlorophycean filaments; *X* = Scarce; *XX* = Abundant; *XXX* = Extremely Abundant.

The data reported in the table confirm the consideration regarding the observation of the different samples. In particular, the sample PEO + Copper, after all the immersion times, is the one with the best antifouling effect excluding the commercial painting.

Microfouling colonization analyses, carried out by light and scanning electron microscope are reported in Fig 7.27.

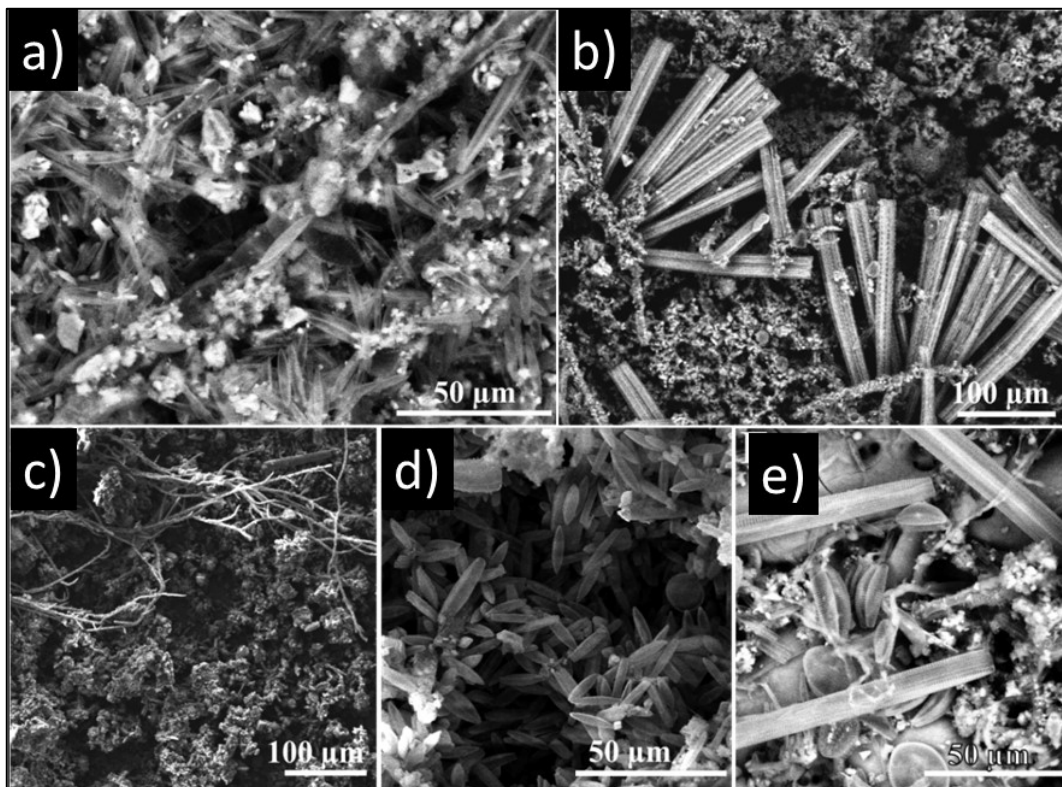


Fig. 7.27 Scanning electron micrographs of the samples during the antifouling test: uncoated (a), abrasive blasting (b), anodizing (c), PEO (d), and PEO + Silver (e).

The analyses highlighted that in all tested samples, except painting, the developed microfouling communities were dominated by diatoms. These photosynthetic microorganisms, together with bacteria and cyanobacteria, are in fact the major constituents of biofilm on submerged surfaces [274]. Almost pennate diatoms, were observed in all tested coatings, represented by the main genera were *Navicula*, *Nitzschia*, *Surirella*, *Ulnaria*, and *Synedra* (Figs 7.27: a, b, d and e). Only a centric diatom belonging to the genus *Melosira* was recorded. The dominance of pennate diatoms over centric in a biofilm is due to the presence of structures (raphe or pores) for the secretion of adhesive exopolymeric substances, which enhance their attaching and gliding capability on a substrate [290].

Starting from the second week, also chlorophycean filamentous microalgae, as shown in Fig. 7.26, appeared (Fig. 7.27c). Sometimes, the presence of these last ones prevented the observation, identification and quantification of small diatom species established on different antifouling coatings, as a consequence underestimating the biodiversity. Therefore, diatom biofilms represent an important step for the subsequent attachment by other fouling organisms [291].

Uncoated (Fig. 7.27a) and abrasive blasting (Fig. 7.27b) samples showed a weak colonization during the first and second weeks, while starting from the third week the surfaces of these samples appeared colonized by the diatom communities, represented by few species.

Anodizing (Fig. 7.27c), PEO (Fig. 7.27d), and PEO + Silver (Fig. 7.27e) samples, instead, were mostly rich in species since the first week. This high biodiversity was observed during all test time. Species biodiversity was greatest on PEO coating samples and lowest on PEO + Copper surface. In this study, all tested substrates were immersed and exposed to the same biological, chemical, physical and hydrodynamic conditions, therefore differences in the colonization by microphytobenthos are due to the diverse coatings.

7.2.5 Antifouling properties in seawater

The image of the samples tested are reported in Fig. 7.30. The antifouling tests in sea water enhance the increase in corrosion properties that PEO can give to the surfaces. In particular, the scratched samples, clearly showed that PEO coating, thanks to its hardness and adhesion to the surface was not easily removed so preventing corrosion of the substrate. Moreover, the samples PEO coated and painted, avoided blistering phenomenon observed instead in painted and scratched samples (Fig. 7.28). As a consequence, PEO coating represent an ideal substrate for painting, particularly in seawater environment. Moreover, the addition of copper powder in PEO coating avoid fouling deposition where the painting is removed.

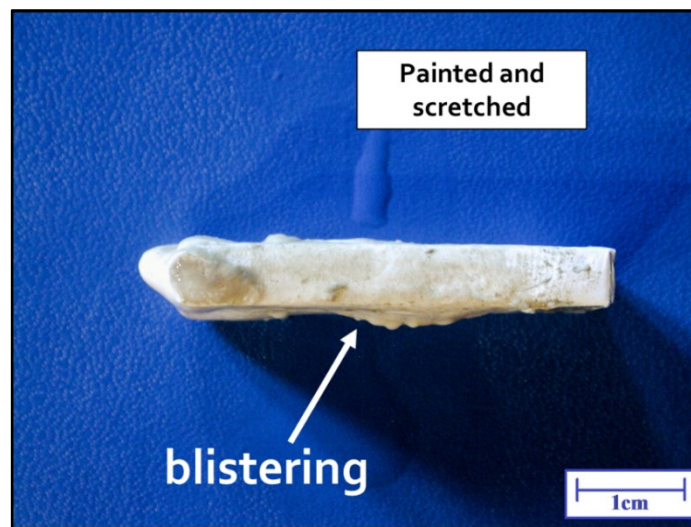


Fig. 7.28 The sample painted and scratched after antifouling test in seawater.

Also in this case, similarly to the test in estuarine water, mostly diatoms were found as foulers on the surfaces. However, the colonization of the surface was lower than in estuarine water tests both because of the more antifouling properties of the tested surfaces and because of the different water temperature and wear condition during the tests.

The most common diatoms found on the surfaces are reported in Fig. 7.29.

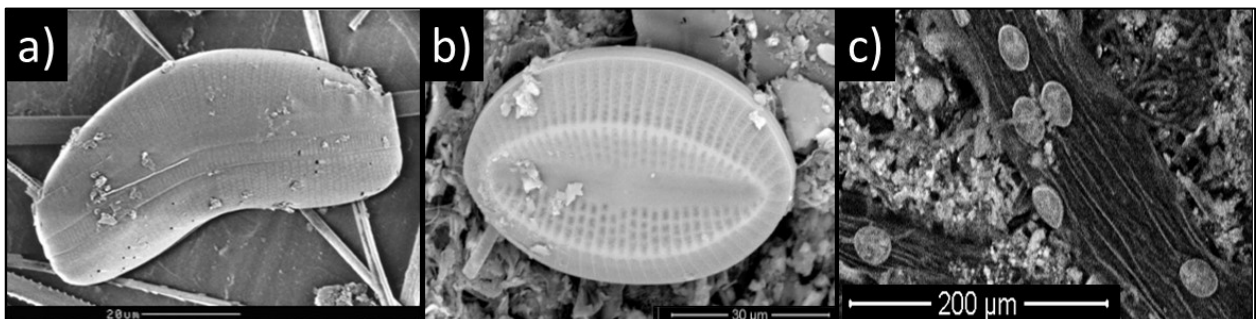


Fig. 7.29 Examples of organisms observed on samples immersed in seawater: a) *Achnanthes brevipes*; b) *Cocconeis marginata* and c) *Chlorophyceans* with epiphytes (*Cocconeis* sp.).

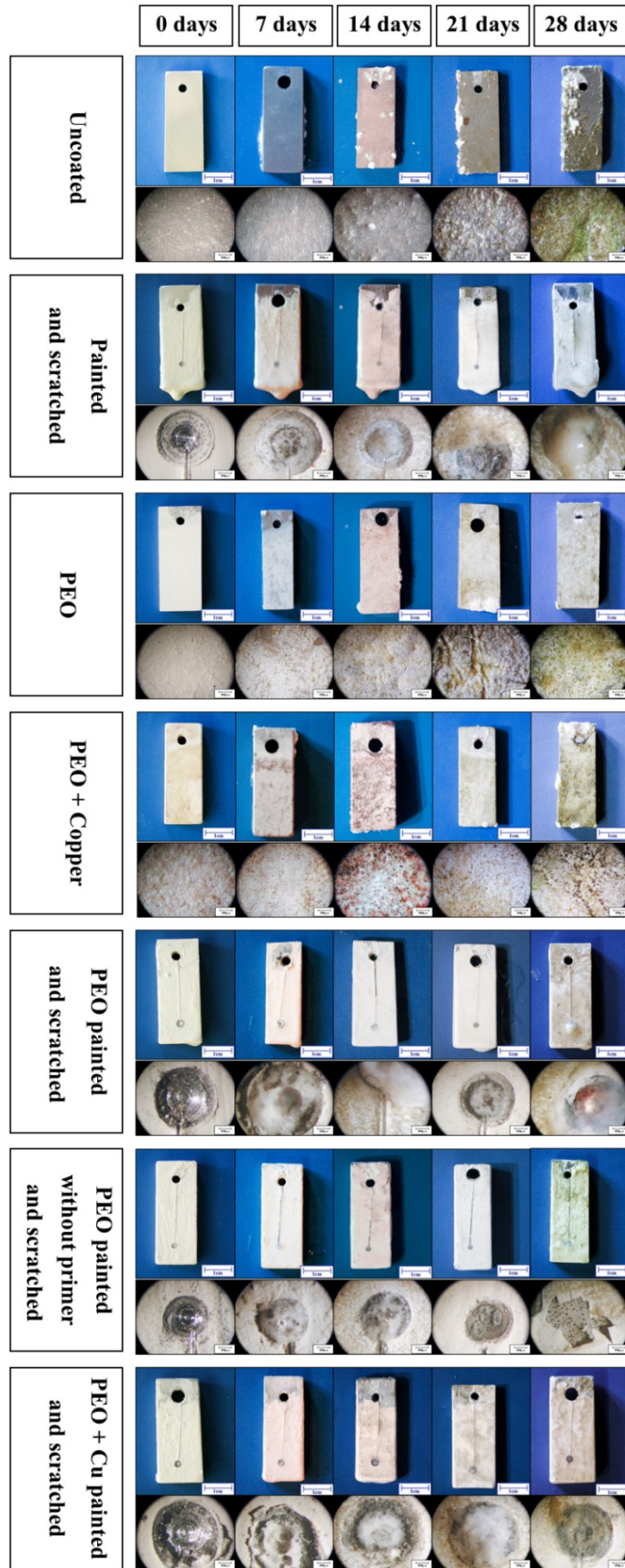


Fig. 7.30 Image of the samples used for the antifouling test in seawater.

7.2.6 Concluding remarks

In this chapter, the effect of the addition of silver or copper particles into PEO coatings on the antifouling properties of 7075 aluminum samples was studied.

The first achieved result was the confirm of the possibility to introduce metallic particles, and in particular silver and copper ones, into PEO coating of AA7075 without modifying its morphology and without modifying the evolution of the PEO process. The antifouling properties of these particle-containing surfaces were tested together with other typical treated surfaces (traditional PEO coating, anodizing and varnished with commercial antifouling painting) and with untreated ones, chosen as comparison.

Moreover, the tests were performed both in estuarine water (river Piave) and seawater (Mariclea port). The experiment was performed leaving the samples immersed into water and valuating the micro fouling colonization after different steps for a total immersion time of one month.

The results show that all the treated samples are characterized by higher corrosion resistance if compared with the untreated ones. It was verified that anodizing and the PEO coating without particles or with silver particles are however very prone to fouling and are colonized faster in comparison with uncoated or abrasive blasted aluminum alloy. This behavior can be linked with the porous surface of PEO and anodized layers and, in the case of PEO coatings containing silver, with the small amount of this element. Nevertheless, it was evidenced that the surface PEO treated with copper particles actually exhibits good antifouling effect. In fact, even after one month of immersion the number of organisms found on the surface of the sample is still low. However, best performance in term of antifouling effect are given by the commercial painting. Nevertheless, the use of this kind of paintings have problems in presence of ruptures in the varnish, in fact in these cases no protection is given to the substrate. The tests performed in seawater showed that copper-containing PEO coating with varnish represent optimum solution as it gives to the sample good corrosion and fouling resistance even in presence of some cracks in the varnish. In fact, it avoids the blistering problem observed when the alloy is painted without using PEO as substrate.

Conclusions

A. Printed circuit boards.

The study of gold recovery from PCBs started with their characterization, which showed that gold was present in the outer surface, above a nickel substrate, whereas copper was inside the PCB. The electronic scraps were crushed and the obtained powders contained, besides 50 wt.% of copper, an amount of gold between 0.03 and 0.3 wt.% and about 0.3 % of silver. The powders were submitted to a pre-treatment with nitric acid, which resulted the most efficient in copper removal, leaving gold in the solid residue. Concentration of reagents, as well as temperature and treatment time, increased recovery yield. The leaching experiments carried out with thiourea showed that the use of ultrasound allowed a gold recovery 30% higher than conventional leaching. Similar results were obtained using thiosulphate as complexing agent. Gold was recovered from the leaching solution by electrodeposition or cementation with zinc powder. Copper, silver and tin, leached during the pre-treatment with nitric acid, were recovered using three different processes to obtain them in form of nanoparticles.

B. PV panels.

In order to recover glass, silicon and silver from PV panels, a combination of a heat treatments and three hydrometallurgical processes was adopted. The characterization of the silicon cells, extracted from photovoltaic panels, confirmed the presence of silver fingers on the front-side of the silicon cells and of aluminium paste on the other side.

In particular, the developed process started with panel delamination, which was necessary to release silicon cells from the encapsulating and protective effect provided by polymer EVA and all the layers that make up the photovoltaic sandwich. This was achieved by heat-treating the panel in a furnace at a temperature of 500 °C for 15 min in order to remove all polymeric parts. The silicon cells were firstly treated with sodium hydroxide solution (2 M solution at 40°C) to remove aluminium. After that, a nitric acid solution, 5 M at 25°C, removed the silver metallic contacts from surface in few minutes.

Successively, even if other methods were tested (electrodeposition or precipitation of silver oxide), the most convenient resulted the recovery silver by adding sodium chloride to the solution, thus inducing the silver chloride precipitation. Different methods to reduce silver chloride to metallic silver were investigated. The most efficient method was the reduction by heating silver chloride in presence of sodium carbonate, as confirmed by EDS analysis. The refining of silicon wafers was instead performed using hydrofluoric acid solution or a mixture of this acid with nitric acid and acetic acid. SIMS analyses confirmed the removal of antireflective (Si_3N_4) and doped layers (P and B).

In conclusion, this part of the research allowed to identify the most convenient process to treat the panels and led to an Italian patent application. Moreover, a European upscaling project, which involved other European partners, was presented to KIC Raw Material, and it was financed with the name of ReSiELP. ReSiELP, which started officially 1st of April 2017, has the aim to upscale to TRL7 the PV panel recycling process developed in this PhD research.

As a consequence, in order to upgrade the process at TRL 7, the following steps were performed: a feasibility study, which proved the validity of the idea; tests at TRL5 to adapt the processes parameters to the higher quantity of PV panels treated; the study of how to perform the automation of the silicon cells separation from glass and copper ribbons, previously performed manually; and the study of the proper disposal of the gaseous emissions generated during the heating treatment. In this last case, analyses showed that off-gases contained, apart from CO₂, also hydrofluoric and acetic acid, so a scrubber with basic solution was designed.

Moreover, the design of all the plant began and, in details, the furnace for the heating treatment was ordered and the other necessary equipment for hydrometallurgical treatment and off-gases treatment will be ordered for the end of October 2017. Moreover, the tests at TRL 5 performed, not only proved the technology, but also allowed to collect the material required by the other partners: 2 kg of silicon for Bay-Zoltan and 20 kg of glass for Cetma.

C. Capacitors and permanent magnets.

In addition to this research, a method for recovering tantalum was studied by means of a thermal treatment coupled with hydrometallurgical processes. In particular, the use of hydrofluoric acid allowed to obtain tantalum fluoride without silica. This represents an advantage, as silica is very difficult to separate from tantalum oxide. This separation treatment can represent a substitute for the sieving process described in the literature, which has the defect of causing the loss of high quantities of raw material.

Moreover, the recovery of neodymium from permanent magnets was studied. In particular, the purity of the neodymium salts was increased by adding, to the hydrometallurgical processes proposed in literature, an ammonia treatment, which allowed to significantly reduce the iron presence in the recovered double salt of neodymium. Moreover, with this treatment it resulted easier to control the process parameters, because iron was precipitated before neodymium, thus an accurate pH control during neodymium recovery was not necessary.

C. Powders and nanoparticles production.

The syntheses of different nanoparticles from wastes were studied and the results showed that the methods developed allowed to recover the metals with high yield and to produce nanoparticles of tin dioxide, silver, copper, cuprous oxide, gold and iron with high purity and with sizes between 2 and 200 nm.

Furthermore, in almost all syntheses, ultrasound application achieved to reduce the sizes of the synthesized particles and this effect derived from the cavitation collapse that produces locally extreme conditions. Another effect is that kinetic is improved: in fact, ultrasound irradiation reduces the time required to complete the synthesis.

As raw material it was used the nitric acid solutions coming from the leaching of PCBs of end-of-life mobile phones. ICP analysis showed that they contained high amount of copper (15960 ppm), iron (1120 ppm), tin (1190 ppm), lead (830 ppm), barium (560 ppm) and silver (540 ppm).

First, tin oxide precursor was precipitated from the solution. The precipitation induced by ultrasound or microwaves allowed to obtain smaller aggregates in comparison with conventional heating plates, as evidenced by SEM analysis. Then, tin oxide precursor was heat treated in furnace at different temperature to convert it to tin dioxide in cassiterite form. XRD confirmed that the conversion was completed after the treatment at 600°C for 2 h. TEM showed that SnO₂ nanoparticles had a size smaller than 10 nm.

Successively, silver was recovered from the solution by precipitation of silver chloride and reducing it to metallic silver with Tollens reaction. The Ag nanoparticles obtained with conventional heating had a size of about 7 nm, whereas the ones synthesized using microwaves and ultrasound were about 2 nm and 0.7 nm, respectively.

Copper was finally recovered from the solution by cementation with iron powder. The recovered copper was used to synthesize copper nanoparticles.

In particular, for copper nanoparticles synthesis the use of L-ascorbic acid in water solution was investigated. It was interesting to notice that, in this case, the use of ultrasound highly reduced both the reaction time and the mean size of the nanoparticles. Specifically, copper nanoparticles with a mean size of about 5 nm were obtained with ultrasound, whereas without ultrasound the reaction took several hours and the final powder produced had a mean size of 1 µm.

Furthermore, the use of L-ascorbic acid as a reducing agent with ultrasound allowed the production of Cu nanoparticles with a size that can be comparable to nanoparticles produced with sodium borohydride, the typical reducing agent used for nanoparticles synthesis.

Preliminary studies were conducted in order to synthesize cuprous oxide nanoparticles. Copper nitrate was used as precursor and D-glucose was used as reducing agent and also in this case the ultrasound assistance allowed the production of nanoparticles with dimensions less than 150 nm.

A method for the synthesis of gold nanoparticles from the gold coming from PCBs was also developed. In fact, in this case it resulted convenient to treat in nitric acid PCBs without grinding and with high stirring. This treatment allowed to use as raw material the gold detached from the board which almost does not contain other metals which can interfere with the synthesis. As a result, nanoparticles with dimensions of about 100 nm were synthesized. Moreover, the Brust synthesis using the same raw material was tested and also in this case the synthesis succeeded, even if dimensions of the nanoparticles were of about 100 nm instead of few nanometers, which are typically obtained.

Finally, zero-valent iron nanoparticles were successfully synthesized using as raw material the goethite coming from the treatment of permanent magnets to recover Neodymium.

Eugenol was tested as reducing agent and compared with sodium borohydride. The synthesized nanoparticles were very polydisperse with dimensions less than 200 nm. However, further studies are required for the optimization of this synthesis, in particular to avoid particles oxidation and the presence of organics residue when eugenol is used.

D. Powders and nanoparticles applications.

Finally, the effect of the addition of silver and copper particles in the electrolyte used to produce PEO coatings on AA7075 was explored. The particles did not influence the mechanism of formation of the oxide coating that resulted adherent, uniform, homogeneous on the surface of all the PEO treated samples and mainly constituted by aluminum and silicon oxides. This fact is interesting because, on the other hand, the simply addition of the particles to the electrolyte during the conventional anodizing process prevented the formation of a good-quality coating. The distribution of the silver or copper particles was uniform and their presence was detected also inside the pores.

The antimicrobial activity of the coatings which contained silver powders was verified both with *E. Coli* and *S. Aureus* bacteria. The presence of the silver particles in the PEO coatings remarkably increased the antimicrobial effect. Regarding *E. Coli* bacteria, all the bacteria died after 3h in contact with the coatings containing silver particles, regardless the different amounts of silver or the sealing treatment. With *S. Aureus* bacteria, the antimicrobial effects were slightly lower, nevertheless a reduction of 5 order of magnitude in the density of bacterial colonies was obtained for the silver-containing coatings.

Moreover, the samples which contain silver powder are characterized also by high fungicidal activity: in fact, all the PEO coated samples containing Ag produce the death of almost all the fungi (*Candida Albicans*) after four hours of contact.

Furthermore, the effect of the addition of silver or copper particles into PEO coatings on the antifouling properties of 7075 aluminum samples was studied.

The results showed that all the treated samples were characterized by higher corrosion resistance if compared with the untreated ones. It was evidenced that the PEO coatings with copper particles actually exhibited good antifouling effect. In fact, even after one month of immersion the number of organisms found on the surface of the sample was still low. Anyway, the best performance in term of antifouling effect were given by the commercial painting. Nevertheless, the use of this kind of paintings shows problems in presence of ruptures in the varnish, in fact in these cases no protection is given to the substrate. In fact, the tests performed in seawater showed that copper-containing PEO coating with varnish represented an optimum solution: the sample exhibited good corrosion and fouling resistance even in presence of some cracks in the varnish. In fact, it avoids the blistering problem observed when the alloy is painted without using PEO as substrate.

The anodic polarization tests showed that the PEO coatings containing the particles exhibited a decrease in the corrosion resistance if compared with the PEO coatings without particles. This fact can be explained with the galvanic couple formed between silver or copper and aluminum. However, it was verified that a sealing treatment in boiling water allowed to obtain coatings with improved corrosion resistance, if compared with untreated sample.

References

- [1] W. Rolf, O.-K. Heidi, S.-K. Deepali, S. Max e B. Heinz, «Global perspectives on e-waste,» *Environmental Impact Assessment Review*, vol. 25, p. 436–458, 2005.
- [2] [Online]. Available: <http://srdata.nist.gov/XPS>.
- [3] [Online]. Available: <http://www.step-initiative.org>.
- [4] [Online]. Available: http://www.repubblica.it/ambiente/2014/06/20/news/nei_rifiuti_elettrici_oro_e_argento.
- [5] B. Viraja, R. Prakash e P. Yogesh, «Procedia,» *Social and Behavioral Sciences*, vol. 37, p. 398, 2012.
- [6] J. Lohse, S. Winteler e J. Wulf-Schnabel, «Collection targets for waste from electrical and electronic equipment (WEEE) the directorate general (DG XI) environment,» Nuclear safety and civil protection of the Commission of the European Communities, 1998.
- [7] S. Matthews, C. Hendrickson, F. McMichael e D. Hart, «Disposition and end-of-life options for personal computers,» Carnegie Mellon University, 1997.
- [8] EEA, «Waste electrical and electronic equipment (WEEE),» European Environment Agency, Copenhagen, 2003.
- [9] [Online]. Available: <http://www.livescience.com/41966-tracking-world-e-waste.html>.
- [10] [Online]. Available: http://www.repubblica.it/economia/affari-e-finanza/2013/02/11/news/la_scommessa_delloro_una_crescita_lunga_12_anni-52371541/.
- [11] [Online]. Available: <http://www.criticalrawmaterials.eu/blog/strategic-metals/>.
- [12] A. Tuncuk, V. Stazi, A. Akcil, E. Yazici e H. Deveci, «Aqueous metal recovery techniques from e-scrap: Hydrometallurgy in recycling,» *Minerals Engineering*, vol. 25, p. 28–37, 2012.
- [13] D. Groot e P. Pistorius, «Can we decrease the ecological footprint of base,» *The Journal of the Southern African Institute of*, vol. 108, p. 161–169, 2008.
- [14] S. Zhang e E. Forssberg, «Mechanical recycling of electronics scrap – the current,» *Waste Management & Research*, vol. 16, n. 2, p. 119–128, 1998.
- [15] S. A. Shuey e P. Taylor, «Review of Pyrometallurgical Treatment of Electronic Scrap,» in *SME Annual Meeting*, Denver, 2004.

- [16] Mark, E. Frank e L. Theo, «Plastics Recovery from Waste Electrical & Electronic Equipment in Non-Ferrous Metal Processes,» Association of Plastics Manufacturers in Europe (APME), 2000.
- [17] H. Madenoglu, *Recovery of Some Metals from Electronic Scrap*, Ege University, 2005.
- [18] P. Sheng e T. Etsell, «Recovery of gold from computer circuit board scrap using aquaregia,» *Waste Management and Research*, vol. 25, p. 380–383, 2007.
- [19] A. Mecucci e K. Scott, «Leaching and electrochemical recovery of copper, lead,» *Journal of Chemical Technology and*, vol. 77, p. 449–457, 2002.
- [20] T. A. S. K. N. N. S. K. F. T. K. Kinoshita, «Metal recovery from non-mounted printed wiring boards via hydrometallurgic processing,» *Hydrometallurgy*, vol. 69, p. 73–79, 2003.
- [21] C. Oh, S. Lee, H. Yang, T. Ha e M. Kim, «Selective leaching of valuable metals from waste printed circuit boards,» *Air & Waste Management Association*, vol. 55, p. 897–902, 2003.
- [22] P. P. J. V. L. A. Quinet, «Recovery of precious metals from electronic scrap by hydrometallurgical processing routes,» *Minerals Metallurgical Process*, vol. 22, p. 17–22, 2005.
- [23] H. Brandl, R. Bosshard e M. Wegmann, «Computer-munching microbes: metal leaching from electronic scrap by bacteria and fungi,» *Hydrometallurgy*, vol. 59, p. 319–326, 2001.
- [24] S. Ilyas, C. Ruan, H. Bhatti, M. Ghauri e M. Anwar, «Column bioleaching of metals from electronic scrap,» *Hydrometallurgy*, vol. 101, p. 135–140, 2010.
- [25] S. A. M. N. S. G. M. Ilyas, «Bioleaching of metals from electronic scrap by moderately thermophilic acidophilic bacteria,» *Hydrometallurgy*, vol. 88, p. 180–188, 2007.
- [26] Y. Park e D. Fray, «Recovery of high purity precious metals from printed circuit boards,» *Journal of Hazardous Materials*, vol. 164, p. 1152–1158, 2009.
- [27] V. Ha, J. Lee, J. Jeong, H. Haia e M. Jha, «Thiosulfate leaching of gold from waste mobile phones,» *Journal of Hazardous Materials*, vol. 178, p. 1115–1119, 2010.
- [28] C. Lee, L. Tang e S. Popuri, «A study on the recycling of scrap integrated circuits by leaching,» *Waste Management & Research*, p. 1–9, 2010.
- [29] M. Alam, M. Tanaka, K. Koyama, T. Oishi e J. Lee, «Electrolyte purification in energy-saving monovalent copper electrowinning processes,» *Hydrometallurgy*, vol. 87, p. 36–44, 2007.
- [30] L. Le, J. Jeong, J. Lee, B. Pandey, J. Yoo e T. Huyunh, «Hydrometallurgical process for copper recovery from waste printed circuit boards (PCBs),» *Mineral Processing and Extractive Metallurgy Review*, vol. 32, n. 2, p. 90–104, 2011.

- [31] Z. Kamberovic, M. Korac', S. Vracar e M. Ranitovic, «Preliminary process analysis and development of hydrometallurgical process for the recovery of copper from waste printed circuit boards,» in *Going Green-Care Innovation 2010 Conference*, Vienna, 2010.
- [32] H. Yang, J. Liu e J. Yang, «Leaching copper from shredded particles of waste printed circuit boards,» *Journal of Hazardous Materials*, vol. 187, p. 393–400, 2011.
- [33] Y. Park e D. Fray, «Separation of zinc and nickel ions in a strong acid through liquid–liquid extraction,» *Journal of Hazardous Materials*, vol. 163, p. 259–265, 2009.
- [34] M. Lanchester, *Green Chemistry. An Introductory Text 3rd Edition*, Cambridge, UK: The Royal Society of Chemistry, 2016.
- [35] M. Poliakoff, J. M. Fitzpatrick, T. R. Farren e P. T. Anastas, «Green Chemistry: Science and Politics of Change,» *Science*, vol. 297, pp. 807-810, 2002.
- [36] C. Abruzzese, P. Fornari, R. Massidda, F. Veglio e S. Ubaldini, «Thiosulphate leaching for gold hydrometallurgy,» *Hydrometallurgy*, vol. 39, pp. 265-276, 1995.
- [37] G. Hilson e A. Monhenius, «Alternative to cyanide in the gold mining industry: what prospects for the future?,» *Journal of cleaner production*, vol. 14, pp. 1158-1167, 2006.
- [38] U. A. S. Orgul, «Reaction chemistry of gold in thiourea solution for a Turkish gold ore,» *Hydrometallurgy*, vol. 62, pp. 71-77, 2002.
- [39] S. Syed, «Recovery of gold from secondary sources,» *Hydrometallurgy*, vol. 115, pp. 30-51, 2012.
- [40] M. Aylmore e D. Muir, «Thiosulfate leaching of gold- a review,» *Minerals Engineering*, vol. 14, pp. 35-174, 2011.
- [41] R. Rath, N. Hiroyoshi, M. Tsunekawa e T. Hirajima, «Ammoniacal thiosulphate leaching of gold ore,» *The European Journal of Mineral Processing and Environmental Protection*, vol. 3, pp. 344-352, 2003.
- [42] A. Grosse, G. Dicinoski, M. Shaw e P. Haddad, «Leaching and recovery of gold using ammoniacal thiosulfate leach liquors (a review),» *Hydrometallurgy*, vol. 69, pp. 1-21, 2003.
- [43] A. Harunobu, F. Toyohisa e Y. Wan-Tai, «Gold Cementation from Ammonium Thiosulfate Solution by Zinc, Copper and Aluminium Powders,» *Materials Transactions*, vol. 43, pp. 485-493, 2002.
- [44] N. K. Swamy K.M., «Ultrasonically assisted leaching,» *Advances in Sonochemistry*, vol. 6, pp. 141-179, 2001.
- [45] L. d. C. M. Luque-Gracia J.L., «Ultrasound: A powerful tool for leaching,» *Trends in Analytical Chemistry*, vol. 22, pp. 41-47, 2003.
- [46] K. Suslik, «The chemical effect of Ultrasound,» *Scientific American*, vol. 260, pp. 80-86, 1989.

- [47] F. P. C. M.D. Luque de Castro, in *Analytical applications of ultrasound*, Elsevier B.V., 2007, pp. 99-137.
- [48] M. A. Pankaj, *Theoretical and Experimental*, New York: Springer Dordrecht Heidelberg London, 2011.
- [49] D. Chen, S. K. Sharma e A. Mudhoo, in *Handbook on Applications of Ultrasound*, 2012, pp. 43,503,506.
- [50] C. Cason, *Gold alloys: study of the microstructural, mechanical characteristics and final optimization of production parameters for the realization of full and cable pipe chains*, Università di Padova, 2016.
- [51] [Online]. Available: <http://www.speciation.net/Database/Instruments/SPECTRO-Analytical-Instruments-Inc/XLAB-2000-;i279>.
- [52] [Online]. Available: <http://www.directindustry.com/prod/spectro-analytical-instruments-gmbh/product-32884-183756.html>.
- [53] [Online]. Available: <https://www.malvern.com/en/products/product-range/zetasizer-range/zetasizer-nano-range/zetasizer-nano-zs>.
- [54] [Online]. Available: <http://new.isvch.ru/tech/>.
- [55] [Online]. Available: https://www.artisanng.com/ViewImage.aspx?Image=Jasco_V_530_View1.JPG%20&Item=78011.
- [56] [Online]. Available: <http://www.chimica.unipd.it/m3/facilities.html>.
- [57] M. Seah, D. Briggs e J. Seah, « Practical Surface Analysis,» *Auger and X-ray Photoelectron Spectroscopy*, vol. 1, p. 543, 1990.
- [58] D. Shirley, «High-resolution X-ray photoemission spectrum of the valence bands of gold,» *Phys. Rev. B*, vol. 55, p. 4709, 1972.
- [59] J. Moulder, W. Stickle, P. Sobol, K. Bomben e J. Chastain, *Handbook of X-Ray Photoelectron Spectroscopy*, Perkin Elemer Corp, 1992.
- [60] [Online]. Available: <http://srdata.nist.gov/XPS>.
- [61] «X-ray Photoelectron Spectroscopy Database 20,» National Institute of Standards and Technology, Gaithersburg, 2000.
- [62] [Online]. Available: https://www.helmholtz-berlin.de/forschung/oe/em/werkstoffe/methoden/thermoanalysis-laboratory_en.html.
- [63] L. Coelho, M. Mouanga, M.-E. Druart, I. Recloux, D. Cossement e M.-G. Olivier, «A SVET study of the inhibitive effects of benzotriazole and cerium chloride solely and combined on an aluminium/copper galvanic coupling model,» *Corros. Sci.*, vol. 110, p. 143–156, 2016.

- [64] [Online]. Available: <https://www.dreamstime.com/royalty-free-stock-photography-marine-fouling-image24143147>.
- [65] L. Morf, R. Gloor, O. Haag, M. Haupt, S. Skutans, F. Di Lorenzo e D. Boni, «Precious metals and rare earth elements in municipal solid waste – Sources and fate in a Swiss incineration plant,» *Waste Management*, vol. 33, pp. 634-644, 2013.
- [66] 2013 Renewable energy data book, U.S. Department of Energy, 2014.
- [67] A. Paiano, «Photovoltaic waste assessment in Italy,» *Renewable and Sustainable Energy Reviews*, vol. 41, pp. 99-112, 2015.
- [68] S. Bilimoria e N. Defrenne, «The evolution of photovoltaic waste in Europe.»
- [69] IRENA, «End-of-life Management. Solar Photovoltaic Panels,» 2016.
- [70] «La termotecnica,» 2012, pp. 69-73.
- [71] A. Luque e S. Hegedus, *Handbook Of Photovoltaic Science And Engineering*, Chichester: John Wiley & Sons, 2011.
- [72] A. Ciftja, T. A. Engh e M. Tangstad, «Refining and Recycling of Silicon: A Review,» 2011.
- [73] A. Luque e S. Hegedus, *Handbook Of Photovoltaic Science And Engineering*.
- [74] O. Breitenstein, *The Physics of Industrial Crystalline Silicon Solar Cells*.
- [75] P. Würfel, *Physics of Solar Cells - From Principles to New Concepts*, Weinheim: WILEY-VCH Verlag, 2007.
- [76] [Online]. Available: <http://www.aleo-solar.com/difference-n-type-p-type-solar-cells/>.
- [77] B. Xakalasho e M. Tangstad, «Silicon processing: from quartz to crystalline silicon solar cells,» *Southern African Pyrometallurgy*, 2011.
- [78] M. A. Green, K. Emery, Y. Hishikawa, W. W., E. Dunlop, D. Levi e A. Ho-Baillie, *Solar cell efficiency tables (version 49)*, WILEY-BLACKWELL, 2016.
- [79] M. S. Islam, M. A. Rhamdhani e G. A. Brooks, «Solar-grade silicon: current and alternative production routes».
- [80] S. Pizzini, «Towards solar grade silicon: Challenges and benefits for low cost photovoltaics,» *Solar Energy Materials and Solar Cells*, vol. 94, pp. 1528-1533, 2010.
- [81] [Online]. Available: http://www.microchemicals.com/products/wafers/silicon_ingot_production.html.
- [82] [Online]. Available: http://www.tsecpv.com/en-global/solar_knowledge/index/zero_house_02.
- [83] A. Müller, K. Wambach e E. Alsema, «Life cycle analysis of a solar module recycling process,» *MRS Proceedings*, vol. 895, 2011.

- [84] E. Klugmann-Radziemska, «Current trends in recycling of photovoltaic solar cells and modules waste,» *CHEM DIDACT ECOL METROL*, vol. 17, pp. 89-95, 2012.
- [85] J. R. Bohland e I. I. Anisimov, «Possibility of recycling silicon pv modules,» in *IEEE*, Anaheim, 2002.
- [86] E. Klugmann-Radziemska, P. Ostrowski, K. Drabczyk, P. Panek e M. Szkodo, «Experimental validation of crystalline silicon solar cells recycling by thermal and chemical methods,» *Solar Energy Materials and Solar Cells*, vol. 94, pp. 2275-2282, 2010.
- [87] R. R. Sondergaard, N. Espinosa, M. Jorgensen e F. C. Krebs, «Efficient decommissioning and recycling of polymer solar cells: justification for use of silver,» *Energy Environ. Sci.*, vol. 7, pp. 1006-1012, 2014.
- [88] E. Klugmann-Radziemska e P. Ostrowski, «Chemical treatment of crystalline silicon solar cells as a method of recovering pure silicon from photovoltaic modules,» *Renewable Energy*, vol. 35, pp. 1751-1759, 2010.
- [89] «Guida al fine vita degli impianti fotovoltaici,» Federazione Italiana per l'uso Razionale dell'Energia .
- [90] A. Müller, K. Wambach e E. Alsema, «Life cycle analysis of a solar module recycling process,» in *20th European Photovoltaic Solar Energy Conference*, Barcelona, 2005.
- [91] [Online]. Available: <http://www.targray.com/solar/crystalline-cell-materials/aluminum-paste>.
- [92] C. E. Latunussa, F. Ardente, G. A. Blengini e L. Mancini, «Life Cycle Assessment of an innovative recycling process for crystalline,» *Solar Energy Materials & Solar Cells*, vol. 156, pp. 101-111, 2016.
- [93] G. Granata, F. Pagnanelli, E. Moscardini, T. Havlik e L. Toro, «Recycling of photovoltaic panels by physical operations,» *Solar Energy Materials and Solar Cells*, vol. 123, pp. 239-248, 2014.
- [94] A. Badiie, I. Ashcroft e R. Wildman, «The thermo-mechanical degradation of ethylene vinyl acetate used as solar panel and encapsulant,» *Internal Journal of Adhesion & Adhesive*, vol. 68, pp. 212-218, 2016.
- [95] A. Doni e F. Dughiero, «Electrothermal Heating Process Applied to c-Si PV Recycling,» *IEEE*, 2012.
- [96] M. L. Marín, A. Jimenez, J. Lopez e J. Vilaplana, «Thermal degradation of ethylene (vinyl acetate),» *Journal of Thermal analysis*, vol. 47, pp. 247-258, 1996.
- [97] I. C. Me Neill, A. Jamieson, D. J. Toshand e J. J. Me Clune, «Thermal degradation of ethylene (vinyl acetate) Kinetic analysis of thermogravimetric data,» *Cur. Polym. J.*, vol. 12, p. 305, 1976.

- [98] J. Kaezaj e R. Trickey, «Thermal degradation of ethylene (vinyl acetate) Kinetic analysis of thermogravimetric data,» *Anal. Chem.*, vol. 41, p. 1511, 1969.
- [99] S. G. Byer, C. Wong, R. T. Yang e J. R. Reinhardt, «Kinetics of the reaction between hydrofluoric acid and calcium oxide for fluoride emission control,» *Environ. Sci. Technol.*, vol. 17, p. 84–88, 1983.
- [100] A. Tewarson, . F. Chu e F. H. Jiang, «Combustion of Halogenated Polymers».
- [101] F. Y. Hshieh e D. H. Benson, «A Brief Study on Toxic Combustion Products of the Polymers Used in High-pressure Oxygen Systems,» NASA Johnson Space Center.
- [102] J. L. Neviase e R. G. Gann, «Evaluation of Toxic Potency Values for Smoke from Products and Materials,» *Fire Technology*, vol. 40, p. 177–199, 2004.
- [103] Y. Yi, H. Kim, T. Tran, S. Hong e M. Kim, «Recovering valuable metals from recycled photovoltaic modules,» *Journal of the Air & Waste Management Association*, vol. 64, n. 7, pp. 797-807, 2014.
- [104] B. V. L'vov, «Kinetics and mechanism of thermal decomposition of silver oxide,» *Thermochimica Acta*, vol. 333, pp. 13-19, 1999.
- [105] G. I. N. Waterhouse, G. A. Bowmaker e J. B. Metson, «The thermal decomposition of silver (I,III) oxide: a combined XRD, FT-IR and Raman spectroscopic study,» *Physical Chemistry Chemical Physics*, vol. 3, p. 3838, 2001.
- [106] [Online]. Available: <https://chem.umn.edu/temperature-dependence-silver-oxide-formation>.
- [107] E. Radziemska, T. Seramak e P. Ostrowski, «Pure Silicon recovering from photovoltaic modules,» *Advances in Materials Science*, vol. 8, pp. 28-34, 2008.
- [108] J. Wu, Y. Li, W. Ma, K. Liu, K. Wei, K. Xie, B. Yang e Y. Dai, «Impurities Removal From Metallurgical Grade Silicon Using Gas Blowing Refining Techniques,» *Silicon*, vol. 6, p. 79–85, 2014.
- [109] H. K. Raut, V. A. Ganesh, A. S. Nairb e S. Ramakrishna, «Anti-reflective coatings: A critical, in-depth review,» *Energy Environ. Sci.*, vol. 4, p. 3779–3804, 2011.
- [110] D. Nagel, C. Frohne e R. Sittig, «Rapid thermal diffusion of aluminum in silicon and its interaction with phosphorus,» *Applied Physics A*, vol. 60, pp. 61-65, 1995.
- [111] M. Tamaro, J. Rimauro, V. Fiandra e A. Salluzzo, «Thermal treatment of waste photovoltaic module for recovery and,» *Renewable Energy*, vol. 81, pp. 103-112, 2015.
- [112] Brevetto US20110108086.
- [113] K. Minetaa e T. H. Okabeb, «Development of a recycling process for tantalum from capacitor scraps.,» *Journal of Physics and Chemistry of Solids*, vol. 16, p. 318–321, 2005.

- [114] K. Hayes e R. Burge, «Coltan Mining in the Democratic Republic of Congo: How tantalum-using industries can commit to the reconstruction of the DRC,» Published by Fauna & Flora International, Cambridge, UK, 2003.
- [115] G. J. Cho, S. B. Cho, S. B. Kim, W. B. . Kim e J. C. Lee. Korea Brevetto KR2004072779, 2004.
- [116] J. Smokovich e C. F. Hafner, «Method for the production of tantalum powder using reclaimed scrap as source material». US Brevetto US20090095130, 2009.
- [117] N. Yuan, H. Dong, J. Meng, F. Huang, S. Cao e J. Tu, «Method for preparing ultrafine tantalum carbide from tantalum capacitor scraps». China Brevetto CN102560127, 2012.
- [118] W. Rommel, M. Hertel e H. Nordsieck, *Recycling und Rohstoffe*, Neuruppin: K. T. Thomé-Kozmiensky; D. Goldmann, 2011.
- [119] L. S. von Brisinski, D. Goldmann e F. Endres, «Recovery of Metals from Tantalum Capacitors,» *Chemie Ingenieur Technik*, vol. 86, p. 196–199, 2014.
- [120] S. Katanoa, T. Wajimaa e H. Nakagomea, «Recovery of Tantalum Sintered Compact from Used Tantalum Condenser Using Steam Gasification with Sodium Hydroxide,» in *ICESD 2014*, Singapore, 2014.
- [121] R. W. Lee, «Hot-pressed neodymium-iron-boron magnets,» *Appl. Phys. Lett.*, vol. 46, pp. 790-791, 1985.
- [122] S. Shirayama e T. Okabe, «Current Status of Rare Earth Elements and Their Recycling Processes,» *J. Soc. Autom. Eng.*, vol. 65, p. 87–94, 2011.
- [123] B. K. Reck e T. E. Graedel, «Challenges in metal recycling,» *Science*, vol. 337, p. 690–695, 2012.
- [124] B. Sprecher, R. Kleijn e G. J. Kramer, «Recycling Potential of Neodymium: The Case of Computer Hard Disk,» *Environmental Science & Technology*, vol. 48, pp. 9506-9513, 2014.
- [125] K. Binnemans, P. T. Jones, B. Blanpain, T. Van Gerven, Y. Yang, A. Walton e M. Buchert, «Recycling of rare earths: A critical review.,» *J. Cleaner Prod.*, vol. 51, 2013.
- [126] J. Lyman e G. Palmer, «Recycling of Neodymium Iron Boron Magnet Scrap,» 1993.
- [127] J. F. Herbst e J. J. Croat, «Neodymium-iron-boron permanent magnets,» *Journal of Magnetism and Magnetic Materials*, vol. 100, pp. 57-78, 1991.
- [128] [Online]. Available: <https://www.supermagnete.de/eng/faq/How-are-neodymium-magnets-produced>.
- [129] [Online]. Available: <http://www.usneodymiummagnets.com/the-production-of-ndfeb-magnets.html>.

- [130] M. Zakotnik, E. Devlin, I. Harris e A. Williams, «Hydrogen Decrepitation and Recycling of NdFeB-type Syntered Magnets,» in *Proceedings of 19th International Workshop on Rare Earth Permanent Magnets & Their Applications*, Nagasaki, 2006.
- [131] J. Cui e L. Zhang, «Metallurgical recovery of metals from electronic waste: A review,» *Journal of Hazardous Materials*, vol. 158, pp. 228-256, 2008.
- [132] G. Cao, *Nanostructure and nanomaterials*, London: Imperial Collage Press, 2009.
- [133] J. C. Hulteen, D. A. Treichel, M. T. Smith, M. L. Duval, T. R. Jensen e a. R. P. V. Duyne, «Nanosphere Lithography: Size-Tunable Silver Nanoparticle and Surface Cluster Arrays,» *Journal of Physical Chemistry*, 1999.
- [134] J. Zeng, Y. Zheng, M. Rycenga, J. Tao, Z.-Y. Li, Q. Zhang, Y. Zhu e Y. Xia, «Controlling the Shapes of Silver Nanocrystals with Different Capping Agents,» *JACS Communication*, 2010.
- [135] P. Anastas e J. Warner, «Green Chemistry: Theory and Practice,» New York, Oxford University Press, 1998, p. 30.
- [136] M. Sillanpää e T. S. R. Pham, *Ultrasound Technology in Green Chemistry*, Victoria, Australia: Springer, 2011.
- [137] R. Varma, in *Encyclopedia of Sustainability Science and Technology*, New York, Springer, 2012, p. 4642–4673.
- [138] J. Suslick e K. Bang, «Applications of ultrasound to the synthesis of nanostructured materials,» *Advanced Materials*, vol. 22, p. 103, 2010.
- [139] I. Bilecka e M. Niederberger, «Microwave chemistry for inorganic nanomaterials synthesis,» *Nanoscale*, vol. 2, p. 1358, 2010.
- [140] J. Gerbec, D. Magana, A. Washington e G. Strouse, «Microwave-enhanced reaction rates for nanoparticle synthesis,» *Journal of American Chemical Society*, vol. 127, p. 15791, 2005.
- [141] G. Patil, D. Kajale, V. Gaikwad e G. Jain, «Preparation and characterization of SnO₂ nanoparticles by hydrothermal route,» *Int.Nano Lett.*, vol. 2, p. 17, 2012.
- [142] B. Cheng, J. Russell, W. Shi, L. Zhang e E.T.Samulski, «Large-scale, solution-phase growth of single-crystalline SnO₂ nanorods,» *Journal of American Chemical Society*, vol. 126, p. 5972, 2004.
- [143] S. Fujihara, T. Maeda, H. Ohgi, E. Hosono, H. Imai e S. Kim, «Hydrothermal routes to prepare nanocrystalline mesoporous SnO₂ having high thermal stability,» *Langmuir*, vol. 20, p. 6476, 2004.
- [144] F. Davar, M. Salavati-Niasaria e Z. Fereshteh, «Synthesis and characterization of SnO₂ nanoparticles by thermal decomposition of new inorganic precursor,» *Journal of Alloys and Compounds*, vol. 496, p. 638, 2010.

- [145] B. Nowack, H. F. Krug e M. Height, «120 Years of Nanosilver History: Implications for Policy Makers,» *Environmental Science and Technology*, 2010.
- [146] S. Virender K., Y. Ria A. e L. Yekaterina, «Silver nanoparticles: Green synthesis and their antimicrobial activities,» *Advances in Colloid and Interface Science*, Vol. 151 di 283-96, p. 145, 2009.
- [147] P. Rauwel, S. K  unal, S. Ferdov e E. Rauwel, «A review on the green synthesis of silver nanoparticles and their morphologies studied via TEM».
- [148] P. Sukdeb, T. Yu Kyung e S. Joon Myong, «Does the Antibacterial Activity of Silver Nanoparticles Depend on the Shape of the Nanoparticle? A Study of the Gram-Negative Bacterium Escherichia coli.,» *Applied and environmental microbiology*, vol. 73, n. 6, p. 712–1720, 2007.
- [149] A. Panacek, L. Kvitek, R. Prucek, M. Kolar, R. Vecerova, N. Pizurova, V. K. Sharma, T. Nevecna e R. Zboril, «Silver Colloid Nanoparticles: Synthesis, Characterization, and Their Antibacterial Activity,» *J. Phys. Chem. B*, vol. 110, pp. 16248-16253, 2006.
- [150] R. Mahendra, Y. Alka e G. Aniket, «Silver nanoparticles as a new generation of antimicrobials,» *Biotechnology Advances*, vol. 27, pp. 76-83, 2009.
- [151] Y. Park, Y. Hong, A. Weyers, Y. Kim e R. Linhardt, «Polysaccharides and phytochemicals: a natural reservoir for the green synthesis of gold and silver nanoparticles,» *IET Nanobiotechnology*, vol. 5, n. 3, p. 69–78, 2011.
- [152] V. K. Sharma, R. A. Yngard e Y. Lin, «Silver nanoparticles: Green synthesis and their antimicrobial activities».
- [153] P. Raveendran, J. Fu e a. S. L. Wallen, «Completely “Green” Synthesis and Stabilization of Metal Nanoparticles».
- [154] K. El-Nour, A. Eftaiha, A. Al-Warthan e R. Ammar, «Synthesis and applications of silver nanoparticles,» *Arabian Journal of Chemistry*, vol. 135, p. 3, 2010.
- [155] Ratyakshi e C. R.P., «Colloidal Synthesis of Silver Nano Particles,» *Asian Journal of Chemistry*, pp. 113-116, 2009.
- [156] S. Sangsuk, «Preparation of high surface area silver powder via Tollens process under sonication,» *Materials Letters*, vol. 64, p. 775, 2010.
- [157] H. Wang, X. Qiao, J. Chen e S. Ding, «Preparation of silver nanoparticles by chemical reduction method,» *Colloids and Surfaces A: Physicochemical and Engineering Aspects*, vol. 256, p. 111, 2005.
- [158] I. Wani, A. Ganguly, J. Ahmed e T. Ahmad, «Silver nanoparticles: ultrasonic wave assisted synthesis, optical characterization and surface area studies,» *Mater.Lett.*, vol. 65, p. 520, 2011.

- [159] A. Pal, S. Shah e S. Devi, «Microwave-assisted synthesis of silver nanoparticles using ethanol as a reducing agent,» *Material Chemistry and Physics*, vol. 114, p. 530, 2009.
- [160] J. Byeon e Y. Kim, «A novel polyol method to synthesize colloidal silver nanoparticles by ultrasonic irradiation,» *Ultrason. Sonochem.*, vol. 19, p. 209, 2012.
- [161] Z. Issaabadi, M. Nasrollahzadeh e S. Sajadi, «Green synthesis of the copper nanoparticles supported on bentonite and investigation of its catalytic activity,» *Journal of Cleaner Production*, vol. 142, p. 3584–3591, 2017.
- [162] M. Raffi, S. Mehrwan, T. Bhatti, J. Akhter, A. Hameed, M. Yawar, L. Masood e M. Hasan, «Investigations into the antibacterial behavior of copper nanoparticles against *Escherichia coli*,» *Annals of Microbiology*, vol. 60, p. 75–80, 2010.
- [163] J. Xiong, Y. Wang, Q. Xue e X. Wu, «Synthesis of highly stable dispersions of nanosized copper particles using L-ascorbic acid,» *Green Chem.*, vol. 13, p. 900–904, 2011.
- [164] M. Blosi, S. Albonetti, M. Dondi, C. Martelli e G. Baldi, «Microwave-assisted polyol synthesis of Cu nanoparticles,» *J. Nanopart. Res.*, vol. 13, p. 127–138, 2011.
- [165] T. Dang, T. Le, F.-B. E. e M. Dang, «Synthesis and optical properties of copper nanoparticles prepared by a chemical reduction method,» *Nanosci. Nanotechnol.*, vol. 2, pp. 1-6, 2011.
- [166] W. Yu, H. Xie, L. Chen, Y. Li e C. Zhang, «Synthesis and Characterization of Monodispersed Copper Colloids in Polar Solvents,» *Nanoscale Research Letters*, vol. 4, p. 465–470, 2009.
- [167] P. Chokratanasombat e E. Nisaratanaporn, «Preparation of ultrafine copper powders with controllable size via polyol process with sodium hydroxide addition,» *Engineering Journal*, vol. 16, pp. 40-46, 2012.
- [168] S. Chandra, A. Kumar e P. Tomar, «Synthesis and characterization of copper nanoparticles by reducing agent,» *J. Saudi Chem. Soc.*, vol. 18, p. 149–153, 2014.
- [169] G. Portenlanger e H. Heusinger, «Chemical reactions induced by ultrasound and γ -rays in aqueous solutions of L-ascorbic acid,» *Carbohydrate Research*, vol. 232, p. 291–301, 1992.
- [170] A. Chatterjee, R. Sarkar, A. Chattopadhyay, P. Aich, R. Chakraborty e T. Basu, «A simple robust method for synthesis of metallic copper nanoparticles of high antibacterial potency against *E. coli*,» *Nanotechnology*, vol. 23, p. 1–11, 2012.
- [171] P. Kanninen, J. Christoffr, J. Merta e K. Kontturi, «Influence of ligand structure on the stability and oxidation of copper nanoparticles,» *Journal of Colloid and Interface Science*, vol. 318, p. 88–95, 2008.

- [172] O. Kharissova, H. Dias, B. Kharisov, B. Perez e V. Perez, «Iron-containing nanomaterials: synthesis, properties, and environmental applications,» *J. Trends Biotechnol.*, vol. 31, p. 240–248, 2013.
- [173] S. Panigrahi, S. Kundu, S. Ghosh, S. Nath, S. Praharaj, S. Basu e T. Pal, «Polyhedron,» vol. 25, p. 1263–1269, 2006.
- [174] M. Jin, G. He, H. Zhang, J. Zeng, Z. Xie e Y. Xia, «Angew. Chem. Int. Ed.,» vol. 50, p. 10560–10564, 2011.
- [175] P. Chowdhury, A. Shaik e J. Chakraborty, «Preparation of stable sub 10 nm copper nanopowders redispersible in polar and non-polar solvents,» *Colloid. Surface A*, vol. 466, p. 189–196, 2015.
- [176] A. Sinha e B. Sharma, «Preparation of copper powder by glycerol process,» *Materials Research Bulletin*, vol. 37, p. 407–416, 2002.
- [177] M. Mohl, P. Pusztai, A. Kukovecz, Z. Konya, J. Kukkola e K. Kordas, «Low-temperature large-scale synthesis and electrical testing of ultralong copper nanowires,» *Langmuir*, vol. 26, p. 16496–16502, 2010.
- [178] B. Su, Y. Jia, S. Zhang, X. Chen e M. Oyama, «Synthesis of Palladium Nanoparticles on Citrate-functionalized Graphene Oxide with High Catalytic Activity for 4-Nitrophenol Reduction,» *Chemistry Letters*, vol. 43, p. 919–921, 2014.
- [179] G. Yang, Z. Zhang, S. Zhang, L. Yu e P. Zhang, «Synthesis and characterization of highly stable dispersions of copper nanoparticles by a novel one-pot method,» *Mater. Res. Bull.*, vol. 48, p. 1716–1719, 2013.
- [180] A. Umer, S. Naveed, N. Ramzan, M. Rafique e M. Imran, «A green method for the synthesis of Copper Nanoparticles using L-ascorbic acid,» *Revista Matèria*, vol. 19, p. 197–203, 2014.
- [181] N. Nishida, A. Miyashita, N. Hashimoto, H. Murayama e H. Tanaka, «Regenerative synthesis of copper nanoparticles by photoirradiation,» *Eur Phys J D*, vol. 63, p. 307–310, 2011.
- [182] A. Umer, S. Naveed, R. Naveed e S. Rafique, «Selection of a suitable method for the synthesis of copper nanoparticles,» *Nano*, vol. 7, p. 1230005, 2012.
- [183] A. Venkata, K. Venkata, P. Karthika e P. Surya, «Copper conductive inks: synthesis and utilization in flexible electronics,» *RSC Advances*, vol. 5, p. 63985–64030, 2015.
- [184] D. Deng, Y. Jin, Y. Cheng, T. Qi e F. Xiao, «Copper nanoparticles: aqueous phase synthesis and conductive films fabrication at low sintering temperature,» *ACS Appl. Mater. Interfaces*, vol. 5, p. 3839–3846, 2013.

- [185] D. Zhang e H. Yang, «Gelatin-stabilized copper nanoparticles: Synthesis, morphology, and their surface-enhanced Raman scattering properties,» *Physica B*, vol. 415, p. 44–48, 2013.
- [186] A. Musa, T. Akomolafe e M. Carter, «Production of cuprous oxide, a solar cell material, by thermal oxidation and a study of its physical and electrical properties,» *Solar Energy Materials and Solar Cells*, vol. 51, pp. 305-516, 1998.
- [187] L. Hongbo, L. Jing, C. Daye, Q. Yanxia e W. Wei, «Dual-functional cubic cuprous oxide for non-enzymatic and oxygen-sensitive photoelectrochemical sensing of glucose,» *Sensors and Actuators B: Chemical*, vol. 220, pp. 441-447, 2015.
- [188] C. Yu, T. Joong Jiat e Z. Hua Chun, «Formation of Colloidal CuO Nanocrystallites and Their Spherical Aggregation and Reductive Transformation to Hollow Cu₂O Nanospheres,» *Langmuir*, vol. 21, pp. 1074-1079, 2005.
- [189] Z. Jiatao, L. Junfeng, P. Qing, W. Xun e L. Yadong, «Nearly Monodisperse Cu₂O and CuO Nanospheres: Preparation and Applications for Sensitive Gas Sensors,» *Chem. Mater.*, vol. 16, pp. 867-871, 2006.
- [190] B. Yakui, Y. Tengfei, G. Qing, C. Guoan e Z. Ruiting, «Shape control mechanism of cuprous oxide nanoparticles in aqueous,» *Powder Technology*, vol. 227, p. 35–42, 2012.
- [191] P. Kankanit, S. Sineenart, M. Wanichaya e P. Wisanu, «Synthesis of CuO Nanoparticles by Precipitation Method,» *Energy Procedia*, vol. 34, p. 740 – 745, 2013.
- [192] [Online]. Available: <http://www.edubio.info/2015/09/benedicts-test-for-monosaccharides-and.html>.
- [193] H. Sohyoung, D. A. Jaffray e C. Allen, «Gold nanoparticles for applications in cancer radiotherapy: Mechanisms,» *Advanced Drug Delivery Reviews*, vol. 109, pp. 84-101, 2017.
- [194] M.-C. Daniel e D. Astruc, «Gold Nanoparticles: Assembly, Supramolecular Chemistry,» *Chem. Rev.*, vol. 104, pp. 293-346, 2004.
- [195] D. Andreescu, T. Sau e D. Goia, «Stabilizer-free nanosized gold sols,» *Journal of Colloid and Interface Science*, vol. 298, p. 742–751, 2006.
- [196] S. Link e E.-S. M.A, «Size and Temperature Dependence of the Plasmon Absorption of Colloidal Gold Nanoparticles,» *The Journal of Physical Chemistry B*, vol. 103, pp. 4212-4217, 1999.
- [197] M. Brust, J. Fink, D. Bethell e D. Schiffrin, «Synthesis and Reactions of Functionalised Gold Nanoparticles,» *J. Chem. Soc., Chem. Commun.*, pp. 1655-1656, 1995.
- [198] E. Lefevre, N. Bossa, M. R. Wiesner e C. K. Gunsch, «A review of the environmental implications of in situ remediation by nanoscale zero valent iron (nZVI): Behavior,

- transport and impacts on microbial communities,» *Science of the Total Environmen*, vol. 565, p. 889, 2016.
- [199] Y. P. Sun, X. Li, J. Cao, W. Zhang e H. Wan, «Characterization of zero-valent iron nanoparticles,» *Advances in Colloid and Interface Science*, vol. 120, p. 47–56, 2006.
- [200] M. Dickinson e T. B. Scott, «The application of zero-valent iron nanoparticles for the remediation of a uranium-contaminated waste effluent,» *Journal of Hazardous Materials*, vol. 178, p. 171–179, 2010.
- [201] F. Fu, D. Dionysiou e H. Liu, «The use of zero-valent iron for groundwater remediation and wastewater treatment: a review,» *J. Hazard. Mater.*, vol. 267, p. 194–205, 2014.
- [202] Y. Sun, X. Li, W. Zhang e H. Wang, «A method for the preparation of stable dispersion of zero-valent iron nanoparticles,» *Colloids and Surfaces A: Physicochemical and Engineering Aspects*, vol. 308, p. 60–66, 2007.
- [203] M. Pattanayak, D. Mohaparata e P. Nayak, «Green synthesis and characterization of zero talent iron nanoparticles from the leaf extract of *Syzygium Aromaticum* (clove),» *Middle-East J. Sci. Res.*, vol. 18, pp. 623-626, 2013.
- [204] Q. Li, J. Linag e Q. Wang, «Plasma Electrolytic Oxidation coatings on lightweight metals,» *Modern Surface Engineering Treatments*, vol. 4, pp. 75-99, 2013.
- [205] B. Jiang e Y. Wang, «Plasma Electrolytic Oxidation Treatment on Aluminum and Titanium alloy,» in *Surface Engineering of Light Alloys*, Cambridge, Dong, H. (Ed.), 2010, pp. 110-180.
- [206] A. Venugopal, J. Srinath, L. Krishna, P. Narayanan, S. Sharma e P. Venkitakrishnan, «Corrosion and nanomechanical behaviors of plasma electrolytic oxidation coated AA7020-T6 aluminum alloy,» *Journal od Material Science Engineering A*, vol. 660, pp. 39-46, 2016.
- [207] F. Hossein e J. Mehdi, «Investigation on the corrosion behaviour and microstructure of 2024-T3 Al alloy treated via plasma electrolytic oxidation,» *Journal of Alloys and Compounds*, vol. 604, pp. 36-42, 2014.
- [208] N. Xiang, R. Song, H. Li, C. Wang, Q. Mao e Y. Xiong, «Study on Microstructure and Electrochemical Corrosion Behavior of PEO Coatings Formed on Aluminum Alloy,» *Journal of Materials Engineering and Performance*, vol. 24, pp. 5022-5031, 2015.
- [209] A. Yerokhin, X. Ni, A. Leyland, A. Matthews e S. Dowey, «Plasma electrolysis for surface engineering,» *Surface Coating Technology*, vol. 122, pp. 73-93, 1999.
- [210] X. M. M. Lu, C. Blawert, E. Matykina, R. Arrabal e U. Z. M. L. Kainer, «Plasma electrolytic oxidation coatings with particle additions – A review,» *Surface and Coatings Technology*, vol. 307, pp. 1165-1182, 2016.

- [211] H. Dong, in *Surface Engineering of Light Alloys*, Woodhead Publishing Limited, 2010, pp. 110-180.
- [212] S. Wernick, R. Pinner e P. Sheasby, *The surface treatment and finishing of aluminum and its alloys*, Teddington: Finishing Publications Ltd, 1987.
- [213] V. F. Henley, *Anodic oxidation of aluminium and its alloys*, Oxford: Pergamon Press, 1982.
- [214] J. Patel e N. Saka, «Microplasmic coatings,» *Am Ceram Soc Bull*, p. 27–29, 2001.
- [215] L. O. Snizhko, P. A. A.L. Yerokhin, N. L. Gurevina, D. Misnyankin, A. Leyland e A. Matthews, «Anodic processes in plasma electrolytic oxidation of aluminum in alkaline solutions,» *Electrochim Acta*, pp. 2085-2095, 2004.
- [216] F. H. Cao, L. Y. Lin, Z. Zhang, J. Zhang e C. Cao, «Environmental friendly plasma electrolytic oxidation of AM60magnesium alloy and its corrosion resistance,» *Trans Nonferrous Met Soc China*, pp. 240-247, 2008.
- [217] J. Martin, A. Melhem, I. Shchedrina, T. Duchanoy, A. Nominè, G. Henrion, T. Czerwiec e T. Belmonte, «Effects of electrical parameters on plasma electrolytic oxidation of aluminum,» *Surf Coat Technol*, pp. 70-76, 2013.
- [218] X. Lu, C. Blawert, U. Kainer e M. L. Zheludkevich, «Investigation of the formation mechanisms of plasma electrolytic oxidation coatings on Mg alloy AM50 using particles,» *Electrochimica Acta*, vol. 196, pp. 680-691, 2016.
- [219] X. Lu, C. Blawert, M. L. Zheludkevich e K. U. Kainer, «Insights into plasma electrolytic oxidation treatment with particle addition,» *Corrosion Science*, vol. 101, pp. 201-207, 2015.
- [220] X. Li e L. Li, «Discovery of Al₂O₃ particles incorporation mechanism in plasma electrolytic oxidation of AM60B magnesium alloy,» *Materials Letters*, vol. 86, pp. 88-91, 2012.
- [221] M. Mohedano, C. Blawert e M. L. Zheludkevich, «Silicate-based Plasma Electrolytic Oxidation (PEO) coatings with incorporated CeO₂ particles on AM50 magnesium alloy,» *Materials and Design*, vol. 86, pp. 735-744, 2015.
- [222] I. Sondi e B. Salopek-Sondi, «Silver nanoparticles as antimicrobial agent: a case study on E. coli as a model for Gram-negative bacteria,» *Journal of Colloid and Interface Science*, vol. 275, p. 177–182, 2004.
- [223] S. Prabhu e E. K. Poulouse, «Silver nanoparticles: mechanism of antimicrobial action, synthesis, medical applications, and toxicity effects,» *International Nano Letters*, 2012.
- [224] L. Yin, Y. Cheng, B. Espinasse, B. P. Colman, M. Auffan, M. Wiesner, J. Rose, J. Liu e E. S. Bernhardt, «More than the Ions: The Effects of Silver Nanoparticles on Lolium Multiflorum,» *Environ Sci Technol*, vol. 45, 2011.

- [225] S. Chernousova e M. Epple, «Silver as Antibacterial Agent: Ion, Nanoparticle, and Metal,» *Angew Chem Int Ed*, vol. 52, pp. 1636 - 1653, 2013.
- [226] A. J. Wesley, «History of the Medical Use of Silver,» *Surgical Infection*, vol. 10, 2009.
- [227] J. Young-Ki, H. K. Byung e J. Geunhwa, «Antifungal Activity of Silver Ions and Nanoparticles on Phytopathogenic Fungi,» *Plant Disease*, vol. 10, 2009.
- [228] C. C. Otto e S. E. Haydel, «Microbicidal clays: composition, activity, mechanism of action, and therapeutic applications,» *Microbial pathogens and strategies for combating them: science, technology and education*, pp. 1169-1180, 2013.
- [229] N. Gokdeniz e K. Asli, «The antifouling performance of gelcoats containing biocides and silver ions in seawater environment,» *J Coat Technol Res*, vol. 7, p. 139–143, 2010.
- [230] T. Liu, Y. Dong, T. G. N. He e F. Zhang, «Films with nanosilvers improve biocorrosion resistance of aluminium in sea water,» *Surface Engineering*, vol. 30, pp. 6-10, 2014.
- [231] M. L. W. Knetsch e L. H. Koole, «New Strategies in the Development of Antimicrobial Coatings: The Example of Increasing Usage of Silver and Silver Nanoparticles,» *Polymers*, vol. 3, pp. 340-366, 2011.
- [232] X. Liu, Y. Mou, S. Wu e H. Man, «Synthesis of silver-incorporated hydroxyapatite nanocomposites for antimicrobial implant coatings,» *Applied Surface Science*, vol. 273, p. 748– 757, 2013.
- [233] M. Długosz, M. Bulwan, G. N. M. Kania e S. Zapotoczny, «Hybrid calcium carbonate/polymer microparticles containing silver nanoparticles as antibacterial agents,» *J Nanopart Res*, vol. 14, pp. 1313-1321, 2012.
- [234] Y. Reyes-Vidala, R. Suarez-Rojas, C. Ruiz, J. Torres, S. Taluc, A. Méndez e G. Trejo, «Electrodeposition, characterization, and antibacterial activity of zinc/silver particle composite coatings,» *Applied Surface Science*, vol. 342, p. 34–41, 2015.
- [235] W. Sang, H. Jin, L. Kabir, S. Yun, S. Ji e S. Youn, «Antifungal Effects of Silver Nanoparticles (AgNPs) against Various Plant Pathogenic Fungi,» *Mycobiology*, vol. 40, pp. 53-58, 2012.
- [236] A. Nasrollahi, K. Pourshamsian e P. Mansourkiaee, «Antifungal activity of silver nanoparticles on some of fungi,» *International Journal of Nano Dimensions*, vol. 1, pp. 233-239, 2011.
- [237] M. Abdallah, E. Abd, M. El-Samawaty, M. Yassin, S. Sayed, S. Farooq, M. Elhindi, M. Bakri e M. Khan, «Antifungal silver nanoparticles: synthesis characterization and biological evaluation,» *Biotechnology and Biotechnological equipment*, vol. 30, pp. 56-62, 2016.

- [238] M. Valiollah, S. Naser e K. Fatemeh, «Evaluation of antifungal activity of silver nanoparticles against some phytopathogenic fungi and *Trichoderma harzianum*,» *Journal of Crop Protections*, vol. 4, pp. 291-300, 2015.
- [239] K. Keuk-Jun, W. Sung, S. Moon, J. Choi, J. Kim e D. Lee, «Antifungal Effect of Silver Nanoparticles on Dermatophytes,» *Journal of Microbiology Biotechnology*, vol. 18, p. 1482–1484, 2008.
- [240] J. Pulit, M. Banach, R. Szczygłowska e M. Bryk, «Nanosilver against fungi. Silver nanoparticles as an effective biocidal factor,» *Acta Biochimica Polonica*, vol. 60, p. 795–798, 2013.
- [241] J. Abkhoo e N. Panjehkeh, «Evaluation of Antifungal Activity of Silver Nanoparticles on *Fusarium Oxysporum*,» *Interantional Journal of Infection Desease*, vol. In press.
- [242] H. Lara, D. Romero-Urbina, J. Pierce, J. CLopez-Ribot, J. Arellano-Jiménez e M. Jose-Yacaman, «Effect of silver nanoparticles on *Candida albicans* biofilms: an ultrastructural study,» *Journal of Nanobiotechnology*, vol. 13, p. 91, 2015.
- [243] D. Monteiro, L. Gorup, S. Silva, M. Negri, E. de Camargo, R. Oliveira, D. Barbosa e M. Henriques, «Silver colloidal nanoparticles: antifungal effect against adhered cells and biofilms of *Candida albicans* and *Candida glabrata*,» *Biofouling*, vol. 27, p. 711–719, 2011.
- [244] D. Wojcieszak, M. Mazur, D. Kaczmarek, P. Mazur, B. Szponar, J. Domaradzki e L. Kepinski, «Influence of the surface properties on bactericidal and fungicidal activity of magnetron sputtered Ti–Ag and Nb–Ag thin films,» *Materials Science and Engineering C*, vol. 62, p. 86–95, 2016.
- [245] Y. Kamikawa, D. Hirabayashi, T. Nagayama, J. Fujisaki, T. Hamada, R. Sakamoto, Y. Kamikawa e K. Sugiharak, «In Vitro Antifungal Activity against Oral *Candida* Species Using a Denture Base Coated with Silver Nanoparticles,» *Journal of Nanomaterials*, pp. 1-6, 2014.
- [246] M. Seah, D. Briggs e J. Seah, «Practical Surface Analysis,» *Auger and X-ray Photoelectron Spectroscopy*, vol. 1, p. 543, 1990.
- [247] «X-ray Photoelectron Spectroscopy Database 20,» National Institute of Standards and Technology, Gaithersburg.
- [248] [Online]. Available: <http://srdata.nist.gov/XPS>.
- [249] S. Chuanyu e Y. Wang, «Influence of electrolyte parameters on the properties of the ceramic coatings deposited on aluminum alloy by plasma electrolytic oxidation,» *Powder Metallurgy and Metal Ceramics*, vol. 54, pp. 101-105, 2015.
- [250] Q. B. Li, C. C. Liu, W. B. . Yang e J. Liang, «Growth mechanism and adhesion of PEO coatings on 2024Al alloy,» *Surface Engineering*, 2016.

- [251] A. Ayday e M. Durman, «Growth Characteristics of Plasma Electrolytic Oxidation Coatings on Aluminum Alloys,» *Acta Physica Polonica A*, vol. 127, pp. 886-887, 2015.
- [252] L. Pezzato, K. Brunelli e M. Dabalà, «Corrosion properties of plasma electrolytic oxidation coated 7075 treated using an electrolyte containing lanthanum-salts,» *Surface and Interface Analysis*, vol. 48, pp. 729-738, 2016.
- [253] S. Wannaparhun, S. Seal e V. Desai, «Surface chemistry of Nextel-720, alumina and Nextel-720/alumina ceramic matrix composite (CMC) using XPS—A tool for nano-spectroscopy,» *Applied Surface Science*, vol. 185, p. 183–196, 2002.
- [254] C. Blawert, W. Dietzel, E. Ghali e G. Song, «Anodizing treatments for magnesium alloys and their effect on corrosion resistance in various environments,» *Advanced Engineering Materials*, vol. 8, pp. 511-533, 2006.
- [255] J. P. Ruparelia, A. K. Chatterjee, S. P. Duttagupta e S. Mukherji, «Strain specificity in antimicrobial activity of silver and copper nanoparticles,» *Acta Biomaterialia*, vol. 4, p. 707–716, 2008.
- [256] A. G. Hassabo, A. A. Nada, H. M. Ibrahim e N. Y. Abou-Zeid, «Impregnation of silver nanoparticles into polysaccharide substrates and their properties,» *Carbohydrate Polymers*, vol. 122, p. 343–350, 2015.
- [257] W. Li, X. Xie, Q. Shi, S. Duan, Y. Ouyang e Y. Chen, «Antibacterial effect of silver nanoparticles on *Staphylococcus aureus*,» *BioMetals*, vol. 24, p. 135–141, 2011.
- [258] W. K. Jung, H. C. Koo, K. W. Kim, S. Shin, S. H. Kim e P. Y. H., «Antibacterial Activity and Mechanism of Action of the Silver Ion in *Staphylococcus aureus* and *Escherichia coli*,» *Applied and Environmental Microbiology*, vol. 74, pp. 2171-2178, 2008.
- [259] N. R. Chowdhury, M. MacGregor-Ramiasa, P. Zilm, P. Majewski e K. Vasilev, «‘Chocolate’ silver nanoparticles: Synthesis, antibacterial activity and cytotoxicity,» *Journal of Colloid and Interface Science*, vol. 482, p. 151–158, 2016.
- [260] C. Holtyn, «The Age of Ships,» Society of Naval Architects and Marine Engineers, 1966.
- [261] R. G. Allan, «Applications for Aluminum Alloys in the Marine Industry a Current Perspective,» *Alumitech 97*, Atlanta, 1997.
- [262] C. H. Holtyn, «The Construction and Service Record of a 306 Ft. Aluminum Trailership,» Society of Naval Architects and Marine Engineers, 1972.
- [263] ASM Handbook: Corrosion, 1994.
- [264] ASM Handbook: Aluminum, 1994.
- [265] S. Brown, Feasibility of Replacing Structural Steel with Aluminum Alloys in the Shipbuilding Industry, University of Wisconsin-Madison, 1999.
- [266] J. R. Davis, «ASM International,» 1999.

- [267] S. Satheesh, M. A. Ba-akdah e L. A. Al-Sofyani, «Natural antifouling compound production by microbes associated with marine macroorganisms — A review,» *Electron. J. Biotechnol.*, vol. 21, pp. 26-35, 2016.
- [268] M. Wahl, «Living attached: Aufwuchs, fouling, epibiosis,» in *Fouling organisms of the Indian ocean: Biology and control technology*, New Delhi, R. Nagabhushanam, M. Thompson, 1997, p. 31–84.
- [269] J. Maki, «Biofouling in the marine environment,» in *Encyclopedia of environmental microbiology*, New York, Wiley & Sons, 2002, p. 610–619.
- [270] D. Gerhart, D. Rittschof e S. Mayo, «Chemical ecology and the search for marine antifoulants — Studies of a predator–prey symbiosis,» *J. Chem. Ecol.*, vol. 24, p. 1905–1917, 1988.
- [271] E. Armstrong, K. Boyd, A. Pisacane, C. Peppiatt e J. Burgess, «Marine microbial natural products in antifouling coatings,» *Biofouling*, vol. 16, p. 215–224, 2000.
- [272] S. Qi, S. Zhang, L. Yang e P. Qian, «Antifouling and antibacterial compounds from the gorgonians *Subergorgia suberosa* and *Scripearia gracillis*,» *Nat. Prod. Res.*, vol. 22, p. 154–166, 2008.
- [273] R. G. J. De Nys, «The impact and control of biofouling in marine finfish aquaculture,» in *Advances in marine antifouling coatings and technologies*, Cambridge, C. Hellio, D. Yebra, 2009, p. 177–221.
- [274] M. Callow e J. Callow, «Marine biofouling: A sticky problem,» *Biologist*, vol. 49, p. 10–4, 2002.
- [275] L. Jackson, «Marine biofouling: An assessment of risks and management initiatives,» in *Global invasive species programme*, 2008.
- [276] L. Chambers, K. Stokes, F. Walsh e R. Wood, «Modern approaches to marine antifouling coatings,» *Surf. Coat. Technol.*, vol. 201, p. 3642–3652, 2006.
- [277] R. Tang e J. Cooney, «Effects of Marine Paints on Microbial Biofilms Development on Three Materials,» *J. Ind. Microbiol. Biot.*, vol. 20, p. 275–280, 1998.
- [278] Y. Yonehara, «Recent Topics on Marine Antifouling Coatings,» *Bull. Soc. Sea Water Sci*, vol. 54, p. 7–12, 2000.
- [279] G. Naser e A. Kacar, «The antifouling performance of gelcoats containing biocides and silver ions in seawater environment,» *J. Coat. Technol. Res.*, vol. 7, p. 139–143, 2010.
- [280] M. Selim, S. El-Safty, M. El-Sockary, A. Hashem, O. Abo Elenien, A. EL-Saeed e N. Fathallahe, «Modeling of spherical silver nanoparticles in silicone-based nanocomposites for marine antifouling,» *RSC Advances*, vol. 7, pp. 63175-63185, 2015.

- [281] T. Szabó, J. Mihály, I. Sajó, J. Telegdi e L. Nyikosa, «One-pot synthesis of gelatin-based, slow-release polymer microparticles containing silver nanoparticles and their application in anti-fouling paint,» *Prog. Org. Coat.*, vol. 7, pp. 1226-1232, 2014.
- [282] C. Ho, J. Tobis, C. Sprich, R. Thomann e J. Tiller, «Nanoseparated Polymetric Networks with Multiple Antimicrobial Properties,» *Adv. Mater.*, vol. 12, p. 957-961, 2004.
- [283] M. Callow, «Ship fouling. Problems and solutions,» *Chemistry and Industry*, vol. 5, pp. 123-127, 1990.
- [284] B. Del Amo, C. Giudice e G. Villoria, «Evaluating anti-fouling paints,» *Eur. Coat. J.*, vol. 1, pp. 8-14, 1990.
- [285] Y. Nirvan, C. P. De e D. Kumar, «Copper Based Antifouling Paints for Prevention of Marine Growth on Ship Hulls,» *Def. Sci. J.*, vol. 32, pp. 55-66, 1982.
- [286] B. B. Moreton, «Copper alloys in marine environments today and tomorrow- part II,» *Corrosion Prevention and Control*, vol. 33, pp. 17-20, 1986.
- [287] G. Williams, A. Coleman e H. McMurray, «Inhibition of Aluminium Alloy AA2024-T3 pitting corrosion by copper complexing compounds,» *Electrochim. Acta.*, vol. 55, p. 5947-5958, 2010.
- [288] Y. González-García, J. Mol, T. Muselle, I. De Graeve, G. Van Assche e G. Scheltjens, «A combined mechanical, microscopic and local electrochemical evaluation of self-healing properties of shape-memory polyurethane coatings,» *Electrochim. Acta.*, vol. 56, p. 9619-9626, 2011.
- [289] P. Whiteside, E. Matykina, J. Gough, P. Skeldon e G. Thompson, «In vitro evaluation of cell proliferation and collagen synthesis on titanium following plasma electrolytic oxidation,» *J Biomed Mater Res A*, vol. 94, pp. 38-46, 2010.
- [290] P. Molino e R. Wetherbee, «The biology of biofouling diatoms and their role in the development of microbial slimes,» *Biofouling*, vol. 24, pp. 365-379, 2008.
- [291] S. A. D. J. S. Patro, «Fouling diatoms of Andaman waters and their inhibition by spinal extracts of the sea urchin *Diadema setosum*,» *Int. Biodeterior. Biodegrad.*, vol. 75, pp. 23-27, 2012.
- [292] P. Tanskanen, in *Electronics Waste: Recycling of Mobile Phones, Post-Consumer Waste Recycling and Optimal Production*, Enri Damanhuri, 2012, pp. 129-150.
- [293] P. A. Kohl, *Modern Electroplating*, 2010.
- [294] D. M. M. Z. G. Bettinelli M., *Impiego dell'ICP-AES nel Laboratorio Chimico: Criteri per la stesura di metodi normalizzati*, 1993.
- [295] [Online]. Available: <http://goldprice.org/spot-gold.html>.
- [296] [Online]. Available: <http://www.sciencedaily.com/releases/2012/07/120706164159.htm>.

- [297] [Online]. Available: <http://www.umicore.com>.
- [298] [Online]. Available: <http://www.wastemamagementrecycling.com>.
- [299] [Online]. Available: <http://www.sonosys.com>.
- [300] [Online]. Available: <http://e-waste-darkside-of-the-technicaladvance.synthasite.com/effects.php>.
- [301] E. Sum, «The recovery of metals from electronic scrap,» *JOM*, vol. 43, pp. 53-61, 1991.
- [302] J. Hoffmann, «Recovering precious metals from electronic scrap,» *JOM*, vol. 44, pp. 43-48, 1992.
- [303] J. Li e J. D. Miller, «Mineral processin and extractive metallurgy review,» vol. 27, pp. 177-214, 2006.
- [304] S. Zheng, Y.-y. Wang e L.-y. Chai, «Research status and prospect of gold leaching in alkaline thiourea solution,» *Minerals Engineering*, vol. 19, pp. 1301-1306, 2006.
- [305] J. Zhang, S. Shen, Y. Cheng, H. Lan, X. Hu e F. Wang, «Dual lixiviant leaching process for extraction and recovery of gold from ores at room temperature,» *Hydrometallurgy*, pp. 114-123, 2014.
- [306] H. Zhang, I. M. Ritchie e S. R. La Brooy, «Electrochemical oxidation of gold and thiourea in acidic thiourea solutions,» *Journal of The Electrochemical Society*, vol. 148, pp. 146-151, 2001.
- [307] F. Xie, H. Li, Y. Ma, C. Li, T. Cai, Z. Huang e G. Yuan, «The ultrasonically assisted metals recovery treatment of printed circuit board waste sludge by leaching separation,» *Journal of Hazardous Materials*, vol. 170, pp. 430-435, 2009.
- [308] S. Wu, «Preparation of fine copper powder using ascorbic acid as reducing agent and its application in MLCC,» *Materials Letters*, vol. 61, p. 1125–1129, 2007.
- [309] S. Ubaldini, P. Fornari, R. Massidda e C. Abbruzzese, «An innovative thiourea gold leaching process,» *Hydrometallurgy*, vol. 48, pp. 113-124, 1998.
- [310] I. Tremblay, G. Deschenes, E. Ghali, J. McMullen e M. Lanouette, «Gold recovery from a sulphide bearing gold ore by percolation leaching with thiourea,» *International Juornal of Mineral Processing*, vol. 48, pp. 225-244, 1996.
- [311] K. Pyrzynska, «Recent developments in the determination of gold by atomic spectrometry techniques,» *Spectrochimica Acta B*, vol. 60, pp. 1316-1322, 2005.
- [312] M. S. Oncel, M. Ince e M. Bayramoglu, «Leaching of silver from solid waste using ultrasound assisted thiourea method,» *Ultrasonics Sonochemistry*, vol. 12, pp. 237-242, 2005.
- [313] P. Lacoste-Bouchet, G. Deschenes e E. Ghali, «Thiourea leaching of a copper-gold ore using statistical design,» *Hydrometallurgy*, vol. 47, pp. 189-203, 1998.

- [314] A. C. Kasper, G. Berselli, B. D. Freitas, J. A. S. Tenório, A. M. Bernardes e H. M. Veit, «Printed wiring boards for mobile phones: characterization and recycling of copper,» *Wastes Management*, vol. 31, pp. 2536-2545, 2011.
- [315] C. M. Juárez e A. Duntra, «Gold electrowinning from thiourea solutions,» *Minerals Engineering*, vol. 13, pp. 1083-1096, 2000.
- [316] L. D. T. Igor V. Minorov, «Complexation of copper(I) by thiourea in acidic aqueous solution,» *Journal of Solution Chemistry*, vol. 25, pp. 315-325, 1996.
- [317] S. G. K. J. K. O. Hwa Young Lee, «Cementation behavior of gold and silver onto Zn, Al, and Fe powders from acid thiourea solutions,» *Canadian Metallurgical Quarterly*, vol. 36, pp. 149-155, 1997.
- [318] T. Groenewald, «Potential applications of thiourea in the processing of gold,» *Journal of the south african institute of mining and metallurgy*, pp. 217-223, 1977.
- [319] H. .. Gomez, H. Lizama, C. Suarez e A. Valenzuela, «Effect of thiourea concentration on the electrochemical behavior of gold and copper electrodes in presence and absence of Cu (II) ions,» *Journal of the Chilean Chemical Society*, vol. 54, pp. 439-444, 2009.
- [320] J. Ficeriova, P. Balaz, E. Dutková e E. Gock, «Leaching of gold and silver from crushed Au-Ag wastes,» *The Open Chemical Engineering Journal*, vol. 2, pp. 6-9, 2008.
- [321] M. E. P. Díaz, I. Gonzàles e G. T. Lapidus, «Electrodeposition of a silver-gold alloy (DORE) from thiourea solutions in the presence of other metallic ion impurities,» *Hydrometallurgy*, vol. 93, pp. 23-39, 2008.
- [322] C. K. Chen, T. Lung e C. C. Wan, «A study of the leaching of gold and silver by acidothioureation,» *Hydrometallurgy*, vol. 5, pp. 207-212, 1980.
- [323] A. E. Bolzàn, R. Piatti e A. Arvia, «Electrochemical processes at gold|thiourea-containing aqueous acid solution interfaces,» *Journal of Electroanalytical Chemistry*, vol. 552, pp. 19-34, 2003.
- [324] J. Bang e K. Suslick, «Applications of ultrasound to the synthesis of nanostructured materials,» *Advanced Materials*, vol. 22, p. 103, 2010.
- [325] N. De La Calle, M. Cabaleiro, F. Costas, S. Pena, I. Gil e C. B. Lavilla, «Ultrasound-assisted extraction of gold and silver from environmental samples using different extractants followed by electrothermal-atomic absorption spectrometry,» *Microchemical Journal*, vol. 97, pp. 93-100, 2001.

Acknowledgments

This work was possible thanks to the help of many people.

First of all, I thank Luca Pezzato, who not only help me during my activity in the labs but also every time I have to fill one of the infinite forms of University (he is the bureaucrat of our research group).

I thank also Katya Brunelli who actually writes or re-writes all my articles, reports and everything written during these three years.

I have also to thank prof. Dabalà who gave me the opportunity of this PhD and the other professors I collaborate with.

I have also to thank Giulia Zanmarchi and Mauro Gobbin for their great patience, Claudio Gennari and Alberto Conte for their very great helpfulness and Claudio Cason for his infinite idio... syncratic humor.

I would like to thank Mattia Lago and Alessio Settimi who also help me a lot in the labs.

Moreover, I have to thanks also all the students and friends I work with: actually most of this work was carried on during their thesis preparation.

Moreover, thank to Michele Toldo, Alberto Franzo, Joele Toldo, Roberto Zamparini and to the companies which helped me during my PhD: FOC Ciscato, IEIS, IVR and Relight.

Last but not least, I would like to thank particularly my parents for their support and all my family.

Thanks also to the CUAMM which has hosted me in the last months and to the good friends I met there. Thanks also to Claudia, actually not only because she hosted me in her apartment.

Finally and less seriously: thanks to El bastijo and El Barrio, il Sabbione, Frank Fioren e Frank Palmer, I Raketten, I miei capanni, La Canzone di Natale, la Pasticcery, and everything beautiful happened during these years.





